



Remote Sensing Probe for the Venusian  
Atmosphere and Tectonics



BLOON

balloon  
local  
observation &  
orbiter  
network

Group 14



This page is intentionally left blank.

# Design Synthesis Exercise

# Remote Sensing Probe for the Venusian Atmosphere and Tectonics

## Final Report

by

### Group 14

K. De hulsters	4649486	G.M.J. van den Dungen	4554566
P.R. Gijsberts	4435133	Q.E. van Woerkom	4676998
S. Lee	4653777	J. Vrijenhoek	4656318
M.R. Menken	4559134	M. Zaremba	4673603
S. Orbons	4668359	V. Santos Costa	4473779
L.P.J. Sträter	4672224		

Project duration: April 20 - July 1, 2020

Tutors:	Dr.ir. F.F.J. Schrijer	TU Delft, Aerodynamics
	Dr.ir. A.H. van Zuijlen	TU Delft, Aerodynamics
Coaches:	Ir. M. Rovira Navarro	TU Delft, Astrodynamics & Space Missions
	Dr. S. Speretta	TU Delft, Space Systems Engineering

# Executive Summary

While Venus is similar to Earth in many ways, the conditions on the planet are in other ways vastly different from any other place in the solar system. Many extreme phenomena found on the planet are not fully understood and research regarding seismic activity on the planet is limited. Therefore, the mission need statement has been defined as: **Design a mission to measure Venus atmospheric conditions and tectonic activity.** This resulted in the following project objective statement: **Design a system to perform in-situ measurements of the Venusian atmospheric conditions and tectonic activity of the crust for 100 terrestrial days, with 11 students over 10 weeks time.** The mission has been named BLOON, which stands for 'Balloon Local Observatory & Orbiter Network'. Firstly, an explanation of the scientific objectives and user requirements is given, followed by more detailed overviews of the different design aspects.

**Scientific objectives and requirements** The scientific goals of BLOON concern the biggest unanswered questions of Venus: the behaviour of its atmospheric and interior dynamics. Besides being curious about Venus as a planet, as humanity learns more about our inhospitable sister planet, we also began to question what can be learned about climate change on Earth from looking at the Venusian greenhouse effect. Thus, BLOON aims to answer the most pertinent question posed by scientific investigators for Venus missions: **What does the Venusian runaway greenhouse effect tell us about the climate on Earth?** Research towards the atmospheric composition and chemical species of the planet will help to get a complete view of the current state and evolution of the Venusian atmosphere. This way, BLOON can try to figure out why Venus evolved to be as it is today and how its runaway greenhouse effect may have taken place. Additionally, the interior dynamics of Venus have not been studied in detail to date, which means that research towards tectonic activity on the planet will have significant scientific value. BLOON is the first mission proposal to incorporate revolutionary seismic studies from a remote airborne station on a planet other than Earth. This will shed light on the question: **How active is the interior of Venus?.** To research these scientific questions three main scientific objectives were set:

- **Atmospheric composition:** Investigate the abundance and isotopic ratios of chemical species in the upper-cloud layer.
- **Atmospheric dynamics:** Investigate meteorological phenomena to validate climate models.
- **Interior dynamics:** Place constraints on the structure and dynamics of the interior.

An analysis of the user requirements shows that all of the user requirements for the BLOON mission can be met. These requirements regard the operational altitude, scientific instruments, measurement resolution, sustainability rules, launcher and payload size and cost budgets. The only exception to this are the requirements regarding reliability. US-SARE-01 and US-SARE-02 mention that the reliability of the singular elements of the mission should be at least 90% and that the probability that 50% of the smaller probes, mentioned later in this executive summary, survive, should be 90%. While the subsystems have been designed to fulfil this requirement, they can not officially be ticked off until testing on a prototype or finished product has been performed to assess its reliability. So, while the requirements are expected to be fulfilled, more research into reliability is recommended before these requirements can be officially ticked off.

**Market analysis** A market analysis flows from the requirements and scientific interests. This market analysis was made by looking into similar previous missions, identifying the relevant stakeholders and performing a SWOT analysis. The previous missions can be used to put a cap on the total mission cost. Furthermore, it was apparent that the BLOON mission should consider a ESA/NASA collaboration. Using ESA Cosmic vision M-class category, which has a funding cap of €500 million, and the NASA frontier category with a budget cap of \$ 850, a budget cap of €750 million was determined. As this category is competitive, the BLOON mission should make use of its strengths and work around its weaknesses. Several identified strengths are that the aerobot carries an innovative seismology suite and that it provides in-situ measurements for a long duration (100 days), while dropsondes are reaching even lower altitudes. With these strengths the mission will be viable in the current market.

**Trade-off and final design** The BLOON mission reached a final design over multiple iterations. While only one concept was chosen in the end, it is also important to first mention which design options did not make the final cut. Firstly, it was decided that the mission should have both an atmospheric segment to perform measurements and a space segment to relay the data. For the space segment, the last two designs left were a single satellite or a satellite with CubeSats that take over some of the tasks of the main satellite. However, due to the risk and issues with the communication budget, the single satellite option was chosen. For the atmospheric segment, also known as the aerobot, the last two options were a variable-altitude balloon that also goes below the cloud layer of Venus or a constant altitude balloon that stays above the clouds and uses small probes, called dropsondes to perform low altitude measurements. Due to the increased mass, issues with the communication budget, power generation and high cost of the variable-altitude balloon, the constant altitude balloon was chosen.

Thus the final design of the mission consists of multiple elements. There is an aerobot, which is a high-altitude balloon that orbits at an altitude of 60 km and includes a gondola with scientific payload. The gondola is suspended on a 50 m long tether from the balloon. 25 dropsondes are placed in the gondola and are dropped at fixed time intervals to perform measurements lower in the Venusian atmosphere. A relay satellite, known as the orbiter, orbits Venus in a highly elliptical orbit and performs some scientific measurements, such as mass spectrometry and cloud imaging. During launch the mission elements are locked inside the launch vehicle. The aerobot is encased in an aeroshell that will protect it during the atmospheric entry. Before the aeroshell enters the atmosphere, it is attached to a transfer module (TRM) that provides its payload of power and performs orbital manoeuvres. The lifetime of the mission consists of multiple steps and phases and involved all of these mission segments. It is summarised with the timeline in Figure 1.

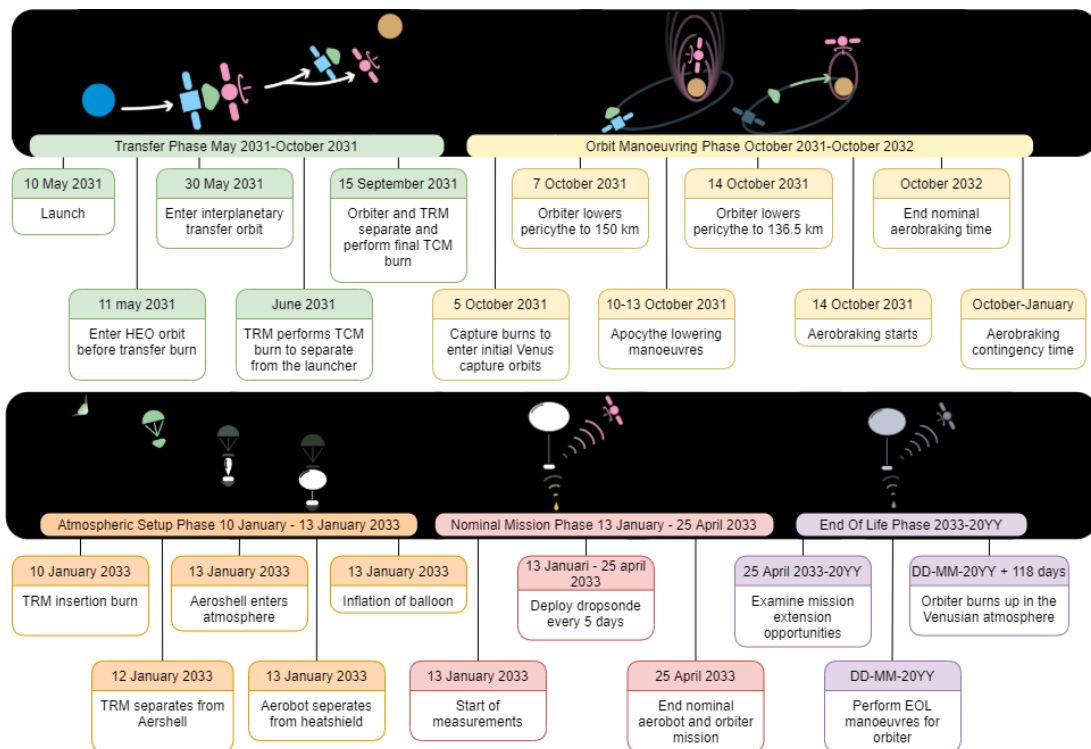


Figure 1: Mission timeline of the BLOON mission

**Instrumentation and planetary science** The scientific mission is divided between the aerobot and the orbiter. The aerobot contains instruments to characterise the atmospheric composition, meteorological processes and conduct seismology observations at 60 km altitude. Investigating the abundance and isotopic ratios of chemical species is done with a trace gas, noble gas and atmospheric compositional analysis suite consisting of a gas chromatograph, neutral mass spectrometer, tunable laser spectrometer, noble gas mass spectrometer, and X-ray fluorescence spectrometer. This is further accompanied with a nephelometer to detect the concentration of aerosols. Moreover the atmospheric dynamics of the upper cloud layer is studied by a meteorology suite consisting of temperature, pressure and accelerometers to measure wind

velocities and perturbations. The seismology measurements is performed by measuring the pressure with two microbarometers that are separated by the 50 m tether. This way an infrasound pressure wave caused by seismic activity in the Venusian crust can be spotted. As mentioned earlier, the aerobot houses 25 dropsondes that carry miniaturised instrumentation for measuring the meteorological processes at the lower altitude levels: temperature, pressure, accelerations and thus velocity. Chemical species could also be measured by dropsondes, but this is to be analysed in a later design stage. A dropsonde is released every 5 days, and during its descent it will conduct sampling while continuously transmitting data back to the aerobot. The orbiter carries two instruments: a context camera to take images of the upper cloud layer and a mass spectrometer to characterise the atmospheric composition at low orbit. The context camera has a large field of view (FOV) mode of 38.5 degrees and a narrow more of 1.7 degrees. The last mode can be used to get the highest resolution imaging, down to 6 m/pixel at pericytherion.

**Astrodynamics** In order to reach Venus, the Falcon 9 launcher will be used. The chosen launch window is in 2031 where the BLOON mission will arrive on Venus on the 5th of October. This configuration allows the Falcon 9 to take around 3960 kg to Venus. It is assumed that the Falcon 9 will perform the escape burn, while the BLOON performs the Venus orbit insertion burns and all subsequent burns. During the interplanetary travel two correction burns are performed, one to separate away from the launch vehicle and one to set the inclination of the capture orbit.

The orbiter will end in a polar capture orbit while the TRM will enter Venus on a  $12.5^\circ$  inclination orbit, in order to insert the aeroshell at a latitude of  $20^\circ$ . After insertion, the orbiter will perform manoeuvres to enter an aerobraking orbit. The aerobraking will be used to lower the apocytherion of the orbiter down to its science orbit, taking a period of 456 days (including contingency). If the operational orbit is reached earlier, the mission can already start, since the data storage on the orbiter has been sized to store all data generated during the nominal mission. The characteristics of the orbiter's science orbit are shown in Table 1.

Table 1: Mission orbit for the BLOON orbiter.

Parameter	Value	Unit
Pericytherion	6251.8	km
Apocytherion	18383.8	km
Semimajor axis	12317.8	km
Orbital period	251.2	mins
Inclination	20	deg

While the orbiter is aerobraking, the TRM will remain in its capture orbit until insertion. This causes a lot of orbital degradation due to third body sun perturbations. Further analysis of this and optimisation of the orbit has to be performed. From the current analysis, the final orbit of the TRM, after the aerobraking period, has an apocytherion of roughly 22,000 km above the center of Venus and a pericytherion of 11,000 km above the center. The inclination does however not change. This orbit is then taken for the analysis of the atmospheric entry of the aeroshell. For entry, this orbit will have its pericytherion reduced to 50 km.

**Atmospheric entry** After the desired orbit around Venus is reached, the aeroshell commences its entry into the atmosphere of Venus at an altitude of 250 km. During this entry it will reach a peak deceleration of  $367 \text{ m/s}^2$ , 130.9 seconds after reaching an altitude of 250 km. While decelerating, the internal payload must be protected from the heat generation. The heat loads are computed using the Fay-Riddell and Tauber models for respectively convection and radiation. This gave a peak heat flux of  $773.5 \text{ W/cm}^2$  and a total heat load of  $17,206.3 \text{ J/cm}^2$ . To keep the internal components cool, a thermal protection system is applied to the aeroshell. This consists of PICA ablative material, which will absorb the incoming heat flux and slowly char. The material is sized such that a sufficient thickness remains to ensure insulation from the boundary layer temperature. At Mach 1.7, a drogue parachute with a diameter of 3.7 m is deployed with a mortar to stabilise the aeroshell. At Mach 0.8, the heat shield is discarded. At Mach 0.3, the main parachute with a diameter of 6 m is deployed by the drogue parachute, which will be used to slow down the segment to 30 m/s at a 55 km altitude. At this altitude, the rest of the aeroshell will be discarded.

At 55 km the balloon will be stretched out between the chute and the payload, and starts inflating itself via the use of off-the-shelf helium high pressure vessels, as shown in Figure 2. After the balloon is filled with gas, the inflation system is dropped and the balloon floats upwards. As the helium density decreases, the volume of balloon increases until an equilibrium is reached at an altitude of 60 km above the surface.

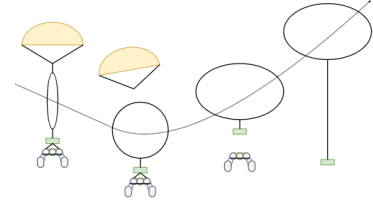


Figure 2: Aerobot deployment stages

**Aerobot aerodynamics** After entry has taken place, the aerobot stays afloat in the atmosphere for 100 days using its 11.5 m diameter superpressure balloon. The working principle behind this balloon is that it is overfilled with lifting gas. At a certain altitude a constant balloon volume is reached. The excess helium causes the lifting gas to maintain a positive pressure difference with the atmosphere, which is called the superpressure. The superpressure aids the balloon in maintaining a constant-density level and improves resistance to atmospheric disturbances, like temperature variations and wind gusts.

**Propulsion** In order to make sure that all elements of the mission can reach their destination, as described earlier in detail, the propulsion subsystem needed to be sized. The two main areas that were analysed for this were the  $\Delta V$  budget and the tank sizing. It was chosen to use a combination of MON-1.3 and MMH bi-propellant. The S400-15 Apogee motor thruster will be used as main thruster of the BLOON vehicles. The the  $\Delta V$  budget and resulting propellant masses are shown below in Table 2.

Table 2: Propellant mass required for mission operations. The propellant mass was computed using Tsiolkovski's equation. The  $\Delta V$  required shown here also includes a safety margin.

Concerns	Manoeuvre	$\Delta V$ (m/s)	Wet mass start	MON-1.3/MMH (kg)
Orbiter	Total	1427	718	264
TRM	Total	1170	2167	668
Both	Total	-	2885	932

Four tanks were designed for the orbiter and the TRM, two main bi-propellant tanks and two helium tanks for each. The bi-propellant tanks are pressurised to 18 bar while the helium tanks have an initial pressure of 300 bar. The helium tanks are used as pressurant for the bi-propellant tanks. Each tank was assumed to be made out of Ti6Al4V alloy, which is likely an overestimation of the mass. In reality a carbon fibre outer shell would be made along with an inner shell made out of titanium in order to minimise weight. An oxidiser fuel ratio of 1.65 was chosen in order to obtain equally sized tanks. This is done in order to simplify manufacturing and the layout of the orbiter and TRM.

**Telemetry, tracking and command** Besides making ensuring the mission arrives at the right location at the right time, it is also important that all the data can be stored and sent back to the ground station. For this the telemetry, tracking and command (TTC) subsystem exists with a detailed design of the antennas, tracking methods and hardware. All user requirements set up in the baseline report regarding TTC are fulfilled. For telemetry, a high gain Ka-, X-, S-band antenna is used on the orbiter as the main link along with two smaller low gain antennas, used for a continuous beacon mode signal that sends the health status of all mission elements back to the ground station. The aerobot communicates using a low gain S-band antenna. Link budget calculations show that all connections close with a 9.6 dB limit for uplink and 1.7 dB limit for downlink, including uncertainty evaluated in a sensitivity analysis. The aforementioned orbital characteristics were partly based on the communication time possible between the aerobot and the orbiter and have been sized such that all data can be sent with a safety factor of 2.

For tracking, two-way ranging at X- and Ka-band is used to determine the initial position in combination with computer models of the orbits of mission elements. Afterwards, Doppler tracking is used to determine the relative speed of the tracked objects. Infrequent very-long-baseline interferometry (VLBI) measurements are used for calibration. For command and data handling, sizing of the on-board computers

---

and required storage was performed. The orbiter contains enough storage for the entirety of the 100 day mission. The aerobot storage allows science storage up to 6 orbits. It was decided to keep the antenna of the orbiter pointed away from Earth for five consecutive orbits to collect aerobot and orbiter measurements and to use every sixth orbit to relay the data back to Earth. The use of redundancies and safety margins has reduced the risks associated with the TTC subsystem to an acceptable level.

**Electrical power supply** To allow each of the subsystems to perform their function, all mission elements should receive the required power. For this, all segments are provided with an electrical power supply. Four out of five power systems are based on a fully-regulated 28 V bus. This has advantages with respect to the stability of the photovoltaic power generation, but is also beneficial for interoperability of the aerobot, aeroshell, and TRM, which are connected for most of the mission. Only the dropsonde operates at a lower voltage, due to the limited mass available.

Power generation is achieved using solar arrays for the aerobot, orbiter, and TRM, because of their long lifetime. This does mean that eclipses must be covered with secondary batteries, and that extensive power management is required. The aeroshell and dropsondes carry primary batteries to cover their shorter operational lifetime, making for considerably simpler and lighter architectures. Most limiting in terms of operational feasibility is the power system of the aerobot, which is limited by lower solar irradiances near the poles and uncertainty in its eclipse time. Radioisotope power remains an alternative that can solve these problems, but is not favoured for its durability penalty.

**Thermal control** Due to extreme conditions on Venus and outer space, the thermal subsystem is crucial to make sure that the mission can succeed. Thermal design has been performed for all segments of the mission. To set up the overall temperature range of each segment, the operational temperatures of each component used in the mission was collected. Before starting with the design, the environmental conditions were analysed. This was done to find the heat fluxes in and out the segments. With the temperature ranges set in place and the environmental conditions defined, the thermal design was performed. For the orbiter and TRM, this consists of multi layer insulation to limit the heat influx, louvres to be able to control the heat radiating away, kapton heaters to heat up the segments during eclipse and a control system to monitor the internal temperature and switch the heaters on and off. Furthermore to make sure the internal heat is evenly distributed, the interior structure is coated with a high emissivity black coating and heat pipes are applied that will transfer heat.

The thermal control subsystem of the gondola and dropsondes both consist of rigid polymer foam for insulation with a white paint surface finish to lower absorptance and increase emissivity. Furthermore, the gondola also has a phase changing material unit, to decrease temperature differences during the night and day cycle, electrical patch heaters to locally increase the temperature and a control system to control this heater. By using these subsystems, the temperature variation of the mission elements stays within the allowed range for all of its equipment.

**Attitude determination and control** Another subsystem that is crucial to the functioning of the mission is the attitude determination and control system (ADCS). This subsystem is required on both the BLOON orbiter and TRM. As the manoeuvres of the orbiter are most time constraint and the required pointing accuracy is high, the orbiter's ADCS is the primary focus of the design. Honeywell HR061 momentum wheels and Jena-Optronik Astro 10 star sensors are selected and reaction control system thrusters are sized to provide 1 Nm torque, this enables the orbiter to control its attitude within the performance requirements. The orbiter will encounter slew rates of 0.5 deg/s during orbit insertion and a rate of 1.1 deg/s is possible for attitude changing manoeuvres between Earth pointing and aerobot pointing. All in all, the orbiter can perform a 180 degree roll manoeuvre in roughly 5 minutes and a 180 degree pitch manoeuvre in about 6 minutes.

Furthermore, the BLOON aerobot will have a passive altitude control system that is inherent to a super-pressure balloon. The aerobot will not be able to control its attitude, which is one of the reasons it has a pointable low gain antenna to allow communications with the orbiter. Similarly the dropsondes have no attitude control, but are designed to have stability during the drop from 60 to 25 km. The use of a patch antenna with a high beam width makes sure no attitude control is required.

**Structures and materials** The structures and materials subsystem ensures that the structural configuration allows for the requirements to be fulfilled. A structural configuration was made for the atmospheric segment by integrating the subsystem items for the aeroshell, dropsonde and gondola. The dropsonde consists of a glass-fibre reinforced pressure vessel with a teardrop-like tail, while the gondola will be a double deck octagonal structure housing the internal subsystems on the top layer and the dropsondes on the bottom layer. Additionally, the aerobot tether is designed to be made out of a Teflon-coated kevlar rope. All atmospheric items are housed in the aeroshell which leads to an estimated aeroshell diameter of 3 m.

For the structures and materials subsystem of the orbiter and TRM, the primary structure and the mechanisms have been designed. All user requirements set up in the baseline report regarding structure and materials are fulfilled. The primary structure of the orbiter consists of a rectangular cuboid with a H-shaped interior. Furthermore, the orbiter uses a solar array drive mechanism to deploy and point the solar panels. The structure of the TRM consists of a closed cylindrical shell which holds all thermally insulated subsystems and a truss structure which is used for mounting the aeroshell, antenna and solar panels. The aeroshell is mounted top down by three bi-pod struts. Global buckling was found to be the driving failure mode in the design for the primary structure of both spacecraft. To minimise weight it was found that the specific stiffness ratio had to be maximised which led to picking aluminium honeycomb panels. For the face sheets aluminium 5083-H321 was found optimal and for the honeycomb core aluminium 3003-H19. A summary of the important parameters of the structural design is given in Table 3.

Table 3: Structural data overview.

Spacecraft	Honeycomb panels		Total structural mass (kg)
	Core (mm)	Face sheet (mm)	
Orbiter	8.6	0.5	131.1
TRM	5.0	0.5	183.3

**Risk, reliability, availability, maintainability and safety** Risks have been identified, assessed and mitigated accordingly throughout the detailed design phase. For example, the risks of component failure have been decreased through the use of safety factors and redundancy. The reliability of the mission segments are analysed by using reliability blocks and analysing the probability of failure. As an example, the amount of dropsondes that has to be taken to the Venus was set to 25 by trading off the added mass with the reliability of the dropsondes. During the operational phase, the availability of the mission is limited to telecommunications, as the mission segments will be in orbit near Venus or in the Venusian atmosphere. Moreover, the maintainability of the system is limited to software updates for the segments near Venus, while ground segments can be maintained through physical interaction. Finally, the safety of the mission will primarily be covered by the responsible authorities of the production phase and the launch phase.

**Design development** This project can be further developed to ensure a launch to Venus on May the 10<sup>th</sup> 2031. In Figure 3 the top level design and development is given, based on the ESA mission development logic. In all stages of the design the three pillars of sustainability have been taken in to account: planetary protection, environmental impact, and socioeconomic impact.

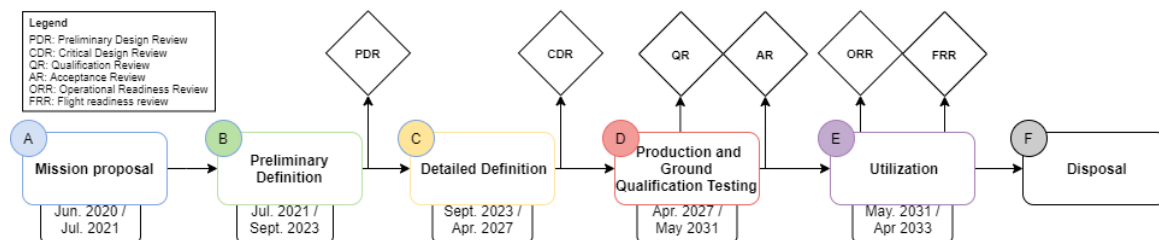


Figure 3: Top level design development logic

# Contents

<b>1</b>	<b>Introduction</b>	<b>1</b>
<b>2</b>	<b>Mission Overview</b>	<b>2</b>
2.1	Mission statement and user requirements . . . . .	2
2.2	Scientific objectives . . . . .	2
2.3	Mission timeline . . . . .	3
2.4	Logistics and operations . . . . .	4
2.5	Market analysis . . . . .	4
2.6	Sustainable development strategy . . . . .	7
<b>3</b>	<b>Design Overview</b>	<b>9</b>
3.1	Trade-off summary . . . . .	9
3.2	Functional flow diagram . . . . .	10
3.3	Aerobot . . . . .	10
3.4	Dropsonde . . . . .	12
3.5	Aeroshell . . . . .	13
3.6	Orbiter . . . . .	14
3.7	Transfer module . . . . .	15
3.8	Launch configuration . . . . .	16
<b>4</b>	<b>Instrumentation and Planetary Science</b>	<b>17</b>
4.1	Design overview . . . . .	17
4.2	Functional analysis . . . . .	18
4.3	Instrumentation: Atmospheric segment . . . . .	19
4.4	Instrumentation: Space segment . . . . .	22
4.5	Sensitivity analysis . . . . .	24
4.6	Verification and validation . . . . .	24
<b>5</b>	<b>Astrodynamics</b>	<b>25</b>
5.1	Design overview . . . . .	25
5.2	Functional analysis . . . . .	25
5.3	Launch and transfer to Venus . . . . .	25
5.4	Aerobraking . . . . .	27
5.5	Operational orbit . . . . .	31
5.6	Delta-V budget . . . . .	33
5.7	Risk analysis . . . . .	35
5.8	Sensitivity analysis . . . . .	35
5.9	Verification and validation . . . . .	36
<b>6</b>	<b>Atmospheric Entry</b>	<b>37</b>
6.1	Design overview . . . . .	37
6.2	Functional analysis . . . . .	37
6.3	Entry model . . . . .	38
6.4	Entry method . . . . .	42
6.5	Entry loads . . . . .	42
6.6	Aeroshell design . . . . .	44
6.7	Aerodynamic characteristics and stability . . . . .	46
6.8	Balloon deployment . . . . .	46
6.9	Risk analysis . . . . .	47
6.10	Sensitivity analysis . . . . .	48
6.11	Verification and validation . . . . .	48
<b>7</b>	<b>Aerobot Aerodynamics</b>	<b>50</b>
7.1	Design overview . . . . .	50
7.2	Functional analysis . . . . .	51
7.3	Balloon thermal model . . . . .	51
7.4	Superpressure fundamentals . . . . .	53
7.5	Envelope sizing . . . . .	54
7.6	Inflation system . . . . .	55
7.7	Aerobot stability . . . . .	56
7.8	Dropsonde aerodynamics . . . . .	57
7.9	Risk analysis . . . . .	58
7.10	Sensitivity analysis . . . . .	58
7.11	Verification and validation . . . . .	59

<b>8 Propulsion</b>	<b>60</b>
8.1 Design overview . . . . .	60
8.2 Functional analysis . . . . .	61
8.3 Design approach . . . . .	61
8.4 Risk analysis . . . . .	63
8.5 Sensitivity analysis . . . . .	63
8.6 Verification and validation . . . . .	63
<b>9 Telemetry, Tracking and Command</b>	<b>64</b>
9.1 Design overview . . . . .	64
9.2 Functional analysis . . . . .	65
9.3 Design approach . . . . .	66
9.4 Risk analysis . . . . .	72
9.5 Sensitivity analysis . . . . .	72
9.6 Verification and validation . . . . .	73
<b>10 Electrical Power Supply</b>	<b>75</b>
10.1 Design overview . . . . .	75
10.2 Functional analysis . . . . .	75
10.3 Design approach . . . . .	77
10.4 Risk analysis . . . . .	86
10.5 Sensitivity analysis . . . . .	86
10.6 Verification and validation . . . . .	87
<b>11 Thermal Control</b>	<b>88</b>
11.1 Design overview . . . . .	88
11.2 Functional analysis . . . . .	89
11.3 Design approach . . . . .	90
11.4 Risk analysis . . . . .	94
11.5 Sensitivity analysis . . . . .	94
11.6 Verification and validation . . . . .	94
<b>12 Attitude Determination and Control System</b>	<b>96</b>
12.1 Design overview . . . . .	96
12.2 Functional analysis . . . . .	96
12.3 Design approach . . . . .	97
12.4 Risk analysis . . . . .	104
12.5 Sensitivity analysis . . . . .	104
12.6 Verification and validation . . . . .	104
<b>13 Structures and Materials: Space Segment</b>	<b>105</b>
13.1 Design overview . . . . .	105
13.2 Functional analysis . . . . .	106
13.3 Design approach . . . . .	106
13.4 Risk analysis . . . . .	111
13.5 Sensitivity analysis . . . . .	112
13.6 Verification and validation . . . . .	112
<b>14 Structures and Materials: Atmospheric Segment</b>	<b>113</b>
14.1 Design overview . . . . .	113
14.2 Functional analysis . . . . .	113
14.3 Design approach . . . . .	114
14.4 Risk analysis . . . . .	117
14.5 Sensitivity analysis . . . . .	118
14.6 Verification and validation . . . . .	118
<b>15 Risk, Reliability, Availability, Maintainability, and Safety</b>	<b>119</b>
15.1 Risk analysis . . . . .	119
15.2 Reliability analysis . . . . .	120
15.3 Availability . . . . .	122
15.4 Maintainability . . . . .	122
15.5 Safety . . . . .	122
<b>16 Design Development</b>	<b>123</b>
16.1 Design and development logic . . . . .	123
16.2 Cost breakdown . . . . .	123
16.3 Sustainability . . . . .	125
16.4 Budget breakdown . . . . .	126
<b>17 Conclusion and Recommendations</b>	<b>129</b>
<b>References</b>	<b>130</b>
<b>A Hardware/Software Diagram</b>	<b>134</b>
<b>B Logic Diagrams</b>	<b>135</b>
<b>C Project Gantt Chart</b>	<b>137</b>

# Nomenclature

## List of abbreviations

ABT	Aerobot
ADCS	Attitude determination & control system
ASG	Atmospheric segment
ASH	Aeroshell
ASI	Atmospheric Structure Instrumentation
BCR	Battery charge regulator
BDR	Battery discharge regulator
BLN	Balloon
BLOON	Balloon Local Observatory & Orbiter Network
CBE	Current best estimate
DROPP	Dropsonde Payload Package
DRS	Dropsonde
DSE	Design synthesis exercise
DSN	Deep Space Network
EPS	Electrical power supply
EVN	European VLBI Network
FOSU	Ultimate design factor of safety
FOSY	Yield design factor of safety
FOV	Field of view
GC	Gas chromatograph
GDL	Gondola
GNC	Guidance, navigation & control
GRP	Glass-Reinforced Plastic
HEO	Highly Elliptical Orbit
HGA	High Gain Antenna
HPBW	Half power beamwidth
IPS	Instrumentation & planetary science
KQ	Qualification test factor
lat	Lateral
LDPC	Low-Density Parity-Check
LEO	Low Earth Orbit
LGA	Low Gain Antenna
LV	Launch vehicle
LW	Launch Window
MAVEN	Mars Atmosphere and Volatile Evolution
MET	Meteorology Science Suite
MLI	Multi layer insulation
MMH	Monomethyl Hydrazine
MON	Mixed Oxides of Nitrogen
MPPT	Maximum power point tracking
NGMS	Noble Gas Mass Spectrometer
NIR	Near-Infrared (radiation)
NMS	Neutral Mass Spectrometer
ORB	Orbiter
OSR	Optical solar reflectors
PCDU	Power conditioning and distribution unit
PCM	Phase changing material
PTFE	Polytetrafluoroethylene

PV	Photovoltaic
RCS	Reaction Control System
RTG	Radioisotope thermoelectric generator
s/c	Spacecraft
SA	Solar array
SM	Structures & Materials
SNR	Signal to Noise Ratio
SNT	System noise temperature
SSG	Space segment
SWOT	Strengths, weaknesses, opportunities, and threats
TCM	Trajectory Correction Manoeuvre
TGO	Trace Gas Orbiter
TLS	Tunable Laser Spectrometer
TNACA	Trace gas, Noble gas And Compositional Analysis suite
TPS	Thermal Protection System
TRL	Technical readiness level
TRM	Transfer module
TTC	Telemetry, tracking & command
UV	Ultraviolet (radiation)
V&V	Verification and Validation
VeRa	Venus Express Radio science experiment
VEX	Venus express
VLBI	Very-long baseline interferometry
VOI	Venus Orbit Insertion
XRF	X-Ray Fluorescence

## List of symbols

$\alpha$	Absorptivity	
$\alpha$	Angle of attack	<i>rad</i>
$\alpha$	Cone half angle	<i>rad</i>
$\beta$	Ballistic coefficient	<i>kg/m<sup>2</sup></i>
$\Delta P$	Superpressure	<i>N/m<sup>2</sup></i>
$\Delta T$	Supertemperature	<i>K</i>
$\dot{Q}$	Heat flow rate	<i>W</i>
$\eta$	Efficiency	
$\gamma$	Specific heat ratio	
$\gamma$	knock-down factor	
$\lambda_m$	Latent heat	<i>kJ/kg</i>
$\mathfrak{R}$	Universal gas constant	<i>J/molK</i>
$\mu$	Standard gravitational parameter	<i>m<sup>3</sup>/s<sup>2</sup></i>
$\nu$	Poisson ratio	
$\omega$	Argument of pericytherion	
$\rho$	Density	<i>kg/m<sup>3</sup></i>
$\sigma$	Stefan-Boltzmann constant	<i>W/m<sup>-2</sup>K<sup>-4</sup></i>
$\sigma$	Stress	<i>N/m<sup>2</sup></i>
$\tau$	Attenuation factor	
$\Theta$	Elevation angle	<i>rad</i>
$\theta$	Cone halfangle	<i>rad</i>
$\varepsilon$	Emissivity	
$\vec{a}_{sol}$	Solar perturbation acceleration	<i>m/s<sup>2</sup></i>

$\vec{B}$	State vector		$I$	Mass moment of inertia	$kgm^2$
$\vec{r}$	Displacement vector		$m$	Second moment of area	$m^4$
$\vec{r}_{os}$	Orbiter-Sun Distance vector		$m$	Specific impulse	$s$
$\vec{r}_{vo}$	Venus-orbiter distance vector		$m$	Solar irradiance	$W/m^2$
$\vec{r}_{vs}$	Venus-Sun distance vector		$m$	Clamping coefficient	
$\vec{v}$	Velocity vector		$V$	Stiffness matrix	
$A$	Area		$m^2$	Boltzmann factor	$J/K$
$A$	Aspect ratio			Equivalent spring constant	
$a$	Acceleration		$m/s^2$	Thermal conductivity coefficient	$W/mK$
$a$	Albedo factor			Length	$m$
$a$	Semi-major axis		$m$	Loss	
$a_m$	Fusion mass fraction			Reference length	$m$
$B$	Buoyancy		$kg$ or $N$	Mach number	
$b$	Semi-minor axis		$m$	Mass	$kg$
$b$	Wingspan		$m$	Mass matrix	
$C$	Capacity		$Ah$	Moment	$Nm$
$C$	Correlation factor			Mass	$kg$
$C$	Specific heat		$J/kgK$	Dynamic viscosity	$Pas$
$C$	Total battery capacity		$J$	Force per unit circumference	$N/m$
$c$	Core			Experimental value to determine helium tank pressure	
$c$	Speed of light		$m/s$	Number of moles	$mol$
$c_p$	Pressure coefficient		$n$	Noise spectra density	$W/Hz$
$C_A$	Axial force coefficient		$N_0$	Nusselt number	
$C_{d0}$	Zero lift drag coefficient		$Nu$	Power	$W$
$C_{dl}$	Lift induced drag coefficient		$P$	Pressure	$N/m^2$
$C_D$	Drag coefficient		$p$	Equivalent force	$N$
$c_f$	Skin friction coefficient		$Peq$	Prandtl number	
$C_L$	Lift coefficient		$Pr$	Heat flux	$W/m^2$
$C_M$	Moment coefficient		$q$	Radius	$m$
$C_N$	Normal force coefficient		$R$	Specific gas constant	$J/kgK$
$cr$	critical		$R$	Transmission bit rate	$bits/s$
$D$	Diameter		$m$	Radius	$m$
$d$	Depth of discharge		$r$	Radius of the apocytherion from the surface	
$d/l$	Diameter to length ratio		$r_a$	Radius of the pericytherion from the surface	$km$
$E$	Energy		$J$	Reynolds number	$m^2$
$E$	Young's modulus		$N/m^2$	Surface area	
$e$	Eccentricity			Sutherland's constant	
$e$	Oswald efficiency factor			Drift	$m$
$F$	Force		$N$	Step	$s$
$F$	Form factor			Orbital period	$s$
$F$	View factor		$s$	Temperature	$K$
$f$	Face sheet			Thickness	$m$
$f$	Frequency		$Hz$	Time	$s$
$G$	Gain			Maximum thickness to chord ratio	
$G$	Shear modulus		$N/m^2$	Velocity	$m/s$
$g$	Venus gravitational acceleration		$m/s^2$	Voltage	$V$
$g_0$	Standard gravity		$m/s^2$	Volume	$m^3$
$Gr$	Grashof number			Wind profile	$m/s$
$h$	Enthalpy		$J$	Location of centre of pressure	$m$
$h$	Height		$m$	Compressibility factor	
$h_c$	Heat transfer coefficient		$W/m^2K$		
$H_{vap}$	Enthalpy of vaporization		$J/kg$		
$I$	Current		$A$		

# 1 Introduction

Venus is one of Earth's neighbours and is, in some ways, more similar to our home planet than any other celestial body in the solar system. Its size and composition might be very similar our own planet's size and composition [1], but in other ways Venus seems almost as far removed from Earth's conditions as possible. A thick and toxic atmosphere traps heat in an extreme greenhouse process that warms up the planet by hundreds of degrees. The surface pressure is more than 90 times higher than the pressure on Earth [1], the upper atmosphere contains sulphuric clouds and a super rotational wind can blow objects all the way around the planet in a matter of days. It is also not yet known whether plate tectonics and seismic activity is present on Venus and, if so, in what form. Due to the similarities to Earth, contrasted with its extreme differences, Venus is a scientifically interest body for study, especially since many of the phenomena on the planet are still not fully understood.

Therefore, this design synthesis exercise (DSE), titled 'Remote sensing probe for the Venusian atmosphere and tectonics', aims to design a mission for a platform to take in-situ measurements of the Venusian atmosphere and to perform infrasound measurements of the planet's seismic activity. The mission has been nicknamed BLOON, which stands for 'Balloon Local Observatory & Orbiter Network'. This final report is meant as an overview of the research done over the last months and summarises the final design in detail. This report is a follow up to the project plan, baseline report and midterm report [2–4].

Firstly, an overview of the mission is given in Chapter 2, followed by an overview of all elements of the design in Chapter 3. Afterwards, the scientific instrumentation of the mission is discussed in Chapter 4. This is followed by the astrodynamics and atmospheric entry of the mission in Chapter 5 and 6. Subsequently, a detailed design of all subsystems is given in Chapters 7, 8, 9, 10, 11, 12, 13 and 14. After these subsystems, multiple analyses are summarised; a RAMS and sustainability analysis in Chapter 15 and design and development logic in Chapter 16. The report is closed with a conclusion and recommendations in Chapter 17.

## Acknowledgements

The group would like to extend their sincere gratitude towards our project tutors, Dr.ir. F.F.J. Schrijer and Dr.ir. A.H. van Zuijlen, and coaches, Ir. M. Rovira Navarro and Dr. S. Speretta, for the extremely valuable feedback and support they have given us in these challenging weeks.

## 2 Mission Overview

For a complete view of the project, this chapter and Chapter 3, provide an overview of the mission and the main design decisions. This chapter first explains the mission statement and user requirements, followed by the main scientific objectives, mission timeline, operations and logistics, and a market analysis.

### 2.1. Mission statement and user requirements

It is important to learn about the conditions and dynamics of Venus, because insight in the planet's super rotation, the origin of the atmosphere and the runaway greenhouse effect could teach us about conserving Earth and preventing global climate change. Furthermore, knowledge on seismic activity of the planet is limited, due to the relatively short time period that landers can survive on the surface of the planet. For example, the Vega 2 lander sent surface data for about an hour. These considerations result in the following mission need statement. **Design a mission to measure Venus atmospheric conditions and tectonic activity.** Based on this statement, the following project objective statement has been formulated: **Design a system to perform in-situ measurements of the Venusian atmospheric conditions and tectonic activity of the crust for 100 terrestrial days, with 11 students over 10 weeks time.**

In order to fulfil these statements, a list of user requirements need to be met. These requirements have been determined in the project guide and are cited in Table 2.1 [5], with minor adjustments made to them during the baseline report [3], which are also cited in the table. The last column shows the compliance of the design with respect to the user requirements. As can be seen, all the user requirements except for the US-SARE requirements are fulfilled. These requirements can be checked off after testing, and a more detailed explanation is given in Chapter 15. The technical discussion of the requirements follows later in this report.

### 2.2. Scientific objectives

As a rocky planet seemingly similar to Earth in size, mass and general composition, robotic missions and Earth observations revealed a dense carbon dioxide-dominant atmosphere and unforgiving surface conditions combining ocean-like pressures, extreme heat and high chemical corrosivity [6]. While lander probes on rocky bodies such as Mars and the Moon operated for a duration of a span of months to years, conventional landers on Venus are subjected to the hellish [7] environment and are only expected to last, at most, a handful of hours. As a result, long-duration scientific experiments were primarily conducted remotely from orbit around Venus, such as NASA's Magellan, ESA's Venus Express and JAXA's Akatsuki. These missions yielded significant scientific value, but posed further scientific questions that demanded in-situ atmospheric missions.

Since the turn of the century, novel in-situ mission proposals have emerged, utilising atmospheric platforms such as balloons, airships or other heavier-than-air vehicles operating at the relatively benign Venusian upper-cloud region at 55-60 km that provides near-Earth operating conditions. The locale presents a unique opportunity to sample the Venusian lower atmosphere composition and conduct meteorological studies to better constrain Venusian atmospheric models [8]. Besides simply being curious about Venus as a planet, as humanity learnt more about our hellish and inhospitable sister planet, we also began to question whether anthropogenic climate change is bringing Earth on a similar trajectory towards a Venus-like planet. Scientific investigators for Venus missions often pose this scientific question: **What does the Venusian runaway greenhouse effect tell us about climate change on Earth?** The vastly different climate on Venus contains surprising analogues to Earth's climate, such as the effect of clouds on the atmospheric radiative balance and the effect of aerosols on the upper atmosphere (such as our ozone layer). Additionally, understanding the global circulation of the extreme Venusian atmosphere leads to a better understanding of Earth's own atmospheric processes. These scientific questions were the basis for balloon-borne mission proposals before 2010, such as NASA's Venus Flagship, the Venus Climate Mission and the European Venus Explorer, but sadly were never realised.

One decade later, the emergence of research on the acoustic coupling effect on seismic waves led to speculation that the dense Venusian atmosphere could be harnessed to detect seismic activity from the upper-cloud region [9]. While surface-based seismological measurements are severely restricted by the

intense surface conditions, a high-altitude and high-endurance platform would allow for long-term continuous observation in the order of months. A mature remote seismology instrument can yield insights into the interior state and dynamics of Venus, which in turn could answer long-standing questions on the disparity between Earth and Venus. While the methodology is immature in practice, the instrumentation is already mature, and there is value in conducting a precursor mission to characterise the acoustic background, paving the way for further instrumentation development. This led to the second major theme of the BLOON mission: **How active is the interior of Venus?**

To research these two very open themes the BLOON mission has three concrete scientific goals for which an aerial based platform hosts a unique opportunity:

- **Atmospheric composition:** Investigate the abundance and isotopic ratios of chemical species in the upper-cloud layer.
- **Atmospheric dynamics:** Investigate meteorological phenomena to validate climate models.
- **Interior dynamics:** Place constraints on the structure and dynamics of the interior.

A more in-depth elaboration of the scientific mission design is provided in Chapter 4, summarising the work done in the baseline and midterm reports [3, 4]. It includes a detailed breakdown on science traceability, instrumentation selection and sizing and requirements on instrumentation operation.

## 2.3. Mission timeline

The mission is divided into six different phases. First is the development phase, in which the design is worked out and built. The next five phases are shown in Figure 2.1. With the launch of the mission, the transfer phase will begin, in which the mission will prepare to make the transfer to Venus itself. Separation of orbiter and TRM happens in this phase too. The third phase is the orbit manoeuvring phase, in which the orbit of the orbiter will be reached by use of aerobraking. After that, the atmospheric segment setup phase is planned, which will include the entry of the aeroshell and the inflation of the balloon. Subsequently, the nominal mission phase will occur, in which most measurements are taken. Finally, in the end of life phase, the mission is extended, if possible after which the orbiter will burn up in the atmosphere.

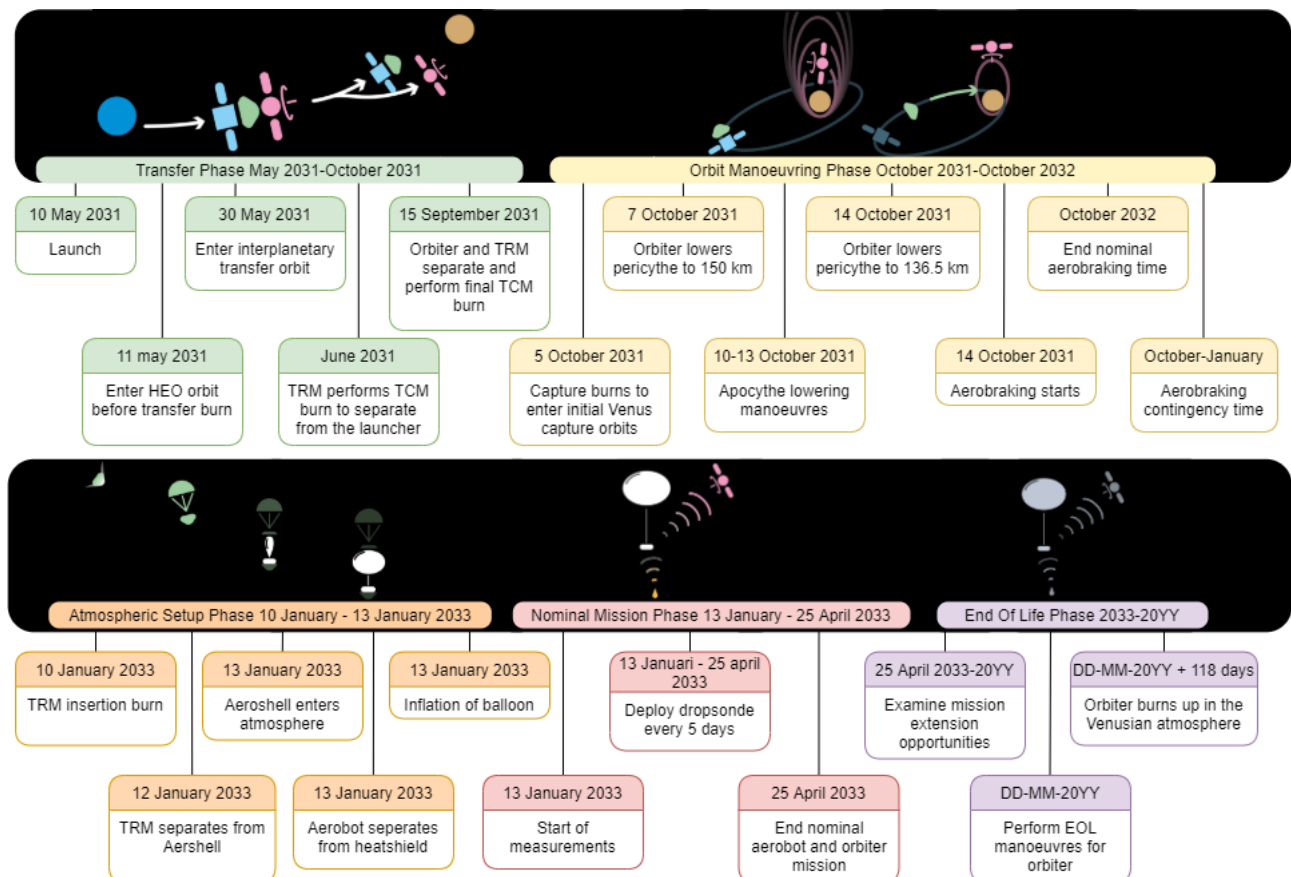


Figure 2.1: Mission timeline of the BLOON mission

## 2.4. Logistics and operations

After completion of the design phase, all segments and their parts are build and tested. When requirements are not met, the parts are redesigned and reproduced. With the parts completed, the mission segments are assembled in parallel. Again the segments will be tested in dedicated testing facilities and if they fail to meet the requirements, they will be redesigned and reproduced. Once all segments meet the requirements the integration of the segments will be done, the integrated parts will then again be tested. First the aerobot and dropsondes will be integrated after which they will be integrated with the aeroshell. All the mission segments will then be integrated and extensively tested, after which it will be placed into the Falcon 9 fairing, which after testing and transport is ready for launch.

After launch, the mission starts. To get a better overview of all the mission segments and the interactions between these segments an operational diagram has been made, see Figure 2.3. The most important interactions of this mission are those between the orbiter and aerobot, the aerobot and the dropsondes and the orbiter and the ground station. These interactions will be responsible for the relay of the gathered scientific data to earth. For a more detailed look into these interaction, a hardware & software block diagram is shown in Appendix A.

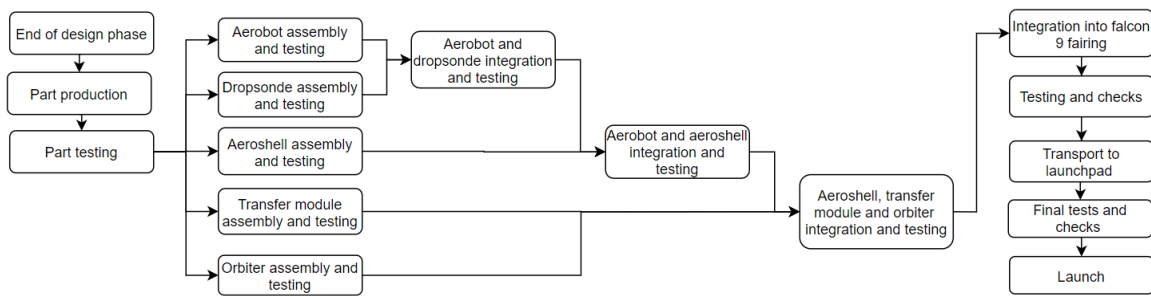


Figure 2.2: Logistics diagram

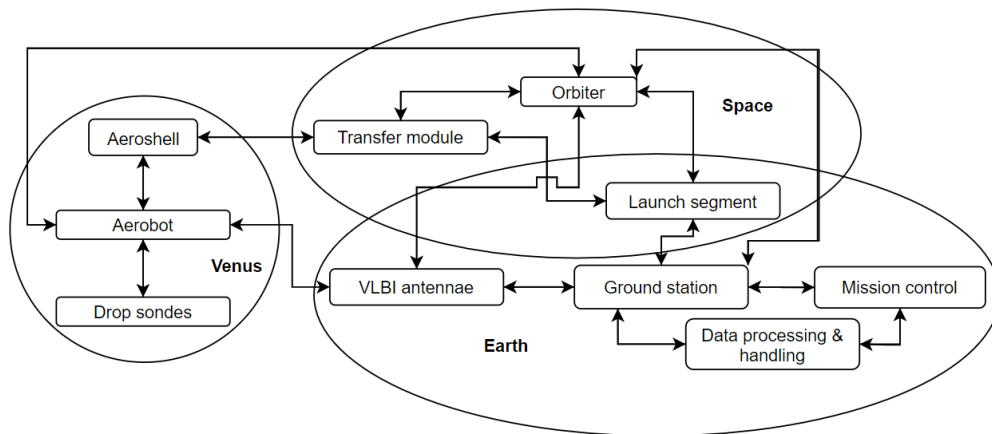


Figure 2.3: Operational diagram

## 2.5. Market analysis

Firstly, a short recap of the market analysis performed in the baseline report [3]. The recap will consist of a description of the state of the market and the identification of stakeholders. Subsequently, the SWOT analysis will be updated to rediscover strengths, weaknesses, opportunities and threats related to the mission. More focus will be put on the technical aspects of the mission during the SWOT analysis. Finally, the development, production, delivery and operational costs will be anticipated by setting cost requirements.

### 2.5.1. State of the market

A cost analysis of missions destined for Venus was performed in the baseline report [3]. An overview of the total mission costs is given in Table 2.2. The costs in 2020 are calculated by taking into account yearly inflation rate of 2% whereby the launch year is taken as the reference year. Note that, the EnVision mission is

still in the proposal phase and that the Magellan mission is significantly more costly than the other missions due to extensive research on aerobreaking.<sup>1,2</sup>

Table 2.2: Cost comparison of missions to Venus [3]

Mission name	Launch year	Cost (million \$)	Cost in 2020 (million \$)
EnVision	2032	608	479
Akatsuki	2010	300	366
Venus Express	2005	288	353
Magellan	1994	680	1138
Pioneer Venus	1978	208	478

### 2.5.2. Stakeholder identification

The stakeholders of the project that were identified in the baseline report are given with a brief description of their respective stake [3]. Several newly identified stakeholders are mentioned as well.

**Governments:** Governments provide funding to space missions and are therefore an important stakeholder to keep into account during the mission design. **Space agencies:** space agencies could be a competitor to our project as they will potentially receive funding for a similar mission. However, they can also be a contributor to the project by means of supplying a launch site. **SpaceX:** SpaceX will be the supplier of the Falcon 9 launch vehicle, therefore it is an important stakeholder in the BLOON mission. **Other private companies:** Other private companies might be interested in our project if they can get financial gain through the sale of services or products. For example, Honeywell Aerospace could profit from selling the reaction wheels used in the orbiter. **Scientific community:** The mission will impact the scientific community, if outstanding research questions are answered with the gathered data. **Media:** The media will provide the BLOON project with exposure to the public which could increase the possibility of funding. For example, spreading information on why BLOON research towards the runaway greenhouse effect on Venus is of high significance and might shift society's view on why BLOON is a relevant space mission. Having public support will exert a positive driving force in favour of BLOON during the mission selection.

### 2.5.3. SWOT analysis

Figure 2.4 shows the updated SWOT analysis for the BLOON mission. The SWOT analysis is performed to establish the key factors that impact the market position of the project. Every stated factor of the mission will be discussed subsequently, so a more in-depth understanding of the mission strengths, weaknesses, opportunities and threats is formed. Note that, the black aspects are related to the group, while the blue aspects are related to the mission and the segments. Furthermore, an overview of the segments is given in Chapter 3, which provides insight into the reasons why the subsequent SWOT aspects are identified.

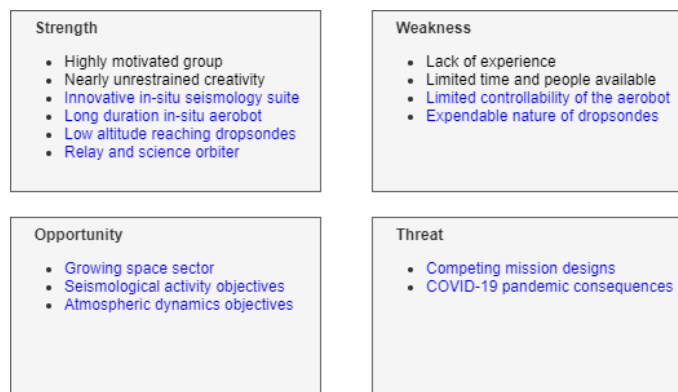


Figure 2.4: SWOT analysis of non-technical and technical mission characteristics

**Strengths:** The first two strengths related to the mission are non-technical aspects. The motivation of the project members is an inherent strength of the group as the project is a first experience with a large space mission design project for all the project members. This works highly motivational and can be regarded as the primary driving force of the project. Secondly, the creativity that is allowed and encouraged in the design process leads to the vast exploration of design options and an innovative final design. A showcase of this is the 50 m tether used for the micro-barometers in the seismology suite.

This leads to the first technical strength of the BLOON mission. An innovative in-situ seismology suite, previously only used in Earth-based research, will be a design driving scientific component. This will be a

<sup>1</sup><https://www.space.com/38311-akatsuki.html>, retrieved June 2020

<sup>2</sup><https://nssdc.gsfc.nasa.gov/nmc/SpacecraftQuery.jsp>, retrieved June 2020

distinctive aspect with respect to other Venus exploration mission and thus a key strength. Next to this, the 100-day in-situ mission time of the aerobot will be the basis for high temporal and spatial resolution of the scientific data, therefore another key technical strength. Thirdly, the scientific measurements performed in the altitude range of 25 to 60 km are done by dropsondes. This prevents the aerobot from entering a more demanding environment, as temperature and pressure increase when descending towards the surface. The task distribution will lead to a more reliable mission and can be considered as a key technical strength. The last identified technical strength is the orbiter having a double purpose as it acts as a communication relay and a science platform with a spectrometer and an imaging camera.

**Weaknesses:** The first two weaknesses of the mission were first identified in the baseline report [3]. A brief update here is required as the lack of experience of the project members has decreased during this project. This first experience with a space mission design project will be an important asset for the members pursuing a space engineering career. Whether this experience is noticeable in the final BLOON mission design is hard to evaluate, therefore lack of experience is still regarded as a weakness. The second weakness of limited available time and people is similarly regarded as a weakness, 11 people working for ten weeks to perform a preliminary design of a Venus exploration mission is considered to be constraining.

The first technical weakness of this project is the limited controllability of the aerobot. It will have a passive altitude control system that is inherent to the way a superpressure balloon works, but no control of the flight path. Secondly, each dropsonde can only operate once. This means that after the 25 dropsondes have been dropped to the surface, the mission is unable to perform in-situ measurements from 60 to 25 km.

**Opportunities:** The opportunities related to the mission have been specified more accurately than previously. The outstanding research questions and mission objectives are more accurately described by splitting them in two separate aspects. The first is the science objective of investigating the Venusian seismological activity, where a major opportunity lies due to minimal research that has been performed by previous missions. Secondly, the science objective of investigating the atmospheric dynamics of Venus is an opportunity for the BLOON mission. Due to the common ancestry of Venus and Earth and the runaway greenhouse effect of the Venusian atmosphere, research on the Venusian atmosphere might lead to insights that are applicable Earth. Finally, a third opportunity lies in the advancement of the space sector in recent decades. Private companies are investing large amounts of money into new technologies that makes it easier and more affordable to set up space missions which applies to our BLOON mission.

**Threats:** Finally, regarding threats there are no new identifications with respect to the baseline report [3]. Both competing designs for Venus missions and consequences of the COVID-19 pandemic on the economy are seen as the largest threats to the success of the mission.

#### 2.5.4. Target cost

To establish a budget cap on the BLOON mission, a collaboration of ESA and NASA is considered. A collaboration between these two agencies would provide access to both American and European companies. In the stakeholder analysis in Subsection 2.5.2 two American companies, namely SpaceX and Honeywell Aerospace were already identified. Furthermore, the BLOON project was initiated at the TU Delft, which has close relations with ESA.<sup>3</sup> A collaboration between ESA and NASA is not unlikely, with the Solar Orbiter being a recent example.<sup>4</sup>

All in all, both the cost guidelines from NASA new frontier missions<sup>5</sup> and from the ESA Cosmic vision M-class missions<sup>6</sup> are utilised. A limit on the total costs of such a mission are approximately €750 million. Looking at the missions in Table 2.2 it can be seen that Pioneer Venus, VEX, Akatsuki and EnVision adhere to a budget cap of this size. Therefore, it would make sense for the BLOON mission to adhere to the cap. Furthermore, the estimation of the operational costs was done by considering the operational costs of Mars rover missions. The cost requirements are then shown in Table 2.1. A cost breakdown analysis is performed in Chapter 16 to evaluate if the requirements are met.

- **Development costs:** Taking the total budget cap of €750 million and other defined cost segments, a target for the development costs was set, resulting in a requirement of €350 million.

<sup>3</sup><https://www.delta.tudelft.nl/article/new-space-institute-tu-delft>, retrieved June 2020

<sup>4</sup>[https://www.nasa.gov/mission\\_pages/sunearth/news/ESA-SolarOrbiter.html](https://www.nasa.gov/mission_pages/sunearth/news/ESA-SolarOrbiter.html), retrieved June 2020

<sup>5</sup><https://science.nasa.gov/solar-system/programs/new-frontiers> Retrieved in June 2020

<sup>6</sup><https://sci.esa.int/web/cosmic-vision/-/47570-call-for-proposals-for-medium-size-missions>, retrieved June 2020

- **Production costs:** Taking the total budget cap of €750 million and other defined costs segments, a target for the production costs could be set. Note that the production costs are estimated also taking into account the several mission segments that need to be produced. It resulted in a production cost requirement of €250 million.
- **Delivery costs:** The delivery costs of the BLOON mission can be capped by looking at the launch cost of a Falcon 9<sup>7</sup>, as the Falcon 9 is the launch vehicle (LV) that resulted from the LV trade off in Chapter 5. Also taken into account was the cost of transfer from Earth to Venus. A total of €100 million was set as a cost requirement.
- **Operational costs:** The operational cost was based on Mars rover missions. It was assumed that the Mars rover mission are a valid reference, because they are recent and of comparable complexity. An overview of Mars rover mission costs is given in Table 2.3.<sup>8,9,10</sup> The requirement for the operational costs was estimated at €44 million for a nominal mission duration of 100 days.

Table 2.3: Overview of operational costs for Mars rover missions

Mission name	Rover name	Launch year	Operational cost	Time
Mars 2020	Perserverance	2020	\$300 million	first martian year
Mars Science Laboratory	Curiosity	2011	\$40 million	for 2021
Mars Exploration Rover	Opportunity	2003	\$14 million	yearly avg.
Mars Exploration Rover	Spirit	2003	\$14 million	yearly avg.

## 2.6. Sustainable development strategy

Throughout the whole design phase sustainability was considered to ensure that all mission aspects comply with international standards. As can be seen in Table 2.1, this led to a number of requirements from ESA's handbooks on sustainability [10]. For the purpose of this report the definition of sustainable development by the Brundtland report was used, which is also adopted by the International Organisation for Standardisation: "development that meets the needs of the present without compromising the ability of future generations to meet their own needs" [11]. From this sustainability is divided into three categories. Firstly, protecting Venus from biological contamination by the BLOON mission. Secondly, the environmental impact that BLOON will have on Earth. Lastly, the socioeconomic impact that BLOON will have on Earth.

### 2.6.1. Planetary protection

Planetary protection is the foremost consideration for sustainability. To ensure that future Venus missions are not compromised by this mission it is important to follow international guidelines. Missions on, flying-by or around Venus are category II missions<sup>11</sup>, which means that requirements are limited to documentation and review [12]. Practises related to a category II mission are based on the requirements of CNES [13]. The design considerations that flowed from this, are end-of-life strategies for all mission elements. These strategies are treated in Chapter 5 and 6. Here it is ensured that that all elements burn up in the atmosphere at end-of-life. Besides this many requirements exist on production procedures which are not treated.

### 2.6.2. Environmental impact

There are no governmental requirements on the greenhouse gasses that space missions emit. That being said it is still a important parameter and should be minimised. The main sources of environmental impact by the BLOON mission on Earth are due to the launch and the production which are discussed in Chapter 16.

### 2.6.3. Socioeconomic impact

Lastly, strict requirements are set by authorities for the safety and health of people in the production process. In Table 2.1, requirements US-SUST-04 till US-SUST-09 are set to make sure all standards are followed. These are important design considerations and are mentioned in the each subsystem chapter. This topic is further treated in more detail in Section 16.3.

<sup>7</sup><https://www.bloomberg.com/graphics/2018-rocket-cost/>, retrieved June 2020

<sup>8</sup><https://spacenews.com/mars-2020-rover-mission-to-cost-more-than-2-billion>, retrieved 11 May 2020

<sup>9</sup><https://www.space.com/budget-cuts-nasa-mars-missions-curiosity-rover.html>, retrieved 11 May 2020

<sup>10</sup><https://www.wired.co.uk/article/mars-rover-opportunity-status-dead>, retrieved 11 May 2020

<sup>11</sup><https://sma.nasa.gov/sma-disciplines/planetary-protection>, retrieved June 2020

Table 2.1: A compliance matrix of the top-level user requirements.

Identifier	Requirement	Compliance	Explanation in
US-PERF-01	The design shall be able to operate in the Venusian atmosphere at altitudes between 25 and 60 km.	✓	Chapter 4
US-PERF-02	The operating time shall allow for all scientific objectives to be met.	✓	Chapter 4
US-PERF-03	Infrasound measurements shall be taken in the 0.01-6 Hz range.	✓	Chapter 4
US-PERF-04	All in-situ measurements shall have at least a 1 km height resolution.	✓	Chapter 4
US-PERF-05	All in-situ measurements shall have at least a 5 terrestrial day temporal resolution.	✓	Chapter 4
US-SARE-01-A	The reliability of the orbiter shall be more than 90%.	<TBD>	Chapter 15
US-SARE-01-B	The reliability of the high-altitude balloon shall be more than 90%	<TBD>	Chapter 15
US-SARE-02	At least 50% of the probes shall operate successfully with a probability higher than 90%.	<TBD>	Chapter 15
US-SUST-01	A plan for contamination control shall be written for each individual part of the assembly.	<TBD>	Chapter 15
US-SUST-02	A planetary protection plan shall be written.	✓*	Chapter 16
US-SUST-03	The design shall not back-contaminate Earth.	✓	Chapter 16
US-SUST-04	Health of all effected shall be ensured conform ISO 45001 standards.	✓*	Chapter 16
US-SUST-05	Safety of all effected shall be ensured conform ISO 45001 standards.	✓*	Chapter 16
US-SUST-06	A life cycle assessment shall be performed as defined in ISO 14044.	✓*	Chapter 16
US-SUST-07	Materials used shall be limited to those listed by ISO/TC20/SC14.	✓	Chapter 16
US-SUST-08	Joining chemicals shall be limited to those listed by ISO/TC20/SC14.	✓	Chapter 16
US-SUST-09	Chemicals used during production shall be limited to those listed by ISO/TC20/SC14.	✓	Chapter 16
US-ENBU-01	Choice for launcher shall be based on existing/foreseeable launchers.	✓	Chapter 5
US-ENBU-01-A	Total system size shall comply with launcher payload requirements.	✓	Chapter 13
US-ENBU-01-B	Total system mass shall comply with launcher payload requirements.	✓	Chapter 5
US-ENBU-01-C	The system shall sustain launch loads as defined by the launcher catalogue.	✓	Chapter 13
US-ENBU-02	The system shall sustain the loads encountered upon entry into the Venusian atmosphere.	✓	Chapter 14
US-COST-01	The development costs of the mission shall not exceed €350 million.	✓	Chapter 16
US-COST-02	The production costs of the mission shall not exceed €250 million	✓	Chapter 16
US-COST-03	The delivery costs of the mission shall not exceed €100 million	✓	Chapter 16
US-COST-04	The operational costs of the mission shall not exceed €44 million	✓	Chapter 16

### 3 Design Overview

This chapter presents an overview of all mission elements mentioned in Chapter 2. The chapters 4-14 will go into detail on specific subsystems of the design, which could make it difficult to see the big picture of the mission. Therefore, this chapter summarises the design of each of the mission elements: the aerobot, dropsondes, aeroshell, transfer module and orbiter. This terminology is also used during the rest of the report and will thus be shortly explained. The aerobot concerns the high-altitude balloon including the payload gondola. The aeroshell is the structure containing all items that perform atmospheric insertion. The transfer module is the structure surrounding the aeroshell and performs manoeuvres before atmospheric insertion. The orbiter concerns the main relay satellite that orbits Venus. Complete functional flow diagrams of the mission can be seen in Figure B.1 and B.2. However, first a summary of the trade-off made during the midterm phase is presented [4].

#### 3.1. Trade-off summary

Before the detailed phase of this project, multiple concepts were evaluated to fulfil the user requirements. For the space segment, also known as the orbiter, two main options were left: a single orbiting satellite or one satellite assisted by multiple CubeSats that take care of some of the critical mission tasks. Figure 3.1 from the midterm report gives summary of the space trade off. It shows that due to the increased risk, mass, delta V requirements and issues with inter-satellite communication, the single orbiting satellite option was chosen.

	Risk	Total mass	Communication	Cost	Delta V requirements	Scientific objectives
Satellite	nominal risk	nominal mass	nominal communication	Costly VLBI operations	nominal Delta V	nominal fulfillment of scientific objectives
Satellite with CubeSats	added risk of CubeSats failure and CubeSat deployment	mass 1 to 41% higher	limited communication possible with atmospheric segment	Costly development	added Delta V for cubesat orbit insertion	better spatial and temporal resolution wind measurements

green	exceed requirements
blue	satisfies requirements
yellow	correctable deficiencies
red	impossible for requirements

Figure 3.1: Summary for the orbiter trade-off.

For the atmospheric segment, also known as the aerobot, two main options remained: a high-altitude balloon with dropsondes or a variable altitude balloon. Figure 3.2 from the midterm report gives summary of this trade off. The trade off shows that due to the increased mass (mainly due to thermal systems), lower communication possibilities below 55 km, increased limits on the power subsystem and the increased cost, it was chosen to opt for the constant altitude balloon. It is important to note that the RTG option in this trade off has changed since the midterm report and that the chosen constant altitude balloon also uses solar power.

	Scientific objectives	Risk	mass	communi- cation	control	power	cost	sustain- ability
variable altitude balloon	longer potential mission duration better vertical resolution, better wind profile	more demanding environment	377kg	limited <55km	limited control needed	only solar, sensitive to latitude	significantly more expensive	Leakage low alti- tudes
constant altitude balloon	better temporal resolution, local regional wind profile, better seismic data quality	deployment mechanism failure	234kg	sufficient data rate, dropsondes possible	no control neccessary	Solar with smaller panels, RTG also possible	nominal cost	chance RTG

green	exceed requirements
blue	satisfies requirements
yellow	correctable deficiencies
red	impossible for requirements

Figure 3.2: Summary for the aerobot trade-off.

### 3.2. Functional flow diagram

The functional flow diagram of this mission can be seen in Figure B.1 and B.2 in Appendix B. This gives an overview of when and which segment has to fulfil which function to make this mission a success. The mission is divided into five different phases, travel to Venus, orbit manoeuvring, atmospheric entry, perform scientific mission and transfer to end of life. For clarification, functions that will be performed by multiple segments, such as 1.1 (orbiter and transfer module), have a double-colored block.

### 3.3. Aerobot

The BLOON aerobot is an autonomous buoyant atmospheric craft comprising a balloon for lift and a gondola, housing most of the atmospheric scientific mission payload. Its mission is to loiter around 60 km altitude above the Venusian surface for 100 days, conducting atmospheric composition and meteorological sampling while releasing dropsondes into the lower parts of the Venusian atmosphere every 5 days. A design overview is given in Table 3.1, while an impression of the design can be seen in Figure 3.3.

Parameter	Value	Unit
Mass	266.3	kg
Gondola diameter	1.3	m
Gondola height	0.58	m
Balloon diameter	12	m
Balloon height	7	m
Length tether	50	m
Solar panel area	2.4	m <sup>2</sup>

Table 3.1: Design overview of the aeroshell.

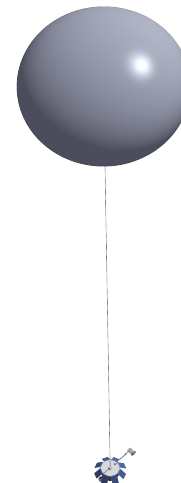


Figure 3.3: The aerobot design.

#### 3.3.1. Design drivers

The aerobot design was primarily driven by the long-endurance requirement of 100 days and the in-situ mission requirements. The design was also heavily influenced by the concentrated sulfuric acid aerosols below 75 km altitude [14] and the high pressure and temperature at lower altitude, both of which has strict requirements for designs.

### 3.3.2. Scientific mission

The aerobot contains about 25 kg of scientific instruments to conduct sampling measurements on the atmospheric composition of chemical species and meteorological characteristics in the upper atmosphere of Venus. The scientific instruments comprise of:

- **Seismology suite** Detects infrasound pressure waves
- **Nephelometer** Detects the concentration of aerosols and cloud particulate properties
- **Trace gas, Noble gas and Atmospheric Compositional Analysis suite**
  - **Gas chromatograph** to separate chemical constituents
  - **Neutral mass spectrometer** to discriminate between molecules of varying masses
  - **Tunable laser spectrometer** to assess the concentration of gaseous species in the sample
  - **Specialised Noble gas mass spectrometer** to assess abundance and isotopic ratios of noble gasses
  - **X-ray fluorescence spectrometer** to identify rock-forming trace elements
- **Meteorology suite** Measures temperature, pressure and wind velocity

The aerobot consists of a pumpkin-shaped balloon of 11.6 m diameter, a 50 m tether and an octagonal gondola of 1.2 m diameter on the bottom of the tether. The gondola houses most of the scientific instruments, the power and communications subsystems while protecting them from the thermal and chemical environment. The internal layout of these components can be found in Figure 3.4 and a render of the outside in Figure 3.5 shows the position of the meteorology suite, nephelometer and microbarometer with a red arrow. To complete the seismology suite the second microbarometer is attached to the base of the balloon, at the top of the tether (not shown).

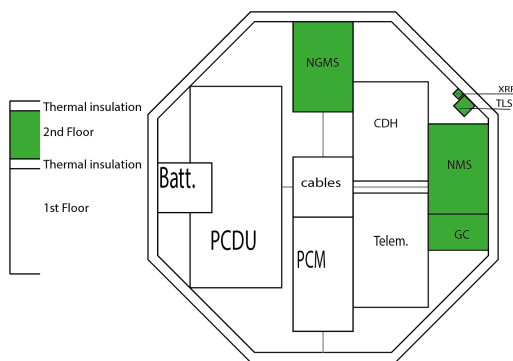


Figure 3.4: Gondola science layout on the inside. The green marked components are the scientific instruments.

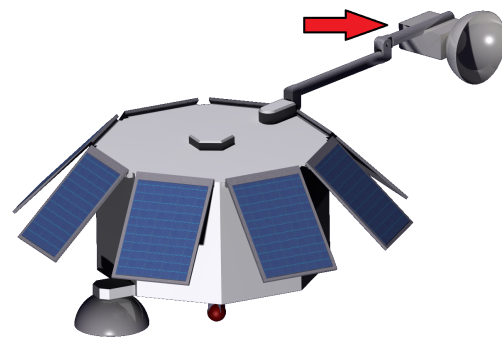


Figure 3.5: Gondola science layout on the outside. Arrow shows location of MET, Neph, and Seismo

In Figure 3.6, the functional breakdown structure specific to the aerobot can be found. Here, functions of the aerobot can be seen, which are the deployment of the balloon, the deployment of other subsystems and the gathering of data.

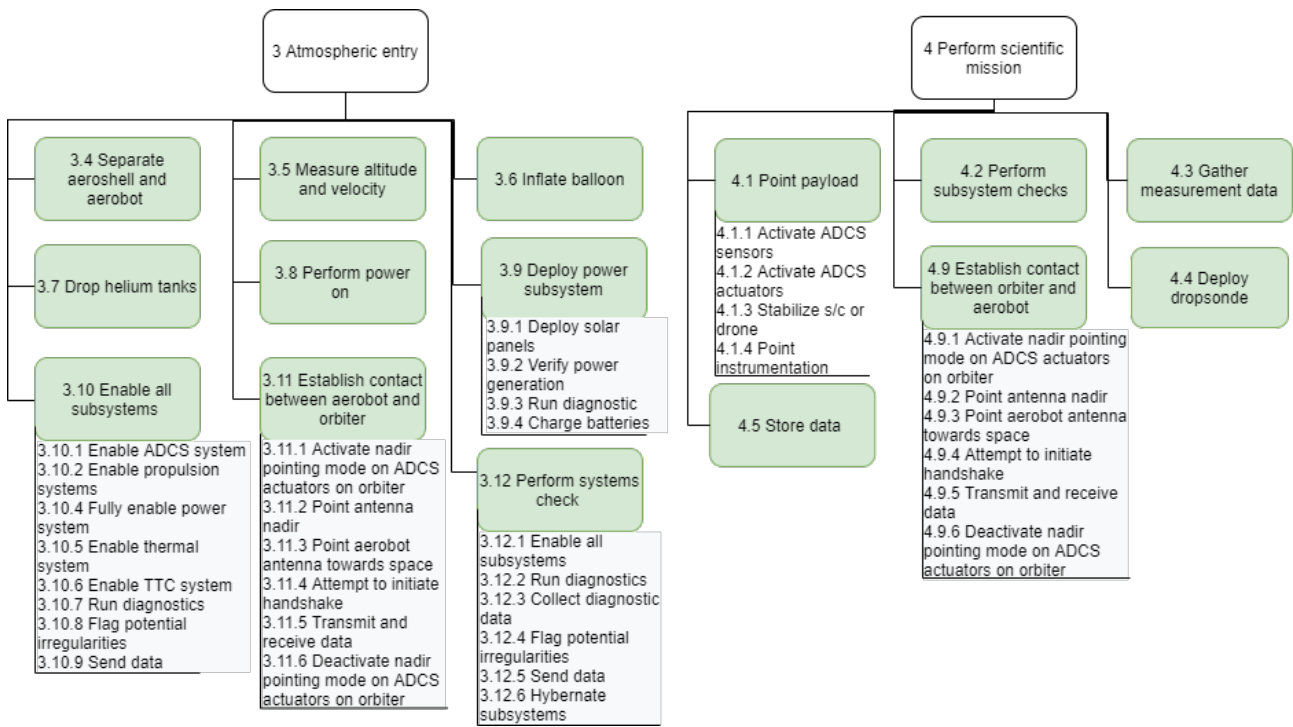


Figure 3.6: Functional breakdown for the aerobot.

### 3.4. Dropsonde

The function of the dropsondes is to take scientific measurements over the 60-25 km range specified in the user requirements. Every 5 days one of these dropsondes are dropped from the aerobot to gather data in more demanding environments than the aerobot is designed for. These dropsondes sent their data to the aerobot before they overheat during their fall to the surface. The dropsondes are tear-drop-shaped canisters consisting of a spherical pressure vessel and an X-tail. The scientific instruments, power and TTC subsystems are inside of the spherical pressure vessel.

Parameter	Value	Unit
Mass	1.7	kg
Height	0.3	m
Diameter	0.1	m
Power	4.4	W

Table 3.2: Design overview of the dropsondes.

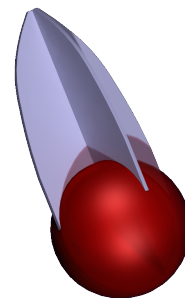


Figure 3.7: The dropsonde design.

#### 3.4.1. Design drivers

The dropsonde payload design was primarily mass- and volume- driven, considering that within a 100-day period more than 20 dropsondes would be released from the aerobot. Bearing in mind the extreme temperatures and pressures the dropsonde subsystems need to fulfil at decreasing altitudes, the subsystems were designed to function within the altitude regime of 60-25 km as per the user requirements, see table 2.1, further concessions to increase dropsonde survival would have led to restrictively heavy masses or the usage of exotic materials whose performance is untested or are too expensive to produce. Since the atmospheric conditions become increasingly more harsh as the dropsonde falls to 25 km, the dropsonde is designed to fall as quickly as possible, to limit the time that it is exposed to these conditions.

### 3.4.2. Scientific mission

The main scientific goal of the dropsonde is to take in-situ measurements in the altitude range of 60-25 km. The dropsonde will be able to make measurements at a height resolution of 1 km. The scientific measurements and instruments of the dropsonde comprise of:

- **Meteorology suite** to measure temperature, pressure and acceleration.
- **Micro Electro-Mechanical Systems** for measuring specific chemical species.
- **Wide-band light sensors** for cloud detection and environmental radiations measurements.

In Figure 3.8, the functional breakdown structure specific to the dropsondes can be found. It shows that the function of a dropsonde solely comprise of gathering and sending scientific data.

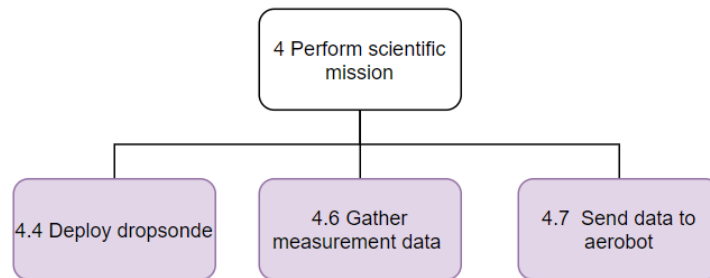


Figure 3.8: Functional breakdown for the dropsondes.

## 3.5. Aeroshell

The aeroshell is responsible for the safe insertion of the atmospheric segment from Venus orbit to atmosphere. The aeroshell consists of a circular cone like heat shield with a back shell. Both the heat shield and the back shell consists of both a sandwich structure to protect the aerobot from high declaration loads and a layer for thermal protection. To stabilise and slow down the aeroshell and aerobot two parachutes are mounted, with which the aeroshell is slow down to 30 m/s at 55 km altitude.

Parameter	Value	Unit
Mass	1091.6	kg
Base radius	3.0	m
Tip radius	0.75	m
Half angle	45.0	deg
Main parachute diameter	6.0	m
Drogue parachute diameter	3.7	m

Table 3.3: Design overview of the aeroshell.

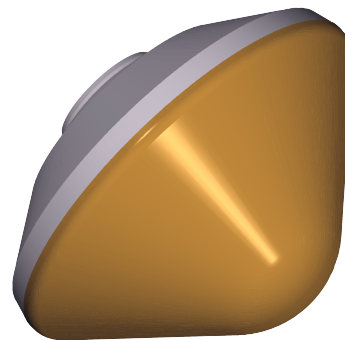


Figure 3.9: The aeroshell design.

### 3.5.1. Design drivers

The aeroshell is designed to protect the aerobot from the loads that it will undergo during atmospheric entry and to slow down the aerobot enough where the balloon can be safely inflated. During the atmospheric entry the aeroshell will experience declarations of up to 40 g's and thermal loading's of 773 W/cm<sup>2</sup>. To make sure that the aerobot does not fail during atmospheric entry, the aeroshell was designed to protect the aerobot from these loads. Furthermore one of the main function of the aeroshell is to slow down and then discard itself at the right altitude and velocity, these functions are reflected in the FBS, see figure Figure 3.10.

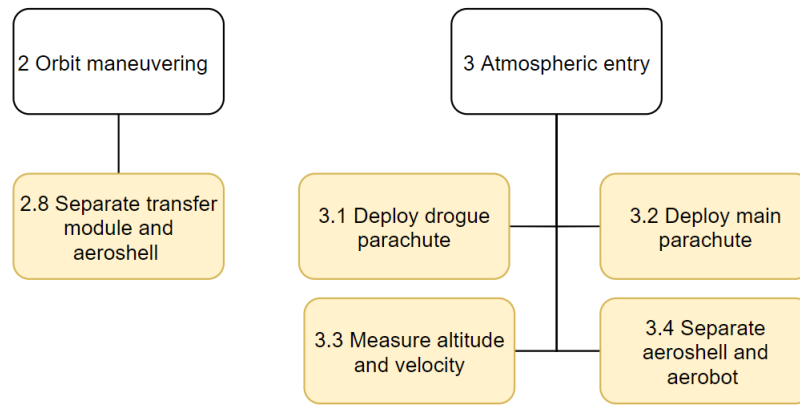


Figure 3.10: Functional breakdown for the aeroshell.

### 3.6. Orbiter

The orbiter functions is responsible for gathering scientific measurements and to relay the data generated by the aerobot and (indirectly) the dropsondes back to earth. To gather the scientific data multiple science instruments are present in the orbiter. For the relay of the data one main antenna is used assisted by multiple smaller antenna's. Power is provided by two solar panels mounted to the side of the orbiter. Orbital manoeuvres and attitude changes are achieved using several thrusters and momentum wheels, while the internal components of the orbiter are protected by honeycomb panels and a thermal control subsystem.

Parameter	Value	Unit
Dry mass	458	kg
Wet mass	720	kg
Main antenna diameter	3	m
Solar panel area	2.3	m <sup>2</sup>
Width	1.7	m
Height	1.2	m

Table 3.4: Design overview of the orbiter.

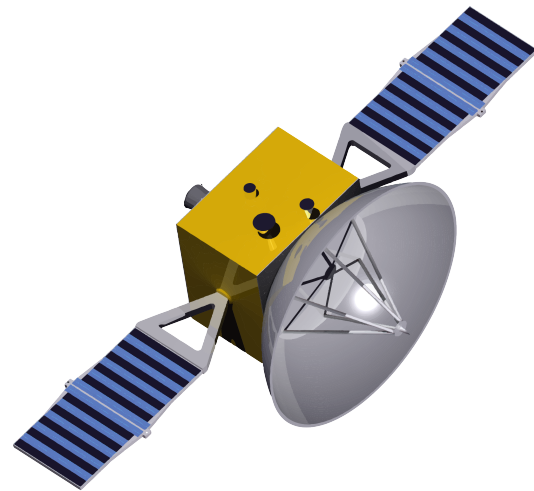


Figure 3.11: The orbiter design.

#### 3.6.1. Design drivers

The orbiter is designed to gather and relay scientific data while in a polar orbit around Venus. The main design drivers of the orbiter are the relay of scientific data to earth, power generation and storage, protection and maintenance of the orbit around the poles of Venus. The communication to earth is designed to transmit data for a distance of 100 million km. The power generation of the orbiter has to take the variable distance from Venus to the Sun and the eclipse time into account. While the components of the orbiter have to be protected from the solar radiation and launch loads. Furthermore to keep the orbiter in the right place at the right time with the correct attitude the ADCS and propulsion subsystems have been designed.

#### 3.6.2. Scientific mission

The orbiter will start making scientific measurements when it arrives in orbit around Venus. The scientific measurements and instruments of the orbiter comprise of:

- **Neutral mass and Ion mass spectrometry suite** for measurements of the neutral and atomic elements of the upper atmosphere of Venus.
- **Orbiter context camera** for making images of Venus, to study the cloud layers and surface of Venus.

In Figure 3.12, the functional breakdown structure specific to the orbiter can be found.

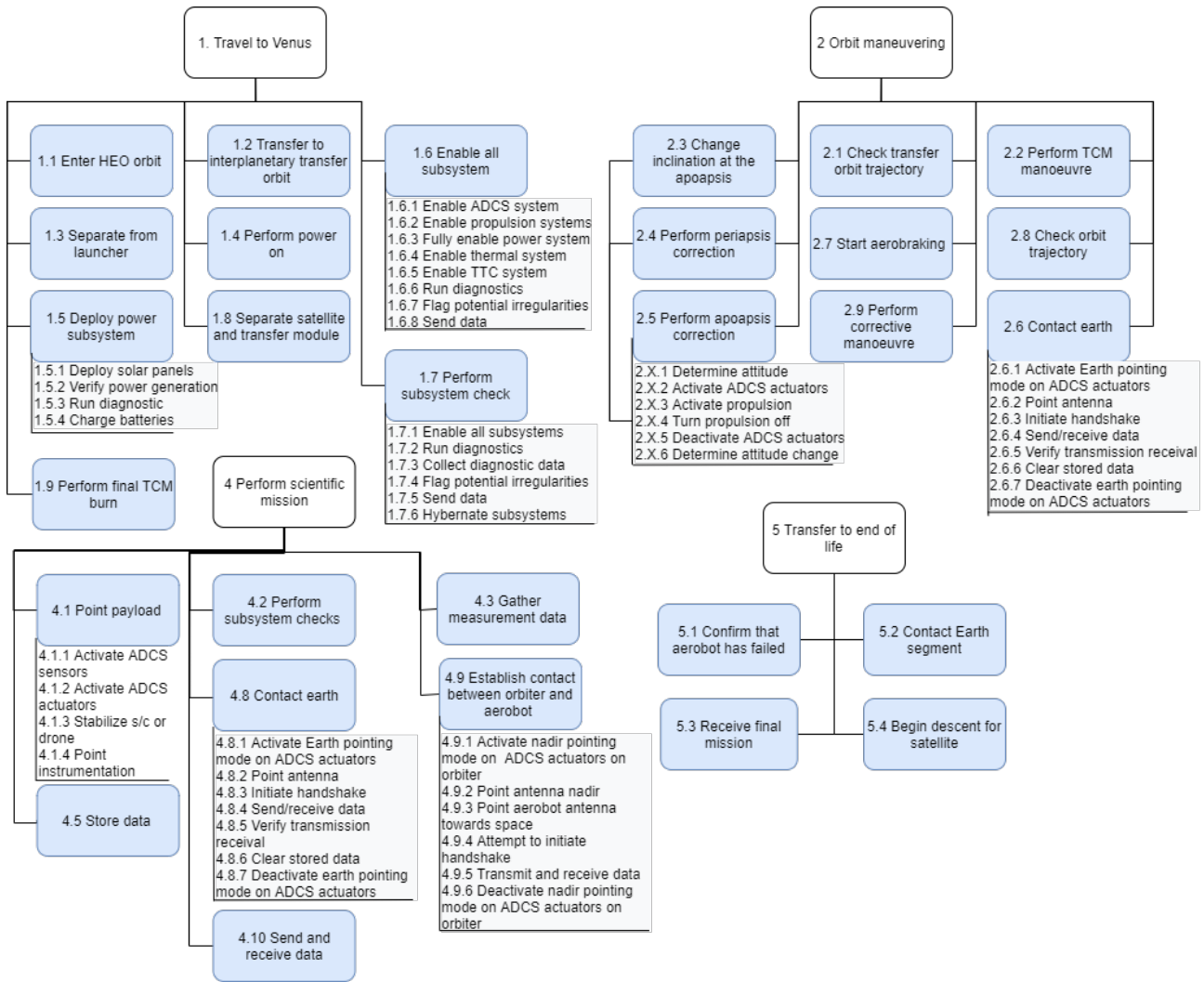


Figure 3.12: Functional breakdown for the orbiter.

### 3.7. Transfer module

It will protect the aeroshell from the environment of space and from the loads that occur during the launch of the vehicle. The transfer module (TRM) consists of struts that both protect the aeroshell and carry the orbiter before they separate. To transfer the aeroshell to Venus and insert it correctly into the atmosphere of Venus, the transfer module is equipped with multiple thrusters and momentum wheels. Furthermore to be able to provide adequate power 2 solar panels are attached to the sides of the transfer module. The generated power will be partly used to for communication using low-gain antenna's and thermal control.

Parameter	Value	Unit
Dry mass	1505.2	kg
Wet mass	2167.0	kg
Radius (shell)	1	m
Height (shell)	1.3	m
Radius (max)	1.6	m
Height (max with aeroshell)	3.2	m
Solar panel area	2.4	m <sup>2</sup>

Table 3.5: Design overview of the transfer module.



Figure 3.13: The transfer module design.

**3.7.1. Design drivers**

The transfer module is designed to provide protection of the aeroshell and aerobot from separation of the launch vehicle till atmospheric entry. The transfer module will be responsible for getting the aeroshell from the transfer orbit around earth to the correct orbit around Venus and then perform the atmospheric insertion burn. Between the launcher separation and atmospheric entry the transfer module is used to provide power, thermal protection for the aeroshell and to make contact with Earth. For an overview of all the functions that the transfer module needs to perform during it lifetime, see figure 3.14.

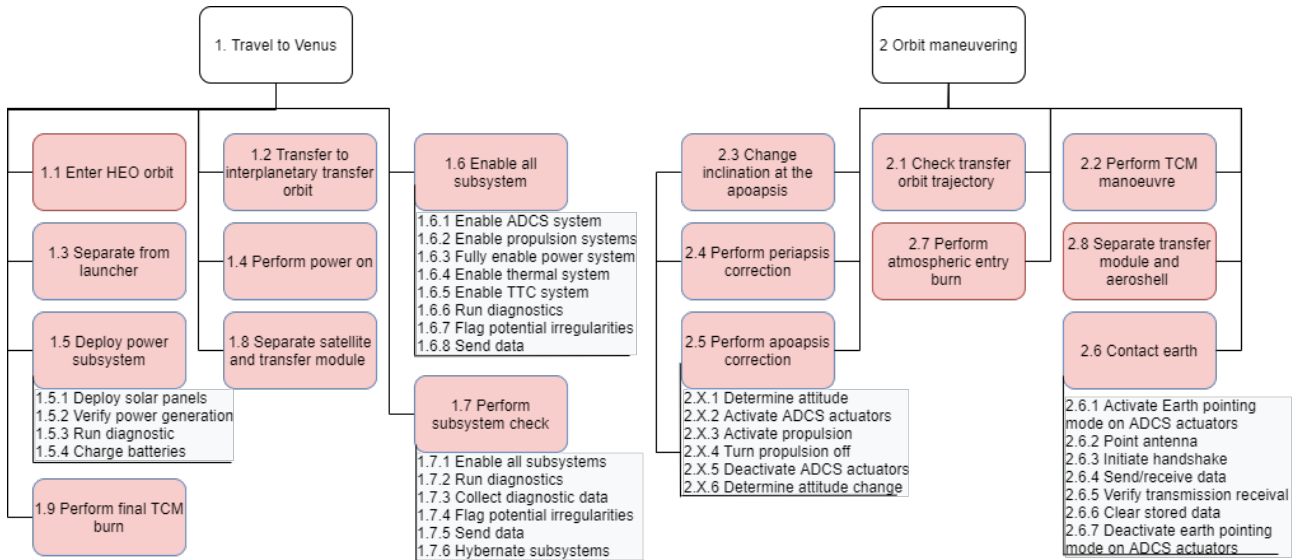


Figure 3.14: Functional breakdown for the transfer module.

**3.8. Launch configuration**

The previous mentioned vehicles will be integrated into the Falcon 9 launch vehicle using the following configuration, see figure 3.15. In this configuration the transfer module which houses the aeroshell is placed below the orbiter, both of which have deployable solar panels.



Figure 3.15: Launch configuration shown inside the Falcon 9 fairing.

## 4 Instrumentation and Planetary Science

One of the main project goals is to determine notable scientific mission objectives with respect to the user requirements and identifying the necessary scientific instrumentation to achieve these objectives. This section treats the design goals and design approach for the scientific mission, and the scientific instruments selection and sizing for the atmospheric and space segments.

### 4.1. Design overview

As the in-situ nature and long endurance of the mission was a given user requirement, the feasibility of in-situ platforms were analysed in conjunction with the expected lifespan of the mission platforms at various altitudes in the Venusian lower atmosphere. Past mission proposals on in-situ scientific missions were studied.

It was found that the atmospheric conditions of lower altitudes were extremely detrimental to the expected mission lifespan, such that a goal of 100 days of operation would prove infeasible without significant developments in technologies for extreme environments. For surface landers, the current state-of-the-art only permits operation on the order of hours. Even high-altitude aerobot mission proposals that loiter in near-Earth atmospheric conditions such as Venus Flagship, European Venus Explorer and Venus Climate Mission suggest a feasible mission lifespan on the order of a week to a month [15–17]; this is in direct contrast with terrestrial balloon-borne missions such as Project Loon, which conducted periodic balloon flights with heavy payloads lasting up to 187 days since 2014 [18].

Viewing the uncertainty of attaining the required 100-days of operational endurance for the in-situ mission, the high-altitude mission parameter was defined, with a target loiter altitude of 60 km as per requirements. To avoid reliability uncertainties leading to a reduction of expected operational lifetime, a reduction of mechanical equipment was preferred, leading to a constant-altitude balloon aerobot architecture with small dropsondes for scientific measurements in lower altitudes [4]. To improve the scientific data return and provide another platform for scientific measurements, it was decided that an orbiting relay would be incorporated into the mission.

Even though the main goal of the orbiter is relaying data back to Earth, it will also make measurements of its own. Two main scientific instruments were defined for the orbiter: a high resolution context camera and an ion and neutral mass spectrometer. The camera is mounted on the side of the orbiter and will take 20,000 images of the planet during the 100 day mission duration, while the mass spectrometer conducts sampling of atomic species in the upper atmosphere of Venus south pole. Further specifics of the camera are given in Section 4.4.

In Table 4.1 the mass and power budgets of all the instruments are summarised.

Table 4.1: Scientific payload

Suite	Mass (kg)	Power (W)
Seismology (gondola)	0.9	1.0
TNACA (gondola)	20	65
Meteorology (gondola)	2.1	3.2
Nephelometer (gondola)	0.5	1.2
DROPP (dropsondes)	0.01	0.035
NMIMS (orbiter)	11	25
Imager (orbiter)	20	12

#### 4.1.1. Approach to sustainability

No trade-offs were performed that were influenced by any of the three pillars of sustainability mentioned Section 2.6. The scientific mission in itself has goals which are focused on the environment on Earth, so in that sense the design was greatly influenced by sustainability. Besides the inherent focus on sustainability

no design considerations were made in picking the instruments which were dictated by the sustainability goals and requirements.

## 4.2. Functional analysis

In Section 2.2 the three main scientific goals of the BLOON mission were set. These goals are divided in a number of objectives which in turn have investigations related to them. The main function is to make sure that all investigations can be done during the operational phase of the mission. In Table 4.2 the science traceability matrix is presented. The table is divided in the three goals and sequentially the objectives and investigations are linked to the instruments that are needed for them. The instruments are explained in their own sections in this chapter and are referenced in the last column of the table.

Table 4.2: Scientific traceability matrix

Objective	Investigation	Instrument
Investigate the abundance and isotopic ratios of chemical species in the upper-cloud layer.		
A. Identify chemical and isotopic signs of a possible past ocean [8].	A. In-situ atmospheric measurement of D and H.	A,B. 4.3.3 C. 4.3.3
B. Determine whether the atmosphere was formed from local planetary processes or foreign introduction[8].	B. Measure noble gases isotopes of radiogenic and non-radiogenic origin and trace gases.	and 4.3.2 D. 4.4.1
C. Characterise the aerosol population in the cloud layer[8].	C. Measure density, particle size distribution, chemical species and optical properties of the cloud layer to ppb level.	E. 4.3.3 and 4.3.5
D. Determine rate of loss of atmosphere due to solar activity[8, 19].	D. Low-orbital measurements of atomic species.	
E. Determine the relation between the cloud and chemical cycles in the atmosphere and the radiation balance [15].	E. Combine investigation C. with vertical-atmospheric temperature profiles.	
Investigate meteorological phenomena to validate climate models		
A. What is the structure of the atmosphere and how do its superrotation and the general circulation work?	Atmospheric pressure with 1% sensitivity; temperature with 0.2 K sensitivity; Vertical wind with 0.1 m/s sensitivity; RMS turbulence levels at 5 min intervals; thermal tides; global and local wind speeds with 1 km height resolution between 25 - 60km; VIS-NIR images of the Venusian clouds at a resolution of 6 m/pixel at pericythe and 0.55 km/pixel at apocythe (narrow FOV mode). [16, 17, 20].	4.3.4, 4.3.5 and 4.4.2
B. How strongly is the atmosphere affected by day/night cycle?		
C. How do strong winds affect its compositional stability and how those winds interact with the surface?		
Place constraints on the structure and dynamics of the Venusian interior.		
A. Determine the atmospheric seismic background in the 1 to 5 Hz and 0.01 to 1 Hz frequency ranges.	A,B.Measure pressure fluctuations due to pressure waves on the order of $3 \cdot 10^{-4}$ Pa for a duration of 30 days [9, 21, 22].	A,B. 4.3.1 C. 4.3.3
B. Demonstrate seismic studies from a remote airborne station on solar system objects with substantial atmospheres such as Venus and Titan.	C. Measure volcanic gas emissions, in terms of chemical compositions, chemical species, and mass flux over time at a ppm-level sensitivity [15].	
C. Characterise species from volcanic ejecta.		

### 4.3. Instrumentation: Atmospheric segment

This section elaborates on the selected instruments for the atmospheric segments, namely the design approach and sizing. Most of the instruments are mounted on the aerobot gondola with the exception of one of the seismology suite elements.

#### 4.3.1. Seismology suite

The seismology suite uses two vertically-separated barometers to distinguish ground-based infrasound waves from atmospheric noise. It was stated in the user requirements that the frequency of the infrasound measurements should be in the 0.01 - 6 Hz range, which is in line with the expected performance of 0.01 Hz - 1 Hz and 1 Hz - 5 Hz frequency ranges for in-situ seismological sensing, described in the Keck Institute for Space Studies' (KISS) report for Venusian seismology [23]. To translate the operational requirements to instrument requirements, the Garcia report states that the velocity amplitude of the infrasonic pressure waves are amplified by a factor  $\sqrt{\frac{\rho(0)}{\rho(z)}}$ , where  $\rho(z)$  refers to the atmospheric density at an altitude  $z$  [24]. At an altitude of 60km, the amplitude factor is  $\sqrt{\frac{64.79}{0.4694}} = 11.75$ , thus meaning that sensitive microbarometers are sufficient to detect seismic events [25]. The KISS report then offers an estimate of the detection sensitivities for the microbarometers, suggesting a pressure sensitivity of on the order of  $10^{-3}$  Pa [23].

The barometers selected are Paroscientific Digiquartz 6000-16B-IS models drawn from a JPL balloon-borne terrestrial experiment in 2017 to test the viability of acoustic-coupling effects to detect seismic activity [21], for future seismic studies on an airborne platform on Venus. The barometers have an accuracy and resolution of  $10^{-3}$  Pa and  $3 \cdot 10^{-4}$  Pa respectively, but did not include the data generation rate [26]. To determine the atmospheric seismic background, continuous sampling is required, which leads to a high data generation rate. With a measurement frequency of 20 samples per second and 29 bits per sample, a data generation rate of 580 bit/s was found per barometer. To reduce the total data generation rate, a lossless STEIM compression scheme of 50% was used from the SEIS seismology experiment on the Mars InSight mission [27], which led to a total data generation rate of 580 bit/s for the entire suite.

The vertical separation would be 50 m as suggested in the KISS report [23], which creates a physical requirement for the gondola and tether design. One of the barometers will be situated directly under the balloon, while another will be situated on the gondola itself below the balloon. To avoid gondola-induced local effects, the bottom-most barometer will be mounted on a boom with the MET instrument. Additionally, the design of the instruments' inlets should compensate for atmospheric perturbations such as altitude increases and gusts, but this is reserved for future research.

Table 4.3: Barometers of the seismology suite engineering budgets [26]

	Number	Value	Total
Mass	2	0.45 kg	0.90 kg
Power	2	0.512 W	1.024 W
Operating temperature range	2	219 K to 333 K	-
Data generation (compressed)	2	290 bit/s	580 bit/s
Size	2	6.66 cm x 6.66 cm x 5.71 cm	506.54 $cm^3$

#### 4.3.2. Nephelometer

A nephelometer measures the concentration of aerosol and cloud particulate properties in the atmosphere, which complements the analyses done by the TNACA suite while characterising the turbidity and albedo of the upper cloud layer. Reliable estimates for operational mass, power, data rate and temperature ranges are known [15, 16] and shown in Table 4.4, however it is noteworthy that the nephelometer operation will be in direct contact with corrosive aerosol species ( $H_2O$ ,  $SO_2$ ) and will required additional chemical protection from the corrosive environment.

Table 4.4: Nephelometer instrument operational requirements

Mass	0.5 kg
Power	1.2 W
Operating temperature range	180 - 350 K
Data rate	320 bit/s
Size	3.9cm x 7.3cm x 12.6 cm + 7.8cm x 8.7cm x 10.9cm [28]

### 4.3.3. Trace gas, Noble gas and Atmospheric Compositional Analysis (TNACA) suite

The TNACA suite consists of several core instruments: A gas chromatograph (GC) to separate complex organic compounds into molecular components; a neutral mass spectrometer (NMS) to discriminate between molecules of varying masses; and a laser spectrometer that can be tuned (TLS) for assessing the concentration of gaseous species in a sample. While the Neutral Mass Spectrometer (NMS) forms the basis for the suite, allowing for the analytical determination of masses of molecules and their isotopic signature, the other instruments bundled together provide an augmented scientific return more than the sum of the individual instruments. The GC is specialised for the analysis of species atmospheric chemistry, and when coupled with an NMS it provides an accurate discrimination between isotopic ratios of H, O, C, N and S [17]. The TLS is a lightweight addition to the NMS, specialised for active trace gas species involved in cloud formation, especially for sulphur- and hydrogen-bearing species down to a sensitivity of ppb level. [16, 17].

Additionally, to characterise noble gas abundances and surface-/volcano-related mineral particles, other specialised instrumentation are added: a specialised noble gas mass spectrometry (NGMS) and an X-ray fluorescence spectrometer (XRF). An NGMS allows for a <1% accuracy measurement of He, Ne, Ar, Kr and Xe abundances and isotopic ratios [17], while an XRF identifies rock-forming trace elements (Al, Na, Mg, Si, K) in lofted surface dust or volcanic aerosol[17].

The suite is expected to be the heaviest and most power-demanding scientific item[15, 16]; between 10 to 18 kg of mass was budgeted based on the Flagship mission concept[15], the Venus Climate Mission (VCM) concept [16], the ESA European Venus Explorer (EVE) mission concept [17] and the Huygens probe [29], which usually includes the NMS alongside a gas chromatograph (GC) or a tuned laser spectrometer (TLS). The power consumption was found to be between 35 W to 60 W for those missions, with the upper limit originating from the VCM's NMS and TLS. To allow for the possibility of accommodating more scientific instruments such as the GC and TLS, a suite upper budget of 20 kg and 65 W was set for both mass and power without contingency factors.

The data generation rate for TNACA was based on the Mars Science Laboratory's Sample Analysis at Mars (SAM) suite, which includes a GC, an NMS and a TLS. The worst-case scenario listed in MSL SAM was a data generation of 11.8 MB (94.4 Mb) over a 6-hour period, leading to a science data rate of 4.37 kbps[30]. The VCM has an average science data rate of 3.6 kbps for both TLS and NMS[16], agreeing with the order of magnitude but did not specify any operation duration for a representative reference of a balloon mission. As TNACA is unable to operate constantly due to the processing times needed per sample, the daily average science data rate would be significantly lower than 4.37 kbps.

Table 4.5: Trace Gas, Noble Gas and Atmospheric Composition Analysis suite operational requirements

Power	65 W	Mass resolution	0.1 AMU
Mass	20kg	Mass range	1 - >150 AMU
Volume	17686.25 cm <sup>3</sup>	Sensitivity	<1 ppb for N and S species, 0.1 ppb Xe and Kr
Operating temperature	250 - 320 K	Accuracy	Abundance and isotope ratios of He, Ne, Ar, Kr, Xe to $\pm 1\%$ . Abundance and isotope ratios of H, O, N, S, C to <10%, Volcanogenic gases H <sub>2</sub> O, SO <sub>2</sub> , HCl, CO to 1%
Average Science Data rate	4370 bit/s		
Size	GC: 20 x 12 x 12 cm NMS: 30 x 20 x 12 cm TLS: 5 x 5 x 15 cm NGMS: 30 x 20 x 12 cm XRF: 2.5 x 2.5 x 5 cm		

#### 4.3.4. Meteorology suite (MET)

The meteorology suite measures local atmospheric temperature, pressure and wind speed, and can be used to constrain Venusian atmospheric dynamics models. These can in turn be extremely valuable for terrestrial general circulation models. Comparing the angular momentum exchange between the atmosphere and the solid planet on Venus with that on Earth not only could explain the Venusian super-rotation phenomena, but also ENSO-connected variations of Earth's rotation period [15]. The sizing was done with respect to the Atmospheric Structure Instrumentation suite used on both the Venus Climate Mission and the Venus Flagship proposals with heritage knowledge from the Mars Volatiles and Climate Surveyor [15, 16].

To avoid gondola-induced effects on the measurements, MET will be mounted on a deployable boom along with one of the seismology barometers as suggested in Venus Flagship. The expected boom length is on the order of 1 meter suggested by Venus Flagship [15], while deployment and mechanisms are briefly discussed in Chapter 14. Due to its small data generation rate at 250 bps, it is planned to conduct sampling every 15 minutes, with the option of increasing the sampling rate. The specifications of the MET remains unchanged from the midterm report, and are listed in Table 4.6.

Table 4.6: ASI suite budgets [15]

Mass	2.1 kg	Pressure range	250 - 2500 mbar
Power requirement	3.2 W	Pressure accuracy	1 mbar
Sampling interval	1 hr	Pressure sensitivity	0.1 mbar
Temperature range	180 - 350 K	Wind speed range	1 - 100 m/s
Temperature accuracy	$\pm 0.5$ K	Wind speed accuracy (1 - 10 m/s)	0.1 m/s
Temperature sensitivity	0.1 K	Wind speed accuracy (10 - 100 m/s)	1 m/s
Data generation rate	250 bit/s	Size	10cm x 10cm x 10cm

#### 4.3.5. Dropsonde Payload Package (DROPP)

Since the dropsondes are single-use probes with an operational lifespan of under an hour, the design approach was to use light, miniaturised instruments with low mass and power requirements, while having a reasonable sampling rate and accuracy. The instrument payloads were mostly based on the 2019 LEAVES drop probe payload design [31] and the ESA Astra 2004 Microprobe study [32], due to their significantly miniaturised form factors compared to other dropsonde payloads such as the Venus Climate Mission [16].

The basic payload contains a temperature and pressure sensor suite and an accelerometer. The temperature sensor would be thin-wire thermocouples connected to a reference temperature sensor such as a platinum resistance thermometer inside the probe. The pressure sensor suite contains multiple pressure sensors which can cover the expected pressure ranges between 25 km to 60 km altitude (1.5 - 0.0236 MPa or 15 - 0.236 bar respectively [25]), and using the pressure data, rough altimetry profile is derived by referencing to a reference atmospheric model and recording the fall duration. The IMU-based accelerometer can be used for rough location derivation, as mentioned in the LEAVES study, the nadir and westward directions can be inferred when the probe has reached a state of terminal velocity [31]. The location determination of the probe would also be done via two-way ranging and Doppler tracking from the aerobot (see Chapter 9).

For extended scientific capability, additional miniaturised instruments could be carried to improve the scientific return of the dropsonde. A list of instruments are listed as follows:

- **Micro Electro-Mechanical Systems (MEMS) sensors for specific chemical species detection** were suggested in the LEAVES proposal, with a high detection resolution would allow for lightweight and widespread characterisation of trace gas abundances in Venusian atmospheric layers[31]. However, while technological maturity is favourable as a result of NASA development, these sensors are highly specific and require prior knowledge of the chemical species in the lower atmosphere[33]. Besides that, the silicon-carbide based semiconductor technology is designed to operate in high temperatures, and would need to be heated when in upper atmospheric levels .
- **Wide-band light sensors** for cloud detection and environmental radiation measurements were suggested in the ESA Astra 2004 Microprobe study [32]. Each sensor head contains a silicon photodiode to cover from around 250 nm to 1100 nm wavelengths, and a thermopile sensor to cover electromagnetic wavelengths to 4  $\mu\text{m}$ . The sensors would be embedded within the dropsonde, and atmospheric interfacing would be achieved via a quartz fibre optic light guide to outside the dropsonde.

As the dropsonde was designed to be lightweight, this design approach was also carried over to the dropsonde instrumentation. Initially, the dropsondes from the Venus Climate Mission and the Venus Exploration of Volcanoes and Atmosphere (VEVA) probe designs were used as reference templates, but the instrument mass of around 2 - 10 kg was found to be unreasonable for a mission with 25 dropsondes not including peripherals [16, 34]. An initial mass budget of 0.6 kg was set for the dropsonde scientific payload, but after referring to the LEAVES and Astra 2004 Microprobe payloads, both sources cite an order of magnitude of mass of under 10 grams and a power consumption of 35 mW [31, 32]. As a result, it was expected that the additional mass budget could either be trimmed for more mass savings per instrumentation, filled with extra instrumentation, or allocated to structural protection of the dropsonde for enhanced mission lifespan.

The scientific data rate for the instrumentation was not provided, but its upper bound will be defined by the available link budget for the dropsonde, and it is expected that the instrumentation sampling rate would fulfil the user requirement of 1 km of vertical resolution as well.

#### 4.3.6. Scientific data generation rate

The seismology suite is the only instrument that is required to operate persistently, setting the baseline for the scientific data generation budget. Including the expected STEIM compression factor of 50%, it leads to a data generation of 50 Mb per day. In contrast, the reference missions with the highest data generation per day, Venus Climate Mission cites only a daily generation of 6.5 Mb per day [16]. While the average data generation rate of the scientific instruments are given in literature, the operational duration, processing time and data handling scheme are not, causing difficulty in determining the data volume per day.

As a first-order estimate, it was assumed that all instruments generate data persistently and no data compression was added besides the seismology suite's compression scheme. This leads to a data generation rate of 5.52 kbps or 477 Mb per day. While heritage suggests that this is a reasonable value, and findings on the Mars Science Laboratory rover experiment suggest higher generation rates are possible [30], it was suggested in Venus Flagship and European Venus Explorer that the nephelometer, MET suite and TNACA suite have sampling times on the order of minutes to an hour, instead of every second. Meanwhile, other data generation rates from dropsonde instruments are unavailable, and the data budget should include provisions for them.

The data generation budget was refined by halving the nephelometer, MET and TNACA instruments' operational hours, leading to an operational hours of 12 terrestrial hours per day (from 24 hours). Subsequently this leads to a data generation budget of 3.05 kbps or 264 Mb per day. This value is viewed as a conservative estimate and is expected to include the data generated by the dropsonde instruments until more granular data on instrument operational and processing times are known; it should be noted that the number of samples per day is variable and dependent on the available link budget and available power. The value of 3.05 kbps was then used for the sizing of the telemetry, tracking and control section, and a breakdown of the data generation rate calculations are included in Table 4.7.

Table 4.7: Data generation rate and data volume sensitivities as a function of hours active.

Instrument	Data generation rate [kbit/s]	Hours active per day [hours]	Daily data generation [kbit/day]			
TNACA	4.37	24 12 8 6	377568	<b>188784</b>	125856	94392
MET	0.25	24 12 8 6	21600	<b>10800</b>	7200	5400
Neph	0.32	24 12 8 6	27648	<b>13824</b>	9216	6912
Seismo	0.58 (compressed)	24 24 24 24	50112	<b>50112</b>	50112	50112
<b>Total data generated per day [kbit]</b>			467928	<b>263520</b>	192384	156816
<b>Average net data generated [kbit/s]</b>			5.52	<b>3.05</b>	2.23	1.82

It can be seen from Table 4.7 that the data generated by the TNACA suite forms the majority of the total data generated, while the seismology instrument forms a constant baseline for data generation.

## 4.4. Instrumentation: Space segment

This section elaborates on the selected instruments on the orbiter, specifically the design approach and sizing. No instruments were planned for the transfer module.

#### 4.4.1. Neutral mass and Ion Mass Spectrometry suite

The Venus Express (VEX) mission shed light on the interaction between solar wind and the upper atmosphere near the north pole, namely on the loss of He, H and O species [35] and classified the ionosphere above the north pole, above 250 km. However, VEX took place during a period of low solar activity. Science questions remain for the classification of the upper atmosphere during a solar maxima and below 250 km. Besides this, important processes on Earth dictated by space physics can be better understood by characterising the weather environments of Venus and comparing the solar cycle response of the upper atmospheres and exospheric escape fluxes and climates [15]. In conjunction with the launch window requirement of the current mission design (see Chapter 5), including a neutral mass and ion mass spectrometer provides an opportunity to characterise the neutral and atomic elements in the upper atmosphere during a solar activity transition towards solar maxima [36]. The current capabilities and operational requirements of the NIMS contains good heritage from various NASA and ESA missions; the measurement requirements are derived from the knowledge gained from the Venus Express mission [35, 37] and MAVEN's Neutral Gas and Ion Mass Spectrometer (NGIMS) instrument [38], while the operational requirements are derived from Cassini's Ion and Neutral Mass Spectrometer (INMS) [39]. The requirements are listed in Table 4.8.

Table 4.8: Neutral mass and ion mass spectrometer measurement and operational requirements

Mass resolution	0.1 AMU (MAVEN), reliable mass separation for $C^+$ , $N^+$ , $O^+$ , $O_2^+$ , $CO_2^+$ , $NO^+$ , $CO^+$ , $N_2^+$ , C, N (VEX findings)
Mass range	2-150 AMU (MAVEN)
Mass	10.29 kg (Cassini)
Power	25 W (Cassini)
Data rate	1510 bit/s (Cassini)
Size	20.3 x 42.2 x 36.5 cm (Cassini)

#### 4.4.2. Orbiter context camera

The orbiter camera will fulfil multiple purposes. It will take 20,000 images of Venus during its planned 100 day operational lifetime and could continue to function afterwards. With its high accuracy, discussed in detail in this subsection, the camera will be used to study the cloud layer of Venus and by using different parts of the light spectrum it can also capture images of the Venusian surface. This allows it to be used in order to study the atmospheric dynamics and possible ground formations that can indicate past tectonic activity. Furthermore, the camera could be used as a science demonstration for visual tracking of the aerobot.

The sizing of the orbiter camera is based on previous similar missions and off-the-shelf components are used when possible. The two most similar missions that used a VIS-camera are Mars Express and the Venus Express and Mars Express [40]. Like the Venus Express, this orbiter camera will make use of a Kodak KAI-1010 CCD [41]. This CCD allows an image resolution of 1024x1024 pixels [42]. This CCD allows 12-bit imaging and thus results in an image size of  $1024 \cdot 1024 \cdot 12 = 12.6$  Mbit/image. A higher resolution might be possible, but this can only be determined at a later phase of the design and is also dependent on other factors, such as the data storage discussed in Chapter 9. The duty cycle of the camera is based on the Mars Orbiter Camera of the Mars Express mission. This camera had a duty cycle of 13% (30 minutes operating time per 4 hour daytime of the orbit) and was able to take roughly 80 1024x1024 12-bit images per 24 hours [40]. Based on an iteration of the data storage and the fact that the most interesting regions to photograph are either at apoclythe and pericythe, it was determined to take 200 images per 24 hours, resulting in a required duty cycle of  $13 \cdot (200/80) = 32.5\%$ , which is rounded to 30%, most likely a conservative estimate due to the significant progress made regarding camera technology since the previous missions. Calculations on the required storage can be found in Section 9.3.

The camera field of view (FOV) angle is also important to determine on a resolution value. It was decided use two different FOV's to capture both detailed and general images. The first FOV is increased to the point of being able to capture Venus in its entirety at apoclythe. Calculating the tangent from the apoclythe to Venus results in a required FOV of 38.5 degrees. This calculation is based on the same code as the one used for the orbit determination and verification of the code can thus be found in Chapter 5. This FOV allows a pixel resolution of 12.8 km/pixel at apoclythe and 0.14 km/pixel at pericythe [40]. The second, more narrow, FOV is calculated using the fact that every orbit one image can be taken from the same location. Over the

course of 100 days this means 550 images from the same location can be taken, based on the orbital period discussed in Chapter 5. By using a FOV of 1.7 degrees, these 550 images can be made to create a 23x23 composite image of the entire planet. For this FOV the pixel resolution is 0.55 km/pixel at apocytpe and 6 m/pixel at pericythe [40], allowing for the highest resolution images of Venus to date.

Like the Venus Express Camera, this camera will take pictures in the UV, visible and near infrared (NIR) region. The sizing of the camera is based on the volume of the Mars Express and Venus Express camera. The Mars Express camera has a mass of 20 kg [40] and has a volume of  $0.042 m^3$ , similar to  $0.041 m^3$  of the Venus Express camera [41]. The dimensions of the Venus Express are chosen as this mission's parameters due to the similarity between missions; these dimensions are 0.65x0.25x0.25 m [41]. Further research is recommended in order to determine the camera mass and dimensions with higher accuracy. The camera could also be used to determine the polarisation of the radiowaves emitted by Venus or from the solar rays that went through the Venusian atmosphere. This can be used to determine scattering parameters of the atmosphere, similar to radio occultation research [43]. However, since this is not one of the predetermined scientific objectives, no further research was performed into this at this stage of the project.

It might also be possible to use the camera for tracking of the aerobot. Using a bond albedo of 0.75 for the Venusian clouds and 0.6 for the balloon for [1] shows that the aerobot would cause a measurable difference in the brightness of a pixel using the narrow FOV option. The aerobot is not encountered at pericythe, but at 20 degrees North latitude, where the minimum distance to the aerobot equals roughly 5000 km. At this distance the pixel size of the narrow FOV mode is roughly 150 m/pixel. With the 12-bit imaging system that allows for 4096 brightness levels and the balloon should lower the brightness of a pixel by 2 or 3 levels. The small FOV method only works if the location of the aerobot is already roughly known within a few degrees, but this is achievable with the methods described in Chapter 9. An algorithm analysing multiple images could use this to identify the position of the aerobot on the photo, but this is also dependent on the variability of the Venusian cloud albedo, which has not been researched in detail to date. This needs to be analysed in the future before this method tracking could truly be implemented in the mission.

## 4.5. Sensitivity analysis

As the scientific payload requirements drive the design of the spacecraft and atmospheric segment buses, factors such as mass, placement, volume, data generation rate and power requirements may lead to unfeasible design decisions on other subsystems. In the DSE project, the significant sensitivity variables were data generation rate and power requirements. The power consumption of the instruments is dependent on the available electrical supply from the aerobot, and the instruments' operational hours in daylight and eclipse were iterated with respect to the mass sensitivity analysis of the power storage subsystem. Meanwhile, the data generation rate impacts the physical sizing of communications hardware in the telemetry, tracking and command division; this generation rate was calculated as a function of instruments' operational hours as shown in the data generation rate section and was done independently of the power constrained operation hours. A future recommendation would be to formally quantify the data generation rate with respect to the instrument operational periods constrained by available power. That said, until more granular operational power consumption of individual instruments are known from instrument development and integration, the exact instrument power consumption and subsequently data generation rate is not final yet.

## 4.6. Verification and validation

The design decisions were made with reference to similar past missions to determine the instrument types and their operational requirements. After getting a range of values of the expected physical sizes, masses, data rates, operational conditions and power requirements of the scientific instruments these were used in further calculations. As these ranges were based on literature review, this means verification and validation was almost completely based on similarity. Besides that, a literature study was performed to validate whether the user requirements had enough scientific value.

**Camera verification and validation** The decided upon FOV's for the camera were compared to the FOV's of other missions to make sure they are within a reasonable range. The pixel resolution at different distances was based on equations from reports on IPS and were validated by applying the equations on data from the Mars Express mission [40]. The same goes for the storage size of an image.

# 5 Astrodynamics

This chapter gives a description of the orbits that occur during the mission and the respective  $\Delta V$  budget. At the end of this chapter the risk analysis, sensitivity analysis and verification and validation are given.

## 5.1. Design overview

The overview of the design choices for the astrodynamics of the BLOON are shown here. These include the key orbits that will be used during the mission after VOI, alongside a sustainability approach.

### 5.1.1. Mission orbits

There are four orbits that define mission phases. These are the capture orbit, the starting aerobraking orbit, the scientific mission orbit and the atmospheric entry orbit of the TRM. Their respective orbital parameters are shown below in tables 5.1, 5.2, 5.3 and 5.4. Here  $r_p$  is the pericytherion radius from the surface of Venus,  $r_a$  is the apocytherion radius from the surface of Venus,  $a$  the semimajor axis and  $T$  the orbital period. Note that the inclination is  $12.5^\circ$  for the orbits of the TRM and  $90^\circ$  for the orbiter. Both TRM and orbiter enter a capture orbit with the same parameters but a different inclination.

Table 5.1: Orbital parameters (noted as Param.) for the capture orbits.

Param.	Value
$r_p$	400 km
$r_a$	218241 km
$a$	115372 km
$T$	5 days

Table 5.2: Orbital parameters (noted as Param.) for the aerobraking orbit of the orbiter.

Param.	Value
$r_p$	136.5 km
$r_a$	70448 km
$a$	41344 km
$T$	25.75 h

Table 5.3: Orbital parameters (noted as Param.) for the mission orbit of the orbiter.

Param.	Value
$r_p$	200 km
$r_a$	12332 km
$a$	12318 km
$T$	4.19 h

Table 5.4: Orbital parameters (noted as Param.) for the entry orbit of the TRM.

Param.	Value
$r_p$	50 km
$r_a$	218658 km
$a$	112338 km
$T$	2.4 days

### 5.1.2. Approach to sustainability

The sustainable development strategy for astrodynamics boils down to ensuring that the orbit around Venus is free of space debris after the mission. This is done by making the TRM burn up in the atmosphere when it inserts the probe, along with making the orbiter aerobrake until it burns up in the atmosphere. Analysis on the aerobraking of the orbiter resulted in a decay into the atmosphere after 98 days.

## 5.2. Functional analysis

The function of the astrodynamics analysis is to investigate the orbits that are required for the duration of the mission. The focus of this analysis was set on determining the sequence of orbits after the VOI. This was done as one of the main requirements for this project was to design the BLOON mission after a successful VOI. However some elements prior to the VOI had to be analysed, as is discussed in the next section.

## 5.3. Launch and transfer to Venus

This section gives the analysis on the launch vehicle (LV) selection, the launch window (LW), the orbits around Earth, the transfer orbit and the capture orbits. These mission aspects take place before or during the VOI but have to be analysed due to their impact on the overall mission design.

### 5.3.1. Launch window and vehicle

The LW is an important part of the mission design that determines the  $\Delta V$  budget for the interplanetary trajectory and VOI. In order to select the LW and launch date the following assumptions were made:

- 8+ years will be required for the design and production phases, based on past missions [40].
- Only the most optimal trajectories, with a duration under one year, were considered for each synodic period. Trajectories that make use of electric propulsion were not taken into account.
- The LV provides the  $\Delta V$  for the Earth escape, while the BLOON provides the  $\Delta V$  for VOI.

The NASA trajectory browser<sup>1</sup> was then used along with a trade-off [4] to select a LW from 2028 onwards. From this, two LWs were chosen with their characteristics shown in Table 5.5.

Table 5.5: Selected LWs to Venus for the BLOON.  $C3 = 0 \Delta V$  is the  $\Delta V$  to enter a zero energy orbit around Venus, HEO  $\Delta V$  is the  $\Delta V$  to enter the interplanetary trajectory from a HEO on Earth. All values are taken from NASA's trajectory browser<sup>1</sup>

Earth escape	Venus arrival	$C3=0 \Delta V$ (m/s)	HEO $\Delta V$ (km/s)	Travel (days)	Years until launch
2031-05-30	2031-10-05	395	3.75	128	11.1
2032-12-10	2033-05-19	305	3.69	160	12.6

Both LWs have similar performance. It was chosen to design for the 2031 LW while keeping the 2032-2033 LW as a backup as a contingency measure against delays. The planned ESA mission "Envision" currently plans to use the 2032 LW for their mission, with the 2031 and another 2034 LW as backups [44]. This validates the current selection of launch windows, as it is planned for a future mission.

The 2031 LW requires a  $\Delta V$  from the launcher of 3.75 km/s. During the midterm phase a selection of 3 LVs was made that could fulfil the mission requirements using the midterm mass estimations. The chosen LVs and their properties are shown in Table 5.6 for the 2031 LW. The payload values to Venus were computed with their respective LV user manuals<sup>2 3</sup> in the midterm [4]. Due to the uncertainty in the mass budget during the midterm phase no selection was made for a LV. Current mass budget estimations give a total mission mass of 2885 kg with a 10% contingency to drymass. All of the chosen launchers fulfil this requirement.

It was decided to size the BLOON mission for one atmospheric probe, with the intent to investigate having multiple probes after sizing of one probe was done. During the midterm it was estimated that multiple probes would be feasible for all LVs. However, with the current mass budget only one probe can fit on the Falcon 9 and Atlas V, while the Falcon Heavy can carry multiple probes. It will be assumed that the mission will only have one probe as one is enough to fulfil the requirements. Then the Falcon 9 will be chosen as the LV. The reduced cost compared to the Atlas V was deemed more important than the decreased reliability. With only one probe, the increased payload mass of the Falcon Heavy offers no benefits over the Falcon 9. During the design and production phase the LV selection will be re-evaluated by taking into account the possibility of having multiple probes.

Table 5.6: Summary of launch vehicle characteristics for insertion into a hyperbolic Venus fly-by trajectory.

Launch vehicle	Cost (million USD)	Launches	Failure rate (%)	Payload (kg)
Atlas V 551 [45]	140	83	1.2	5058
Falcon 9 (expendable) [46]	62	84	2.4	3961
Falcon Heavy (expendable) [46]	90	3	0.0	11101

### 5.3.2. Earth orbit and transfer trajectory

After launch the BLOON will orbit Earth until the LV performs the escape burn. This orbit impacts the design of the thermal and power subsystems. An estimation of this orbit and its duration is therefore to be made. The NASA trajectory finder gives the date for departure from Earth, thus the BLOON has to be orbiting Earth prior to this. It will be assumed that the BLOON will be flown to a LEO orbit, where after the orbit will be raised to a HEO orbit. The launch date of the BLOON will be set to 20 days before the escape. This is enough time to launch, go into a HEO orbit and prepare for escape. The 20 day margin will also act as a measure against unforeseen launch cancellations due to bad weather or other aspects, giving the mission enough time to perform the most optimal interplanetary trajectory insertion burn should delays occur.

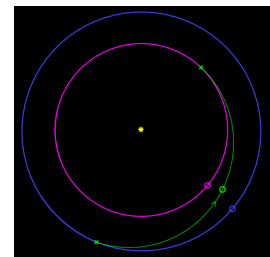


Figure 5.1: Interplanetary trajectory for the 2031 LW.

<sup>1</sup>[https://trajbrowser.arc.nasa.gov/traj\\_browser.php](https://trajbrowser.arc.nasa.gov/traj_browser.php), retrieved on 12 May 2020

<sup>2</sup><https://www.spacex.com/about/capabilities>, retrieved on 8 May 2020

<sup>3</sup><https://space.skyrocket.de/>, retrieved on 11 May 2020

Subsequently it will be injected into the escape trajectory. The trajectory that will be used is shown in Figure 5.1. The green line is BLOON, blue Earth and pink Venus.

### 5.3.3. Planetary capture

When the orbiter arrives at Venus it will perform the VOI burn. The orbiter and TRM will separate 20 days before VOI. Both will perform their capture burns, and land in orbits with a different inclination, but the same pericytherion and apocytherion. It was chosen to have the capture orbit be a five day orbit, with a pericytherion at 6451.8 km and an apocytherion at 224293 km from the center of Venus. The orbiter will have a polar orbit while the TRM will orbit Venus with a 12.5 degree inclination, with its argument of pericytherion at 12.5 degrees North latitude. This differs from the orbits estimated during the midterm [4] due to the third body perturbation from the Sun, discussed in the next section.

## 5.4. Aerobraking

Aerobraking will be used to lower the orbiters orbit. After the midterm phase a trade-off was performed between direct insertion into the mission orbit (lowering its orbit by use of chemical propulsion) against aerobraking. This trade-off was performed with a lot of uncertainty associated with the mass budget of the mission due to the early stage of the design. From this analysis it was concluded that aerobraking would be more beneficial for the mass budget, leading to aerobraking being chosen to enter the missions orbit. However since then mass budgets have significantly changed. A new trade-off analysis on this matter is required in order to determine whether aerobraking is still the most optimal method of orbit lowering for the BLOON orbiter. However, this would require a design of a direct insertion system that is of the same level of detail. Due to time constraints, this analysis will be kept as a recommendation for the future, while the results of the initial trade-off will be taken as correct.

### 5.4.1. Assumptions and methods

The following assumptions are made to perform an aerobraking analysis of the orbit:

- A 4 step Runge-Kutta integration scheme will be used to calculate the position, velocity and accelerations of the orbiter over time. Explanation of how this is set-up is given in Chapter 6.
- A time step of 10 seconds will be taken between each integration point. This assumption has been verified, giving a difference of less than 1% in orbital position compared to 1 second time step.
- The  $C_D$  of the orbiter was assumed to be 2.2 [47]. The  $C_D$  at low densities depends on the atmospheric composition, density and orbiter shape [48]. More detailed analysis is required to determine the  $C_D$ . However the  $C_D$  of satellites at low densities is in the range of 2 to 3 [47] [48]. Therefore a value of 2.2 is a safe assumption.
- The orbiter was assumed to always face perpendicular to the travel path, with the full area of the orbiter antenna and solar panels. This gives a total area of 9.5 m<sup>2</sup>. The area of other satellite components are ignored. The ADCS subsystem is able to maintain the orbiter in this configuration (see Chapter 12), therefore this assumption is valid.
- While aerobraking is being performed the TRM will sit in its capture orbit until the distance between the Earth and Venus is less than 100 million km. This will take approximately 464 days<sup>4</sup>.
- Lowering the orbit into an aerobraking orbit will take at most 8 days after VOI. This leaves 456 days over for aerobraking.
- A 20% margin will be taken for the aerobraking. Therefore from the simulations the aerobraking should be finished after 380 days. This is done in order to account for the uncertainty in the atmospheric density at high altitudes among other uncertainties.
- Orbital decay due to radiation pressure will not be taken into account. The current estimations of how much  $\Delta V$  is required to compensate for radiation decay is 1 m/s over a period of 3 years.
- Orbital decay due to third body Sun perturbation is sized separately for the duration of aerobraking. It will be assumed that the orbit will be at constant pericytherion for the duration.
- The antenna can be heated up to 390 K. No maximum temperature is reported for the multi-junction GaAs solar cells used [49]; instead, their maximum temperature is estimated based on data from the Akatsuki array, which could reach 493 K without significant degradation [50]. A better estimation of the maximum allowable temperature before damage occurs will have to be done in the design phase,

<sup>4</sup><https://theskylive.com/how-far-is-venus>, retrieved 1 June 2020

to optimise the aerobraking pericytherion.

- NASA's atmospheric model of Venus will be used as a model of the atmosphere <sup>5</sup>.
- In order to determine a minimum allowable altitude for the aerobraking, a thermal analysis was performed. Using NASA's atmospheric model of Venus, a result of an altitude of 136.5 km was obtained.
- Since no aerodynamic analysis was done for the solar panel and antenna, the method for thermal analysis that is used in Chapter 6 could not be used. A model that calculates the stagnation point heat flux was used. This leads to an overestimation of the actual temperature during aerobraking.
- The simulation runs at a pericytherion of  $136.5 \pm 0.2$  km, starting at a higher altitude and decaying a bit due to drag. In reality, aerobraking will be done at a constant altitude of 136.5 km.

With these assumptions in place, the aerobraking simulation was executed. First, the minimum altitude was determined by a thermal analysis of the orbiter. Secondly, the starting apocytherion altitude was based on an estimate. The speed at the apocytherion was then obtained using the energy equation (5.1). The simulation was then run for 3283200 steps of 10 seconds (resulting in 380 days simulated time). The simulation was stopped whenever the pericytherion decayed lower than 136.3 km, and increased back to 136.7 km.

$$\frac{1}{2}V^2 - \frac{\mu}{r} = \frac{\mu}{2a} \quad (5.1)$$

$$T = 2 \cdot \pi \cdot \sqrt{\frac{a^3}{\mu}} \quad (5.2)$$

Based on the results of the first simulation the next iteration would start at a lower or higher apocytherion depending on the final height. This was done until convergence was reached, where the final apocytherion height after 380 days was slightly lower than the desired apocytherion for the mission. The mass that was assumed for the orbiter is the wetmass at which aerobraking takes place, assuming an orbiter drymass of 454 kg.

### 5.4.2. Third body Sun perturbation

An important aspect that has to be analysed for the aerobraking duration is the third body perturbation due to the Sun. Solar perturbation is given by Equation 5.3.

$$\vec{a}_{sol} = \mu_{Sun} \cdot \left( \frac{\vec{r}_{vs} - \vec{r}_{vo}}{r_{os}^3} - \frac{\vec{r}_{vs}}{r_{vs}^3} \right) \quad (5.3)$$

Where  $\vec{a}_{sol}$  is the resulting acceleration vector on the orbit,  $\mu_{Sun}$  the gravitational constant of the Sun,  $\vec{r}_{vs}$  the distance between Venus and the Sun,  $\vec{r}_{vo}$  the distance between Venus and the perturbed body and  $\vec{r}_{os}$  the distance between the Sun and the perturbed body. The following assumptions were used:

- Equation 5.3 requires a planet-centric coordinate frame. The positive Z direction was defined to point towards the North pole whereas the x and y direction lie in the equatorial plane (see Figure 5.2).
- The VOI is assumed to take place at the apohelion of Venus.
- The initial orbiter/TRM orbit will be parallel to the travel path of Venus around the Sun.
- Its assumed that the orbital plane of Venus around the sun lies exactly in the equator of Venus, and remains constant throughout a year. In reality there is a  $177.36^\circ$  obliquity to the orbit [1].
- The Sun-Venus distance was modelled using inputs from the Venus fact sheet [1]. A time step of 1 s was used for the duration of one Venusian year. This returned an orbit with slightly higher perihelion than the orbit of Venus, giving  $6 \cdot 10^7$  m more at perihelion. This is likely due to rounding in the fact sheet. Using the full model of the distance made the simulation run slowly, so a datasheet was created with the distance every half an Earth day.

From this equation it can be noted that the further away the orbiter/TRM is from Venus, the higher the perturbation. This is of utmost importance for aerobraking due to the fact that aerobraking starts at a HEO orbit around Venus for the orbiter, whereas the TRM remains in a HEO orbit. After capture the orbiter will spend one full orbit in the capture orbit, before orbital manoeuvres lower the orbit down to the aerobraking

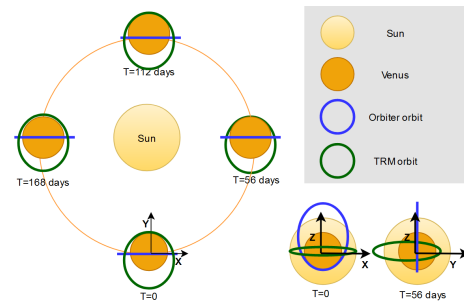


Figure 5.2: Reference frames used for orbit analysis. Blue orbit represent the orbiter while green represents the TRM.

<sup>5</sup><https://software.nasa.gov/software/MFS-32314-1>, retrieved 5 May 2020

orbit. The impact of the Solar perturbation on one capture orbit of the orbiter is shown in Figure 5.3 and Figure 5.4. Figure 5.3 shows the effect of Solar perturbation on Y coordinate, using the aforementioned coordinate system shown in Figure 5.2. The 10-day orbit has a change in Y that is 11.3 times bigger than the change of the five day orbit. In order to minimise this effect, it was therefore decided to choose the five day capture orbit. This should be feasible as the burn time the orbiter will require to enter the 5-day orbit from the interplanetary transfer orbit is lower than the burn time VEX needed to enter its 9-day orbit Chapter 8 (the safety factor used for the capture manoeuvre was based, along others, by the burn time of the VEX, therefore a lower burn time allows the safety factor to still be valid). Having a 5-day capture orbit instead of a 10-day also allows for a faster transfer to the aerobraking orbit, which gives more time for aerobraking. Figure 5.4 gives a 3-dimensional view of the change in y-coordinate, with an elongated y-axis. The wireframe represents Venus. While these changes in orbit can also be avoided by performing a correction manoeuvre, lowering the capture orbit is more beneficial due to the fact it also increases aerobraking time.

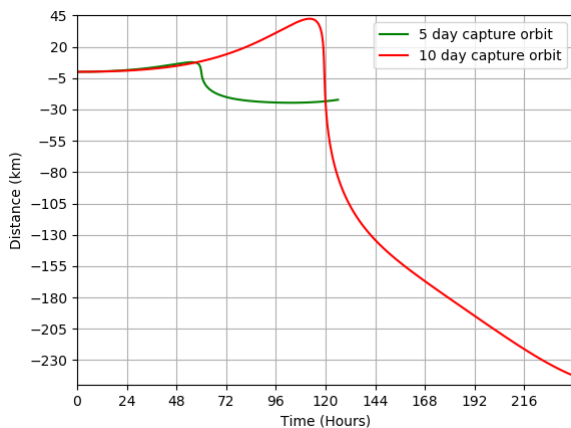


Figure 5.3: Effect of third body Solar perturbation on the orbiter during one orbit, shown as the change in Y coordinate over time. Red shows the 10 day-orbit while green shows the results for the 5 day orbit.

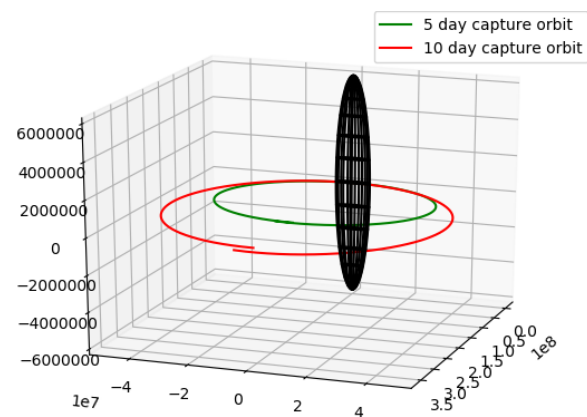


Figure 5.4: Effect of third body Solar perturbation on the orbiter during one orbit, shown as the orbital path. Red shows the 10 day orbit while green shows the results for the 5 day orbit.

The perturbation is much more severe for the orbit of the TRM. In Figure 5.5 and Figure 5.6 the effects are shown for the 464 days before the atmospheric entry. An oscillatory behaviour is seen in Figure 5.3 for the orbital height. This oscillatory behaviour occurs with a period of a quarter Venusian year. The change in pericytherion has a close to 1 to -1 relation to the change of the apocytherion, meaning that an increase in pericytherion gives a decrease in apocytherion, a behaviour which is also described by K.F. Wakker [48]. From Figure 5.3 it is clear that the perturbation is much more severe on the 10 day orbit than on the 5 day orbit. Figure 5.6 furthermore shows that the longitude of the ascending node changes over the duration, while other orbital parameters stay relatively constant. The inclination changes by less than  $0.1^\circ$  for the 5 day orbit, while the 10 day one changes slightly more. A big disconnect can be seen in the last orbit of the 10-day capture orbit. This is due to the effect of solar perturbation. The argument of pericytherion remains very close to the old argument. In order to insert into the atmosphere from the 10 day perturbed orbit an extra  $\Delta V$  of 300 m/s would be required, whereas the 5 day orbit requires an extra 180 m/s  $\Delta V$ , including the extra  $\Delta V$  needed for the VOI. An optimisation scheme has to be done in order to obtain the best TRM orbit, as will be discussed in Section 5.8. However the 5 day orbit will be assumed from this point on wards. Feasibility of VOI into a 5-day capture orbit is discussed in Chapter 8. Lowering the orbit from a 10-day capture orbit to a 5-day capture orbit here reduces the total  $\Delta V$  required for insertion, which is desired. Instead it was also attempted to correct these perturbations by use of correction manoeuvres. This yields the most  $\Delta V$  required however.

Due to the uncertainty of the severity of the perturbation, the highest increase in pericytherion will be taken (which occurs around 390 days) as the final increase, in order to ensure that insertion will be possible. The end result of the perturbation is that the apocytherion decreases by 5634.66 km and the pericytherion increases by 4809 km. This gives an orbit for the entry of the TRM with an apocytherion at 218658 km and a pericytherion at 11261.6 km above the center. This orbit is used in Chapter 6.

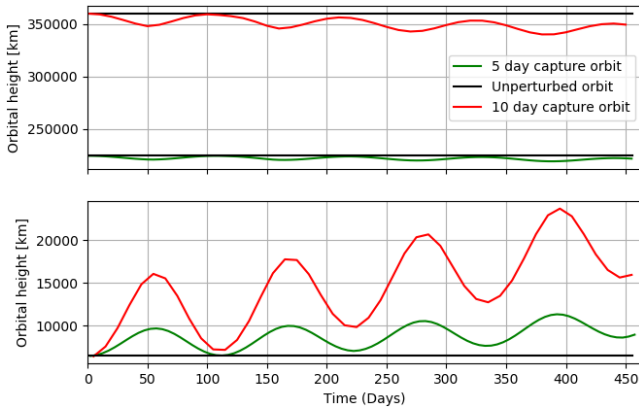


Figure 5.5: Effect of third body perturbation on the TRM over a 464 days, shown as the orbital radius over time. Red shows the 10-day orbit while green shows the 5-day orbit, whereas black is the unperturbed orbit. The top graph gives the change in apocytherion while the bottom graph gives the change in pericytherion.

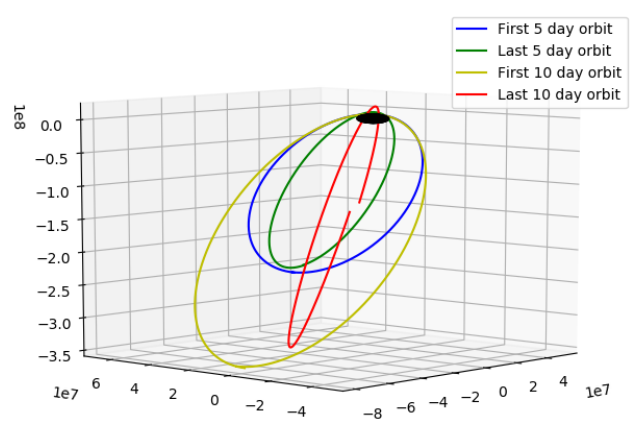


Figure 5.6: Effect of third body perturbation on the TRM over a 464 days, shown as the initial and final orbit that the TRM traverses over the duration. Red and yellow shows the results of 10-day orbit while green and blue shows the results of the 5-day orbit.

### 5.4.3. Aerobraking thermal analysis

During aerobraking a lot of convective heat will be created. If aerobraking is too fast or the density too high, the antenna and solar panel will overheat and be permanently damaged. To prevent overheating of the solar panels, the panels will be pointed such that the OSR coated back receives the sunlight shortly before entering the atmosphere, cooling the them down. As mentioned in a previous section, the heat flux at the stagnation point will be evaluated and be assumed to be the average heat flux. This was done for both the solar panel and the antenna. The heat flux was determined by Equation 5.4[51]. Where  $K_s$  is an empirical factor which can be calculated using Equation 5.5 [52].

$$q_{conv,s} = K_s \cdot \rho^{1/2} \cdot V^3 \quad (5.4) \quad K_s = 0.1106 \left( \sum \frac{c_{0,i}}{M_{0,i} \gamma_{0,i}} \right)^{-1/2} \left( \frac{1}{R_n} \right)^{1/2} \quad (5.5)$$

Where  $c$  is the mass fraction,  $M$  molecular weight and  $\gamma$  the transport parameter, this value was calculated using the Venusian atmospheric composition (96.5%  $\text{CO}_2$  and 3.5%  $\text{N}_2$ ).  $R_n$  is the effective nose radius, estimated using empirical data [53]. This is however not the only heat flux. A description of the full thermal model can be found in chapter 11, where the convective heat transfer is replaced with the values found with the above mentioned method. Results of several aerobraking altitudes can be seen in figures 5.7 and 5.8. An altitude of 136.5 km was chosen, as any lower altitude would overheat the solar panels.

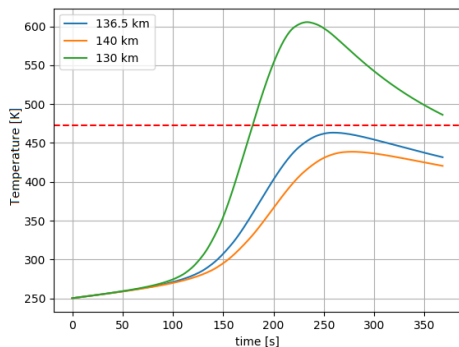


Figure 5.7: Solar panel temperature for different altitudes

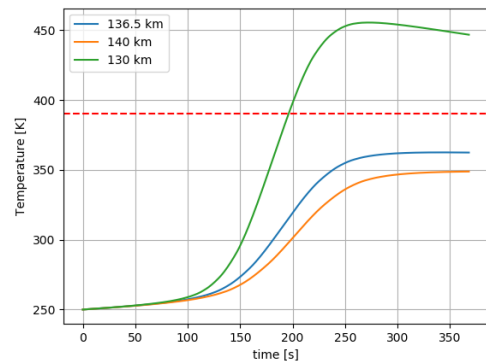


Figure 5.8: Antenna temperature for different altitudes

### 5.4.4. Orbiter aerobraking results

The aerobraking simulation was run for 32832000 steps of 10 seconds, with wet mass of 473 kg. The pericytherion where aerobraking starts was set at 136.7 km and decays to 136.3 km over time, whereafter the orbit is raised to 136.7. In reality the orbit will have a constant altitude at 136.5 km. Starting at an apocytherion of 76500 km from the center of Venus, it gives a reduction in apocytherion to just above 18000 km after

380 days. The starting apocytherion can therefore be slightly higher. The results are shown in Figure 5.9 for the apocytherion height over time, and a 3D representation of the orbital path is given in Figure 5.10.

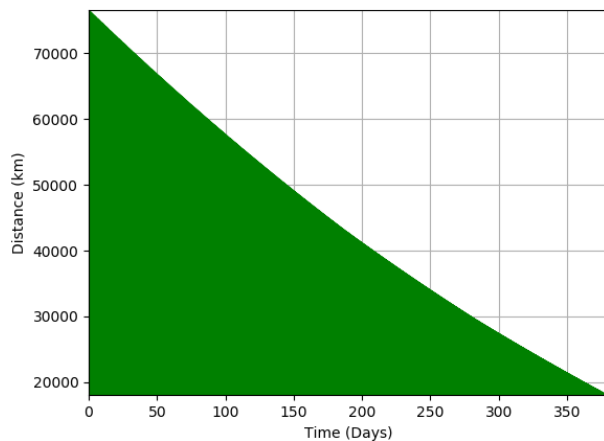


Figure 5.9: Apocytherion height over time during aerobraking from the center of Venus

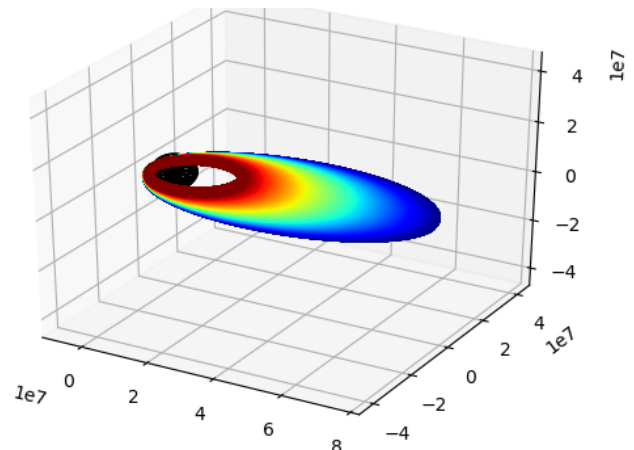


Figure 5.10: Orbital path over time during aerobraking. Initial orbit is coloured blue, whereas final orbit is coloured crimson.

However the possibility remains that aerobraking will be finished faster or slower than allocated. In case aerobraking is finished earlier two outcomes are possible; The TRM can insert earlier into the atmosphere or the orbiter can start taking measurements while the TRM waits until the nominal insertion time. The orbiter is capable of storing all scientific data from the aerobot for the 100-day duration, making the first approach feasible. The second approach does not affect the design of the TRM.

If however aerobraking takes longer than 456 days two outcomes are also possible. Depending on the orbital height of the orbiter the TRM may be able to still insert earlier. Data transmission between orbiter and aerobot may still be feasible, although it will not be optimal. If the orbiter is still too far away from Venus, the TRM may require to wait until the orbiter is closer. As shown in Figure 5.5 the change in pericytherion over time shows an oscillatory behaviour. Waiting until the next local minima of this oscillatory behaviour before entering the atmosphere will still allow for the manoeuvre to remain within the allocated  $\Delta V$  budget, as the worst case scenario was taken in Subsection 5.4.2.

## 5.5. Operational orbit

464 days after arriving on Venus, the orbiter will have reached its mission orbit and the TRM will insert into the atmosphere. The atmospheric entry of the TRM is described in Chapter 6. This section describes how the orbital parameters were determined for the orbiter and the EOL operation of the orbiter. Two constraining factors were taken into account to analyse the required mission orbit, namely a science constraint and a TTC constraint. TTC requires the orbit to be a polar orbit in order to allow for communications throughout the mission timeline. This polar orbit is also beneficial for science. The end result is that the TTC constraint determined the apocytherion, while the science constraint determined the pericytherion.

### 5.5.1. Science constraint

The orbiter carries a mass spectrometer to measure the ionosphere of Venus. The VEX mission analysed the ionosphere of the North pole of Venus during a period of low Solar activity, at a 250 km pericytherion [35] [20]. The ionosphere has yet to be analysed below 250 km. It was therefore decided to set a pericytherion of 200 km. A polar orbit with the South pole as the argument of pericytherion ( $\omega$ ) was chosen, due to the fact it is expected to have a similar structure as the North pole and no previous measurements were performed here [35]. Setting the  $\omega$  at the south pole allows the BLOON to verify this expectation. This furthermore allows the camera of the BLOON to map the northern hemisphere in more detail, like how VEX mapped the southern hemisphere. Solar activity impacts the composition and distribution of the upper atmosphere. Nominal mission operations start during a period of increasing Solar activity near a maxima [36]. However current predictions show that Solar cycle 26 is expected to have low activity. Due to the uncertainty associated with the prediction of Solar activity this leads to two possible mission outcomes. The first is that BLOON will complement the data from VEX for altitudes below 250 km during low Solar activity, or that BLOON will map the ionosphere during high Solar activity. Both outcomes provide valuable data towards

the understanding of the Venusian atmosphere.

The latitude of the aerobot is also constrained by science. Most of the atmospheric and ground phenomena, such as super rotation occur near the equator and thus prefer a low latitude for optimal research possibilities. Research of the Venusian super rotation shows that the intensity of the flow slowly decreases above  $20^\circ$  latitude and is lower than the background flow at  $30^\circ$  latitude [54]. Study of the surface of the planet shows that the Atla region of the planet, often mentioned as the most interesting region for seismic region, stretches from roughly  $20$  to  $30^\circ$  North and  $20$  to  $25^\circ$  South [55]. All in all, the science considerations seem to strongly prefer a latitude not higher than  $20$  (or at most  $30$ )  $^\circ$ .

### 5.5.2. TTC constraint

The pericytherion of the orbiter and the latitude of the aerobot is limited by the science constraint. This still leaves the apoclytherion of orbiter. Firstly, it is important to mention that communication prefers a polar orbit for the orbiter with the apoclytherion above the northern hemisphere allow for maximum communication with the aerobot. A polar orbit limits the impact of the Sun to the antenna temperature by multiple orders of magnitude and makes the temperature of the planet the dominant factor. At the frequency bands used for this mission, discussed in Chapter 9, the Sun can add up to  $10^5$  K of noise to the antenna, significantly limiting its usage [56]. Therefore, a polar orbit is essential for high data rate communication.

For the other parameters, an optimum can be found. One of the main limiting factors is curvature of Venus which limits communications. This lack of communication can be optimised by a higher apoclythe, which in turn also negatively effects the link budget due to the increased distance. All in all, an optimal apoclythe can be found for each latitude. The plots in figures 5.11 and 5.12 show the optimal apoclythe as a function of the latitude with the impact of the space and data rate losses in dB on the z-axis.

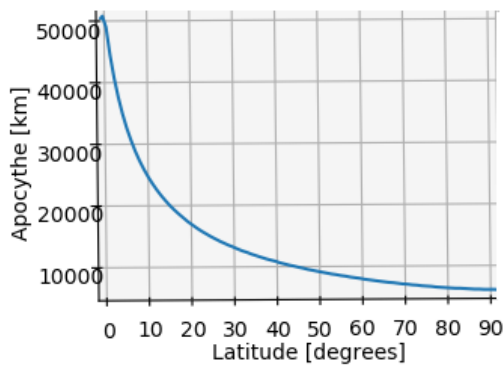


Figure 5.11: The impact of the latitude on the optimum apoclytherion of the orbiter, top-view.

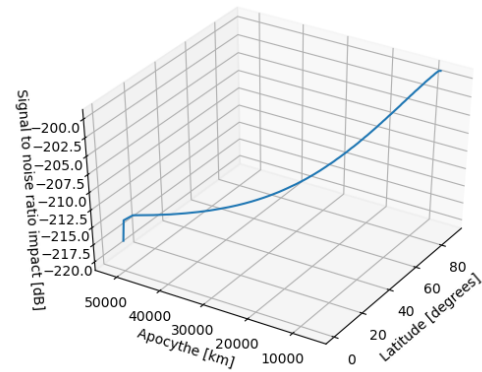


Figure 5.12: The impact of the latitude on the optimum apoclytherion of the orbiter, side-view. The z-axis represents the SNR dB decrease due to space losses.

However, this plot does not yet constrain the orbit completely. It seems to indicate that a high latitude with a low apoclythe is beneficial. However, the final decision now has to be made based on a combination of other parameters. For example, a higher apoclythe is beneficial for propulsive manoeuvres. However, a higher apoclythe is disadvantageous for the camera resolution mentioned in Chapter 4 and impacts the pointing accuracy of the system, mentioned in Chapter 9, as well. The communication window must also be large enough to transmit the data with the antennas available (roughly 50%), since a higher apoclythe might be beneficial, but would require antennas that do not fit on certain mission elements. On the other hand, a low apoclythe would result in issues with atmospheric defocusing, an issue previously not taken into due to its small impact at usual eccentric orbits, as discussed in Chapter 9. In combination with the fact that roughly  $20$  degrees north latitude is beneficial for science purposes and all the parameters discussed previously, a value of  $20^\circ$  north latitude was chosen for the aerobot. This results in an optimal apoclytherion of  $13,332$  km from the surface or  $18,384$  km from the centre of Venus.

### 5.5.3. Mission orbit

With the orbital constraints set, the mission orbit of the orbiter can be characterised by the values shown in Table 5.7. The orbital period was computed by using of Equation 5.2. The distance of the pericytherion and the apocytherion are shown from the centre of Venus. From the surface the pericytherion is at a height of 200 km and the apocytherion at a height of 12332 km. The eclipse period was computed by using a orbit analysis, similar to the TTC analysis.

Table 5.7: Orbital parameters for the orbiter.

Parameter	Value	Unit
Pericytherion	6251.8	km
Apocytherion	18383.8	km
Semimajor axis	12317.8	km
Orbital period	251.2	mins
Inclination	20	deg
Max. eclipse period	2470	s

### 5.5.4. EOL manoeuvre

At the end of mission operations the orbiter will burn up in the Venusian atmosphere. The method that was chosen to accomplish this is using aerobraking. The pericytherion of the orbit will once again be lowered to 136.5 km, where the orbit will slowly decay. During the EOL aerobraking the orbiter will be able to keep performing measurements until internal temperatures disable the orbiter. This will take roughly 98 days. The orbital decay over time will also give information on the density of the atmosphere at lower altitudes.

## 5.6. Delta-V budget

This section gives the  $\Delta V$  budget for the required orbital manoeuvres. This budget is setup using the energy equation (5.1) and literature. The main assumption used is impulsive burns. Safety factors to incorporate non-impulsive burns and propellant margins are given in Chapter 8.

### 5.6.1. Trajectory correction manoeuvres

After the LV inserts the BLOON into an interplanetary trajectory two TCMs are required. The first manoeuvre will separate the BLOON from the upper stage of the LV. This occurs some time after Earth escape. The BLOON will be set on the correct trajectory to Venus while the LV will be launched on a heliocentric orbit with a very low probability of collision with other planets. It is assumed that this manoeuvre will require 10 m/s  $\Delta V$  [4]. It will be performed by the TRM. The second TCM will be performed near Venus in order to insert the mission components in the desired orbit. Based on the pioneer mission [57] it is assumed that the orbiter and TRM will separate 20 days before arrival. Each element will perform its own burn, taking an estimated 10 m/s  $\Delta V$ , setting the element on a course to a capture orbit with the correct inclination. In reality the value will be slightly different for each element, but not more than 10 m/s. Afterwards each element will perform its own capture manoeuvre, as will be explained in the next section.

### 5.6.2. Capture manoeuvres

The following assumptions are made to determine the  $\Delta V$  of the capture orbit:

- The pericytherion of the capture orbit will be 400 km, based on VEX<sup>6</sup> and Akatsuki [58].
- The  $\Delta V$  required to enter an escape orbit given by the chosen LW will be assumed to be the one for an orbit with a pericytherion of 400 km. This is equal to 395 m/s.
- An impulsive burn is performed at the pericytherion of the escape orbit to enter the capture orbit

With these assumptions, Equation 5.1 and Table 5.5 give a total  $\Delta V$  of 536.29 m/s for the VOI for both the orbiter as the TRM, as they will both enter a 5 day capture orbit with a different inclination.

### 5.6.3. Orbiter: transfer to aerobraking orbit

In order to insert into the aerobraking orbits a few sequential manoeuvres are required, shown below in Table 5.8. First the pericytherion has to be lowered in order to minimise the  $\Delta V$  needed to lower the apocytherion. It is assumed that the pericytherion will be initially lowered to 150 km from the 400 km of the capture orbit (Man1). This requires a  $\Delta V$  of 5.42 m/s. Following this 2 manoeuvres will be performed to lower the apocytherion to the required aerobraking altitude (Man2-3). The reason for 2 manoeuvres is expanded upon in Chapter 8. This will require a total  $\Delta V$  of 252.62 m/s. Afterwards a final manoeuvre is performed at the apocytherion to lower the pericytherion to the aerobraking altitudes, requiring 0.98 m/s (Man4). When aerobraking is finished the pericytherion has to be raised to 200 km, requiring 11.40 m/s

<sup>6</sup><https://sci.esa.int/web/venus-express/-/38947-orbit-insertion>, retrieved 1 June 202

(Man5). These set of manoeuvres require a total of 270.2 m/s  $\Delta V$ .

Table 5.8: Aerobraking manoeuvres that have to be performed.

Number	Where	$\Delta V(\frac{m}{s})$
Man1	Apocytherion	5.42
Man2-3	Pericytherion	252.62
Man4	Apocytherion	0.98
Man5	Pericytherion	11.40
Total	x	270.2

#### 5.6.4. Orbiter: stationkeeping and end-of-life

In order to maintain the orbiter in its mission orbit, stationkeeping manoeuvres are needed. The following assumptions are made in order to analyse these.

- Only Solar radiation, Solar third body perturbation and drag decay are considered. The J terms of Venus, along with other decay modes can be neglected [59].
- Stationkeeping is assumed to be required for 2 Earth years after mission start, in order to account for possible mission extensions.
- Drag decay effects are analysed over a period of 1 month and normalised for the mission duration. This gives a  $\Delta V$  of 5.8 m/s over a period of 2 years (not including aerobraking).
- For the third body Solar perturbation decay, an assumption is made that 50 m/s is needed for the 2 years after aerobraking and 50 m/s for during the aerobraking. This is based on the fact Venus express had a change in pericytherion of 170 km over 1 Venusian year <sup>7</sup>, on an orbit with 72000 km apocytherion. This gives a 52.59 m/s  $\Delta V$  over an Earth year [4]. Although aerobraking takes longer, since it rapidly decays to a lower orbit it is assumed that 50 m/s will be needed. The same is assumed for stationkeeping required at the mission orbit. Both assumptions are overestimations.
- Solar radiation decay is analysed over a period of 1 year, using Equation 5.6 for decay due to the Sun [48] [60]. Here  $\vec{a}_{rad}$  is the resulting acceleration,  $\rho_{sat}$  the reflectivity of the orbiter, assumed to be 0.6,  $W_{Sun}$  the incoming radiation from the Sun taken at perihelion [1],  $r_{rad}$  the distance to the perihelion, A the area and m the mass. A similar equation was used for decay due to albedo (5.7). Here it is assumed that Venus "radiates" the albedo from an altitude of 100 km. The geometric albedo of Venus was taken and multiplied by the radiation at perihelion. The effects of both the albedo and the solar radiation were assumed to be on the entire area of the orbiter. Even with this assumption the decay was less than 0.5 m/s  $\Delta V$  over a period of 1 year. A conservative assumption of 1 m/s will be taken.
- The  $\Delta V$  required for the RCS is calculated in Chapter 12 and is computed to be 46.86 m/s.

$$\vec{a}_{rad} = (1 + \rho_{sat}) \cdot \frac{W_{Sun}}{\frac{r_{os}^2}{r_{rad}^2}} \cdot \frac{1}{c} \cdot \frac{A}{m} \cdot \frac{\vec{r}_{os}}{r_{os}} \quad (5.6)$$

$$\vec{a}_{albedo} = (1 + \rho_{sat}) \cdot \frac{W_{albedo}}{\frac{r_{vo}^2}{r_{albedo}^2}} \cdot \frac{1}{c} \cdot \frac{A}{m} \cdot \frac{\vec{r}_{vo}}{r_{vo}} \quad (5.7)$$

The overall result is that stationkeeping will require a  $\Delta V$  of 150.16 m/s. Along this, as mentioned in the previous section, the orbiter will lower its pericytherion at EOL. This requires 11.40 m/s  $\Delta V$ .

#### 5.6.5. Transfer module : atmospheric entry burn

As will be discussed in Section 5.8 some uncertainty remains regarding the Solar decay of the TRM due to the fact no validation could take place. The degree of uncertainty is also unknown. It will be assumed that the final discussed in Subsection 5.4.2 is correct. The capture orbit has a 12.5 ° inclination such that the aerobot ends up at 20 degree latitude after insertion. The  $\Delta V$  required in order to go from the final orbit to the atmospheric entry orbit is 97.5 m/s. A safety factor of 1.5 will be taken due to the uncertainties, giving a total of 146.2 m/s. After the entry burn the TRM has to separate from the aeroshell. It will be assumed that the TRM will perform a 20 m/s retrograde burn one and a half day after the entry burn is performed. This is done so it provides power to the aeroshell up until one day before entry occurs.

<sup>7</sup><https://sci.esa.int/web/venus-express/-/37357-operational-orbit>, retrieved 12 may 2020

### 5.6.6. $\Delta V$ budgets for TRM and the orbiter

In Table 5.9 a summary of the total  $\Delta V$  budget is given. Propellant related safety factors are obtained and discussed in Chapter 8. They are however applied here in the  $\Delta V2$  column.

Table 5.9:  $\Delta V$  budget of the BLOON mission for both the orbiters and the TRM.  $\Delta V1$  gives the  $\Delta V$  budget without safety factors while  $\Delta V2$  gives the budget with safety factors from the propulsion subsystem.

Platform	Manoeuvre	$\Delta V1$ ( $\frac{m}{s}$ )	$\Delta V2$ ( $\frac{m}{s}$ )	Platform	Manoeuvre	$\Delta V1$ ( $\frac{m}{s}$ )	$\Delta V2$ ( $\frac{m}{s}$ )
Orbiter	TCM	10.0	10	TRM	TCM	20.0	20.0
Orbiter	Capture	536.3	955.9	TRM	Capture	536.3	955.9
Orbiter	Aerobraking	270.2	313.4	TRM	Entry	146.2	170.9
Orbiter	Stationkeeping	116.3	134.7	TRM	Separation	20.0	23.2
Orbiter	EOL	11.4	13.2				
Orbiter	Total	944.2	1427.3	TRM	Total	723.7	1170.0

## 5.7. Risk analysis

Risks related to astrodynamics are given in this section, along with their mitigation strategies. Risks related to the propulsion system and burns are given in Chapter 8. The following scales were used to subjectively assess probability and severity of the risks. Probability: 1 = Negligible, 2 = Low, 3 = Concerning, 4 = Likely, 5 = Certain. Severity: 1 = Negligible, 2 = Low effect on mission success, 3 = Partial mission success, 4 = Significant reduction in mission capability, 5 = Critical failure of mission.

- AD1 **Launch occurs too late due to delays:** Could occur due to bad weather conditions or other delays. Changes the  $\Delta V$  budget of the mission. Probability = 3, Severity = 4. **Mitigation:** Launch days before the Earth escape burn. New probability = 1, Severity = 4
- AD2 **Aerobraking takes longer:** impacts the communication of the mission negatively. Probability = 3, Severity = 3. **Mitigation:** Taking a 20% margin in allowable aerobraking time and bringing extra fuel. More in depth simulation to determine time required. New probability = 1, Impact = 2.
- AD3 **Atmospheric density higher due to high Solar activity:** May cause the orbiter to overheat. Probability = 3, Severity = 3. **Mitigation:** Prior to and during launch Solar activity should be actively monitored. The first dive into the atmosphere at 150 km gives more information about the atmospheric density. This can be used to better model a new altitude during the mission. New probability = 3, Severity = 1.

## 5.8. Sensitivity analysis

A list of the sensitivity analysis performed for astrodynamics is given here.

### 5.8.1. LV and LW sensitivity

The current wet mass estimation for the mission gives a total mass of 2885 kg with a 10% overall drymass contingency included. This leaves 1075 kg left over to fit in the Falcon 9. As will be described later, some of this mass is needed for the fairings between orbiter, TRM, and the LV adaptor. Even then the overall BLOON mission mass can still increase by at least 835 kg without changing the LV. Such increase might take place if more scientific payload is added. A lower launch mass than the maximum allowable furthermore allows for non-optimal LWs to be used, in case delays occur. Those require a bigger  $\Delta V$  from the LV, which can be supplied due to the lower payload mass.

### 5.8.2. Third body perturbation

The current model predicts the effects of third body perturbation by the Sun to be feasible for the design. An attempt was made to validate this model by taking the VEX as an example. The ESA states that over a period of one Venusian sidereal year the Venus express experienced a 170 km increase in pericytherion<sup>5</sup>. In this source no mention is made about the oscillating pericytherion or a decrease in apocytherion. Nor is it mentioned at what the starting position is of Venus relative to the Sun. Running the simulation with input data from the Venus express assuming a polar orbit yielded very different results than the 170 km states by ESA. Instead an oscillatory behaviour was observed, with much lower overall increase in pericytherion. The code verification for the third body perturbation can be found Section 5.9, where the conclusion is drawn

that Equation 5.3 is implemented correctly with its given assumptions. Multiple reasons can remain for the discrepancy between simulation and actual VEX results, mentioned below:

- The assumption that the orbit is polar and lies perpendicular to the orbital plane of Venus around the Sun is incorrect. This assumption is likely to be one of the reasons as the perturbation is strongest when the orbit of the perturbed body is in the same plane as the body it is orbiting and the perturbing body [48] [60]. Taking the obliquity to orbit into account does not return the same results as VEX.
- Other perturbations that were not considered cause the discrepancy. While other perturbations would likely affect the result over aerobraking period, they are unlikely to account for the discrepancy.
- A more refined time step was needed for the simulation and the Venus-Sun distance. Currently the distance is rounded off to the nearest half a day. The effect of this should not be the sole reason for the discrepancy, but should account for some error. Furthermore steps of 10 seconds were taken for each integration. A comparison was made between the results for two 10 day orbits using a 10 s time-step versus a 1 s time step. The orbits pericytherion was set at 400 km above the surface of Venus on a polar orbit. The 10 s time-step showed an increase of 16.336 km while the 1s time-step gave an increase of 16.315 km, a difference of less than 1 %.
- Some crucial information could be missing regarding the 170 km increase experienced by VEX. An attempt was made to find more information regarding this to no avail, with the exception of ESA's SPICE kernel of the VEX mission <sup>8</sup>. However not enough time remained to work this out.

In order to determine the true effect of the third body perturbation of the Sun a more detailed simulation is needed for the TRM, as the TRM is the one most affected. Should the influence prove to be too severe it may be a killer requirement for this mission setup, as the propellant mass might severely increase. It can also be the case however that the orbit can be set up in such a way that less  $\Delta V$  is required for the TRM than currently estimated.

### 5.8.3. Aerobraking

The aerobraking time required is dependent on the drag coefficient, density, frontal area, mass and initial starting orbit. Lowering the drag coefficient, frontal area and atmospheric density or increasing the mass and initial starting orbit apoclytherion lead to an increase in aerobraking time required. A change in parameters that give an increase in time required can be mitigated by either increasing the frontal area or lowering the starting orbit. The approach is taken that in general the starting orbit will be changed while keeping the frontal area the same. This causes a change in required  $\Delta V$  for the aerobraking. Depending on the input parameters the  $\Delta V$  of aerobraking can change by  $\pm 20$  m/s for moderate changes in the drag coefficient, density, frontal area and mass. However lowering the apoclytherion of the orbit has a much bigger impact depending on the final altitude. An altitude of 12000 km from the center of Venus results in an increase of more than 150 m/s. The apoclytherion is however not expected to change so drastically.

## 5.9. Verification and validation

V&V for astrodynamics mostly included verifying the code with hand calculations and unit tests. For every simulation the inputs and boundary conditions also were verified. The inputs for the code were verified by comparing the results with Kepler orbit using Equation 5.1. Code verification for the 4 step Range-Kutta is furthermore also mentioned in Chapter 6.

**Third body perturbation verification:** Most of the verification and validation was done on the third body perturbation code. This was done by changing inputs and verifying that the resultant accelerations made sense with the given coordinate system. Furthermore the resulting accelerations at random times to computations by hand. The Venus-Sun distance model was also verified by comparing it to hand calculated values at different points in time. While a discrepancy was seen between this and the actual Sun-Venus distance it was deemed to be acceptable. Attempts at validation of the perturbation were also made to no avail. Similar verification was also applied to the radiation pressure codes.

**Communication window verification:** The verification of the communication window is done using unit tests or plotting of the result. Edge cases such as a window where there is no possibility for the aerobot to communicate with the orbiter, are put into the program, as well as hand-calculated answers. Plotting is used to confirm calculated intersections and to confirm the orbital parameters.

<sup>8</sup><https://www.cosmos.esa.int/web/spice/spice-for-vex>, retrieved 14 June 2020

# 6 Atmospheric Entry

In this chapter the entry methods, loads and simulations will be discussed. Firstly, a design overview will be shown, after which functions of the aeroshell will be identified. Next, the entry will be modelled and based on loads, the aeroshell design is determined, including aerodynamic characteristics and balloon deployment. Finally risk analysis is performed, sensitivity analysis is done and models are verified and validated.

## 6.1. Design overview

Table 6.1 summarises the design of the entry and aeroshell. In the following sections decisions and calculations that have led to these values will be shown. Figure 6.1 shows the rendering of the aeroshell.

Table 6.1: Entry design overview

Parameter	Value	Unit	Parameter	Value	Unit
Aeroshell shape	circ. cone	-	Drogue surf. area	3.7	m <sup>2</sup>
R/D	0.25	-	Main chute surf. area	6	m <sup>2</sup>
Halfangle	45	deg	Flightpath angle	-8	deg
Mass	858.25	kg	Total heatload	17.2	kJ/cm <sup>2</sup>
Diameter	3	m	Max deceleration	367	m/s <sup>2</sup>

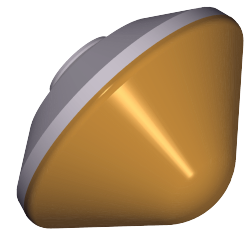


Figure 6.1: Aeroshell design

### 6.1.1. Approach to sustainability

In the atmospheric entry methodology and design sustainable design practises must be followed as well and should follow the planetary protection guide, as stated in Subsection 2.6.1. It is imperative to ensure deorbiting of the transfer module, so that there is no space debris left. After 24 hours from insertion to the orbital entry, the transfer module will separate from the aeroshell and perform a final burn with a  $\Delta V$  of 50 m/s in retrograde direction. From this point, an effort was made to simulate the transfer module orbit to make sure it will burn during entry. It was assumed that the transfer module has a similar frontal area as the aeroshell and a drag coefficient of 2. The simulation confirmed that transfer module will burn in the atmosphere and its trajectory will be as shown in the Figure 6.2.

While the aeroshell enters the atmosphere its ablative coating will partially decompose in the atmosphere. When the entry phase is completed the leftover shell will be jettisoned and eventually crash on the surface. Before the mission is executed an analysis must be done to estimate the impact location such to document the potential contamination of Venus. Next to keeping Venus contamination free, the sustainability of the materials and their production is considered; the thermal protection system is made up from non-toxic materials.

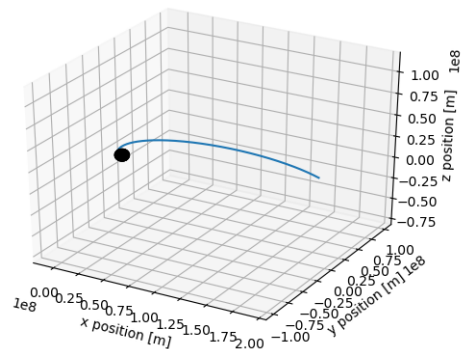


Figure 6.2: Transfer module after aeroshell separation

## 6.2. Functional analysis

The function of modelling the entry is to determine critical load cases: highest deceleration, heatload, peak heatflux and to verify that insertion it at the correct latitude. Other areas that were included are stability of entry and the final conditions. With such a model established, the required protective characteristics of the aeroshell can designed. The shell must transmit the deceleration loads induced by the atmosphere to the aerobot. Additionally, it must protect the aerobot from the heat loads. These functions flow into the requirements in Table 6.2.

Table 6.2: Requirements on the entry system

Identifier	Requirement	Compliance	Explanation in
EN-01	The entry system shall decelerate the aerobot to 30 m/s at 50 km altitude.	✓	Section 6.5
EN-02	The entry system shall protect the aerobot from the atmospheric deceleration loads.	✓	Subsection 6.6.1
EN-03	The entry system shall protect the aerobot from the atmospheric heat loads.	✓	Subsection 6.6.2
EN-04	The entry system shall remain stable during descent.	✓	Section 6.7
EN-05	The entry system heat shield material shall sustain the peak entry heat flux.	✓	Subsection 6.6.2

### 6.3. Entry model

Firstly, before any other matters, the general model for body needs to be developed. After careful consideration, the following guidelines for the model were created:

- It should be able find the trajectory for a body in presence of an other massive body.
- It should be able to model the drag force for entry and aerobraking.
- It should allow for other, custom force, velocity change and mass change function.
- The simulation should have 3 degrees of freedom
- It should perform analyses consisting of 1 million points in less than 15 minutes.
- The simulation should be convergent and stable.

A program that satisfies the given conditions, would not only be useful for entry, but also for aerobraking and 3 dimensional orbit analysis.

#### 6.3.1. Assumptions and frame of reference

The first simplification is a point mass. That means that simulation does not include rotations of the body, therefore fixing 3 degree of freedom model. This was the most questionable assumption, but later validation has proven its validity. Secondly, the coordinate system was chosen as a Venus centred non-rotating frame with Cartesian coordinates. With that settled, the next assumption is that Venus is not rotating. The justification for it is that rotation of Venus is so minor over the length of the entry (Venus day is about 116.75 Earth days), that its influence can be discarded. With those assumption, it was enough to produce a model for aerobraking and entry.

#### 6.3.2. Equation of motion and approach to solving

Using Newton's law of dynamics, considering a custom force, velocity change and mass change function model, the following governing equation can be derived

$$\vec{F}(t, \vec{r}) = \left( m_0 + \frac{\partial m}{\partial t}(t, \vec{r}) dt \right) \cdot \frac{\partial}{\partial t} \left( \frac{\partial \vec{r}}{\partial t} + \Delta \vec{V}(t, \vec{r}) \right). \quad (6.1)$$

The aim is to have a very generic model, therefore functions  $F$ ,  $\frac{\partial m}{\partial t}$ ,  $\Delta V$  could be customised, yielding an analytical solution impossible. Therefore, a numerical approach was chosen. Firstly, state variables are chosen to form a vector  $B$  consisting of  $[V_x, V_y, V_z, r_x, r_y, r_z, m]$ . Secondly, the equation is rewritten to the following form:

$$\frac{\partial \vec{y}}{\partial t} = \vec{f}(t, \vec{y}), \quad (6.2)$$

yielding

$$\begin{bmatrix} a_x \\ a_y \\ a_z \\ v_x \\ v_y \\ v_z \\ m' \end{bmatrix} = \begin{bmatrix} \vec{F}(t, \vec{B})_x / B_m \\ \vec{F}(t, \vec{B})_y / B_m \\ \vec{F}(t, \vec{B})_z / B_m \\ \vec{B}_{v_x} + \Delta V(\vec{B})_x \\ \vec{B}_{v_y} + \Delta V(\vec{B})_y \\ \vec{B}_{v_z} + \Delta V(\vec{B})_z \\ \frac{\partial m}{\partial t}(\vec{B}) \end{bmatrix}, \quad (6.3)$$

which will be further referred to in short hand form

$$\frac{\partial \vec{B}}{\partial t} = f(t, \vec{B}). \quad (6.4)$$

Knowing the initial values, one can solve such an equation using a four step Range-Kutta integration scheme with step size  $s$ , by defining

- $\vec{k}_1 = \vec{f}(t, \vec{B})$ ,
- $\vec{k}_2 = \vec{f}(t + s/2, \vec{B} + s\vec{k}_1/2)$ ,
- $\vec{k}_3 = \vec{f}(t + s/2, \vec{B} + s\vec{k}_2/2)$ ,
- $\vec{k}_4 = \vec{f}(t + s, \vec{B} + s\vec{k}_3)$ .

Then, a new state will be equal to

$$\vec{B}_{n+1} = \vec{B}_n + \frac{1}{6}s(\vec{k}_1 + 2\vec{k}_2 + 2\vec{k}_3 + \vec{k}_4) \quad (6.5)$$

and time, with  $s$  as step size

$$t_{n+1} = t_n + s. \quad (6.6)$$

This process will be repeated until program reaches the desired end condition and returns the state and time history.

### 6.3.3. Custom forcing, velocity change and mass change functions

Firstly, it is assumed that there is no continuous change in mass. Secondly, events with a discrete mass change are identified. The only time it happens is when the heat shield is discarded, which happens at the deployment Mach number. Therefore mass change functions can be defined as

$$\frac{\partial m}{\partial t} = \left\{ \begin{array}{l} 0, \text{ if } M > M_{\text{heatshield}} \\ \frac{m_0 - m_{\text{heatshield}} - m}{dt}, \text{ if } M \leq M_{\text{heatshield}} \end{array} \right\}. \quad (6.7)$$

Secondly, no significant external velocity changes will take place. Finally, there are 3 major force contributions: gravity, drag, lift. As is identified in Section 6.4, lift is not a concern for this mission. The gravity force influence can be modelled via following equation:

$$F_g = -\frac{\mu m}{|\langle x, y, z \rangle|^3} \langle x, y, z \rangle. \quad (6.8)$$

Drag force can be modelled with a step function that is 0 when it is above the limit of the VIRA model of 250 km altitude, while otherwise it has value as shown

$$D = \left\{ \begin{array}{l} 0 \text{ if } |\langle x, y, z \rangle| > 6.3018 \cdot 10^6 \\ -\frac{0.5m\rho\bar{v}|\bar{v}|}{\beta}\chi, \text{ if } |\langle x, y, z \rangle| \leq 6.3018 \cdot 10^6 \end{array} \right\}, \quad (6.9)$$

where  $\beta$  is ballistic coefficient defined by  $\frac{m}{C_D S}$  and  $\chi$  is compressibility correction factor defined by

$$\chi = \frac{C_{p\text{stagnation}}}{2}.$$

There will be additional drag forces applied when parachutes will be deployed. Those are assumed to have constant  $C_D$  and follow equation

$$D = \begin{cases} 0 & \text{if } M > M_{parachute} \\ -0.5\rho C_D S \vec{v}|\vec{v}|, & \text{if } M \leq M_{parachute} \end{cases}. \quad (6.10)$$

#### 6.3.4. Ballistic coefficient and compressibility correction factor

In order to determine the ballistic coefficient, the drag coefficient needs to be determined. As explained in Section 6.4, entry will be performed at a 0 degree angle of attack, therefore the axial force coefficient will be equivalent to the drag force coefficient. Using a method shown in [61], composite shapes like a circular cone with spherical tip instead of an apex, can be modelled using the summation of their respective coefficients, with a reference length change. It is important to mention that this method assumed a Newtonian approach with (infinite Mach number), which says that the stagnation point of the pressure coefficient is equal to 2. In a real case, this can be approximated with

$$c_{p,stag} = \frac{2}{\gamma M^2} \left[ \left( \frac{(\gamma+1)^2 M^2}{4\gamma M^2 - 2(\gamma-1)} \right)^{\frac{\gamma}{\gamma-1}} \left( \frac{1-\gamma+2\gamma M^2}{\gamma+1} \right) - 1 \right], \quad (6.11)$$

where  $\gamma$  can be found in Equation 6.42. This correction is encapsulated into aforementioned  $\chi$ . Force and moment coefficients for the circular cone of half the apex angle  $\theta$  and the origin at the apex, reference area being the maximum cross section and the reference length being length of the cone  $\alpha$  smaller than  $\theta$ , as stated in [61].

$$C_A = 2 \sin^2(\theta) + (1 - 3 \sin^2 \theta) \sin^2(\alpha), \quad (6.12) \quad C_M = -\frac{2}{3} \sin(2\alpha), \quad (6.14)$$

$$C_N = \cos^2(\theta) \sin(2\alpha), \quad (6.13) \quad \frac{x_{cp}}{L_{ref}} = \frac{2}{3 \cos^2(\theta)}. \quad (6.15)$$

The same coefficients for the sphere are also given by [61], with the origin at most upstream point of the sphere, the reference area being the maximum cross section, the reference length being the radius, and  $\theta$  being half the apex angle of the tangent cone.

$$C_N = \frac{2}{3} \cos^2(\theta) \sin(2\alpha), \quad (6.17)$$

$$C_A = 1 - \sin^4(\theta) - \frac{(1 + 3 \sin^2(\theta)) \cos^2(\theta)}{2} \sin^2(\alpha), \quad (6.16)$$

$$\frac{x_{cp}}{L_{ref}} = -1. \quad (6.18)$$

Which can be summed up by [61]

$$C_A = \sum_i \frac{S_i}{S} C_{A_i}, \quad (6.19) \quad C_M = \sum_i \frac{S_i}{S} \left[ \frac{L_i}{L} C_{M_i} + \frac{x_i}{L C_N} \right], \quad (6.21)$$

$$C_N = \sum_i \frac{S_i}{S} C_{N_i}, \quad (6.20) \quad x_{cp} = \frac{\sum_i S_i C_N x_{CP_i}}{S C_N}. \quad (6.22)$$

The aeroshell in this mission will be composed of one cone and a sphere, with a removed third construction cone to remove the influence of the apex of the base cone. This construction can be seen in Figure 6.3 from [61]. The following derivation is based on the derivation of aerodynamic coefficients for the Viking aeroshell from [61]. Firstly, the ratio of the reference area of the sphere to the base of the cone:

$$\sigma_1 = \left( \frac{2R}{D} \right)^2. \quad (6.23)$$

Ratio of distances from tip to point of intersection of sphere with cone in x directions to length of the cone:

$$\sigma_2 = \frac{L_{A1}}{L_{A2}} = \frac{2R \cos(\theta)}{D}. \quad (6.24)$$

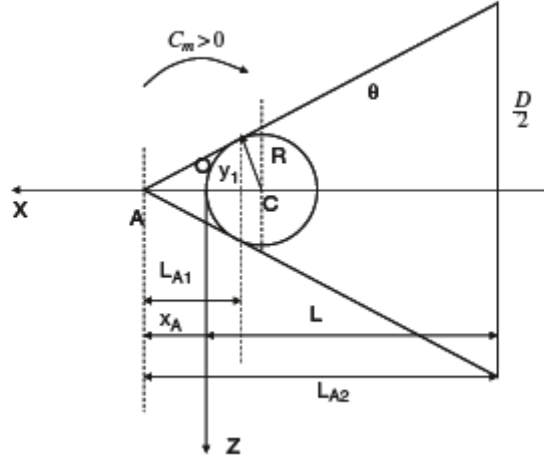


Figure 6.3: Entry capsule construction from circular cones and sphere for Viking like aeroshell. [61]

For the sphere, force and moment coefficients with respect to the tip with adjustments to the referenced surface and length are

$$C_{As} = \sigma_1^2 C_A, \quad (6.25) \quad C_{Ns} = \sigma_1^2 C_N, \quad (6.26)$$

$$C_{Ms} = -\frac{R}{D} C_{Ns}. \quad (6.27)$$

Similarly for the cone, with removed influence of the cone with a length of  $L_{A1}$ :

$$C_{Ac} = (1 - \sigma_2^2) [2 \sin^2(\sigma) + (1 - 3 \sin^2(\theta)) \sin^2(\alpha)], \quad (6.28)$$

$$C_{Nc} = (1 - \sigma_2^2) \cos^2(\theta) \sin(2\alpha), \quad (6.29)$$

$$C_{Mc} = -(1 - \sigma_2^3) \frac{2}{3} \sin(2\alpha) + \frac{x_A}{D} C_{Nc}. \quad (6.30)$$

Now, the total moments and forces are simply sums of the spherical and conical components

$$C_A = C_{As} + C_{Ac}, \quad (6.31) \quad C_N = C_{Ns} + C_{Nc}, \quad (6.32)$$

$$C_M = C_{Ms} + C_{Mc}. \quad (6.33)$$

Overall, those equations can be represented in the form

$$C_A = a \sin^2(\alpha) + b, \quad (6.34) \quad C_N = c \sin(2\alpha), \quad (6.35)$$

$$C_M = d \sin(2\alpha). \quad (6.36)$$

Given that, the location of the center of pressure  $x_{cp}$  is not a function of the angle of attack because

$$\frac{x_{cp}}{D} = \frac{c_M}{c_N} = \frac{c}{d}. \quad (6.37)$$

Considering the derivation above, the values a, b, c, d are all functions of  $\theta$  and  $\frac{R}{D}$ . The static margin is defined as

$$SM = \frac{x_{CG} - x_{cp}}{D} \quad (6.38)$$

and should be positive. For stability,

$$\frac{dc_{Mg}}{d\alpha} = \frac{d}{d\alpha} (c_M - \frac{x_{cg}}{D} C_N) = \frac{d}{d\alpha} (f \sin(2\alpha)) = 2f \cos(2\alpha) \quad (6.39)$$

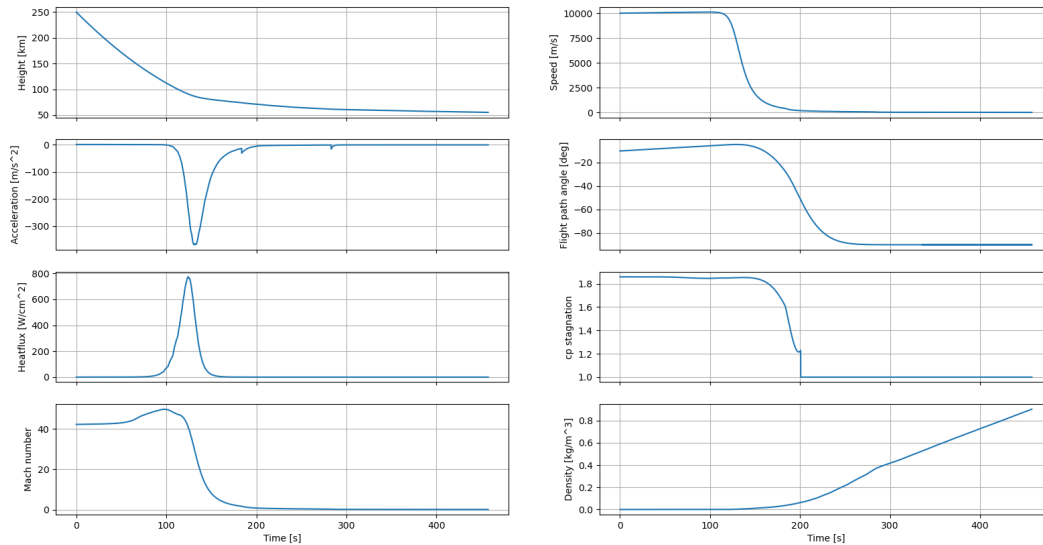


Figure 6.4: Entry summary

at the location of  $x_{cg}$  needs to be negative, for some  $f$ , which is dependent on the R/D ratio and  $\theta$ .

## 6.4. Entry method

In this section, 2 entry methods are analysed, out of which the ballistic entry method is used.

Lifting entry is an entry where the angle of attack is not 0 in order to create lift. Usually, the angle of attack is a fixed value, but it can be variable too. The benefit of a lifting entry is a slower deceleration, that yields lower stresses on the structure. This allows for example a manned entry, where maximum loads are in the order of 10g, while ballistic entries like Pioneer probes can reach even more than 300g. Having a lifting entry requires some form of active control of the angle of attack. After consideration, all of the equipment on board will be able to sustain higher g loads and therefore a ballistic entry seemed to be preferable due to mass, complexity and reliability reasons.

## 6.5. Entry loads

The initial and final conditions of entry also set the requirements on entry. In 5.4 the insertion orbit was determined and requirements on balloon deployment set requirements on the final speed and altitude (no more than 30m/s at 55km altitude). With those constraints, knowing the geometrical properties of the aeroshell from Section 6.6, a simulation was performed. The summary of the entry can be seen in Figure 6.4.

### 6.5.1. Accelerations

Maximum deceleration acting on the aeroshell is  $367 \text{ m/s}^2$  at 130.9 seconds from reaching 250 km. The next two peaks are at Mach 1.7 and 0.3, when the parachutes deploy. Drogue parachute deployment happens at such a high Mach number to make sure that the capsule is stable in the transonic and subsonic regime, where stability analysis was no longer valid. At Mach 0.8 the heat shield is discarded as well. Drogue parachute deployment causes  $30.5 \text{ m/s}^2$  deceleration and the main parachute deployment causes  $15.6 \text{ m/s}^2$  deceleration. The sudden jump in  $cp_{stagnation}$  is due to different mode of calculating it, where supersonic theory is switched to subsonic. At 55 km altitude, the final speed is 29 m/s and balloon deployment begins. The flight path angle at 200 km altitude is -8 degrees.

### 6.5.2. Thermal loads

The aeroshell will enter the atmosphere with a tremendous amount of kinetic energy which will mainly be converted to heat. Only a fraction is transferred to the aeroshell by radiation and convection. Nonetheless, this heatflux is generally in the order of 1,000 to 10,000  $[\text{W}/\text{cm}^2]$ . A proper modelling of radiative and con-

vective heat transfer is vital to accurately size the thermal protection system (TPS) required to protect the aerobot during entry at Venus.

**Convective heat transfer** The convective heat transfer at the stagnation point is modelled by application of a simplified version of the Fay-Riddell model

$$q_w = 0.76Pr^{-0.6}(\rho_e\mu_e)^{0.4}(\rho_w\mu_w)^{0.1}\sqrt{\left(\frac{du_e}{dx_s}\right)}(h_e - h_w), \quad (6.40)$$

where  $q_w$  is the heat flux at the stagnation point. The subscript  $e$  and  $w$  respectively stand for edge and wall conditions. The corresponding velocity gradient for a spherical nose with radius  $r_{nose}$  is defined as

$$\left(\frac{du_e}{dx_s}\right) = \frac{1}{r_{nose}}\sqrt{\frac{2(P_e - P_\infty)}{P_e}}. \quad (6.41)$$

Here the boundary layer is assumed to be frozen with a non-catalytic wall. Due to the hyper-sonic and high temperature nature of the flow during atmospheric entry, the perfect gas laws cannot be applied. To approach this situation better, the imperfect gas laws together with the effect of varying vibrations modes are used. To determine the imperfect gas properties the Venusian atmosphere was assumed to fully consist of  $CO_2$ , a reasonable assumption considering its 96.5% prevalence [62]. The effect of molecular vibrational modes on the specific heat ratio of  $CO_2$  was determined using

$$\gamma = -8.175 \cdot 10^{-10}T^3 + 0.000001665T^2 - 0.001233T + 1.5336, \quad (6.42)$$

by R.A. Braeunig<sup>1</sup>. Additionally the viscosity  $\mu$  in Equation 6.40 cannot be assumed to be constant. The temperature dependence of the dynamic viscosity is computed with the Sutherland model

$$\mu = \mu' \left(\frac{T'}{T}\right)^{3/2} \frac{T' + S}{T + S}. \quad (6.43)$$

where  $'$  indicated the baseline which is taken at 193.15 K. This model is considered poor in approximating inter molecular interaction. However, due to assumption of a pure  $CO_2$  atmosphere the application of Equation 6.43 is justified [63]. It must be noted that the dynamic viscosity will also be slightly influenced by high pressures, which will be less than 10% [64]. However, further calculating this effect was deemed to be out of the scope of this design phase. The free stream density, pressure and temperature were determined by interpolating the Venus International Reference Atmosphere (VIRA) [25]. Dissociation of molecules and the formation of plasma are not analysed; an added safety margin will be introduced in the thermal protection system sizing to cope with this uncertainty. With the gas properties determined using the above equations the relation between the edge and free stream velocity is determined. This is done using normal shock wave theory<sup>2</sup> in which Equation 6.42 is applied to account for the imperfect nature of the gas.

**Radiative heat transfer** The radiative heat absorption during re-entry is modelled by the radiative heat relation established by Tauber for the Pioneer missions [65]. For velocities between 10,028 and 12,000 [m/s] this is

$$q_{rad} = 8.497 \cdot 10^{-63} V_\infty^{18} \rho_\infty^{1.2} r_{nose}^{0.49} \quad (6.44)$$

and for less than 10,028 [m/s]

$$q_{rad} = 2.197 \cdot 10^{-22} V_\infty^{7.9} \rho_\infty^{1.2} r_{nose}^{0.49}. \quad (6.45)$$

The model has been developed and validated for the pioneer mission to Venus. Due to the decision to employ the same shape as the pioneer mission, a 45° rounded cone, it can also be used to accurately represent the radiation heat loads of this mission. The radiation heat flux in Equation 6.44 and Equation 6.45 are uncoupled, representing purely the gross absorbed radiation. However, a large part of this radiation will be radiated back to the environment. The amount of coupling between incoming and outgoing radiation can

<sup>1</sup><http://www.braeunig.us/space/atmmodel.htmvenus>, retrieved 13 June 2020

<sup>2</sup><https://www.grc.nasa.gov/WWW/BGH/normal.html>, retrieved 26 May 2020

be estimated by using the Goulard number [66]

$$\Gamma = \frac{2q_{rad}}{0.5\rho_{\infty}v_{\infty}}, \quad (6.46)$$

from which the net radiative heat flux can be computed using Tauber-Wakefield [67]

$$q_{rad_{coupled}} = \frac{q_{rad}}{1 + \kappa\Gamma^{0.7}}, \quad (6.47)$$

where  $\kappa$  is an atmosphere specific constant which equals 3 for Venus. **Total heat transfer** By combining the coupled radiation and convective heat transfer the total heat flux and heat load could be determined for the stagnation point. These results can be seen in Figure 6.4. Representing a peak heat flux of 773.4 [cm<sup>2</sup>] and a total heat load of 17,206.3 [J/cm<sup>2</sup>].

## 6.6. Aeroshell design

In the following section a preliminary sizing of the aeroshell, thermal protection system and parachute is considered.

### 6.6.1. Structural design

In section 6.3 it was determined that there are 2 parameters driving the design of aeroshell: R/D ratio and the halfangle of the apex of the cone. As a starting point, the same values as in mission Pioneer Venus were chosen; a 45 degrees halfangle and R/D of 0.25. The value of 45 degrees for the halfangle was kept due to volume considerations where the fairing diameter was a limiting factor and the halfangle of 45 degrees offered a good volume. As is shown in 6.10, higher angles might be beneficial for heat loads, but they offer a lower internal volume. R/D has to be analysed in a later design phase in more detail, but its variation does not affect acceleration and heat loads significantly. This fixed the shell geometry, which will be formed by a sandwich panel which will carry the aerodynamic loads exerted on the thermal protection layer. In order to size the required sandwich thickness and composition, the critical failure mode, N=2 general buckling [68], is evaluated. This was done by modelling the behaviour of a sandwich conical shell under hydrostatic pressure. This can be summarised by the following expression by Cohen [69]

$$SF \cdot P/E = \frac{C \cdot \gamma (t_{face}/r_{base})(t_{core}/r_{base})^{1/5}}{1 - \kappa (t_{core}/r_{base})^{0.5}}, \quad (6.48)$$

where  $\gamma$  and  $\kappa$  are factors driven by the cone geometry determined as follows

$$\gamma = 4.2r_{base}^{2.5} / [L((r_{base} + r_{nose})/2\cos\alpha)^{1.5}], \quad (6.49) \quad \kappa = 0.155\gamma / \cos^2\alpha \quad (6.50)$$

and  $P$  the aerodynamic pressure. Factor  $C$  is a correlation factor which ranges from 0.9 to 1.1, here the worst case scenario of 1.1 is taken. To simplify the analysis a 1.5 ratio between the core and face sheet mass is assumed. The expected weight penalty of this assumption is no more than 2% [68]. Due to the critical nature of this structure a 1.5 load safety factor is introduced as  $SF$  in Equation 6.48. Additionally, a 25% thickness safety factor is introduced as recommended by Davies [70] and finally 10% weight is added to account for layer adhesion. This results in the following sizing in Table 6.4 for the aeroshell structure. It must be noted that the above methodology only applies for the front shell. However, for the current design stage the structure of the back shell is assumed to be the same.

Table 6.3: Sandwich materials

Part	Material	$\rho$ [kg/m <sup>3</sup> ]	E [MPa]
Face	Aluminium 2014-T6	2800	73100
Core	Divinycell	76	49

Table 6.4: Aeroshell structural sizing

Section	$t$ face [mm]	$t$ core [mm]	Mass [kg]
Front shell	1.2	65.9	103.9
Back shell	1.2	65.9	99.8

### 6.6.2. Thermal protection system

To protect the structure of the aeroshell and the payload in its interior from the high heat flow, a heat shield is required. For entry vehicles ablative materials are often used to form the heat shield. The material chars

and decomposes during entry by absorbing the incoming heat flux. Heritage missions to Venus utilised the same Carbon Phenolic ablative materials. However, thanks to the lower peak heat flux a different, more weight effective material can be applied. A choice was made for Phenolic Impregnated Carbon Ablators (PICA), which is more mass efficient, but has a lower max peak heat flux tolerance. However, thanks to the low entry angle the max peak heat flux is considerably lower than previous mission.

Table 6.5: Ablative material properties

Properties	PICA-M4-B-D [71] [72]
Density, $\rho$	0.26 [g/cm <sup>3</sup> ]
Effective heat of ablation, $h_{ea}$	3.67·10 <sup>8</sup> [J/kg]
Thermal conductivity, $k$	0.201 [W/mK]
Nominal design peak heat flux. $q_{peak}$	1200 [J/cm <sup>2</sup> ]

The required PICA recession layer thickness can be sized as following

$$t_{recession} = \frac{heatload \cdot SF}{h_{ea} \cdot \rho_{PICA}} \cdot 1.25 + 0.0254. \quad (6.51)$$

SF is a safety factor of 25% to account for an unexpected increase in the heat load. Additionally, a 25% margin is introduced for a differential recession of the gap filler [73]. This is needed as PICA is only produced in smaller tiles. And finally, a 0.0254 [m] thickness is added as a manufacturing margin [73]. The benefit of PICA as a TPS really comes to light in sizing the required insulation. Thanks to its high porosity, the heat is rejected at the reaction surface instead of storing it by conduction. Therefore, it can be directly attached to the surface of the aeroshell with just a 20% increase in thickness to account for insulation [71]. Here again a manufacturing margin must be added, now 0.00508 [m]. Before sizing the TPS thickness the variation of the heat load over the body must be taken into account. The heat flux illustrated in Figure 6.4 are at the stagnation point, the most heavily loaded point of the aeroshell body. It has been shown that the heat rate varies along a sphere [74] with

$$\frac{q}{q_{stag}} \approx \cos(\theta), \quad (6.52)$$

where  $\theta$  is the angle from the centerline, which is valid for values up to 45°. Finally, the backshell must be considered briefly. Even though its contribution to the TPS mass will be marginal it must be accounted for. In the mission sizing done by Prabhu [75] 6% TPS mass was taken for a backshell on a Pioneer aeroshell derived Venus mission. Following the above methodology and relation leads to the thermal protection system sizing in Table 6.6.

Table 6.6: PICA Thermal protection system properties

	$t$ ablative layer [cm]	$t$ insulation layer [cm]	TPS mass [kg]
Frontshell nose	6.04	1.28	33.66
Frontshell sidewall	5.78	1.23	233.13
Backshell	-	-	18.68

### 6.6.3. Drogue and main parachute

Parachute characteristics are chosen such that they are comparable to the Mars Exploration Rover, as those can sustain high forces (more than 80 000 Newton) and are similar in size and shape to <sup>3</sup>. Parachutes will have a drag coefficient of 0.5 and the drogue parachute will be ringsail shaped, while the main chute will be a disk gap band to reduce oscillatory motion. Main materials will be nylon and polyester, allowing for heat resistance but also low weight. For lines either Kevlar or Zylon will be used. The drogue parachute will be deployed by a mortar and will have a 3.7 m diameter, while the main parachute will be 6 m in diameter and will be pulled by the drogue parachute. As the decelerator analysis is a complicated matter and there were

<sup>3</sup>[https://mars.nasa.gov/mer/mission/spacecraft\\_edl\\_parachute.html](https://mars.nasa.gov/mer/mission/spacecraft_edl_parachute.html), retrieved in June 2020

no wind tunnel tests capabilities, precise parachute analysis was left as a recommendation. Due to that, the total mass of the system was assumed to be 15.4 kg, which is similar to the Mars Exploration Rovers, that had higher surface areas and loads, giving a significant margin as the level of confidence in this value is low.

## 6.7. Aerodynamic characteristics and stability

The aerodynamic characteristics and stability during entry are discussed in this section.

### 6.7.1. Summary of aerodynamic properties

Aerodynamics coefficients presented below are assuming an infinite Mach number. For actual simulation, a correction factor  $\chi$  mentioned in Section 6.3 is applied.

Table 6.7: Aeroshell aerodynamic coefficients

Parameter	Value	Parameter	Value
$C_A$	$-0.1228 \sin^2(2\alpha) + 0.9219$	$x_{cp}/D$	-0.616
$C_N$	$0.448 \sin(2\alpha)$	$C_D$	0.9219
$C_M$	$-0.276 \sin(2\alpha)$	$\beta$	131.7 kg/m <sup>2</sup>
$C_{Mg}$	$-0.6 \sin(2\alpha)$	Frontal surface area	7.06 m <sup>2</sup>

### 6.7.2. Center of pressure and gravity

The center of pressure was calculated as stated in the Section 6.3, yielding a value of -0.616 D, meaning that the center of pressure is located 1.848 meters from the leading edge. As stated in Subsection 14.3.5, the center of gravity is located at 1.059 m from the leading edge. Therefore, the static margin is equal to 0.263.

### 6.7.3. Stability

For stability only static stability is analysed. Dynamics stability and an off-center center of gravity is left as a recommendation. For stability the derivative of the moment around center of gravity with respect to angle was calculated. Using methods stated in the Section 6.3, the moment coefficient with respect to tip is equal to  $-0.276 \sin(2\alpha)$  and normal force coefficient is equal to  $0.448 \sin(2\alpha)$ . Changing the reference point to  $x_{CG}$  yields a formula for the moment coefficient  $C_{Mg} = -0.6 \sin(2\alpha)$ . Calculating the derivative with respect to  $\alpha$  and setting it to be smaller than 0 yields the stability requirement for the center of gravity perfectly aligned with symmetry axis of the vehicle,

$$\frac{d}{d\alpha}(-0.6 \sin(2\alpha)) < 0 \Rightarrow -1.2 \cos(2\alpha) < 0, \quad (6.53)$$

which is true for  $|\alpha| < 45$  deg. Meaning that the capsule is stable at high Mach numbers as long as it is inserted with the right attitude. At lower Mach numbers a stable configuration is achieved by releasing the drogue parachute.

## 6.8. Balloon deployment

At 55 km, the heat shield is dropped and the balloon is stretched between the main chute and the payload, as shown in Figure 6.5. After 15 seconds a set of pyrovalves start the inflation system and the balloon fills up. A model for the inflation process is described in Chapter 7. The same model was used to calculate weight, buoyancy, chute and balloon drag as the aerobot descends and inflates. Chute and balloon drag is calculated with:

$$D_{ch} = C_{D_{ch}} 1/2 \cdot \rho v^2 A_{ch}, \quad (6.54) \quad D_{bln} = C_{D_{bln}} 1/2 \cdot \rho v^2 A_{bln}, \quad (6.55)$$

where the chute is the same as the main entry chute. The drag coefficient for the balloon is assumed to be 0.5. The cross-section the drag is acting on is calculated by computing the new semi-major axis as the inflated volume increases after each time step, and by assuming that the height of the balloon is fully stretched

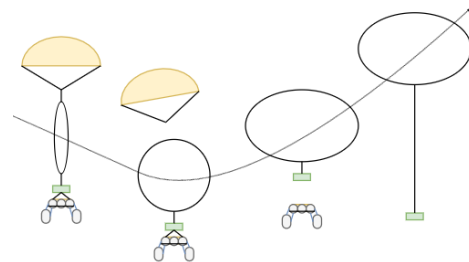


Figure 6.5: Aerobot deployment stages

out. The buoyancy is calculated with:  $B = \rho V g$ . Where the ambient density is determined via linear interpolation between 1 km resolution atmosphere data. The acceleration can be found by summing the forces and dividing it by the total mass. The new velocity and the distance travelled is calculated using a simple forward Euler scheme. Figure 6.6 and Figure 6.7 show the altitude versus time. The main chute is cut when the balloon is almost filled up. At this stage, the balloon continues to descend as the buoyancy cannot support the weight of both the payload and the helium tanks. When the balloon is completely filled, the helium tanks are dropped and the aerobot floats upwards to its equilibrium state. After inflation a winch lowers the gondola down 50 m below the balloon.

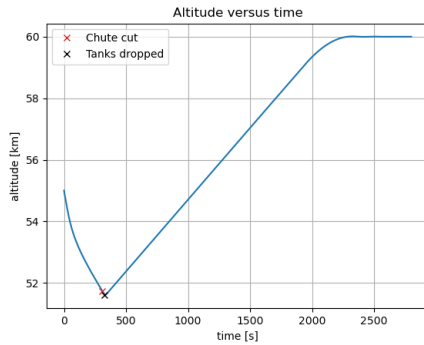


Figure 6.6: Altitude versus time during entire deployment

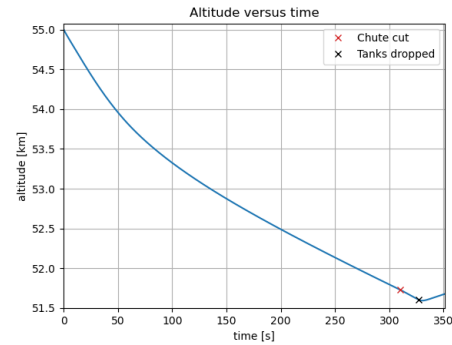


Figure 6.7: Altitude versus time during inflation phase

## 6.9. Risk analysis

In this section, risk assessment for the entry is performed and mitigation strategies are given. It is important to notice that analysis was focused on the most impactful or likely events and therefore the list is not complete. The scales used can be found in Chapter 15.

- AE1 **Wrong insertion orbit:** Because of a wrong burn time, the entry capsule can be inserted into a wrong orbit, resulting in mission failure. Probability = 1, Severity = 5; **mitigation:** Perform extensive simulations, perform checks after and during burn. Bring spare fuel to correct the orbit.
- AE2 **Drogue deployment malfunction:** Drogue parachute deployment is a complicated process that happens at high Mach numbers, which could cause tangling. Probability = 2, Severity = 3; **Mitigation:** The drogue parachute is deployed by a mortar for correct separation and direction of deployment. Additional checks for drogue folding should be performed.
- AE3 **Main deployment malfunction:** The main parachute is very large, due to that it could not inflate correctly. Probability: 2, Impact = 4; **Mitigation:** The main parachute is deployed by a drogue parachute pulling it out, allowing for controlled deployment.
- AE4 **Structure malfunction:** The aeroshell will experience very high aerodynamic loading during entry, which could cause disintegration. Probability = 1, Severity = 5; **Mitigation:** Safety margins are added to aeroshell structure and FEM analysis shall be performed. The design should be checked by multiple teams.
- AE5 **Heatshield disintegration:** Peak heat flux or total heat load exceeds the design parameters, as a result the aerobot will burn up during entry. Probability = 3, Severity = 5; **Mitigation:** introduce a 25% heat load safety factor in the TPS sizing and validate heatshield performance with plasma testing.
- AE6 **Heatshield point load:** During assembly and handling a point load can occur on the heat shield, potentially creating a weak spot which can then lead to disintegration. Probability = 2, Severity = 4; **Mitigation:** Additional protection must be placed around the TPS during handling.
- AE7 **Inflation system malfunction:** During balloon deployment a pyrovalve might not fire, which will result in less helium gas being pumped into the balloon. This would hurt the balloon performance in several ways. Luckily, pyrovalves are known to be incredibly reliable.<sup>4</sup> Probability = 1, Severity = 3; **Mitigation:** test reliability of pyrovalves.
- AE8 **Chute cutting malfunction:** A malfunction in the chute cutting system might mean that the chute

<sup>4</sup><https://www.space-propulsion.com/spacecraft-propulsion/valves/pyrotechnic-valve.html>, retrieved in June 2020

does not eject, which will entangle with the balloon when it starts to rise. Probability = 1, Severity = 2; **Mitigation:** test reliability of the chute cutting mechanism.

AE9 **Tank dropping malfunction:** A malfunction in the tank dropping system might mean that the tanks are not dropped, which will not allow the balloon to float to the target altitude. Probability = 1, Severity = 4; **Mitigation:** test reliability of tank dropping system.

### 6.10. Sensitivity analysis

The structural and thermal design of the aeroshell is subject to two main inputs; total heat load for TPS sizing and the max deceleration for the structural design. In Table 6.8 3 different entry parameters are varied of which in Figure 6.8 the impact on heat load and deceleration can be seen.

Table 6.8: Case description and difference to nominal

Case	Difference to nominal
a	Nominal
b	Halfangle increase to 70deg
c	Halfangle decrease to 15deg
d	Flightpath angle -29.7deg
e	Flightpath angle -14.2deg
f	R/D increase to 0.5
g	R/D decrease to 0.1

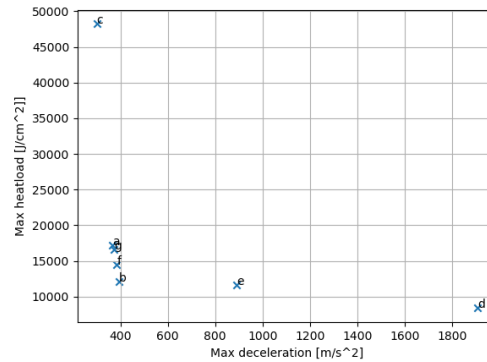


Figure 6.8: Heatload vs. max deceleration during different cases

Considering the excursion between nominal, case b and case c, the halfangle could be varied to optimise the design. However, due to the volumetric requirements for the aeroshell payload, the half angle cannot be increased without increasing the overall diameter of the construction. The latter is not possible due to the launch fairing constraints. Varying the flight path angle (see case a, e and d) has an significant impact on deceleration and heat loads, thus also on the design. A more steep would decrease the required TPS mass. However the required structural mass will increase significantly to sustain the higher deceleration loads. Changes to the entry flight path angle must be carefully monitored in the following design stages to minimise the risk of a redesign of the entry system.

### 6.11. Verification and validation

**General verification** The models above were verified by simple unit tests, but also by analysing the model parameters and outputs along the flight path with respect to the leading expressions. **Flight path validation** Validation of model with gravity and constant ballistic coefficient was done using the Venus Pioneer probe data from [76]. A summary of the validation can be seen in the Figure 6.9, Figure 6.10, Figure 6.11. This validation shows adequate convergence, therefore the model was considered to be validated.

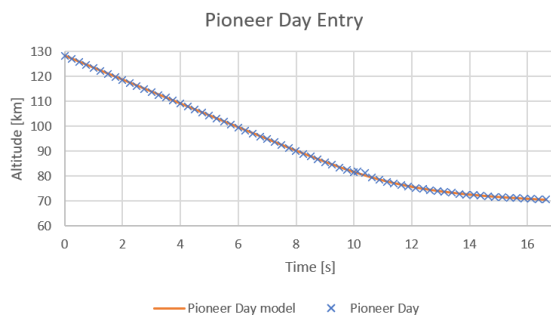


Figure 6.9: Model vs. data from Pioneer Day probe

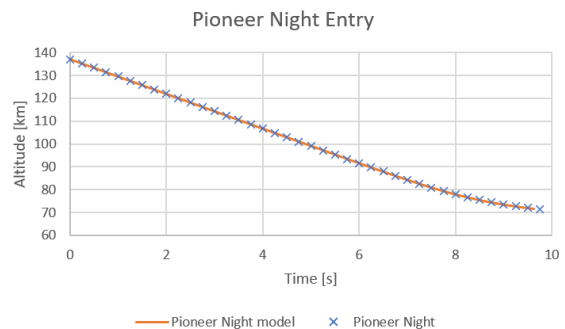


Figure 6.10: Model vs. data from Pioneer Night probe

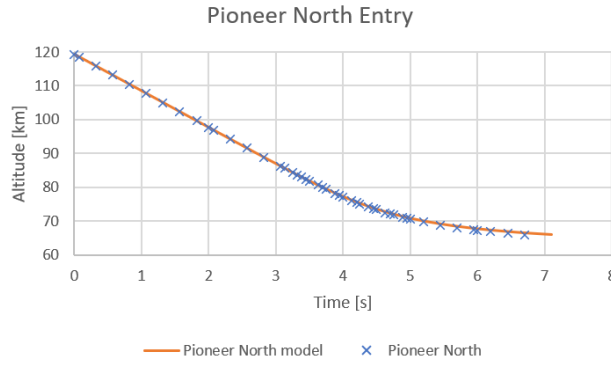


Figure 6.11: Model vs. data from Pioneer North probe

**Drag and ballistic coefficient validation** For the drag and ballistic coefficient, another test was performed. The equations for the Axial, Normal, Moment coefficients and  $x_{cp}/D$  for Viking entry vehicle in [61] were compared to the output of coefficients model in Table 6.9.

Table 6.9: Comparison of force, moment and center of pressure.

Coefficient	Model	Referenced value [61]
$C_A$	$1.728 - 1.614 \sin^2(\alpha)$	$1.769 - 1.65 \sin^2(\alpha)$
$C_N$	$0.1141 \sin(2\alpha)$	$0.1144 \sin(2\alpha)$
$C_M$	$-0.119 \sin(2\alpha)$	$-0.1191 \sin(2\alpha)$
$\frac{x_{cp}}{D}$	-1.043	-1.041

Moreover, the aeroshell shape closely resembles a cone, the aeroshell axial force coefficient was thus compared to the cone drag coefficient in Table 6.10, assuming Mach = 0 and  $\alpha = 0$ .

Table 6.10: Drag coefficient comparison.

Coefficient	Model	Referenced value for 45deg cone [77]
$C_D$	0.46094	0.5

**Entry heat validation** The entry heat model was validated by inputting the Pioneer North probe's flight data and comparing the results to observed values from literature.

Table 6.11: Entry heat validation

Value	Model	Reference value [78]	Deviation
Peak convective heat flux [ $W/cm^2$ ]	7378	7200	+2.47 %
Peak radiative heat flux [ $W/cm^2$ ]	3103	3400	-8.74 %
Peak total heat flux [ $W/cm^2$ ]	9834	11000	-10.6%
Integrated convective heat load stagnation point [ $W/cm^2$ ]	15639	14000	+11.7%

The deviations in Table 6.11 are within a very acceptable margin for the current design phase. The most influential driver for the model discrepancies is expected to be the atmospheric model used. Small differences in atmospheric compositions, density, pressure etc. flow through into the entry heat model.

# 7 Aerobot Aerodynamics

This chapter details the design process, inflation system and stability of the pumpkin-shaped superpressure balloon of the aerobot and the aerodynamics related to the dropsondes.

## 7.1. Design overview

Table 7.1 summarises the design of the aerobot balloon. The upcoming sections describe the decisions and calculations that have led to these values. Figure 7.1 shows the lobed gore design of the pumpkin-shaped superpressure balloon.

Table 7.1: Design overview

Parameter	Value	Unit	Parameter	Value	Unit
Superpressure @262.8 K	3562	Pa	Surface area	319.1	m <sup>2</sup>
Max superpressure	9705	Pa	Diameter	11.66	m
Helium mass	24.75	kg	Height	7	m
Structural mass	53.94	kg	Nr. of gores	48	
Tank mass	23.5x5	kg	Eccentricity	0.8	

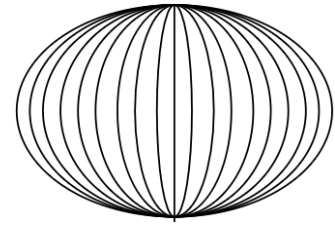


Figure 7.1: Lobed gore design

### 7.1.1. Approach to sustainability: lifting gas trade-off

The higher density profile in the Venusian atmosphere, opens up the possibility of using other lifting gases that would normally be unsuitable on earth, so alongside helium and hydrogen, nitrogen gas is also considered. Assuming a dry aerobot mass (without lifting gas) of 100 kg, the required lifting gas mass to maintain a 60 km altitude can be calculated with the balloon equilibrium equation:

$$\rho_{amb}V - \rho_{gas}V = m \tag{7.1}$$

Where  $m$  is the dry aerobot mass, the lifting gas mass is represented with  $\rho_{gas}V$  and the 'amb' refers to ambient conditions, which for the density at 60 km is 0.4694 kg/m<sup>3</sup>. Ideal gas law ( $P = \rho RT$ ) is used to calculate the lifting gas density. Where  $R$  is the specific gas constant. The results are summarised in Table 7.2, which shows that hydrogen is the lightest option, while nitrogen is much heavier.

Table 7.2: Lifting gas properties at 60 km

	Density (kg/m <sup>3</sup> )	Volume (m <sup>3</sup> )	Volume w.r.t. H <sub>2</sub>	Mass (kg)	Mass w.r.t. H <sub>2</sub>
H <sub>2</sub>	0.02175	223.4	1	4.859	1
He	0.04318	234.6	1.050	10.13	2.085
N <sub>2</sub>	0.3022	598.1	2.677	180.75	37.20

From a sustainability perspective, nitrogen is an excellent choice. It's an abundant resource on earth and not damaging to health or materials. The downside is the large mass budget impact. N<sub>2</sub> also needs a larger balloon volume, which means the balloon envelope will need to resist higher loads, increasing structural mass. Hydrogen then seems like the best choice, but has downsides that make it unsuitable. Firstly, H<sub>2</sub> is highly flammable and currently no mitigation exists that would reduce the safety risks to a manageable level. Secondly, the small atomic size of H<sub>2</sub> means that it has a high likelihood of diffusing through the envelope, which strains the endurance requirement. The second-best choice, helium, is not constraint by safety risks, but has the same diffusion problem. Helium is also scarce and a non-renewable resource on earth, because it's continuously escaping to space. The use of helium however is still defensible, provided that it's used in low quantities. Projections show that shortages are not expected to occur for another 40 years, and the use of a few tens of kilograms of helium pales in comparison to the yearly commercial production [79]. This makes helium the best lifting gas candidate, while care is taken to minimise the amount used.

## 7.2. Functional analysis

The balloon has to keep the aerobot floating at the operational altitude for the duration of the mission. Requirements flow out from user requirements and vehicle functions and have been summarised in Table 7.3. The upcoming sections describe how these requirements are fulfilled.

Table 7.3: Requirements on the aerobot balloon

Identifier	Requirement	Compliance	Explanation in
US-PERF-01	The design shall be able to operate in the Venusian atmosphere at altitudes between 25 and 60 km.	✓	7.4, 7.8
US-PERF-02	The operating time shall allow for all scientific objectives to be met.	✓	7.5
ABT-01	The aerobot will be able to operate at a constant density level at 60 km altitude.	✓	7.4
ABT-02	Lifting gas diffusion losses cannot exceed 13% of the initial mass. (at this value the superpressure reduces to zero)	✓	7.5
ABT-03	The aerobot will be able to return to equilibrium after a vertical gust velocity of up to 3 m/s [14]	✓	7.7
ABT-04	The gondola will be able to restore itself to a stable configuration after a horizontal gust velocity of up to 57 m/s	✓	7.7

## 7.3. Balloon thermal model

Establishing requirements for the balloon demands the evaluation of the temperature variations at the target altitude. Temperature influences the superpressure values in the balloon, which in turn affects the required strength of the balloon envelope. A model was build that accounts for solar flux, albedo, infrared radiation and convection [80], at 0° latitude and a constant ambient temperature (262.8 K). The results of this simulation are shown in Figures 7.2 - 7.5. Since, the model requires parameters like surface, diameter and mass as inputs, the balloon was first sized with guesses for the temperature changes. These values were then refined with further iterations.

### 7.3.1. Model equations

The model simulates a full revolution of the balloon around the Venusian equator, assuming a stationary sun relative to the venus surface, which is a proper assumption because of the long length of a Venusian day. The first step is calculating the air mass that the solar flux travels through before hitting the envelope. The air mass is calculated with [81]:

$$AM = CF \cdot \frac{P_{amb}}{P_0} \left( \sqrt{1229 + (614 \sin(\Theta))^2} - 614 \sin(\Theta) \right) \quad (7.2)$$

Where  $\Theta$  is the elevation angle of the sun, which is 0° at sunrise and 90° at noon. The case where the sun is above the horizon for the balloon, but not yet for the planet surface directly below it, is neglected. The correction factor ( $CF$ ) is determined with the maximum solar attenuation. The Venusian solar constant is 2601.3 W/m<sup>2</sup> and at 60 km, the maximum solar flux is measured at 1520 W/m<sup>2</sup> [1, 82], which indicates that the solar attenuation at noon will be:  $\tau = 1520/2601.3 = 0.5843$ . The air mass at this attenuation can be computed by solving the following equation [81]:

$$\tau = 0.5 \left( e^{-0.65AM} + e^{-0.95AM} \right) \quad (7.3)$$

This outputs the air mass that the solar flux passes through at noon. Now Equation 7.2 can be solved for the correction factor, which results in a value of 265. The elevation of the sun relative to the balloon changes throughout the day. At 60 km altitude, the average wind speed is 77 m/s, which indicates that the balloon takes an average of 5.8 terrestrial days to complete one revolution around Venus. Every second the elevation angle will thus increase with  $2\pi$  divided by the revolution time in seconds. At every data point, the model

computes solar intensity from the air mass and the solar attenuation. Then the solar heat flow rate is:

$$\dot{Q}_{sun} = \alpha I_{sun} A \quad (7.4)$$

$\alpha$  is the effective solar absorptivity of the balloon envelope and  $A$  is the cross-section of the balloon that the solar flux acts on. The cross-section is taken to be the cross-sectional area at the equator of the pumpkin-shape, which overestimates the incoming solar flux. As a safety factor the solar intensity is also multiplied with 1.5 at every data point, which also increases the albedo heat flux [14]. The albedo heat flow rate is calculated from the solar flux by:

$$\dot{Q}_{albedo} = \alpha a I_{sun} S \cdot F \sin(\Theta) \quad (7.5)$$

Where  $a$  is the bond albedo of Venus set at 0.77 [1], the sine term corrects for the fact that at lower elevations less solar flux is reflected towards the balloon,  $S$  is the surface area of the envelope and  $F$  is the view factor, which is the fraction of the surface area that the flux acts on. At 60 km, the view factor is equal to 0.43 [81]. The caveat to this equation is that it is assumed that the bond albedo, which is measured as the light reflected into space, is the same as the albedo acting on the balloon inside the Venusian cloud layer.

The model distinguishes between two types of infrared radiation heat. The first type is the infrared radiation from the Venusian surface. Venus emits black-body radiation at an effective temperature of 226.6 K [1]. The ground heat flow rate is then computed with:

$$\dot{Q}_{ground} = \varepsilon \sigma T_{eff}^4 S \cdot F \quad (7.6)$$

Where  $\varepsilon$  is the effective infrared emissivity and  $\sigma$  is the Stefan-Boltzmann constant. The other radiation type, is emitted by the balloon envelope to the ambient environment:

$$\dot{Q}_{env} = \varepsilon \sigma (T_{env}^4 - T_{amb}^4) S \quad (7.7)$$

Heat convection is caused by the movement of gases. External convection concerns the interaction between the atmosphere and the envelope, and internal between the envelope and the helium. The external and internal convection heat flow rate is calculated with:

$$\dot{Q}_{conv,ext} = h_{ext}(T_{env} - T_{amb})S \quad (7.8) \quad \dot{Q}_{conv,int} = h_{int}(T_{env} - T_{He})S \quad (7.9)$$

Where  $h$  is convective heat transfer coefficient, which is a function of temperature and will have to be computed at every data point. Finding the external and internal values for  $h$  involves the Prandtl and Grashof numbers. The  $Pr$  is the ratio between momentum and thermal diffusivity, and the  $Gr$  is defined as the ratio between buoyancy and viscous forces:

$$Pr = \frac{C_p \mu}{k} \quad (7.10) \quad Gr = \frac{\rho^2 g D^3 |T_1 - T_2|}{T_1 \mu^2} \quad (7.11)$$

Where  $C_p$  is the heat capacity of the gas,  $\mu$  the gas dynamic viscosity,  $k$  the gas thermal conductivity,  $g$  the gravitational acceleration on Venus and  $D$  the balloon diameter.  $T_1$  is either the ambient or helium temperature and  $T_2$  is the envelope temperature. The internal and external Prandtl and Grashof numbers are computed at every data point and are used to calculate the Nusselt number. Separate empirical relations exist for external and internal conditions [81]:

$$Nu_{ext} = 2 + 0.45 \cdot (Gr Pr)^{0.25} \quad (7.12) \quad Nu_{int} = 0.13 \cdot (Gr Pr)^{1/3} \quad (7.13)$$

Finally, for both conditions the convective heat transfer coefficient can be computed via:

$$h = \frac{k Nu}{D} \quad (7.14)$$

At each data point the temperature change due to the incoming and outgoing heat flow rates is computed according to the first law of thermodynamics,  $\dot{Q}_{in} - \dot{Q}_{out} = \Delta \dot{Q}$ . The accumulation of heat flow rate, relates to the temperature change by [80]:

$$\Delta \dot{Q} = C_v m \frac{\Delta T}{\Delta t} \quad (7.15)$$

Here,  $C_v$  is the isochoric heat capacity of either the envelope or the helium, since the superpressure balloon will have a constant volume during nominal operations.  $m$  is the mass of either the envelope or the helium and  $\Delta t$  is the time interval. Evaluating Equation 7.15 for the envelope and helium heat flow rates results in two expressions for the temperature change:

$$\Delta T_{env} = \frac{\dot{Q}_{sun} + \dot{Q}_{albedo} + \dot{Q}_{ground} - \dot{Q}_{env} - \dot{Q}_{conv,ext}}{C_{v,env}m_{env}} \Delta t \quad \Delta T_{He} = \frac{\dot{Q}_{conv,int}}{C_{v,He}m_{He}} \Delta t \quad (7.16)$$

### 7.3.2. Thermal model results

Figures 7.2 - 7.5, show the results from the balloon thermal model. Overall, the envelope gains heat from the solar, albedo and ground flux, while it loses heat from infrared emission and external convection. Internal convection heats up the helium gas until noon, when the envelope starts cooling down and the helium gas can start losing heat to the envelope. Figure 7.2 shows that at noon the albedo flux almost equals the solar flux. This is attributed to the high albedo and to the large surface of the balloon that is in contact with the albedo flux at this elevation angle.

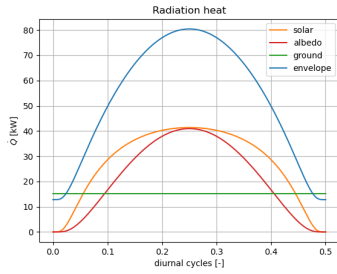


Figure 7.2: Radiation heat from sunrise to sunset

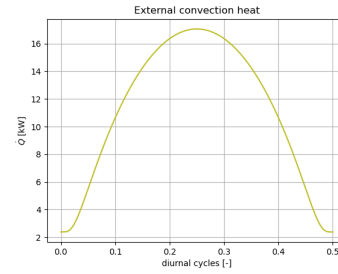


Figure 7.3: External convective heat from sunrise to sunset

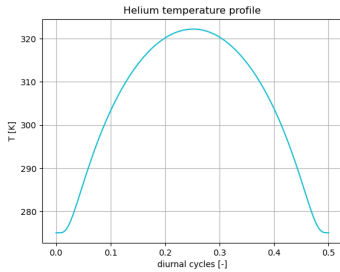


Figure 7.4: Temperature profile from sunrise to sunset

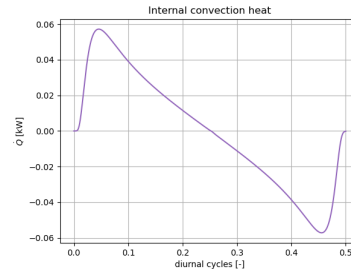


Figure 7.5: Internal convective heat from sunrise to sunset

For a full temperature range, the nightside temperatures should also be investigated. Diurnal variations in the ambient temperature are still highly uncertain. On the surface, temperature variations are extremely small due to low solar flux absorption [83]. This absorption increases with altitude and at 65 km, the nightside temperature at high latitudes can reduce to about 23 K less than the average temperature [84]. This variation is assumed to be same for 60 km altitude, but because of the high uncertainty an additional 1.5 safety factor is added, which results in a 228.3 K lower limit.

## 7.4. Superpressure fundamentals

The superpressure balloon is a common technology for high-altitude scientific ballooning on earth and was the working principle behind the Vega balloon mission on Venus. The idea is that the balloon is 'overfilled' with lifting gas. After inflating to a constant volume the excess gas overpressurises the balloon compared to the ambient environment, which increases the balloon's resistance to atmospheric disturbances like gusts and temperature changes.

Assuming negligible gas diffusion, constant volume and ambient pressure changes, mass conservation can be applied to the helium gas before and after a temperature change. Expressing the mass as an ideal gas reduces to equating the gas densities:

$$\frac{P + \Delta P_1}{RT_1} = \frac{P + \Delta P_2}{RT_2} \quad (7.18)$$

At the lowest temperature, the superpressure will be equal to zero. The ambient superpressure is calculated by equating the coldest conditions to the ambient. At the hottest temperature, the maximum superpressure is found. The required balloon volume is evaluated by solving the equilibrium at the desired 60 km altitude. For a given dry mass, the balloon volume and helium mass is calculated by solving the equilibrium state again with Equation 7.1. The results set the sizing requirements for the balloon envelope and are summarised in Table 7.4.

Table 7.4: Requirements based on temperature range

Parameter	Value	Unit
Highest gas temperature	322.2	K
Lowest gas temperature	228.3	K
Superpressure @262.8 K	3562	Pa
Max superpressure	9705	Pa
Helium density	49.70	g/m <sup>3</sup>
Helium mass	24.75	kg
Balloon volume	498	m <sup>3</sup>

## 7.5. Envelope sizing

### 7.5.1. Envelope laminate material

Based on prior work by JPL, the balloon envelope is constructed out of a special laminate designed to combat the acidic environment in the cloud layer and minimise helium diffusion through the skin [14, 85, 86]. A 15  $\mu\text{m}$  layer of the fluoropolymer aclar 33C is used to prevent any sulphuric acid from seeping into the envelope. To prevent the possibility of manufacturing defects leading to a mission failure, a second redundant layer of aclar is added. Having two pinholes at the same spot is statistically very improbable, so this guarantees acid protection.

The third layer in the laminate consists of 8  $\mu\text{m}$  thick aluminium foil. The foil acts as a barrier for the helium and drastically minimises leakage. Lastly, biaxially oriented polyethylene terephthalate (BoPET), also known as Mylar, forms the backbone of the laminate and carries the tensile stresses. The load tapes, which fix the gores together at the seams, contain zylon fibres. 6  $\mu\text{m}$  polyurethane adhesive layers are used to fix the laminate layers together and the load tapes to the seams. the properties of the laminate are listed in Table 7.5. The BoPET and zylon fibre geometry is discussed in the following paragraph.

Table 7.5: Laminate properties [86]

Parameter	Value	Unit
Areal density	156	g/m <sup>2</sup>
Permeability	1.6	cm <sup>3</sup> /m <sup>2</sup> /bar/day
Solar absorptivity	0.17	
Infrared emissivity	0.74	



Figure 7.6: Laminate constituents

### 7.5.2. Envelope geometry

The balloon sizing is based on a lobed gore design, which decreases required film strength and has a pumpkin-shaped envelope. In comparison to the lightweight VEGA balloons, the NASA's ULDB program showed that as payload masses increase, it becomes harder to handle the combined forces at the base of balloon, preventing them from increasing the mission duration to the goal of 100 days. This issue was solved by adopting a pumpkin-shape balloon with a height over diameter ratio of 0.6 [87].<sup>1</sup> The gores of balloon are connected to each other via load tapes. The aerobot balloon will maintain the same height over diameter ratio and will be constructed from 48 gores with 48 load tapes.

To calculate the geometric properties, the balloon is modelled as a oblate spheroid. The volume equation can be rewritten to solve for the semi-major axis ( $a$ ) and the semi-minor axis ( $b$ ):

$$V = \frac{4}{3}\pi a^3 \sqrt{1-e^2} \quad (7.19)$$

The height over diameter ratio corresponds to an eccentricity of 0.8, which is defined as:

$$e^2 = 1 - \frac{b^2}{a^2} \quad (7.20)$$

<sup>1</sup>[https://sites.wff.nasa.gov/code820/spb\\_design\\_approach.html](https://sites.wff.nasa.gov/code820/spb_design_approach.html), accessed June 2020

Consequently, the surface area of the balloon is computed with the following equation:

$$S = 2\pi a^2 + \pi \frac{b^2}{e} \ln \left( \frac{1+e}{1-e} \right) \quad (7.21)$$

### 7.5.3. Stress analysis

Determining the geometric properties of the load bearing structure requires an analysis of the stresses on the envelope. According to the load tape design philosophy, it is assumed that the balloon skin only carries tension in the zonal direction (left-right), while meridional tension (top-bottom) is carried by the load tapes [88]. The zonal tension per length is given by:

$$T_z = r_c \Delta P \quad [N/m] \quad (7.22)$$

Where  $\Delta P$  is the superpressure inside the balloon and  $r_c$  is the curvature radius of the gore. The radius of curvature can be chosen independent of the balloon size, but its minimum value at the balloon equator depends on the semi-major axis (a):

$$r_c = a \frac{\pi}{N} \quad (7.23)$$

Where  $N$  is the number of gores. Assuming that the BoPET layer of the laminate carries the entire load, the required BoPET thickness can be found by dividing Equation 7.22 by the tensile strength. Meridional tension per load tape depends on the maximum cross-section of the balloon, and can be written as [88]:

$$T_m = \frac{\pi}{N} a^2 \Delta P \quad (7.24)$$

In addition to meridional tension, the load tapes carry the payload weight,  $W = m_{pay} \cdot g$ . The required area of the zylon fibres can be found by dividing the tension by the tensile strength. The tape length is expressed as half the circumference of the ellipse drawn by the semi-major and semi-minor axes. The load tape will have a width of 10 cm, centred at each seam. The characteristics of the design are summarised in Table 7.6. A safety factor of 1.5 is applied for the BoPET and load tape thicknesses.

Table 7.6: Mass properties and material thicknesses

Parameter	Value	Unit
Envelope mass	49.79	kg
Load tapes mass	4.16	kg
BoPET thickness	30	$\mu\text{m}$
Load tape thickness	56	$\mu\text{m}$

## 7.6. Inflation system

As described in Section 6.8, the aerobot inflates its balloon shortly after deployment. Five overpressurised helium tanks will fire sequentially every 10 seconds and fill up the balloon until they are either dropped or until they are no long overpressurised relative to the environment. MT Aerospace provides several options for helium high pressure vessels at 310 bar MEOP. Their 75 L tank can hold 3.12 kg of helium.<sup>2</sup> Their largest tank is 120 L, but information on the helium capacity is not known. Instead, it can be extrapolated from the 75 L tank using ideal gas law, which results in a capacity of 4.992 kg for gaseous helium [89].

The tanks are arranged below the gondola and will be dropped when balloon is filled with enough gas. Flexible hoses attach the tanks to the balloon. The configuration is shown in Figure 7.7. At a certain time after deployment, pyrovalves open the tanks.<sup>3</sup> If the interaction between the tank and the balloon is modelled as a convergent-diverging nozzle, the mass flow is equal to<sup>4</sup>:

$$\dot{m} = AP_0 \sqrt{\frac{\gamma}{RT_t}} M^* \left( 1 + \frac{\gamma-1}{2} M^{*2} \right)^{-\frac{\gamma+1}{2(\gamma-1)}} \quad (7.25)$$

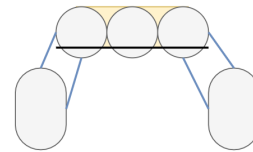


Figure 7.7: Inflation system structure

<sup>2</sup><https://artes.esa.int/projects/hehvp-helium-high-pressure-vessel>, accessed June 2020

<sup>3</sup><https://www.space-propulsion.com/spacecraft-propulsion/valves/pyrotechnic-valve.html>, accessed June 2020

<sup>4</sup><https://www.grc.nasa.gov/WWW/K-12/airplane/mflchk.html>, accessed June 2020

Where  $A$  is the cross-section of the hose, which has a 2mm inner diameter,  $P_0$  is the tank pressure,  $T_0$  is the tank temperature, which is assumed to be same as ambient temperature,  $\gamma$  is the specific gas ratio, which is 1.667 for helium, and  $M^*$  is the mach number in the nozzle throat. The gas velocity in the tank is assumed to be zero and the mach number in the balloon is calculated by applying isentropic conditions:

$$\frac{P_0}{P_1} = \left(1 + \frac{\gamma - 1}{2} M_1^2\right)^{\frac{\gamma}{\gamma - 1}} \quad (7.26)$$

Here,  $P_1$  is assumed to be the ambient pressure. As long as  $M_1 > 1$ , the throat conditions remain choked ( $M^* = 1$ ) and the mass flow rate is maximised. As the tank empties, the pressure difference and the exit mach number decrease. At some point after the exit velocity becomes subsonic, the throat will unchoke ( $M^* < 1$ ). However, the model shows that the tanks are dropped before this happens, so this behaviour is neglected. After each interval, the remaining helium mass is computed with  $m_{i+1} = m_i + \dot{m}_i \Delta t$ . The high pressures make the ideal gas law inaccurate, so the new tank pressure is calculated with the van der Waals equation:

$$\left(P_0 + a \frac{n_t^2}{V_t^2}\right) (V_t - n_t b) = n_t \mathfrak{R} T_t \quad (7.27)$$

Where  $a$  and  $b$  are the van der Waals constants. For helium  $a = 3.46e - 3 \text{ m}^3\text{Pa/mol}^2$  and  $b = 2.38e - 5 \text{ m}^3/\text{mol}$ .  $V$ ,  $n$  and  $\mathfrak{R}$  are the volume, number of moles and universal gas constant. The number of moles is computed by dividing the mass with the molar mass of helium. As the balloon descends the temperature increases, and thus the tank pressure as well. However, this never exceeds the 1.25x proof pressure [89]. The resulting total mass flow is shown in Figure 7.8. At each new peak a tank is opened via a pyrovalve. The massflow cuts to zero when the tanks are dropped.

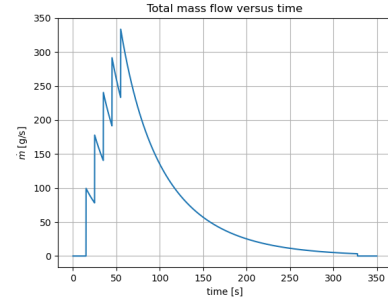


Figure 7.8: Helium mass flow into the balloon

## 7.7. Aerobot stability

Aerobot stability is affected by two types of gust loads: horizontal gusts swing the the gondola like a pendulum and vertical gusts induce an altitude change. The gust load can be modelled by:

$$G = C_D 1/2 \cdot \rho v_G^2 A \quad (7.28)$$

### 7.7.1. Horizontal gust loads

When a gust hits the gondola, three moments act on it. The gust load moment  $M_G$  is described with:

$$M_G = C_D 1/2 \cdot \rho v_G^2 A \cdot l \cdot \cos(\phi) \quad (7.29)$$

Here,  $C_D$  is the drag coefficient of the gondola. For a octagonal cylinder at a Reynolds number of  $4e6$ , the drag coefficient is 1.1 [90].  $\rho$  is the ambient density ( $0.4694 \text{ kg/m}^3$ ),  $v_G$  is the gust velocity relative to the airspeed. At 60 km, the maximum and minimum wind velocities are 110 and 53 m/s, respectively [82]. This indicates that the worst-case scenario will result in a gust velocity of  $110 - 53 = 57 \text{ m/s}$ . The probability of this occurring is considered very low. Information on the gondola can be found in Chapter 14.  $A$  is the cross-section of the gondola, for which the maximum value is  $2.522 \times 0.575 \text{ m}^2$ . The length of tether  $l$  is 50 m and  $\phi$  is the radial displacement. The gondola also experiences a local drag moment that dampens the oscillation and acts in the opposite direction of the radial velocity:

$$M_D = C_D 1/2 \cdot \rho (l\omega)^2 A \cdot l \quad (7.30)$$

Where  $\omega$  is the radial velocity. Lastly, weight induces a moment:  $M_W = mg \sin(\phi) \cdot l$ , which acts opposite to the gust load moment. Per definition the moments sum up to the change in angular momentum:  $M_G - M_D - M_W = \dot{H}$ , which is converted to radial coordinates:

$$\dot{H} = \frac{d}{dt} mlv = ml^2\alpha \quad (7.31)$$

Solving the equations results in Figure 7.9, where the radial displacement is given as a function of time. Due to the high input gust velocity, the largest displacement is  $78.5^\circ$ . However, this is still recoverable and normally the geometry of the balloon envelope would also interrupt the flow, reducing the displacement. In conclusion, the aerobot can handle a large perturbation from a sudden and unlikely high horizontal gust velocity.

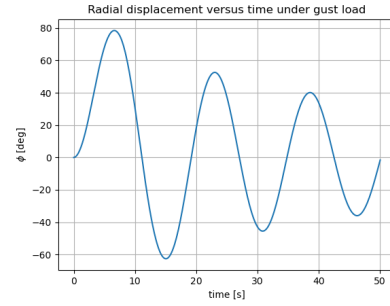


Figure 7.9: Gondola displacement for a 57 m/s gust

### 7.7.2. Vertical gust loads

The Vega mission experienced vertical gust velocities of 3 m/s. To calculate the perturbation altitude a model is set up that computes acceleration, velocity and displacement. The model accounts for buoyancy ( $B = \rho Vg$ ), balloon drag (Equation 6.55), weight ( $mg$ ) and gust loads (Equation 7.28) in the vertical direction, with a balloon drag coefficient of 0.5. The gondola drag is neglected, because of the small size compared to the balloon. The results for gust loads up- (+3 m/s) and downwards (-3 m/s) are shown in Figure 7.10. When the aerobot reaches the maximum perturbation altitude, the gust load is cut off to show that it returns to the 60 km equilibrium state. The maximum and minimum perturbations are +387 and -367 m, respectively. These perturbations are small and the ambient temperatures in this altitude range stays well within the operational temperature range of the aerobot.

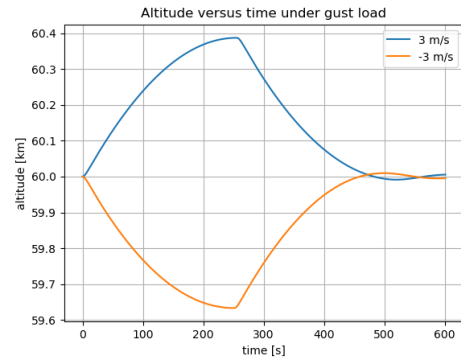


Figure 7.10: Up- and downwards vertical displacement after gusts

## 7.8. Dropsonde aerodynamics

To model fall time and drift distance, dropsonde aerodynamic Dropsonde aerodynamics are modelled to compute fall time and drift distance, which determines power and communication requirements. Optimised shapes are able to achieve drag coefficients of  $0.045^5$ . Without wind tunnel tests and FEM analysis, assessing the dropsonde drag coefficients is difficult, so 0.15 is assumed to allow for margins. Topological optimisation is left as a recommendation. Dropsonde dimensions are taken from Subsection 14.3.1 and wind is assumed to vary linearly with 0 at the surface to 80 m/s at 60 km altitude. The governing equations in the model are:

$$\frac{d^2h}{dt^2} = -\frac{1}{m} \left( 0.5C_D S \rho(h) \left( \frac{dh}{dt} \right)^2 - mg \right) \quad (7.32)$$

$$\frac{d^2s}{dt^2} = \frac{1}{m} 0.5C_{D_{side}} S_{side} \rho(h) \left( w(h_{bln}) - w(h) - \frac{ds}{dt} \right)^2 \quad (7.33)$$

and verified with equations assuming terminal velocities:

$$V = \sqrt{\frac{2mg}{\rho(h)SC_D}} \quad (7.34)$$

$$\frac{ds}{dt} = w(h_b) - w(h) \quad (7.35)$$

The result of validation can be seen in Table 7.8. The whole fall can be seen in Figure 7.11, while results can be seen at Table 7.7.

<sup>5</sup><https://www.grc.nasa.gov/WWW/K-12/airplane/shaped.html>

Table 7.7: Dropsonde fall time and drift

	Time (s)	Drift (km)
Until 25 km	642.3	18210.3
Total	1958.6	104078.2

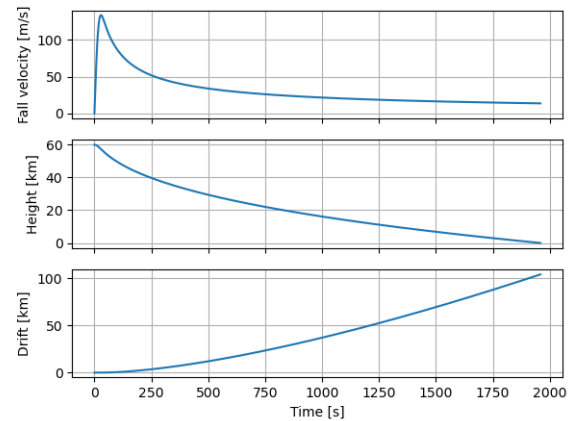


Figure 7.11: Dropsonde fall simulation

Table 7.8: Dropsonde fall time and drift model convergence and verification

Time to 25 km height (s)	Drift to 25 km height (m)	Model
642.3	18126	original model
637.3	18761	verification model

## 7.9. Risk analysis

The scales that were used to assess probability and severity of the risks are given in Section 15.1.

- BLN1 **Helium temperature is higher than expected.** Probability = 4, Severity = 5; **mitigation:** aside from the 1.5 multiplier that is already in place on the solar flux, the additional 1.5 safety factor on the balloon structure should prevent this. New probability = 1, New severity = 5.
- BLN2 **Aclar manufacturing defects allow acid to penetrate the balloon.** Probability = 3, Severity = 4. **mitigation:** Another layer of aclar is added to the laminate. Two defects at the exact same spot is statistically extremely unlikely. New probability = 1, New severity = 4.
- BLN3 **Balloon is ruptured by inflation process.** Probability = 3, Severity = 5. **mitigation:** Extensive testing is required to discover the optimal inflation process. New probability = 1, New severity = 5.

## 7.10. Sensitivity analysis

### 7.10.1. Thermal model sensitivity

The balloon thermal model assumes a constant ambient temperature. At 60 km, the temperature is 262.8 K, but this is an average and over 100 days this might vary by several degrees. Figure 7.12 shows the helium temperature profile, when the average temperature is increased by 5 and 10 K. At these temperatures the maximum helium temperature change, respectively, becomes 62.6 and 65.8 K, which is several degrees higher than the designed for 59.5 K. For this reason, safety factors have been applied to the incoming solar flux and the envelope strength, which will be able to handle temperature fluctuations.

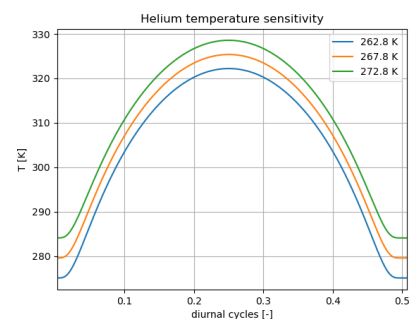


Figure 7.12: Helium temperature sensitivity

### 7.10.2. Vertical gust load sensitivity

The information on the vertical gust velocity is supplied by the short-lived Vega balloons [14]. For a longer duration mission the encountered gust velocities might be much higher. In Figure 7.13, the vertical displacement is shown when the gust velocities are doubled. It indicates that even with these increased velocities the displacement is limited to about a 1.5 km in both directions, which is also well within the operational temperatures.

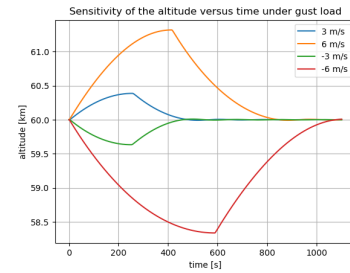


Figure 7.13: Helium temperature sensitivity

## 7.11. Verification and validation

During the process of making the models used in this chapter unit testing was continuously done to verify the correctness of the models. Afterwards, some separate V&V activities were done with existing models and real-world data:

**Thermal model verification** Verification for the balloon thermal model involved unit testing with hand calculations and comparing the model output to a graph of a different thermal model from [91]. This model describes the temperature at around 53-55 km altitude and shows a gas temperature that's about 31 K higher than the ambient temperature at 55 km. This is significantly lower than our thermal model, which is expected because of the lower solar flux that is received at 55 km, compared to 60 km.

**Inflation model verification** The inflation model was once again unit tested with hand calculations and similarities of the tank pressure curve were observed with that of the JPL inflation test [86]. The inflation time is the time between firing of the inflation system and the dropping of the tanks, which is shown in Figure 6.7 to be 320 seconds, which is a reasonable number considering the Vega balloon inflation took 230 seconds [92].

**Balloon design validation** The overall balloon design can be validated by comparing its payload-to-total mass ratio to the JPL balloon [14]. A rough comparison can be made by simply inputting the JPL payload mass of 44.1 kg into the same equations. This results in a payload-to-total mass ratio of 0.5907, which is slightly higher than the 0.5728 for the JPL balloon. The small variation is likely caused by difference in operational altitudes, safety factors and overall design decisions, but it shows that the number is in the correct range.

# 8 Propulsion

The propulsion subsystem is responsible for performing the orbital manoeuvres required to bring BLOON to the correct destination. Design of this subsystem has been limited to first order tank estimations and computation of the  $\Delta V$  budget. At the end of this chapter a risk, sensitivity and V&V analysis is performed.

## 8.1. Design overview

During the midterm, a selection for MON/MMH bi-propellant was made. This selection has remained the same, with MON-1.3 being chosen as oxidizer. The O/F ratio of the propellants will be 1.65, with 1.65 times more MON-1.3 than MMH. The thruster that will be used for the BLOON is the Apogee motor model S400-15, from the same thruster family that was used for VEX [93], Exomars and other interplanetary missions [94], along with the 10N thrusters for RCS from the same family. With the thruster and the propellant selected the  $\Delta V$  budget was setup as seen in Table 8.1. Here the total  $\Delta V$  includes the safety factor.

Table 8.1: Propellant mass required for mission operations. The safety factor is applied to the manoeuvres  $\Delta V$ , giving the fuel mass required in the last column by use of Tsiolkovskis equation (8.1, rounded to the nearest decimal. The total  $\Delta V$  includes the safety factors)

Concerns	Manoeuvre	$\Delta V$ (m/s)	Safety factor	Wet mass start	$I_{sp}$	MON-1.3/MMH (kg)
Orbiter	TCM	10	1	718.0	321	2.3
	VOI	536.3	1.78	715.7	321	187.4
	Aerobraking	270.2	1.16	528.3	321	50.1
	Orbital decay	116.3	1.16	456.2	291	22.1
	EOL transfer	11.4	1.16	454.3	291	1.9
TRM	TCM	20	1	2167.0	321	18.9
	VOI	536.3	1.78	2148.1	321	562.6
	Insertion	146.2	1.16	1585.5	321	83.8
	Separation	20	1.16	414	321	3.0
Orbiter	Total	1427.3	-	718.0	-	263.7
TRM	Total	1170.0	-	2167.0	-	668.3
Both	Total	-	-	-	-	932.1

To establish the tank size, tank pressure and lay-out had to be determined. It was chosen to use main tanks with 1.8 MPa pressure, with two helium pressurant tanks at 30 MPa starting pressure. This was the choice for both TRM and orbiter, based off past missions [95] [96]. All tanks are spherical. It is assumed that the tanks will be made out of Ti6Al5V alloys, without anything else. In reality the tank mass will likely be lower as a combination of titanium and carbon fibre composite can be used. For the main tanks the thickness is taken as 2 mm, more than twice what is required, in order to account for extra mass inside the tank against sloshing. The resulting tank and propulsion system mass is shown in Table 8.2.

Table 8.2: Propulsion system dry masses.  $t$  gives the tank thickness,  $V$  the volume and  $m$  the mass. The main tank and helium tank masses are multiplied by two.

Platform	Part	$V$ (m <sup>3</sup> )	$t$ (mm)	$m$ (kg)	Platform	Part	$V$ (m <sup>3</sup> )	$t$ (mm)	$m$ (kg)
Orbiter	Main Tank	0.122	2.0	10.6	TRM	Main Tank	0.314	2.0	22.2
Orbiter	He Tank	0.00700	4.0	3.3	TRM	He Tank	0.0180	5.5	8.4
Orbiter	Thruster	-	-	4.30	TRM	Thruster	-	-	4.30
Orbiter	Plumbing	-	-	5.68	TRM	Plumbing	-	-	11.6
Orbiter	Total	-	-	38.39	TRM	Total	-	-	74.2

### 8.1.1. Approach to sustainability

Due to the limited availability of "green" propellants, highly toxic and carcinogenic propellants have to be used for the BLOON mission. This is done due to the nature of space missions. Use of green propellants would reduce thruster efficiency, reliability and massively increase required propellant mass. Therefore, MON-1.3 and MMH were deemed acceptable for use during the BLOON mission.

## 8.2. Functional analysis

In this section the compliance of the design with subsystem requirements is checked. New requirements have been added, along with old requirements being removed. This is shown in Table 8.3.

Table 8.3: Requirements on propulsion.

Identifier	Requirement	Compliance	Explanation in
PR-01	The propulsion subsystem shall have a reliability of 99%	✓	Subsection 8.3.1
PR-02	The helium tanks shall be able to withstand atleast 30 MPa internal pressure	✓	Subsection 8.3.4
PR-03	The main tanks shall be able to withstand atleast 1.8 MPa internal pressure	✓	Subsection 8.3.4
PR-SP-01	The propulsion subsystem of the orbiter shall provide a $\Delta V$ of 1427.3 m/s.	✓	Section 8.1
PR-TRM-01	The propulsion subsystem of the TRM shall provide a $\Delta V$ of 1170.0 m/s.	✓	Section 8.1

## 8.3. Design approach

This section describes the design approach for various propulsion subsystem components. First the thruster design is described, followed by the  $\Delta V$  budget and propellant design. Finally the tank design is given.

### 8.3.1. Thruster

During the midterm phase [4], MMH and MON were selected as the propellants. A thruster designed for these was needed. Upon investigating past missions, the Apogee motor model S400-15 [94] was selected, which was also used in ExoMars and VEX. This thruster has a nominal  $I_{sp}$  of 321 s, a nominal thrust of 425 N and a massflow rate of 0.135 kg/s. One main thruster is to be used in both the orbiter and the TRM. Multiple thrusters may be needed on the TRM, discussed in the next section. Finally, as can be seen in Table 8.1 some burns are performed at 291  $I_{sp}$ . Those burns are not performed by the main thruster but instead by the RCS. The chosen RCS thrusters are the 10N bi-propellant thrusters from the same family [94].

### 8.3.2. $\Delta V$ budget

The  $\Delta V$  budget assuming impulsive burns is given in Chapter 5. Here, safety factors related to the propulsion subsystem are added. In general three different safety factors were added: 1 for burns that are assumptions with an overestimation, 1.16 for short duration burns and 1.78 for the capture burns.

The burns with a safety factor of 1 (no safety factor) are the TCM, the TRM separation burn and the orbit decay due to solar radiation. All these burn use assumptions that are likely to be a big overestimation. These are also short duration burns that will not be influenced too much by a non-impulsive burn.

Burns with a safety factor of 1.16 are the orbital decay, EOL transfer, aerobraking manoeuvres and atmospheric entry of the TRM. These burns have a 1.1 safety factor for redundancy and to account for non impulsive-burns. The impulsive-burn inefficiency was verified using the thrust and massflow rate of the thruster in the orbital code. Retrograde burns were performed at the pericytherion, giving a decrease apoc-ytherion. A theoretical  $\Delta V$  was determined with Tsiolkovski, Equation 8.1 and compared to the results of the program. This yielded a difference in  $\Delta V$  of only a few percent (reasoned to be the case in [59]). Burns performed at the apoc-ytherion are assumed to have no inefficiency. This is a good assumption due to the lower speeds and bigger distances at the apoc-ytherion. The only burn that has a long duration in this category is the aerobraking orbit lowering. In order to minimise the inefficiency, this manoeuvre was changed to 2 consecutive burns of equal  $\Delta V$ . By doing so the burn time became low enough that the impact on the

$\Delta V$  required was minimal. Alongside the 1.1 safety factor a 1.05 safety factor was added in order to account for difficult to extract propellant volume from the tanks [47], giving a total safety factor of 1.16.

$$\Delta V = I_{sp} \cdot g_0 \cdot \ln\left(\frac{m_0}{m_f}\right) \quad (8.1) \quad \ln\left(\frac{P_1}{P_2}\right) = \frac{\Delta H_{vap}}{R} \left(\frac{1}{T_2} - \frac{1}{T_1}\right) \quad (8.2)$$

Finally a safety factor of 1.78 was given to the capture burns, based off past missions [4]. This is likely to be an overestimation for the orbiter, as the orbiter's capture manoeuvre has a shorter duration than those the past missions. The TRM has a higher burn time however. A solution to this would be to include multiple thrusters or to insert into a capture orbit that requires less  $\Delta V$  and subsequently lower the orbit. Since more analysis on the optimal insertion with respect to solar gravity decay is needed Chapter 5, it was assumed that the 1.78 safety factor should hold for this burn, and no optimisation was done. Performing such an optimisation, including burn time, is left as a future recommendation. More detailed analysis for the insertion burn of the orbiter is also required to more accurately determine the propellant mass.

### 8.3.3. Propellant

The total propellant mass was computed with a 10% contingency on the BLOON drymass. A drymass of 454.3 kg was assumed, whereas for the TRM a 1502 kg was used. An O/F ratio of 1.65 was chosen in order to keep the tank sizes equal for fuel and oxidizer. This is done to simplify production and layout. This was also done for VEX and ExoMars [93, 96], and is within the range of O/F ratios for the thruster. MON-1.3, which equates to 98.7% N<sub>2</sub>O<sub>4</sub> and 1.3% NO, was chosen in order to reduce the freezing point of NTO, as NTO has a low freezing point at 1 bar of -9.3 °C [97]. Adding 1.3% NO reduces the freezing point to -11.2 °C at 1 bar. MON-1.3 furthermore has a low boiling point at 21.15 °C, which makes the operational range of this fuel at 1 bar very limited. In order to compute the boiling point of NTO at 1.8 MPa pressures, the Clausius–Clapeyron equation (8.2) was used. In this equation,  $P_1$  and  $T_1$  are the initial pressure and temperature (1 bar and 21.15 °C respectively),  $P_2$  and  $T_2$  the final pressure and temperature,  $\mathfrak{R}$  the universal gas constant and  $\Delta H_{vap}$  the specific heat of vaporisation. Using this equation resulted in a boiling point of 87.81 °C. It was attempted to also compute the freezing point at 18 bar. This was however not successful due to the lack of online chemical properties. The assumption will be made that it behaves similar to a standard phase diagram<sup>1</sup>, of which the freezing point increases slower than the boiling point increases with pressure. A safety factor was taken by keeping the MON tank at 40 °C. MMH has a high boiling and low melting point, with -52.4 °C melting and 87.5 °C boiling at 1 bar [98]. Analysis of the boiling point at 18 bar returned a temperature of 185 °C. Thus boiling and freezing point of MMH will not be an issue.

### 8.3.4. Tank

The tank was assumed to be made out of Ti6Al4V [99], with all tanks being circular. This is a lightweight aerospace grade titanium, also used in the manufacturing of the balloon helium tanks Chapter 7. The circular pressure equation using a thin walled assumption (Equation 8.3) was used in order to size all tanks.

$$\sigma = \frac{P \cdot r}{2 \cdot t} \quad (8.3) \quad P_t = \frac{Z \cdot R \cdot T \cdot (m - \dot{m} \cdot t)}{V} \quad (8.4) \quad T_t = \frac{T_{t-1}}{\left(\frac{P_{t-1}}{P_t}\right)^{\frac{n-1}{n}}} \quad (8.5)$$

Where  $r$  is the tank radius and  $t$  the shell thickness. To size the pressurant tanks, the ideal gas law was used along with the method described in [95]. Helium was chosen as this is the most efficient pressurant, along with a tank pressure of 30 MPa taken from previous missions [93] [96]. The EOL tank pressure was assumed to be 2.5 MPa, higher than the pressure of the main tank. This was done as a safety as a safety factor, to ensure the pressurisation to 18 bar at EOL. Two helium tanks will be used for each vehicle, one for each of the main tanks. The densities of MMH and MON-1.3 were used to determine the tank volume [98] [97]. Along this, an ullage of 7.5% [47] was used. The tank pressure for the main tank was set to 1.8 MPa as mentioned before. An analysis was performed on the pressurant tank pressure over time during the main burn, using an adiabatic constant volume assumption, in order to determine whether the helium tank pressure remains above the propellant pressure. This was done by taking into account the change in volume in the main tank correspondent to a massflow rate of 0.135 kg/s. The pressure was determined according to Equation 8.4 for a given time, whereafter the new temperature was determined with Equation 8.5. This process was iterated until it converged. In Equation 8.5  $n$  is an experimental value taken from [95] and in

<sup>1</sup>[https://en.wikipedia.org/wiki/Phase\\_diagram#/media/File:Phase-diag2.svg](https://en.wikipedia.org/wiki/Phase_diagram#/media/File:Phase-diag2.svg), retrieved 5 June 2020.

Equation 8.4  $Z$  is the compressibility factor. This assumption is conservative as the environment is not adiabatic. All tanks ended with a pressure higher than the propellant tanks. The results are shown in Figure 8.1 and Figure 8.2.

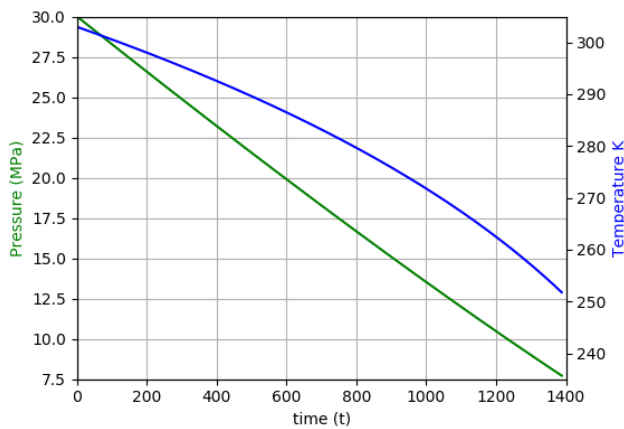


Figure 8.1: Helium tank pressure and temperature during the insertion burn of the orbiter.

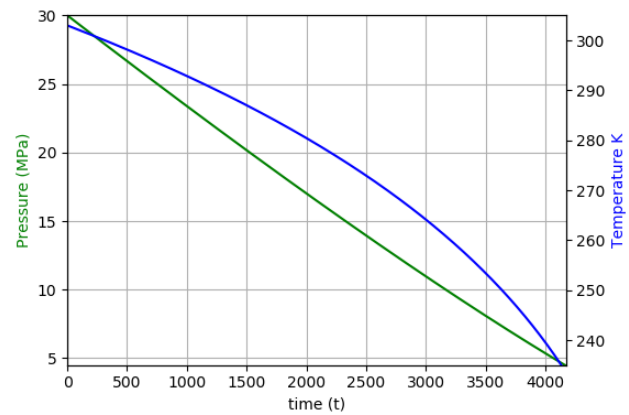


Figure 8.2: Helium tank pressure and temperature during the insertion burn of the TRM

## 8.4. Risk analysis

This section describes the risks of the propulsion subsystem. For a description of the scales, see Section 15.1.

- PR1 **Tank over-pressurisation:** This can cause the tank to explode. Probability: 2, Severity: 5. **Mitigation:** By designing the tank for twice the nominal pressure the chances of the tank exploding are lowered. Also reduces the impact of over-pressurisation. New probability: 1, Severity: 3.
- PR2 **Tank depressurisation:** Thrusters may not be able to operate. Probability: 2, Severity: 5. **Mitigation:** Setting the nominal tank pressure above the minimum operating pressure of the thrusters, along with extra pressurant mitigates the impact and probability. New probability: 1, Severity: 2.
- PR3 **Propellant sloshing:** May lead to momentum coupling with the spacecraft. Probability:3, impact:4. **Mitigation:** Anti sloshing geometries inside the tank. Extra thickness was assumed for the tank in order to estimate the mass of anti-sloshing geometry. New probability: 1, Severity: 2.
- PR4 **Thruster failure:** Could cause mission failure. Probability: 2, impact: 5. **Mitigation:** A main thruster was chosen that has never failed. The RCS thrusters have redundancy. In case the main thruster fails some manoeuvres may be performed using the RCS thrusters. New probability: 1, Severity: 4.
- PR5 **Propellant freezing:** Freezing of the propellants leads to a thruster failure. Probability: 2, Severity: 5. **Mitigation:** Heating the high freezing point tank. New probability: 1, Severity: 5.
- PR6 **Propellant evaporation:** Could reduce the efficiency of the thruster near EOL. Probability: 3, Severity: 3. **Mitigation:** Computing the boiling point at the tank pressure and keeping the tanks below the boiling point reduces the probability of significant evaporation. New probability: 1, Severity: 3.

## 8.5. Sensitivity analysis

A sensitivity analysis was performed in order to determine how much more drymass can taken given the Falcon 9 mass constraint. Assuming a fairing and adaptor mass of a total of 240 kg leaves 835 kg over for the propulsion system. Assuming 10 kg would be required in increase tank mass gives a maximum extra drymass for the orbiter of 579 kg or 610 kg for the TRM.

## 8.6. Verification and validation

Verification for the propulsion subsystem included mostly code verification and unit testing. Hand calculations were also used in order to verify pieces of code and calculations. Furthermore, the design choice logic was verified by analysing past missions and looking at their propulsion subsystem characteristics. The Clausius–Clapeyron equation code was validated using data from water. This gave a 2.67% difference for the boiling point of water at 1.8 MPa, with the actual value being higher.

# 9 Telemetry, Tracking and Command

Telemetry, tracking and command takes care of the communication between different mission elements, determining the position of different mission elements and making sure that each mission element receives commands. This chapter discusses the detailed design of every of these subsystems. The chapter starts with a complete overview of the design for each subsystem of TTC in Section 9.1. This is followed by a functional analysis in Section 9.2, which explains the roles the TTC subsystem design fulfils. Afterwards, a more extensive explanation and calculation of the subsystem is provided in Section 9.3, split per subsystem. A risk and sensitivity analysis is also given in Section 9.4 and Section 9.5, respectively. Afterwards, an overview of the verification and validation of the TTC subsystem is given in Section 9.6.

## 9.1. Design overview

The design overview section provides an outline of the TTC subsystem, split per element of the subsystem. A mass and power budget is given and the approach of sustainability is discussed.

### 9.1.1. Telemetry design overview

The main goal of the telemetry element is to receive and transmit data to all mission elements. This is done by means of multiple antennae. The aerobot has two 0.2 m diameter S-band LGA's. The first one is attached to the bottom of the gondola and is used for dropsonde communication. Each dropsonde is equipped with an S-band patch antenna. The other antenna is at the top of the gondola and communicates with the orbiter. When the signal reaches the orbiter, it is picked up by the main high gain antenna. This antenna has a diameter of 3.0 m and can transmit and receive at three different frequency ranges, which allow it to communicate with both the aerobot and Earth. Communication with Earth is done via 34 m antennas of the Deep Space Network (DSN) [100]. Five consecutive orbits are used for aerobot communication and every sixth orbit is used to send all the stored data back to Earth. This ratio allows for the optimal combination considering the iterated data rates and communication time available.

A continuous beacon mode signal is sent to Earth that lets the ground station know whether the aerobot or orbiter are experiencing issues. If this is the case, the satellite can order a downlink session earlier in order to send telemetry back down and/or to receive commands. This beacon mode signal is sent by a low gain X-band antenna, of which the satellite has two. One is on top of the main high gain antenna and the second one is mounted on the side of the satellite. The TRM is also equipped with a 0.2 m diameter low gain antenna at X-band frequency in order to relay its telemetry to the orbiter. Besides the antennae, all mission segments also have transceivers or receivers, which are present twice for redundancy. The exact specifics of these hardware components are given in Section 9.3 and the mass budget later on in this section. In order to provide a complete overview of all telemetry connections, a communication flow diagram has been made, which is shown in Figure 9.1. It also contains information on tracking, data rate and storage, which will all be explained later.

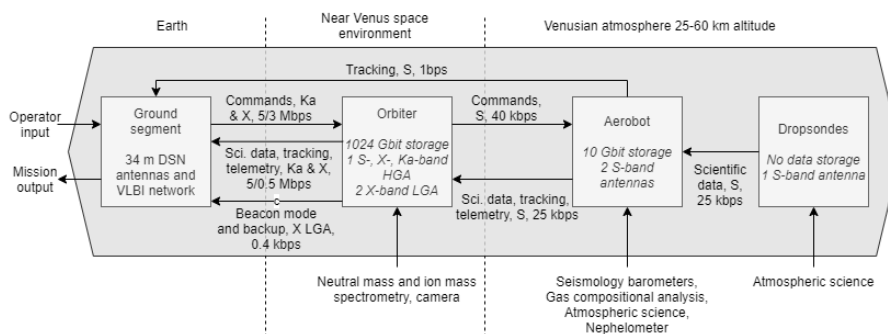


Figure 9.1: A communication flow diagram, depicting the inner working of the TTC subsystem.

### 9.1.2. Tracking design overview

The tracking of the orbiter is done by means of two-way ranging and Doppler tracking. Two-way ranging is used to determine the distance between Earth and the the orbiter. The exact accuracy and considerations for two-way ranging can be found in Subsection 9.3.6. Once the connection has been established, Doppler tracking is used to keep track of the relative speed of the orbiter afterwards to keep the antennas pointed correctly during the connection session. Both of these methods are assisted by computer models of the location of Venus and the orbital parameters of the orbiter. A similar method is used for the aerobot, but then the connection is between the orbiter and the aerobot instead of the orbiter and Earth. Finally, VLBI is also used infrequently during the mission for both the orbiter and the aerobot. VLBI will not be used as a main tracking method, but is used as a calibration on the other tracking methods. VLBI measurements will be performed directly on the downlink signal, not requiring special downlink antennas. The aerobot is an exception, which requires a VLBI antenna, since no other direct aerobot - Earth connection has been designed. This mission will make use of the European VLBI Network (EVN) for these measurements [101].

### 9.1.3. Command and data handling design overview

The command and data handling subsystem takes care of the processing and storage of all information. The command data rates are discussed in Section 9.3 and are taken into account in the antenna sizing.

The dropsonde has an on-board computer, sized based on CubeSats with a similar processing power, with a safety margin. Besides the limited storage available on the on-board computer itself, no specific storage system is present on the dropsonde due to their short lifespan and constant data transmission cycle after deployment. The aerobot has an on-board computer and solid state recorder of 10 Gbit, which allows for storage of the dropsonde data and for up to 6 orbits of the orbiter.

The orbiter also has an on-board computer and separate solid state recorder. The on-board computer is sized based on the required 5 Mbit/s ( 5 MIPS). Two 512 Gbit NEMO solid state recorders are used on the orbiter. <sup>1</sup> Due to the many different connections that come together in the orbiter, it was decided to also place a data handling/acquisition unit. Finally, it is important to note that all cabling is not considered to be part of the TTC subsystem. Instead the cable harness is discussed in Chapter 10. A complete overview of the command and data handling system is given by the data handling diagram in Figure 9.2. The data storage values (for example 1024 Gbit) indicate the storage present on the element, while the data rate values (for example 40 kbit/s) indicate how much a data a certain antenna can transfer. While not mentioned in the table, all elements can run on the bus voltages of the power subsystem, as mentioned in Chapter 10, with the exception of the orbiter's high gain antenna. This antenna functions at 60 V. More background information for the storage, power and data rate values is given in Section 9.3.

### 9.1.4. Mass and power budget

The mass and power of each segment in the design has been determined. How the values are calculated can be found in Section 9.3. The list in Table 9.1 provides an overview of the mass and power of each element and the total mass and power of the TTC subsystem. Segments that are not active during the peak power usage have an asterisk behind their name. Most critical peak power moments are during the communication phase. Transceiver/receiver/transmitter power is included in the antenna power.

### 9.1.5. Approach to sustainability

Besides the functional level of the design, is also important to make sure that the sustainability is taken into account. In general the antennas do not require the use of toxic or unsustainable materials. The only point of concern could be the data handling systems. Computers contain heavy metals such as lead, chromium, cadmium and mercury <sup>2</sup>. While it is attempted to minimise the usage of these metals, they are still necessary for the design of current computers. Since no alternative exists, these materials have to be used and their handling during production should follow health guidelines. Furthermore, by using a constant beacon mode signal, the total power spent by the TTC subsystem is minimised, making the design more sustainable.

## 9.2. Functional analysis

As mentioned in the introduction to this chapter, the main goal of the TTC subsystem is to handle the communication of all mission elements, to track all different segments in operation and to make sure that

<sup>1</sup><https://spaceequipment.airbusdefenceandspace.com/payload-products/payload-data-handling-with-memory/nemo/>

<sup>2</sup><https://www.independent.co.uk/environment/toxic-metals-danger-in-your-computer-5371933.html>

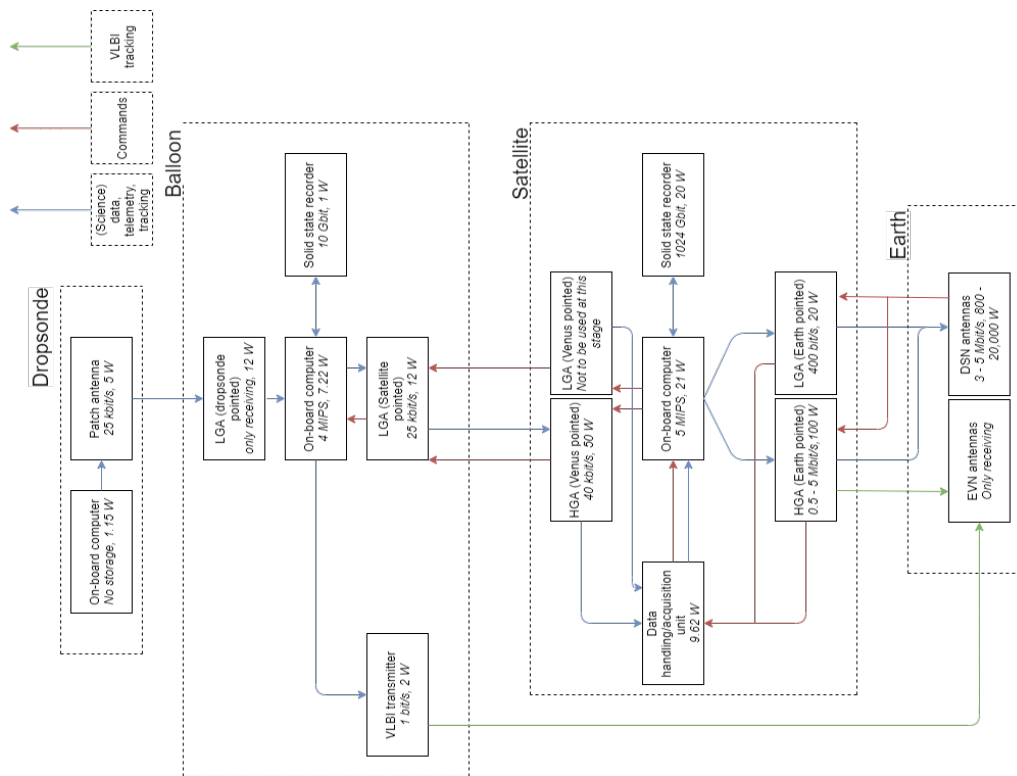


Figure 9.2: An overview of the data flow and system in all mission elements.

all data is stored and handled correctly, including commands. The function of the TTC subsystem also extends to the analysis of the data transmission rates in order to make sure that all data reaches the ground station, or any other mission segment for that matter, within the desired time frame.

These larger functions of the TTC subsystem flow into main requirements. Not only the data rates and error rates need to be established, but the transmission and encryption method also need to be specified. Besides exact values for the tracking accuracy of the system in both distance and speed, the pointing of antennas is also an important parameter that determines the performance of the system. Finally, other parameters that impact the performance of the TTC subsystem, such as the latitude of the aerobot, are mentioned. The compliance of the design with respect to the predetermined requirements is checked. In some cases, a previously determined value of the requirement has been changed due to iteration after the baseline report. As long as this change does not change the success or failure of the subsystem, it is shown with an asterisk behind the check mark. Certain requirements that in the end did not belong to this subsystem have been removed. This analysis is summarised in one table that can be seen in Table 9.2, placed at the end of the chapter due to its size. The last column in the table shows in which part of the chapter more explanation on the requirement can be found.

### 9.3. Design approach

The design approach section discusses the reasoning behind the design decisions made, including detailed calculations and specifications. The section is split up by telemetry, tracking and command & data handling.

#### 9.3.1. Telemetry design approach

The telemetry design first discusses the reasoning behind the chosen frequency bands. This is followed by a discussion of the link budgets, data rates. Then the sizing of the telemetry components is discussed. Finally, the transmission times of the antennas are discussed.

#### 9.3.2. Frequency bands

Three main frequency bands used are S-, X- and Ka-band. Ka-band is used for interplanetary communication between the orbiter and Earth. Due to their high frequency (27 - 40 GHz [102]), Ka-band is capable of higher gains, smaller beamwidths and decreased space losses [56] and are the highest frequency supported by the DSN [100]. Therefore, Ka-band is used for orbiter - Earth communication. Based on the data of the

Table 9.1: Overview of the TTC mass and power budget.

Segment	Item	Mass [kg]	Peak power [W]
Dropsonde	On-board computer	0.1	1.15
	Transceivers (2x)	0.2	0
	S-band antenna	0.05	2
Aerobot	On-board computer (MAC-100)	3.2	7.22
	Data storage (10 Gbit)	3.4	1
	S-band transceiver (2x)	3.0	0
	S-band receiver (2x)	3.4	0
	S-band antenna (2x)	0.18	12
	VLBI transmitter	1.2	0
	VLBI antenna*	0.04	10
Orbiter	Data handling and acquisition unit	5.5	9.62
	On-board computer	3.5	21
	512 Gbit NEMO data storage (2x)	13.2	20
	High gain multi-frequency antenna	36.4	100
	Low gain antenna (2x)*	0.4	40
	Main transceivers (2x)	15.2	0
TRM	On-board computer	1.4	8.4
	Data storage ( 17 Gbit)	5.4	6.5
	Low gain antenna	0.2	20
	Main transceivers (2x)	15.2	0
Dropsonde	Total mass	0.35	3.2
Aerobot	Total mass	14.4	20.2
Orbiter	Total mass	74.2	150.6
TRM	Total mass	22.2	34.9
Aeroshell	Total mass	0	0

DSN, the downlink frequency of 8.425 GHz and uplink frequency of 7.168 GHz have been established [103].

X-band is used on the orbiter as well. The main reason for this is that two-way ranging is significantly more accurate when two frequency bands are used due to the estimates that can be made of the impact of the interplanetary medium, as shown by the Cassini mission [104]. Therefore, both Ka- and X-band are used during two-way ranging. X-band is also used on the low gain antennas of the orbiter, since current technology for small low gain antennas at high frequencies is most detailed for X-band. Furthermore, most space based antennas on Earth are made for X-band, which allows the low gain antennas to be picked up by other satellite dishes as well, besides the DSN. Based on the data of the DSN, the downlink frequency of 32.05 GHz and uplink frequency of 34.45 GHz have been established for Ka-band [103]. For aerobot - orbiter and dropsonde - aerobot communication, the S-band frequency is used. X- or Ka-band for the aerobot has been eliminated due to the increased atmospheric attenuation at these frequency bands, as researched by the VeRa mission [105]. Furthermore, S-band has a significantly increased beamwidth (up to 4 times larger than X-band), which relieves the pointing accuracy requirements [56]. This is useful for the dropsonde, since its small size limits the tracking hardware. The frequency chosen equals 2300 MHz, the same as the S-band frequency chosen by the DSN [103]. All frequency bands are also shown in Figure 9.1.

### 9.3.3. Link budgets and data rate

For uplink signals, a minimum signal to noise ratio (SNR) of 9.6 dB is used. This value corresponds to a bit error rate of  $10^{-5}$  for an unfiltered BPSK signal and is recommended to be used for all systems that do not have intensive (post-)processing techniques, in the case of this mission all elements except for signals sent to Earth [106]. This value has also been used for NASA mission uplink signals, such as the Cassini mission [104]. For downlink signals, a value of 1.7 dB is used. This value corresponds to LPDC precoded GMSK, corresponding to a bit error rate of  $10^{-5}$  [106]. Even though methods seem to exist that allow an

SNR down to 0.31 dB, as the Reed Solomon concatenated with C.E. used by Cassini [104], these methods require significantly more power to run and use a high data rate. All inter-element connections (for example aerobot to orbiter) also use 9.6 dB. The connections have been sized such that complete flows of data also adhere to the SNR limits. For example, a signal from the aerobot, sent to the orbiter, relayed to Earth must have a combined signal to noise ratio of 1.7 dB. This means that a single SNR caused by the orbiter - Earth connection is higher than 1.7 dB to account for losses made before the signal reaches the orbiter. The most critical path is via the aerobot and the orbiter and results in a SNR of 1.9 dB, giving a 0.2 dB margin. This method works by sending a digital signal to the orbiter, which is then received and recreated by the orbiter. This recreated signal is then relayed to Earth. The method for these combined link budgets is discussed in the sensitivity analysis in Section 9.5. The overview of link budgets in dB is given in Table 9.3 and 9.4.

Table 9.3: A link budget breakdown of dropsonde, aerobot and TRM communication links.

Parameter	Dropsonde to aerobot (S)	Aerobot to orbiter (S)	Orbiter to aerobot (S)	Aerobot to Earth (X, VLBI)	TRM to orbiter	Unit
Transmit power	3.0	10.8	17.0	10.0	13.0	dBW
Transmitter loss	-1.5	-2.2	-2.2	-0.5	-0.7	dB
Transmitter gain	3.0	0.97	34.8	5.4	22.6	dB
Atmosphere loss	-10.0	-2.0	-2.0	-8.0	-2.0	dB
Free space loss	-132.6	-184.5	-184.5	-259.7	-226.8	dB
Pointing accuracy	-3.0	-0.7	-3.0	-0.15	-0.8	dB
Receiver gain	0.97	34.8	0.97	56.3	46.0	dB
Antenna reception	-2.2	-1.5	-1.5	-0.97	-0.97	dB
Boltzmann factor	228.6	228.6	228.6	228.6	228.6	dB
Data rate loss	-44.0	-44.0	-46.0	-0.0	-40.0	dB
SNT	-31.4	-30.6	-31.0	-27.0	-27.8	dBK
Signal to noise ratio	10.9	9.6	11.0	4.3	11.2	dB

Table 9.4: A link budget breakdown of the remaining communication links.

Parameter	Orbiter to Earth (Ka/X)	Earth to orbiter (Ka/X)	Earth to Orbiter (X, LGA)	Orbiter to Earth (X, LGA)	Unit
Transmit power	20.0/20.0	29.0/43.0	43.0	13.0	dBW
Transmitter loss	-0.7/-0.7	-0.7/-0.7	-0.7	-0.7	dB
Transmitter gain	57.3/46.0	79.0/67.0	66.0	22.6	dB
Atmosphere loss	-6.0/-6.0	-6.0/-6.0	-6.0	-6.0	dB
Free space loss	-282.6/-271.0	-283.2/-269.6	-269.6	-271.0	dB
Pointing accuracy loss	-0.6/-0.03	-0.6/-0.03	-0.75	-0.75	dB
Receiver gain	79.0/68.2	57.3/46.0	22.6	68.2	dB
Reception antenna loss	-0.97/-0.97	-0.97/-0.97	-0.97	-0.97	dB
Boltzmann factor	228.6/228.6	228.6/228.6	228.6	228.6	dB
Data rate loss	-67.0/-57.0	-64.8/-67.0	-44.8	-26.0	dB
SNT	-24.0/-24.0	-27.8/-27.8	-27.8	-24.0	dBK
Signal to noise ratio	3.1/3.2	10.0/12.6	10.6	3.0	dB

The power values of all antennas were iterated based their resulting SNR and by looking at similar missions, such as Venus Flagship [15], and general statistics [56], it was checked whether these voltages would be realistic. Using 35 or 50 Ohm cabling, all voltages fit within the values mentioned in Chapter 10. The exact power values can be found in Section 9.1. Transmit and reception antenna losses were based on statistical values of the specific antenna used [56] and are in the range of 0.6 - 0.85. In most cases parabolic antennas are used. The only exception is the dropsonde antenna, where a patch antenna was chosen due

to its high beamwidth of up to 180 degrees [56]. All other antenna gains are calculated using  $\eta(\frac{\pi D}{\lambda})^2$  with a standard efficiency  $\eta$  of 0.6 [56]. Based on an iterative process, the size of each antenna was determined. Their values can be found in the mass budget table. The antenna on the aerobot that communicates with the orbiter sits on top of a vertical structure and is flipped 90 degrees, thus pointing horizontally. This is done since the communication window with the satellite, which is discussed in Chapter 5, most of the time requires the antenna to point roughly 90 degrees (= sideways) with respect to the planet's surface. Because of this, this top antenna also has a gimbal that allows for accurate pointing.

Atmospheric losses are also accounted for in these budgets. Research by the Marinier V shows that atmospheric attenuation at the level of the aerobot is roughly 2.0 dB [43]. At an altitude of 25 km (for the dropsondes), atmospheric attenuation increases to 10 dB [43]. Furthermore, a value of 6 dB was taken into account for any atmospheric attenuation caused by Earth and atmospheric defocusing. Due to the desert or dry locations of the DSN [103], rain attenuation is not an issue as long as the required availability is below 98% [56]. Due to the high apocynthion of the orbiter, defocussing is expected to be in the order of fractions of decibels [107], but since the exact transmission time is not fully determined and atmospheric defocusing has a high variability, a safety margin of a few dB was taken into account. Free space losses are calculated using standard equations and a distance of 100 million km [56]. The pointing accuracy error is based on the accuracy of the star sensors, discussed in Chapter 12, and fulfil the 0.03 rad requirement. The data rates have been iterated to fit the link budgets and also be sufficient for all necessary data to be sent. Finally, the system noise temperature is based on the antenna noise temperature (730 K at Venus and otherwise given by the Deep Space Network [103]) and the added noise to the cable losses within the antenna [56].

Finally, an explanation of the data rates is given. An overview of all data rates in bit/s can be found in Figure 9.2 and has been sized by combining the data generation rates from Chapter 4 and transmission times discussed in Subsection 9.3.5. The 25 kbit/s data rate of the dropsonde is significantly higher than the data generation rate, discussed in Chapter 4, and allows the dropsonde to still send its data even if the connection with the aerobot was shortly interrupted. The data rate of the aerobot antenna to the orbiter was determined using an iterative process, also dependent on subsystems such as power and structures. The exact data rate of 25 kbit/s was based on the transmission time available and is thus discussed later in this section. The same goes for the 5 Mbit/s downlink of the orbiter. Even in a 1:1 ratio of data rate to bandwidth, the maximum required bandwidth at the orbiter is 5 MHz and 40 kHz for the orbiter, both values that can easily be attained with the antennas and hardware used for the TTC subsystem [40].

#### 9.3.4. Telemetry sizing

As explained before, the sizing of the antennas is based on the gain they can produce (parabolic antennas). The mass of the antenna is then based on a heritage value of a 9.2 kg antenna with a diameter of 1.5 m [40], scaled by the area of the actual antenna to be used. Based on values for larger antennas of Cassini and Venus Flagship [104] [15], this method seems to slightly overestimate the mass of larger antennas, but this is beneficial as it adds a small safety margin. This method no longer holds for a small patch antenna, which is why the dropsonde antenna has been sized based on an off-the-shelf component<sup>3</sup>. The height to diameter ratio of parabolic antennas is based on the ratio of the Cassini mission [104]. The mass of the transceivers and transmitters is based on heritage data from SMAD in combination with the required antenna power [47]. Due to redundancy every transmitter/transceiver/receiver is present twice.

#### 9.3.5. Transmission time

The data rates and antenna sizes described previously have all been optimised so that they can send all data within the available time. Calculations regarding transmission time are discussed in this subsection.

Firstly, the dropsondes will communicate for their entire lifetime after deployment, since they will only have roughly 10 minutes before they fall below 25 km. Aerobot - orbiter communication is available for roughly 46.44% of the mission duration, based on the communication window described in Chapter 5. This allows for roughly 2 hours of communication time per orbit. Including a 10 kbit/s telemetry and house keeping data rate from SMAD [47], a 25 kbit/s data rate would allow all data of the single orbit to be sent up in 53 minutes. This leaves room for possible commands to be sent up, for which SMAD gives an 8 kbit/s value [47], allowing a temporal compression factor of 5 with the 40 kbit/s link from the orbiter to the aerobot. Furthermore, the 2 hours leaves time to send two orbits worth of data, which is needed since one orbit every

<sup>3</sup><https://www.isispace.nl/product/s-band-patch-antenna/>

six orbits is only used for Earth downlink. In this case the total communication time would be 106 minutes. This 2-hour session also fits with the slew rates, explained in Chapter 12.

The transmission time of the orbiter is one orbit for every six orbits, roughly once every 24 hours. Based on the maximum 25 kbit/s link from the aerobot to the orbiter and the 40 kbit/s link of commands that can be prepared for the aerobot, a total amount of 5.62 Gbit of useful information can be generated in one day. Another 10 kbit/s telemetry and house keeping signal from the orbiter (instead of the aerobot) adds 0.86 Gbit. To this the data of a dropsonde of  $642.3 \cdot \frac{25}{1000} = 16.1$  Mbit is added. And the data of the 200 daily images is added, which equals 2.52 Gbit for 2000 1024x1024 images at a bit per pixel rate of 12.<sup>4</sup> Together this adds up to 9.7 Gbit. At the Ka-band data rate of 5 Mbit/s this takes roughly 35 minutes to send to the ground station. Each connection with the DSN requires a 1 hour set-up and tear-down cycle, which includes the tracking of the spacecraft [108]. Since the DSN can only be scheduled for an integer multiple of hours, this means 2 hours are required per cycle. This allows a 25% safety factor for possible issues. This orbiter will also send telemetry from the TRM back to Earth after the separation between the TRM and the orbiter, but before atmospheric insertion. The data is sent from the TRM to the orbiter using a low gain X-band antenna and is relayed with the high gain antenna of the orbiter. Finally, the beacon mode signal is sent continuously in order to be picked up at any time. A special DSN beacon mode session is scheduled every 2 orbits and takes 1 hour per session (40 minute set-up and tear-down), similar in frequency as other beacon mode signals in previous missions [108]. There is some flexibility in this schedule due to the continuous nature of the beacon mode signal.

### 9.3.6. Tracking design approach

The tracking system of this mission consists of three different active tracking methods: two-way ranging, Doppler tracking and VLBI. Each of them will be elaborated on, including how they are used in this mission and what accuracy they can attain. Besides these three active tracking methods, orbital models of the orbiter and the aerobot will also be used to predict the position of the mission elements and to greatly reduce the time of the other active tracking methods to converge [40].

Firstly, two-way ranging. This method is also the first method to be used from a temporal standpoint. With this method the distance and location of an object in space can be determined. This method will be used from Earth in order to locate the orbiter and from the orbiter in order to locate the aerobot. It works by measuring the time it takes for a signal to travel back and forth through the vacuum of space [109]. Combined with constant iterations of the antenna position and measurements of the antenna power, this method converges towards the location of the object to be found. This iterative technique is also the reason for the rotating vertical structure and gimballed antenna mentioned in Subsection 9.1.1. Due to the narrow beamwidth of the high gain antenna, the low gain antenna can be used to get a rough estimate of the aerobot's location if the high gain antenna loses track of it. The accuracy of the method can be greatly increased by performing it on two separate frequency bands. This can then be used to determine the impact the interstellar medium (plasma) has on the signal. While the Viking missions were able to get an accuracy of 200 m using dual S- and X-band, the Cassini mission was able to attain an accuracy of 7 cm using dual X- and Ka-band, even though this final method required significantly more power time to converge and will thus not be used on this mission [110] [111] [104]. However, even the error of the Viking mission is small enough from an angular standpoint that other mistakes in antenna pointing due to star sensors and the pointing hydraulics and mechanisms are multiple orders of magnitude larger, which means that at this stage of the design, no extra calculations for two-way ranging are required.

Once the position of the object has been determined and the communication starts, Doppler tracking is used to keep track of the movement of the object during transmission. Doppler tracking works by analysing the frequency shift caused by the relative speed of an object and the adjusted frequency can be calculated using  $f = (1 + \frac{\Delta V}{c}) \cdot f_0$  [40]. Since the frequency of the transmitted signals is known, this method can be inverted in order to determine the relative speed of the objects and thus the antenna can remain pointed correctly, constraining the direction of the velocity change using orbital models. Current Doppler tracking can give an accuracy of up to 0.02 mm/s [112], which also allows it to perform science measurements on the relative speed of objects. By performing simultaneous Doppler of the aerobot - dropsonde and the aerobot - orbiter with orbital models, the speed of the dropsonde with respect to the Venusian surface can be calculated, which is used for measurements of the wind speed at different altitudes.

<sup>4</sup>[http://pluto.jhuapl.edu/soc/lorri\\_about.html](http://pluto.jhuapl.edu/soc/lorri_about.html)

VLBI is the final active tracking method and uses multiple radio telescopes in order to increase its resolution to measure the time difference between the arrival of a signal across the telescopes. This way, a triangulation of the angular position can be made [113]. In order to determine the actual position, an estimate of the phase interference fringes is made [113]. The Vega missions were able to achieve an accuracy of 1 m/s in speed and the Event Horizon Telescope can achieve an accuracy of 25 microarcseconds, which is roughly 12 m at a distance of 100 million km. Since the previously described methods can achieve a sufficient accuracy and due to the low availability and high cost of VLBI, VLBI will not be used as the main tracking method, but will instead at infrequent times to calibrate the other position measurements and to perform a small number of aerobot velocity measurements. VLBI on the orbiter will be done using the science downlink signal and the aerobot has an extra X-band antenna made to transmit a signal for VLBI purposes. This mission will make use of the European VLBI Network (EVN) for these measurements [101].

### 9.3.7. Command and data handling design approach

The command and data handling design approach subsection is split up per mission element. To get a full overview of the command and data handling elements, the data handling diagram in Figure 9.2 can be used.

### 9.3.8. Dropsonde command and data handling

The sizing of the dropsonde on-board computer is based on the computer mass of similarly sized CubeSats. Due to the unique nature of their usage, this method was deemed most accurate at this design phase. To account for the uncertainty of this method an margin of  $2\sigma$  will be used. For this the ISIS OBC, CubeSat World - Basic OBC, CubeSat World - Advanced OBC, Hyperion CP400.85 and Endurosat OBC have been used <sup>5, 6, 7, 8, 9</sup>. This results in an average mass of 50 g with a standard deviation of 28 g and an average power of 0.650 W with a standard deviation of 0.250 W. With  $2\sigma$  margins, the decided upon on-board computer mass is 106 g and the power consumption is 1.15 W. This mass is almost equal to the ISIS OBC (94 g), which is why the data storage of the dropsonde is based on this OBC. This means that the OBC will have 2x2 GB data storage. Outside of the OBC no storage is present due to the short lifetime of the dropsonde.

### 9.3.9. Aerobot command and data handling

The aerobot has an OBC based on the Venus Flagship mission [15]; the MAC-100 computer, which weighs 3.2 kg, uses 7.22 W, has a data handling speed of 5 MIPS and has an internal clock with a maximum drift below  $10^{-9}$  s per day [114]. This OBC has been chosen due to the similarities between the two missions and the fact that it can process the 65 kbit/s combined aerobot data rate [15]. The OBC itself has 12 MBit of storage, but this is not enough to store all the required data. The aerobot storage has been designed to store all data it could receive over a period of 6 orbits of the orbiter, including the data of two dropsondes. This equals  $(15,485 \cdot 6 \cdot (20,000 + 40,000) + 25,000 \cdot 642.3 \cdot 2) / 10^9 = 6.07$  Gbit. This has been increased to 10 Gbit to add a significant safety factor for unexpected issues regarding storage. Using a statistical estimate for solid state recorders with an R-squared value of 0.8873, a storage mass of 3.4 kg has been calculated [40].

### 9.3.10. Orbiter command and data handling

The on-board computer has been sized based on statistical data of 0.7 kg/MIPS [40]. The 5 Mbit/s maximum data rate requires roughly 5 MIPS [56], resulting in an on-board computer mass of 3.5 kg. Due to the uncertainty of using statistical analysis, one standard deviation is added for power (3.3 W/kg + 2.7 W/kg SD), resulting in an estimate of 21 W. Due to the different connections coming together at one point, a data handling/acquisition unit will be used to guide the process. The sizing of this unit is based on the number of channels it needs to handle at the same time. Based on the correlation between data rates and channels in SMAD [47], a value of 200 channels is used. Using an average of 2.75 kg/100 channels [40], a data handling/acquisition unit of 5.5 kg is sized with a power of 9.62 W (1.75 W/kg). The data storage of the orbiter is sized in order to store all data received from the aerobot and generated by itself during the mission. This results in  $(20,000 \cdot 12.6 + (20,000 + 45,000) \cdot 86,400 \cdot 100) / 10^{12} = 0.813$  Tbit. For this, off-the-shelf, space-grade solid state recorders by Airbus will be used, called NEMO.<sup>10</sup> It can store 512 Gbit and thus two will be used.

<sup>5</sup><https://www.isispace.nl/product/on-board-computer/>

<sup>6</sup><https://hyperiontechnologies.nl/products/cp400-85-processing-platform/>

<sup>7</sup><https://cubesatworld.com/product/basic-obc-imu/>

<sup>8</sup><https://cubesatworld.com/product/advanced-obc/>

<sup>9</sup><https://www.endurosat.com/cubesat-store/cubesat-obc/onboard-computer-obc/>

<sup>10</sup><https://spaceequipment.airbusdefenceandspace.com/payload-products/payload-data-handling-with-memory/nemo/>

Together they weigh 13.2 kg and use 20 W of power.

### 9.3.11. TRM command and data handling

The on-board computer is sized in a similar manner as the orbiter's version, but only uses 2 MIPS and thus weighs 1.4 kg and uses 8.4 W [56]. While the data rate of the TRM is only 10 kbit/s, the preferred communication time is to be kept at a few hours in order to limit usage of the high power antenna on the orbiter. At the moment, this is estimated to be roughly 1% of the time during cruise after separation with the orbiter. This would result in a required processing speed of the computer of  $10\text{ kbps}/1\% = 1\text{ Mbit/s}$ . Due to the uncertainty of this value, a factor 2 safety factor is taken, resulting in 2 Mbit/s, roughly equalling 2 MIPS [56]. The storage of the TRM is sized using the same statics as the aerobot and is based on the fact that it should be able to store 10 kbit/s for a period of 20 days, which equals the period between separation with the orbiter and arrival at Venus, described in Chapter 5.

## 9.4. Risk analysis

Risks concerning TTC are identified to check that all high probability or impact risks are mitigated. The meaning of the 1 - 5 scales are discussed in Section 15.1.

- TTC1 **Failure of telemetry hardware:** The failure of a transceiver/transmitter/receiver would make it impossible for the antenna to function. Probability = 3, Severity = 4; **mitigation:** Having redundant components for every telemetry hardware component. New probability = 3, New severity = 1;
- TTC2 **Unavailability of the ground station:** If this is unavailable, data can not be sent. Probability = 3, Severity = 4; **mitigation:** Extra storage for the entire lifetime of the orbiter and separate tracking methods that use different ground stations (DSN and EVN). New probability = 3, New severity = 1;
- TTC3 **Mistakes in antenna pointing:** Wrongly pointed antennas could cause mission elements to not communicate properly. Probability = 2, Severity = 4; **mitigation:** Low gain antennas with large beamwidths and a specialised pointing system on the aerobot. New probability = 2, New severity = 2;
- TTC4 **Software bugs:** A software bug could prevent the system from operating properly. Probability = 2, Severity = 4; **mitigation:** The computer system can do a full reset and commands can be sent again from the ground station. New probability = 2, New severity = 2;
- TTC5 **Low SNR:** The SNR can be lower than expected. Probability = 2, Severity = 4; **mitigation:** Safety factors in transmission times make lower data rate transfer possible. New probability = 1, New severity = 3;
- TTC6 **Delay of telemetry data:** Due the lack of ground communication, important telemetry could be sent too late. Probability = 2, Severity = 4; **mitigation:** A beacon mode signal allows the ground station to know the mission health at all times. New probability = 1, New severity = 3;
- TTC7 **Unpredictable aerobot motion:** Due gusts and unexpected drift the aerobot could perhaps not communicate with the orbiter. Probability = 3, Severity = 4; **mitigation:** For unexpected movements caused by gusts, a rotating boom has been implemented and the LGA of the aerobot has a gimbal in order to remain pointed. Aerobot insertion at 20 degrees North latitude is performed, which ensures that any drift would be Northwards, which is beneficial and would only further increase the possible communication time. New probability = 2, New severity = 2;

## 9.5. Sensitivity analysis

It is important to make sure that the TTC design is stable. Therefore, this section will discuss the sensitivity of the design to changes based on uncertainties in different parts of the design and specific calculations. The change in the component mass estimates are not discussed in this section. Discussion on the techniques and safety factors used for these parameters can be found in Section 9.3.

For this section the impact of different parameters on the link budget are analysed. The most limiting SNR runs from the aerobot to Earth via the orbiter. The signal to noise ratios of 3.1 dB and 9.6 dB combine to 1.9 dB. This combination is done by calculating the percentage of the signal that consists of non-noise and then multiplying the values. For example, two signals with 80 and 70% non-noise would together have  $0.8 \cdot 0.7 = 56\%$  noise or a SNR of 1.05 dB. This method mimics the total SNR created by reconstructing the digital signal received on the orbiter to a new digital signal that is relayed to Earth. The 1.9 dB combination value leaves a 0.2 dB margin with the desired minimum 1.7 dB SNR. However, only 2 hours of transmission time is used every sixth orbit, while 4 hours are available. This means that, if an issue arises, the data rate

can be halved and still fulfil the requirements. In this case the SNR's combine to 5.0 dB (6.1 and 12.6 dB respectively). This means that the maximum errors in the sensitivity analysis can allow for an extra SNR reduction of  $5.0 - 1.7 = 3.3$  dB. The plot in Figure 9.3 shows the possible uncertainty in each of the parameters from the link budget. No margin in the transmit power is taken, since this uncertainty is implemented in the transmitter loss. For this, it is taken into account that the true transmitter and receiver losses can be as low as 0.6, instead of the average 0.7 value used [56]. The transmitter gain is calculated using an efficiency of 0.5 instead of the average 0.6 value [56]. For the free space loss, an uncertainty of 25% is used, which allows for a mission period of almost 200 days instead of 100. For the system noise temperature a slightly higher value of the Venusian surface temperature of 738 K is used to account for planetary variation [1] and the cable losses previously mentioned are also worked into this SNT calculation. It shows that the total uncertainty is roughly 3.3 dB and thus equals the allowed margin. This is no coincidence; in the original link budget iteration it was made sure that the budgets would also pass the sensitivity analysis.

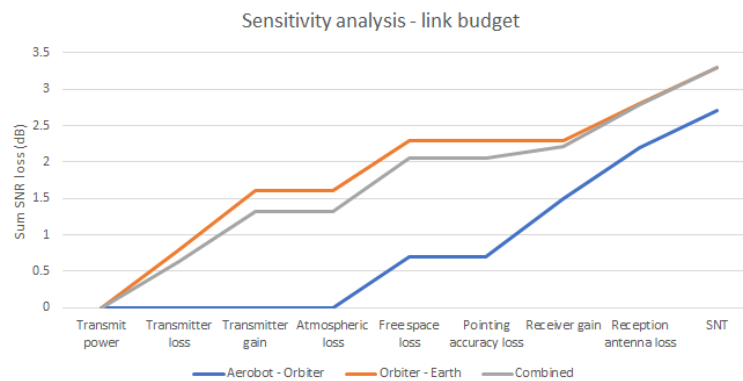


Figure 9.3: A cumulative sum of the extra link budget losses caused by margins in the sensitivity analysis, shown in dB for each individual connection and the two connections combined.

## 9.6. Verification and validation

Verification and validation of the TTC subsystem was performed to make sure that all calculations are correct. Firstly, all design decisions made have been checked and compared to similar missions. The frequency absorption bands have been verified based on radio occultation of Venus, which deemed X- and Ka-band infeasible within the lower atmosphere [105].

**Code verification and validation** Secondly, all models and code used during the TTC design have been verified. The code that calculated the link budgets has been validated by inputting the parameters of the Cassini and Venus Flagship missions [15, 104]. These projects have extensive link budgets available and it was shown that the python program used for this mission results in the same values down to a machine error number of significant digits. The communication window code also impacts TTC, but is explained and verified in Chapter 5.

**Requirement verification** Thirdly all requirements are verified. The verification of most requirements is based on similarity. While new techniques are used, most techniques are based on similar missions and mission plans, such as Akatsuki, Venus Flagship and Cassini [15, 104, 107]. Many of the components that are sized based on statistical estimates, use appropriate safety factors, usually related to the standard deviation of the estimation. When possible, off-the-shelf space grade components are used to as verification.

Table 9.2: Requirements on telemetry, tracking and command

Identifier	Requirement	Compliance	Explanation in
TTC-01-A	The mission elements be able to encode communications to the LDPC and precoded GMSK format.	✓	9.3.3
TTC-01-B	The mission elements be able to decode communications from the LDPC and precoded GMSK format.	✓	9.3.3
TTC-02	The mission elements shall be able to detect bit errors with a probability of $10^{-5}$ .	✓	9.3.3
TTC-03-A	The mission elements shall be able to send communication if one transmitter fails.	✓	9.3.4
TTC-03-B	The mission elements shall be able to receive communication if one receiver fails.	✓	9.3.4
TTC-SP-01	The pointing accuracy of the main antenna to Earth shall be at a minimum 0.03 rad.	✓	9.3.3
TTC-SP-02	The link budgets shall be at least 1.7 dB for downlink and 9.6 dB for uplink.	✓*	9.3.3
TTC-SP-02-A	The spacecraft shall be able to send downlink communications at a bit rate of 5 Mbit/s.	✓	9.3.3
TTC-SP-02-B	The spacecraft shall be able to receive uplink communications at a bit rate of 5 Mbit/s.	✓	9.3.3
TTC-SP-02-C	The spacecraft shall be able to send communications in the frequency range of S-, X- and Ka-band.	✓	9.3.2
TTC-SP-02-D	The spacecraft shall be able to receive communications in the frequency range of S-, X- and Ka-band.	✓	9.3.2
TTC-SP-03	The spacecraft shall be able to store at least 1024 Gbit of data.	✓	9.3.9
TTC-SP-06-A	The spacecraft shall be able to receive commands from the ground segment.	✓	9.3.7
TTC-SP-07	The internal clock of the system shall be precise to $10^{-9}$ seconds of drift per day.	✓	9.3.10
TTC-SP-08-A	The position tracking accuracy of the space segment shall be at minimum 1000 km.	✓	9.3.6
TTC-AT-01	The pointing accuracy of the low gain atmospheric probe antenna shall be 50 degrees.	✓	9.3.3
TTC-AT-02	The link budgets shall be at least 1.7 dB for downlink and 9.6 dB for uplink.	✓*	9.3.3
TTC-AT-02-A	The atmospheric probe shall be able to send communications at a bit rate of at least 25 kbit/s.	✓	9.3.3
TTC-AT-02-B	The atmospheric probe shall be able to receive communications at a bit rate of at least 40 kbit/s.	✓	9.3.3
TTC-AT-02-C	The atmospheric probe shall be able to send communications in the frequency range of S-band.	✓	9.3.2
TTC-AT-02-D	The atmospheric probe shall be able to receive communications in the frequency range of S-band.	✓	9.3.2
TTC-AT-03	The atmospheric probe shall be able to store at least 10 Gbit of data.	✓	9.3.10
TTC-AT-07-A	The position tracking accuracy of the atmospheric segment shall be at minimum 20 km.	✓	9.3.6
TTC-AT-07-B	The velocity tracking accuracy of the atmospheric segment shall be at minimum 1 m/s.	✓	9.3.6
TTC-AT-08-D	The tracking transmitter power of each element shall be 12 W.	✓*	9.3.3
TTC-AT-10	The atmospheric probe shall be above 19.5 degrees latitude.	✓	5.5.2

# 10 Electrical Power Supply

During the entirety of the mission, all instruments and equipment require some level of electrical power to operate at the desired levels. It is the responsibility of the electrical power supply that this power is provided at the right times and in the right form. Its design is detailed in the following chapter. First, Section 10.1 provides an overview of the overall system design, followed by an analysis of the functionality necessary for a requirements-compliant power system in Section 10.2. The design approach is presented in Section 10.3, risks are detailed in Section 10.4, and the design sensitivity to parameter changes is found in Section 10.5. Finally, the approach to verification and validation is shown in Section 10.6.

## 10.1. Design overview

The description and design of the power system is split into the power management and distribution architecture, solar panel design, battery design, and approach to sustainability. A summary of system properties can be found in Table 10.1. Power consumptions and time fractions per subsystem and operational phase are listed in Table 10.2.

### 10.1.1. Power management and distribution

Four out of five segments operate on a fully regulated 28 V bus, mainly to isolate sensitive equipment from voltage swings due to solar cell output variation. An additional consideration here is system interoperability: the aerobot, aeroshell, and TRM power systems are connected for most of their operational lifetimes. The odd one out is the dropsonde: due to the mass constraints, it is not possible to fully regulate the voltage delivered by the battery.

### 10.1.2. Solar array

The aerobot, TRM, and orbiter use photovoltaic cells to generate power, since their long mission lifetime and high power consumption prohibit the use of primary batteries. Because of the long eclipse time, use of a radioisotope power source was investigated for the aerobot, but durability concerns outweighed the limited mass benefits compared to a photovoltaic system. Only if the aerobot power consumption were to increase considerably, photovoltaic power could become unfeasibly heavy, necessitating the use of radioisotope power. Lacking attitude determination, the aerobot has static solar panels on all sides, though this does increase the required solar cell area. Thermal control requires that the TRM and orbiter have wing-mounted solar panels.

### 10.1.3. Batteries

The design principles of the primary batteries for the dropsonde and aeroshell are similar, although the different time and power scales make for significantly different results. The dropsonde battery currently consists of two parallel batteries, but it was found that a power consumption reduction of 5% could reduce this to only a single battery. The secondary batteries design is also similar, but it can be clearly seen that the higher cycle life of the orbiter affects its mass efficiency significantly. Improvements could potentially be made here with usage of high-energy batteries at lower depths of discharge.

### 10.1.4. Approach to sustainability

Sustainability played an important role in the power system design: it was the deciding factor in the choice to provide the aerobot with a photovoltaic system instead of a radioisotope thermal generator, which would have been more mass-efficient and reliable otherwise. All other segments also utilise either photovoltaic power or primary batteries, making the power system relatively durable. Still, it was not possible to design a fully renewable and sustainable power system: lithium had to be used in the batteries. Furthermore, a limited amount of rare-Earth materials was used for power management, as in most electrical circuitry.

## 10.2. Functional analysis

The function of the power system is to supply all equipment with the required operational power. This can be divided into three subtasks: generation, storage, and management and distribution. While interdependent, these functions drive the design in different ways, so they will be treated separately.

Table 10.1: Design summary of the power system for each segment

Segment	Element	Specifics	Mass (kg)
Aerobot	Architecture	Fully regulated 28 V bus with MPPT	
	Management	Power conditioning and distribution unit	9.2
	Solar array	2.7 m <sup>2</sup> AZUR SPACE 4G32C (12s75p)	9.5
	Secondary battery	LG Chem INR18650 MJ1 (7s33p)	15.8
TRM	Architecture	Fully regulated 28 V bus with MPPT	
	Management	Power conditioning and distribution unit	11.7
	Solar array	2.4 m <sup>2</sup> AZUR SPACE 4G32C (13s30p)	11.6
	Secondary battery	LG Chem INR18650 HG2 (7s7p)	3.3
Orbiter	Architecture	Fully regulated 28 V bus with MPPT	
	Management	Power conditioning and distribution unit	13.3
	Solar array	2.4 m <sup>2</sup> AZUR SPACE 4G32C (13s31p)	12.5
	Secondary battery	Saft VL51ES (5s2p)	15.1
Dropsonde	Architecture	Unregulated bus	
	Primary battery	Saft LO 35 SX (1s1p)	0.04
Aeroshell	Architecture	Fully regulated 28 V bus	
	Primary battery	EaglePicher LCF-134 (11s19p)	7.3

Table 10.2: Power consumption profile of the operational segments. Further breakdown of each subsystem's power consumption can be found in Section 16.4.

Consumption (W)	Cruise	Operations	Comms.	Slew	Burn	VLBI	Dropping	Science
Orbiter	554.5	587.1	711.2	690.8	714.1			
TRM	538.8	538.8	571.4	642.5	698.7			
Aerobot	30.4	39.9	57.7			43.1	50.3	143.3
Aeroshell	102.0							
Dropsonde							4.4	
Fraction of operational time (-)								
Orbiter								
Cruise	1.00	0.00	0.00	0.00	0.00			
Burn	0.00	0.00	0.00	0.00	1.00			
Orbit, eclipse	0.00	0.13	0.87	0.00	0.00			
Orbit, sunlight	0.00	0.48	0.37	0.14	0.00			
TRM								
Cruise	1.00	0.00	0.00		0.00			
Burn	0.00	0.00	0.00		1.00			
Orbit, eclipse	0.00	1.00	0.00		0.00			
Orbit, sunlight	0.00	0.24	0.76		0.00			
Aerobot								
Cruise	1.00	0.00	0.00			0.00	0.00	0.00
Loiter, eclipse	0.00	0.70	0.20			0.01	0.00	0.08
Loiter, sunlight	0.00	0.35	0.20			0.00	0.02	0.25

Power generation has the requirement that it should be of sufficient magnitude to allow all power consumptions to be fulfilled. However, it can significantly drive the design, as the choice of the power source can affect the functional requirements on the storage and management and distribution.

The energy storage functionality flows from the power generation concept chosen: if power cannot be generated at all times, energy storage should be sufficiently large to allow for power delivery over the duration generation is not possible. This includes eclipse periods for photovoltaic systems, or the pre-operational phase for primary battery systems.

Finally, power management and distribution is considered. Functionally, this can be further split into two aspects: power management, referring to power conditioning and battery charge and discharge control, and power distribution, referring to load protection, connection, and switching. Although functionally separate, these tasks are practically less distinct and are hence considered as one design aspect.

Based on these three functions, the top-level requirements on the power system flow into a set of subsystem requirements. These are listed in Table 10.3, together with an indication of compliance and a reference to the relevant section where the requirement is treated.

### 10.3. Design approach

The design of the power system of this mission can be divided in three components: the solar array, batteries, and the power management and distribution elements. The approach to design of each part is similar across all segments and will generally not be treated distinctly, unless necessary.

#### 10.3.1. Power management and distribution

The power system is not only responsible for generation and storage of energy, it must also regulate and distribute this energy according to spacecraft needs. Two basic architectures can be distinguished within the power system design: photovoltaic (PV) systems and primary battery-driven systems. Since the design rationale behind each architecture differs slightly, the specifics of each will first be discussed, followed by a more general treatment of the resulting load path efficiencies and power management architectures.

First, the aerobot architecture is considered; a block diagram is shown in Figure 10.1 and loads are listed in Table 10.4. The aeroshell is connected as if it were a power supply, as it provides the connection to the TRM during cruise, and provides power with its primary battery before entry. Heaters do not list a voltage, as they are assumed to operate at any voltage. To be able to interconnect with the aeroshell and the TRM, a 28 V fully regulated bus architecture was chosen.

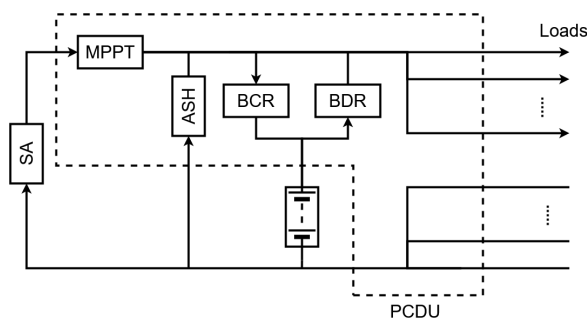


Figure 10.1: Block diagram of the aerobot power architecture.

Equipment	Power (W)	Voltage (V)
Mass spectrometer	65.0	28
Seismometers	1.0	11±5
MET	4.4	10
On-board computer	7.2	29±7
Solid state recorder	1.0	29±7
Antenna	12.0	28
VLBI antenna	2.0	10
Heaters	5.0	-

Table 10.4: Aerobot loads.

The TRM is a more typical PV system, whose architecture is shown in Figure 10.2 and Table 10.5. Because of the big difference in solar flux over its lifetime, big voltage swings are expected in the output. As such, the choice was made for a fully regulated bus with maximum power point tracking, since not all instruments support big voltage swings. Additionally, it improves the efficiency of the solar array at non-optimal conditions. Since only the motor valve and solar array drive mechanism are unable to operate at 28 V, the power loss incurred by a regulated bus is small. Note that the aeroshell is connected as a load for the TRM.

The orbiter is electrically independent of other segments. Similar to the TRM, it is affected by the big difference in solar flux between Earth and Venus, such that the choice was again made for a maximum power point tracking regulated bus, as shown in Figure 10.3. This incurs a very low power loss overhead, since nearly all equipment can be operated at the regulated 28 V, as seen in Table 10.6. Notable exception is

Table 10.3: Requirements on the power system.

Identifier	Requirement	Compliance	Explanation in
EPS-01	The power cabling shall be protected from thermal and mechanical stresses.	✓	10.3.1
EPS-02	The power system shall be able to generate sufficient power to provide all loads with the required power levels.	✓	10.3.2
EPS-03	The power management and distribution system shall be able to supply each load with the current and voltage it needs.	✓	10.3.1
EPS-03-A	The power distribution system shall be able to convert electric currents from bus voltage to load voltage, if they do not match.	✓	10.3.1
EPS-03-B	The power management system shall be able to deliver variable power levels to equipment, depending on their individual operational modes.	✓	10.3.1
EPS-SP-01	The power system shall be able to sustain expected periods without power generation.	✓	10.3.3
EPS-SP-01-A	The orbiter power system shall be able to store sufficient power to survive 41 minutes of eclipse and 6 minutes of aerobraking per orbit.	✓	10.3.3
EPS-SP-01-B	The TRM power system shall be able to store sufficient power to survive 41 minutes of eclipse per orbit.	✓	10.3.3
EPS-SP-02	The power system shall be able to sustain the expected lifetime number of charge-discharge cycles.	✓	10.3.3
EPS-SP-02-A	The orbiter power system shall have at least 80% energy capacity after 1600 orbits.	✓	10.3.3
EPS-SP-02-B	The TRM power system shall have at least 80% energy capacity after 50 orbits.	✓	10.3.3
EPS-SP-03	The power system shall generate sufficient power over the entire mission lifetime.	✓	10.3.2
EPS-SP-03-A	The TRM shall be able to support all required electrical loads after 595 days of operation.	✓	10.3.2
EPS-SP-03-B	The orbiter shall be able to support all required electrical loads after 695 days of operation.	✓	10.3.2
EPS-AT-01	The power system shall be able to sustain expected periods without power generation.	✓	10.3.3
EPS-AT-01-A	The aeroshell shall be able to support operational electrical loads for 24 hours.	✓	10.3.3
EPS-AT-01-B	The aerobot shall be able to store sufficient power to operate for 72 hours of eclipse every 120 days.	✓	10.3.3
EPS-AT-02	The power system shall be able to sustain the expected lifetime number of charge-discharge cycles.	✓	10.3.3
EPS-AT-02-A	The aerobot shall have at least 80% energy capacity after 100 days.	✓	10.3.3
EPS-AT-03	The power system shall generate sufficient power over the entire mission lifetime.	✓	10.3.2
EPS-AT-03-A	The aerobot shall be able to support all required electrical loads after 695 days of operation.	✓	10.3.2
EPS-AT-03-B	The dropsonde shall be able to support all required electrical loads after 695 days of storage.	✓	10.3.2

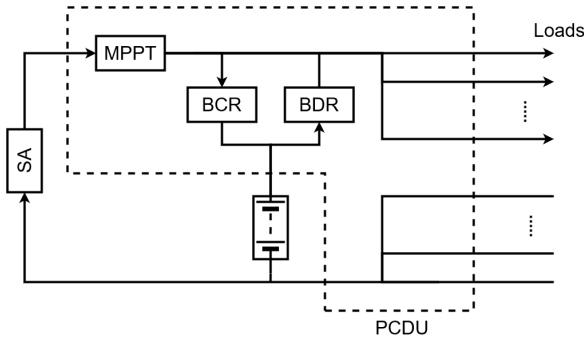


Figure 10.2: Block diagram of the TRM power architecture.

Equipment	Power (W)	Voltage (V)
Spectrometer	23.3	28
Motor valve	7.9 - 35.0	24±3
On-board computer	21.0	29±7
Data storage	20.0	29±7
Data processor	9.6	29±7
High-gain antenna	100.0	60
Low-gain antenna	22.0	28
Reaction wheels	76.0 - 320.0	28
Star sensors	16.0	28
Heaters	160.0	-
SA drive mechanism	3.2	32
Camera	12.0	28

Table 10.5: TRM loads.

the high-gain antenna, which operates at a higher voltage of 60 V, such that its regulator losses are relatively high. Still, it is expected that the increased efficiency of the solar arrays outweighs this performance penalty.

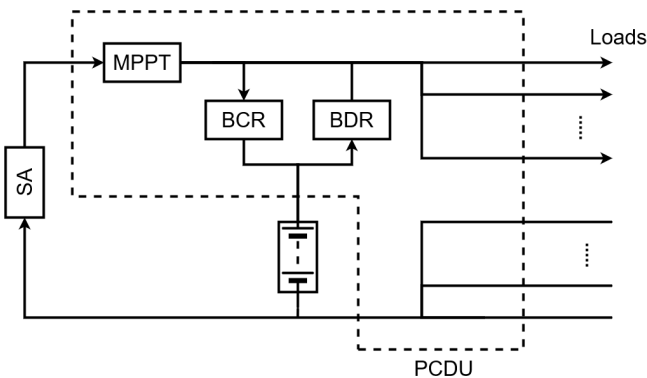


Figure 10.3: Block diagram of the orbiter power architecture.

Equipment	Power (W)	Voltage (V)
Spectrometer	23.3	28
Motor valve	7.9 - 35.0	24±3
On-board computer	21.0	29±7
Data storage	20.0	29±7
Data processor	9.6	29±7
High-gain antenna	100.0	60
Low-gain antenna	22.0	28
Reaction wheels	76.0 - 320.0	28
Star sensors	16.0	28
Heaters	160.0	-
SA drive mechanism	3.2	32
Camera	12.0	28

Table 10.6: Orbiter loads.

The power management and distribution design of the dropsonde is relatively straightforward, as can be seen from Figure 10.4 and Figure 10.7. It consists only of a primary battery switched in series with nearly fully parallel-connected loads. No separate power conditioning or distribution units (PCDU) are present; these are too heavy for the lightweight dropsonde. Loads are operated at 3.0 V using a regulator, which is close to the battery discharge voltage of 2.8 V. The antenna is connected separately, as it requires 7.0 V.

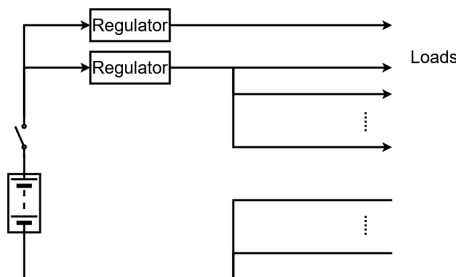


Figure 10.4: Block diagram of the dropsonde power architecture.

Equipment	Power (mW)	Voltage (V)
Processor	1100	3.0
Antenna	2000	7.0
Accelerometer	35	3.0
Thermometer	2	3.0
Barometers	5	3.0
DROPP	35	3.0

Table 10.7: Dropsonde loads.

The aeroshell system is connected with the aerobot and TRM power system: the aerobot is connected as a load and the TRM as a power source. This is also the reason for the aeroshell bus voltage choice, chosen to

be 28 V to match the TRM. Some load switching and regulation during operation is expected. The aeroshell does not include its own PCDU, but uses that of the aerobot. This does not incur too much cabling overhead, since a significant part of the load paths need to go through the aerobot.

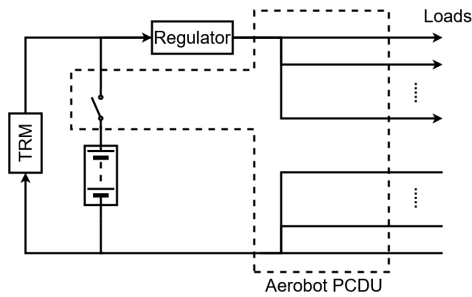


Figure 10.5: Block diagram of the aeroshell power architecture.

Equipment	Power (W)	Voltage (V)
Aerobot support	30.4	28
Barometers	0.005	3.0
Aerobot heater	50.0	-
Pyrotechnical connections	-	-

Table 10.8: Aeroshell loads.

The three PV systems all require PCDUs since battery charge/discharge control is needed for eclipses. Additionally, the PCDU provides fault protection and isolation, such that electrical failures are less likely and do not affect other equipment; this is necessary to achieve high reliability. The Terma Modular Medium Power Unit [115] is used, as its modularity allows usage in all three PV systems. Because of the critical role fulfilled by the PCDU, the number of modules is sized to support single point failure free operations. The resulting number and type of modules for each PCDU can be found in Table 10.9. Noted should be that the aerobot could benefit from a smaller PCDU: its mass and power consumption are not in proportion to the power controlled. Use of a smaller PCDU could be considered in further design.

Table 10.9: Number of modules and resulting PCDU properties for the different systems.

Module	ABT	TRM	ORB	Note
Equipment power distribution	2	2	2	2 per 900 W distributed power
TM/TC interface	1	1	1	1 per system (internally redundant)
Battery C/D regulation	2	4	6	2 per 300 W discharge power
Heater power distribution	2	2	2	2 per 400 W heater power
Array power regulation	3	6	6	3 per 500 W array power
Pyro firing drive	2	0	0	2 per pyrotechnical system
Width (m)	0.235	0.235	0.235	
Height (m)	0.156	0.156	0.156	
Length (m)	0.304	0.379	0.429	
Mass (kg)	9.2	11.7	13.3	

Another significant portion of power-related mass is the cabling, which can be relatively heavy, since insulation is required against the high temperatures and radiation. On the other hand, exact determination of the mass can be difficult until late in the design, due to the high dependency on component lay-out. As such, its mass is derived from previous spacecraft to be 6.8% of the dry mass [116]. This includes power cabling and data cabling. Unfortunately, it does not leave sufficient room in the mass budget for an additional fully-redundant harness. The cabling mass is not included in the power system mass, but is listed separately on the subsystem level. Because of the low current (>50 mA) required by the barometer, cabling through the 50 m long tether is very light-weight with an estimated mass of under 0.01 kg/m [117]. As such, tether cabling mass is considered within the margins supported by the 6.8% figure and will be neglected. Because of the small amount of electrical connections and low current at which they operate, the total aeroshell cabling mass is also bounded at 1 kg, which would allow for up to 50 m of cabling [117].

Naturally, there are some power losses associated with transmission of power from the source to the load. For sizing of the solar array and batteries, it is important that these path efficiencies are determined. To determine these, the individual inefficiencies of different electrical components are considered. Cable power transmission efficiency is taken to be  $\eta_{\text{cable}} = 0.98$ , based on [116]. For the Terma Modular Medium

Table 10.10: Properties of considered solar cells, under lab conditions. Exact testing conditions differ depending on solar cell model, but all are around  $1367 \text{ W/m}^2$  at  $25^\circ\text{C}$ . Data obtained directly from manufacturer data sheets.

Solar cell		Efficiency (%)	Voltage (mV)	Gradient (mV/K)	Current (mA)	Gradient (mA/K)
Spectrolab XTE-SF	BOL	31.7	2435.0	-6.3	480.6	0.2
	EOL	27.3	2118.5	-6.8	475.8	0.3
AZUR SPACE 3G30C	BOL	29.5	2411.0	-6.7	504.4	0.2
	EOL	26.5	2246.0	-7.2	486.6	0.3
AZUR SPACE 4G32C	BOL	31.8	3025.0	-8.6	433.5	0.0
	EOL	28.7	2793.0	-9.8	423.8	0.5
CESI CTJ30	BOL	29.1	2320.0	-6.0	455.0	0.3
	EOL	24.7	2157.6	-6.0	414.1	0.5

Power Unit, obtained is that  $\eta_{\text{MPPT}} = 0.95$ ,  $\eta_{\text{BCR}} = 0.96$ , and  $\eta_{\text{BDR}} = 0.94$  for the array conditioning, battery charge regulation, and battery discharge regulation, respectively. The battery itself also has a power loss associated with its charging and discharging, at about  $\eta_{\text{bat}} = 0.98$  [117]. Generic voltage regulators, either buck or boost, are taken to have a slightly lower efficiency of  $\eta_{\text{reg}} = 0.90$  [118]. All these path losses are included as part of the power subsystem entry in the power budget, Table 10.2. Path losses differ between eclipse and sunlight: listed are the eclipse losses, which are highest.

### 10.3.2. Solar array

The orbiter, TRM, and aerobot operate for significant amounts of time, which eliminates batteries as a primary power source. Instead, they will be powered with solar arrays: these are lightweight, durable, sustainable, and cost-effective. Radioisotope power was also considered for the aerobot, since its eclipse periods can last up to 3 days, but this option was discarded. The mass benefits of a radioisotope system were expected to be small compared to the significant durability penalty.

Five different commercial-off-the-shelf solar cells were considered, one each from Spectrolab and CESI, and three from AZUR SPACE. All five are space-qualified and have some degree of flight heritage. Performance data acquired from manufacturer datasheets is presented in Table 10.10. The given temperature gradients are not expected to be valid over all temperatures; no manufacturers report any ranges on their data sheets, however. For now, it is assumed that temperatures will remain within the bounds of validity.

End-of-life performance was estimated for an equivalent  $1 \text{ MeV}$  electron fluence of  $1e15$  electrons per  $\text{cm}^2$ , based on ESA's SPENVIS model [119]. The mission is modelled as two segments: a 20-day parking orbit around Earth followed by a two-year stay in solar orbit. Rather arbitrarily, a 300 km by 40000 km parking orbit is used. The solar orbit is placed at 0.72 AU from the sun, representing both the transfer to Venus and orbit around it, assuming the weak Venusian magnetosphere does not block protons. Modelled are trapped electron and proton fluxes according to AP-8 and AE-8 for solar minima and maxima, respectively, and total solar particle mission fluences according to ESP-PSYCHIC with a 99.9% confidence level over the full ion range. Assumed is  $100 \mu\text{m}$  CMX coverglass; as shown later, this is applicable for the used panels.

The optimal solar cell is taken to be the one with the highest end-of-life efficiency at operational temperatures. Although mass optimisation is the goal, the mass of the solar cells themselves is likely to be small compared to the substrate that must support it. A higher efficiency will therefore improve system-wide mass more than a reduced solar cell mass. The choice for a cell is first made with an arbitrary estimate of operational temperatures. This choice is validated and, if necessary, adjusted using the temperature found for the resulting solar panels. For all three photovoltaic systems, the 4G32C turns out to be optimal.

The solar cells are assumed to operate at their maximum power points. It is also assumed that current increases proportionally with incident sunlight, and that voltage increases with its logarithm [118]. Besides that, it is assumed only temperature influences the solar cell performance. The received sunlight  $J$  is affected by the incidence angle  $\theta$  and atmospheric losses as

$$J = J_{\text{solar}} \eta_{\text{atm}} \cos \theta, \quad (10.1)$$

where  $\eta_{\text{atm}} = 1.0$  in space, and  $\eta_{\text{atm}} = 0.6$  near the Venusian equator [120]. To take into account the longer path length for light, atmospheric losses are estimated as  $\eta_{\text{atm}} = 0.4$  near the poles, for lack of better data.

Table 10.11: Solar cell design conditions. Temperatures are the cell temperatures, obtained as described in Section 11.3.

Segment	Situation	Irradiance (W/m <sup>2</sup> )	Temperature (K)	Fluence (1 MeV e <sup>-</sup> /cm <sup>2</sup> )
Orbiter	Earth cruise	1367	292	0
	Venus orbit	2620	353	1e15
TRM	Earth cruise	1367	292	0
	Venus orbit	2620	353	1e15
Aerobot	Venus pole	1048	298	1e15

The incidence angle  $\theta$  is bounded as  $5^\circ$  for pointed systems [116], and is approximated as  $45^\circ$  for the aerobot body-mounted panels near the poles. The incident solar irradiance  $J_{\text{solar}}$  is given in Table 10.11 for different operational conditions. Based on this, the maximum power point voltage and current of a single cell become

$$V_{\text{mp}}(T) = \frac{\ln J}{\ln J_0} \left( V_{\text{mp},0} + \frac{dV_{\text{mp}}}{dT} (T - T_0) \right) \quad (10.2) \quad \text{and} \quad I_{\text{mp}}(T, J) = \frac{J}{J_0} \left( I_{\text{mp},0} + \frac{dI_{\text{mp}}}{dT} (T - T_0) \right), \quad (10.3)$$

where subscript 0 indicates lab conditions and subscript mp denotes values at the maximum power point of the solar cell. Note that different values for the current and voltage exist for beginning and end-of-life, because of degradation phenomena affecting electrical characteristics.

Besides degradation from radiation, there are also array-level degradation sources, such as cover glass ( $\eta_{\text{cg}} = 0.99$ ), cell mismatch ( $\eta_{\text{cm}} = 0.99$ ), parameter calibration ( $\eta_{\text{pc}} = 0.97$ ), and UV cover glass darkening and micrometeorite impacts ( $\eta_{\text{UV,mm}} = 0.9975$  per year) [118]. Additionally, a shadowing factor  $\eta_{\text{sh}} = 0.25$  is included for the aerobot, as up to 75% of its solar cells is shadowed from sunlight at any point in time [117]. These factors make for an average power generation per cell of

$$P_c(T, J) = I_{\text{mp}}(T, J) V_{\text{mp}}(T) \eta_{\text{cg}} \eta_{\text{cm}} \eta_{\text{pc}} \eta_{\text{sh}} \eta_{\text{UV,mm}}^L, \quad (10.4)$$

where  $L$  is the time in years during which the solar cells have been exposed to UV and micrometeorites at end-of-life. Since the aerobot is always protected by the aeroshell or Venusian atmosphere, it has  $L = 0$ ; for the other systems,  $L$  equals the operational lifetime.

The solar panel string length is determined by the bus voltage: the ratio depends on the choice for buck or boost MPPT regulation. In the current design, both would differ little besides a small efficiency difference at 92% for buck and 91% for boost regulation [118]. As such, buck regulation is chosen, requiring a solar cell string voltage that is at least 10% higher than the bus voltage [118]. The string length becomes

$$n_s = \left\lceil 1.1 \frac{V_{\text{bus}}}{V_{\text{mp}}(T)} \right\rceil, \quad (10.5)$$

where  $\lceil x \rceil$  denotes rounding up. The cell voltage should be the lowest value expected in operational conditions. For the aerobot, this is end-of-life near the poles. For the orbiter and TRM, this can be the voltage at beginning-of-life near Earth and at end-of-life near Venus, depending on cell characteristics.

While the number of cells in series fulfils the voltage requirement, the number of parallel strings is used to comply with power generation requirements. For operational modes in full sunlight, the power required is straightforwardly determined as the sum of the individual loads divided by their electrical path efficiencies. When eclipses are to be considered, the power generation required increases to

$$P_{\text{req}} = \frac{\sum_e \frac{P_e t_e}{\eta_e} + \sum_s \frac{P_s t_s}{\eta_s}}{\sum_s t_s} \quad (10.6)$$

where  $P$  is the power,  $\eta$  the electrical path efficiency from array to load associated with a certain operational mode. The time spent in eclipse is indicated as  $t_e$ , and the time in sunlight as  $t_s$ . Subscript  $e$  denotes eclipse, and  $s$  sunlight. The orbiter and TRM have similar and predictable eclipse times of about 40 minutes, with the orbiter also experiencing "eclipse" for about 6 minutes during each aerobraking pass. The aerobot has an eclipse time of about three days, as estimated in Subsection 7.3.1. Due to the stochastic nature of the wind, the aerobot is sized to generate sufficient power in just two days, and allows for partial shutdown of

equipment. This allows balloon survival if nighttime lasts longer or daytime lasts shorter than expected. With the power required known, the number of strings in parallel can be determined to be

$$n_p = \left\lceil \frac{P_{\text{req}}}{n_s P_c(T, J)} \right\rceil. \quad (10.7)$$

Since this number differs depending on power required, operating temperature and incident solar irradiance, the maximum over all expected operational conditions must be taken.

With its configuration known, the solar array mass can be estimated by dividing it in three components:

$$m_{\text{SA}} = m_{\text{SA}, c} + m_{\text{SA}, \text{OSR}} + m_{\text{SA}, \text{sub}} \quad (10.8)$$

where  $m_{\text{SA}, c}$  is solar cell mass,  $m_{\text{SA}, \text{OSR}}$  is optical solar reflector (OSR) mass, and  $m_{\text{SA}, \text{sub}}$  is substrate mass. These masses will be calculated in the rest of this section. Explicitly not included are the masses of the solar array drive mechanism and yoke: these are counted as part of the structures and mechanisms mass.

First, the contribution of the solar cells is considered, consisting mainly of the cell mass itself, or 1780 mg per cell for the AZUR SPACE 4G32C. Besides that, each cell has an external diode to prevent back-current damage, and is covered with cover glass to protect against radiation. As they are known to be compatible with the 4G32C, the AZUR SPACE silicon by-pass diode and Qioptic CMX 100  $\mu\text{m}$  type cover glass are used. They weigh 30 mg per unit and 0.26 kg/m<sup>2</sup>, respectively [121, 122]. Alternatives could be considered in detailed design, but are not expected to perform too differently. This makes for a solar-cell related mass of

$$m_{\text{SA}, c} = n_s n_p (m_c + m_d) + A_{\text{SA}} \rho_{\text{cg}}, \quad (10.9)$$

where  $m_d$  is the mass of a bypass diode,  $A_{\text{SA}}$  the solar array area, and  $\rho_{\text{cg}}$  the cover glass area density.

To achieve low temperatures even at the high solar irradiance near Venus, the backside and part of the front of the solar panels is covered with optical solar reflectors. Covering half the front results in favourable temperatures; determination of a better-performing fraction is left for future design stages. Qioptic CMX solar reflectors are used; a more detailed trade-off could be executed in later design. A thickness of 210  $\mu\text{m}$  is chosen, which equals the solar cell thickness, to prevent radiation from hitting cells from the sides. The area density becomes 0.55 kg/m<sup>2</sup> [123], such that an optical solar reflector mass of

$$m_{\text{SA}, \text{OSR}} = \frac{A_{\text{SA}}}{2} (\rho_{\text{cg}} + 3\rho_{\text{OSR}}) \quad (10.10)$$

is obtained, where  $\rho_{\text{OSR}}$  is the area-specific density of the reflectors.

The solar array area is calculated directly from the number and area of solar cells required, according to

$$A_{\text{SA}} = n_s n_p \frac{A_c}{\eta_{\text{ff}}}, \quad (10.11)$$

with  $\eta_{\text{ff}}$  the fill factor, as an array cannot be perfectly covered with solar cells. For the aerobot array, this is estimated as 0.88 [116]. For the arrays with OSRs, it is approximately 0.50, as only half is covered in cells.

From the area, the structural mass of the substrate can be determined. It is sized such that the natural frequencies do not exceed 1 Hz during spacecraft burns [118]. It is expected that launch loads are not limiting, since the panels are clamped in launch configuration. The same type of honeycomb panel is used as for the spacecraft structure, with aluminium 5083-H321 face sheets and A3003-H19 for the core. The reader is referred to Subsection 13.3.1 for justification, details, and material properties. Optimising for stiffness, a core height to face thickness ratio of  $h_c = 4t_f$  is chosen [124]. The natural frequencies become

$$f_{n, \text{lateral}} = 0.560 \sqrt{\frac{EI}{m_{\text{SA}} L^3}} \quad (10.12) \quad \text{and} \quad f_{n, \text{axial}} = 0.250 \sqrt{\frac{AE}{m_{\text{SA}} L}}, \quad (10.13)$$

where  $L$  is the length of a single solar panel,  $E = \frac{2}{\sqrt{76}} E_{\text{A5083-H321}}$  the panel stiffness,  $I = \frac{38}{3} t_f^3 b$  the panel's moment of inertia, and  $A$  the solar panel cross-sectional area [40, 125]. Face sheet thicknesses achieving lateral natural frequencies above 1 Hz were found numerically to be 0.77, 0.60, and 0.48 mm for the orbiter,

TRM, and aerobot, respectively. With these thicknesses, all sheets achieve axial natural frequencies above 1 Hz. The resulting solar array substrate mass becomes

$$m_{SA, sub} = A_{SA} t_f (4\rho_{A5083-H321} + 2\rho_{A3003-H19}), \quad (10.14)$$

finishing the solar array component sizing. The resulting solar panel properties are shown in Table 10.12.

Table 10.12: Solar array design properties.

Segment	Solar cell	Configuration	Area (m <sup>2</sup> )	Mass (kg)
Aerobot	AZUR SPACE 4G32C	12s75p	2.72	9.5
TRM	AZUR SPACE 4G32C	13s30p	2.35	11.6
Orbiter	AZUR SPACE 4G32C	13s31p	2.43	12.5

### 10.3.3. Batteries

Since the orbiter, TRM, and aerobot operate on photovoltaic power, a secondary power source is required for eclipse periods. This role will be filled by secondary batteries, considering their low cost, high reliability, and low environmental impact. The aeroshell and dropsondes, with their short operational lifetimes, will operate on primary batteries, as only one discharge cycle is necessary. The sizing of both types of batteries will be explained in this subsection, as it is a similar process with only a few key differences.

To cover the wide range of operational requirements, a broad selection of commercially available battery cells was examined, shown in Table 10.13. All Saft and EaglePicher cells are space-qualified, the Panasonic NCR18650B was successfully flown on MarCO [126], and LG Chem sees their batteries fit for space qualification in the near future [127]. The batteries are assessed in terms of specific energy, specific power, and, for secondary batteries, cycle life. Reliability and cost are not compared for lack of data, but there are no reasons to expect that these differ significantly between batteries.

For secondary batteries, the depth of discharge (DoD) is also shown, as it reduces the energy extracted from a battery. This means that usable specific energies are lower than the shown values by a factor DoD. Shown in the table are the DoD values for which the cycle life is tested and published by the manufacturer. Generally, it is possible to increase cycle life significantly by reducing the DoD; this does mean that battery performance becomes less certain. At the risk of lower-than-expected cycle life, it is thus possible to achieve higher performance than described here. Because of the stringent requirements on reliability and lack of theoretical data on lithium-ion behaviour, this is not considered in the current design.

Whereas data such as cycle life at a given DoD can often be taken directly from the manufacturer data sheet, specific energy and specific power are not always given. When absent, the specific energy and specific power of a battery cell are calculated as

$$E_{sp} = \frac{E_c}{m_c} = \frac{C_c V_c}{m_c} \quad (10.15) \quad \text{and} \quad P_{sp} = \frac{P_c}{m_c} = \frac{IV}{m_c}, \quad (10.16)$$

where  $C$  is the nominal capacity of the cell,  $V$  is the nominal discharge voltage,  $I$  is the nominal discharge current, and  $m$  is the mass of a single battery cell. From these values, the optimal battery cell type is determined by estimating the mass required to fulfil a given power profile. This estimate becomes

$$m_{bat} = \max\left(\frac{E_{req}}{E_{sp} d \eta_p}, \frac{P_{req}}{P_{sp}}\right), \quad (10.17)$$

with  $E_{req}$  the energy to cover a discharge cycle,  $P_{req}$  the power required during discharge,  $d$  the DoD of the battery, and  $\eta_p = \eta_{BDR} \eta_{cable} \eta_{reg}$  the electrical path efficiency from the battery to the loads. Note that  $\eta_{reg} = 1$  if a load operates at bus voltage, since no regulator is required then.

The resulting battery mass estimate allows for relative comparison of batteries with respect to mass-specific performance for different energy, power, and cycle life requirements. It should be noted that a discrete number of batteries must be used, such that mass-specific performance does not equal mass-optimality, particularly when a low number of cells is used. The discrepancy resulting from this is significant

Table 10.13: Properties of considered battery cells, as obtained from manufacturer data. The lower half are primary cells.

Battery cell	Specific energy (Wh/kg)	Specific power (W/kg)	Cycle life (-)	DoD (-)
Saft VES 180	157.7	105.6	6500	0.8
Saft VL 51ES	168.5	112.9	2000	0.8
Saft VES 16	152.4	102.1	2000	0.8
Saft MP 176065 xlr	165.3	82.7	1400	1.0
EaglePicher LP32975	114.0	57.0	2000	1.0
EaglePicher LP33037	135.0	67.5	2000	1.0
EaglePicher LP33450	121.9	60.9	2000	1.0
Panasonic NCR18650B	253.9	126.9	500	1.0
LG Chem INR18650 HG2	204.2	698.0	400	1.0
LG Chem INR18650 MJ1	259.6	296.7	400	1.0
Saft LS 14250	485.4	14.2	-	-
Saft LS 33600	680.0	10.0	-	-
Saft LO 35 SX	205.3	186.7	-	-
Saft LO 26 SHX	247.1	131.8	-	-
Saft G 36/2	264.4	233.3	-	-
EaglePicher LCF-134	457.6	208.0	-	-
EaglePicher LCF-136	389.8	169.5	-	-

for the dropsonde design, as described in Section 10.5, such that the Saft LO 35 SX is used, instead of the Saft G 36/2, which has better mass-specific performance. All other systems follow the approach described.

To finish the battery design, the number of cells in parallel and in series it to be determined. The number of cells in series is determined based on the voltage allowed by the battery regulators, such that

$$n_s = \text{round}(V_{\text{bat}}/V_c). \quad (10.18)$$

In above equation,  $V_c$  refers to the nominal voltage over a single battery cell, and  $V_{\text{bat}}$  refers to the required battery voltage, which is 23.5 V for the Terma battery charge/discharge regulator used [128].

The total number of battery strings is determined from two points of view: energy and power. To fulfil the total energy requirement, the energy of strings can be added together, such that

$$n_{p,E} = \frac{E_{\text{req}}}{n_s V_c C_c D \eta_{\text{EOL}} \eta_p}. \quad (10.19)$$

Both primary and secondary of batteries suffer from some type of end-of-life degradation: following the convention used in Table 10.13, secondary batteries have 80% of original capacity at end-of-life, such that  $\eta_{\text{EOL}} = 0.80$ . Primary batteries suffer from self-discharge, which is at most 3% per year at nominal conditions across all primary battery cells investigated. Assuming a storage period of 2.5 years for both the aeroshell and dropsonde batteries, the "end-of-life" degradation becomes  $\eta_{\text{EOL}} = 0.93$  at the point of discharge.

The number of strings to reach sufficient power levels is calculated as

$$n_{p,P} = \frac{P_{\text{req}}}{n_s V_c I_c \eta_p}, \quad (10.20)$$

where no end-of-life correction is used; no power degradation is specified on the manufacturer data sheets.

The number of strings to actually put in parallel naturally becomes the maximum of the numbers required for energy and power. With this, it is possible to estimate the mass of the total battery as

$$m_{\text{bat}} = 1.4 n_s n_p m_c, \quad (10.21)$$

where the factor 1.4 represents an estimated 40% parasitic mass fraction resulting from thermal and structural support required for cell integration into a full battery [129].

Table 10.14: Resultant battery properties. Listed are maximum achievable energy and power, not operational values.

Segment	Type	Configuration	Energy (Wh)	Power (W)	Mass (kg)
Dropsonde	Saft LO 35 SX	1s1p	6	6	0.04
Aerobot	LG Chem INR18650 MJ1	7s33p	2939	3359	15.8
Aeroshell	EaglePicher LCF-134	11s19p	2391	1087	7.3
TRM	LG Chem INR18650 HG2	7s7p	480	1642	3.3
Orbiter	Saft VL 51ES	5s2p	1820	1219	15.1

## 10.4. Risk analysis

The power system is a very critical mission element, particularly considering its failure directly leads to full failure of most other subsystems. This makes it difficult to recover from a power failure, since it directly implies loss of communication and loss of command over the spacecraft, such that ground control intervention is near impossible. As such, it is necessary to map the risks and mitigate them, to be able to provide as reliable a system as possible. A list of risks was identified, and judged on their probabilities and impacts, after which they were mitigated to the best extent. For the scale refer to Section 15.1.

- EPS1 **Solar cell failure:** Due to manufacturing defects, unexpected operational conditions, or micrometeorite impacts, solar cells can fail, leading to entire string failure. Probability = 5, Severity = 3; **Mitigation:** The design margin of 25% includes 10% margin at launch [116], such that unexpected string failure does not impact compliance with requirements at EOL. Probability = 5, Severity = 1.
- EPS2 **Battery cell failure:** Due to manufacturing defects, unexpected operational conditions, or micrometeorite impacts, battery cells can fail, leading to entire string failure. Probability = 5, Severity = 3; **Mitigation:** The launch margin also allows for limited battery string failure, such that requirements compliance remains unaffected with the failure of single strings. Probability = 5, Severity = 1.
- EPS3 **Orbital injection failure:** It is possible that orbital injection fails, such that eclipse time increases, making the spacecraft unable to survive eclipse. Probability = 2, Severity = 5; **Mitigation:** Beyond the 10% operational margin, it is possible to turn off scientific instrumentation on the orbiter during eclipse. Additionally, the orbiter has the capability to increase its battery's DoD, at the cost of a reduction in cycle life. Probability = 2, Severity = 3.
- EPS4 **Short-circuits:** Electrical equipment can fail, leading to short-circuits that could damage other connected components. Probability = 2, Severity = 4; **Mitigation:** The equipment power distribution module included in all three PCDUs has latching current limiters that switch off when the expected current is exceeded, isolating equipment failures. Probability = 2, Severity = 3.
- EPS5 **Exposure to acid:** Venus clouds contain significant amounts of acid, which can damage the solar cells. If the balloon drops into the cloud layer momentarily, exposure could affect photovoltaic performance. Probability = 5, Severity = 3; **Mitigation:** The cover glass used is resistant against corrosion and will cover the solar panels without gaps, protecting the cells. Probability = 5, Severity = 1.
- EPS7 **Extended eclipse time:** Due to the stochastic nature of the winds, it is possible that nighttime operations must last longer than expected, depleting the available battery capacity. Probability = 4, Severity = 4; **Mitigation:** The 10% design margin is available also for such cases. Additionally, if this design margin becomes smaller due to other defects, non-critical loads such as scientific instrumentation can be reduced during nighttime. Probability = 4, Severity = 1.
- EPS8 **Aerobraking erosion:** While aerobraking, collisions with high-velocity atomic oxygen particles result in solar cell degradation [130]. Probability = 5, Severity = 3; **Mitigation:** During aerobraking, the solar panels will be oriented with the backside facing the flow. Probability = 5, Severity = 1.

## 10.5. Sensitivity analysis

Naturally, it is possible that the design conditions change, that design errors are found, or that parameters are optimised. This could result in design changes that also affect the power system. Determine design points that are very sensitive to change, in particular with respect to the system mass, is therefore useful. Naturally, the most important property for the power system is the power required. As such, the mass sensitivity of all segments to changes in average power consumption is plotted in Figure 10.6.

As expected, power system mass changes proportionally with respect to power consumption for most segments. None of the systems show disproportionate mass increases until power consumption increases with 30%, such that requirement compliance is likely to remain feasible within the mass budget even for significant increases in the power required.

Notable is that the Saft G 36/2 dropsonde power mass drops by 50% at a 5% decrease in power. This makes sense: the design requires two Saft G 36/2 cells, but only barely. Based on this, the design is altered to use the Saft LO 35 SX, which has a higher power and capacity per cell, in spite of worse mass-specific characteristics. Even lower masses are possible with the EaglePicher LCF-134, but its operating temperatures do not match the current thermal system. This is left for further design.

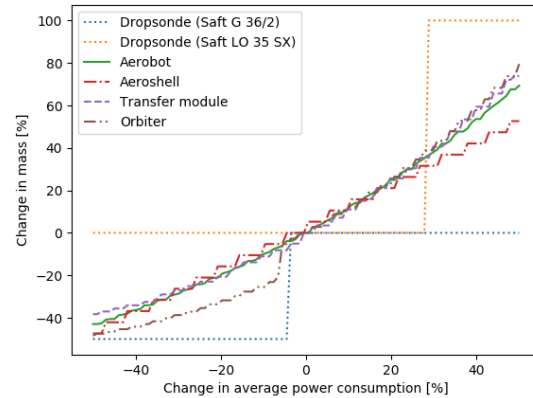


Figure 10.6: Mass sensitivities to changes in average power consumption.

## 10.6. Verification and validation

The aforementioned methodology and results had to be verified and validated to ensure their accuracy. This verification and validation was carried out in different steps, as described below.

**Solar cell verification** To verify the fundamental solar cell model, the efficiencies derived from the current and voltage characteristics of the solar cells were compared with the lab efficiencies given on the manufacturer data sheets. All efficiencies match up to the number of significant digits available on the data sheet.

**Battery cell verification** The sizing methodology for the batteries is verified similarly to that of the solar cells. The specific energy and voltage of batteries are compared with that on the supplier data sheet, matching up to the number of digits specified there. This is the case for both primary and secondary batteries.

**Battery validation** The validity of the whole-battery sizing method is determined by comparison of the model with the characteristics of a cell brick as described in [131]. A battery was sized, consisting of the same cells and achieving the same properties as given. The resulting specific energy of 185 Wh/kg indeed approaches the 191 Wh/kg obtained from the physical battery.

**VEX comparison** To validate the used solar cell temperature and irradiance models, they are compared with Venus Express operational data. The Venus Express array generated about 1400 W at end-of-life near Venus, with an effective solar cell area of 2.65 m<sup>2</sup> at 20.2% efficiency [132]. Solar panel operating temperatures are not known, but are expected to be around 80°C, similar to the orbiter design. Lacking better data, properties of the GADGET 1 solar cells are approximated with the AZUR SPACE 3G28C, which is also a triple-junction GaAs cell from the same time period. The resulting estimates for total array efficiency of 20.3% and required solar cell area of 2.46 m<sup>2</sup> both approach Venus Express values within 10%, indicating that the solar cell model has physically meaningful results even at high temperatures and irradiances.

**Akatsuki comparison** Battery and solar panel performance is also compared with Akatsuki data. Akatsuki's solar array generated 950 W near Venus after 1e15 1 MeV electron fluence with a solar cell area of 2.02 m<sup>2</sup> [133], implying an efficiency of 17.9%. The solar panel operating temperature is known to reach up to 142°C [50]. For lack of data, the solar cells are approximated as AZUR SPACE 3G28C, which also reach 28% efficiency [50]. Again, the effective efficiency and solar cell area are approximated to within 10%.

Additionally, the Akatsuki batteries are considered, which delivered up to 750 Wh at 39.6 V during eclipses lasting up to 90 minutes. A derivative of the Hayabusa cells, with a capacity of 23.5 Ah at 3.6 V, was used in an 11s2p configuration at a 44% DoD. Sizing for the same eclipse energy and power results in the exact same 11s2p configuration, showing that the used battery model is valid.

# 11 Thermal Control

The thermal conditions in and around the atmosphere of Venus are considerable harsher than on earth. The orbiter and transfer module experience a solar flux 1.9 times higher and an albedo 4.8 times higher compared to earth, while the dropsonde will be exposed to temperatures as high as 540 K during its decent to 25 kilometres. To stop the components of the segments from overheating, thermal control is needed. There are multiple methods of thermal methods, all with their advantages and drawbacks. For each segment the most optimal control methods will be chosen.

## 11.1. Design overview

The thermal design of all the mission segments can be seen in Figure 11.1 and Table 11.1. The design can be split up into: surface finishes, insulation, heaters, louvres, heat pipes and PCM's. Surface finishes and insulation is used to limit the heat flow in and out of the segments, while heaters and louvres are used to increase heat flow. To distribute the heat more evenly heat pipes are used and PCM's minimise temperature differences during the diurnal cycle.

Table 11.1: Thermal control design overview

Mission segment	Control method	Specifics	Mass (kg)	Power (W)
Orbiter	MLI	Outer cover: Silver reflector	0.63	
		Inner layer: AAerotherm S10-150	3.62	
		Inner cover: Kapton laminate	1.42	
	Louvres	Orbital SPARTAN , sized to 1.86 m <sup>2</sup>	7.50	
	Kapton heaters	Total of 75.9 cm <sup>2</sup>	0.020	196-592
	Heat pipe	4 m, 1.26 cm diameter, 5080 Wcm	1.32	
	Control system	Thermal controller and thermostats	1.2	1
Transfer module	MLI	Outer cover: Silver reflector	0.57	
		Inner layer: AAerotherm S10-150	3.38	
		Inner cover: Kapton laminate	1.28	
	Louvres	Orbital SPARTAN , sized to 1.86 m <sup>2</sup>	7.50	
	Kapton heaters	Total of 41.0 cm <sup>2</sup>	0.017	160 - 320
	Heat pipe	4 m, 1.26 cm diameter, 5080 Wcm	1.65	
	Control system	Thermal controller and thermostats	1.2	1
Gondola	White paint	Silicone based	3	
	Insulation	Rigid polymer foam, 4.0 cm	9	
	Heaters	Electrical patch heater	0.001	5
	PCM	Alkane 18 + conductive material	12	
	Control system	Thermal controller and thermostats	1.2	1
Dropsonde	White paint	Silicone based	0.01	
	Insulation	Rigid polymer foam 3.4 mm	0.007	

### 11.1.1. Approach to sustainability

The thermal design does not influence the sustainability of the mission as much as some other subsystems. However it was taken into consideration during the design phase. For example, very toxic surface finishes were not considered, nor were PCM that are either toxic or rare. Rigid polymer foam can cause negative health effects, however other insulation materials where either as toxic or would increase the volume or mass of the thermal subsystem too much.

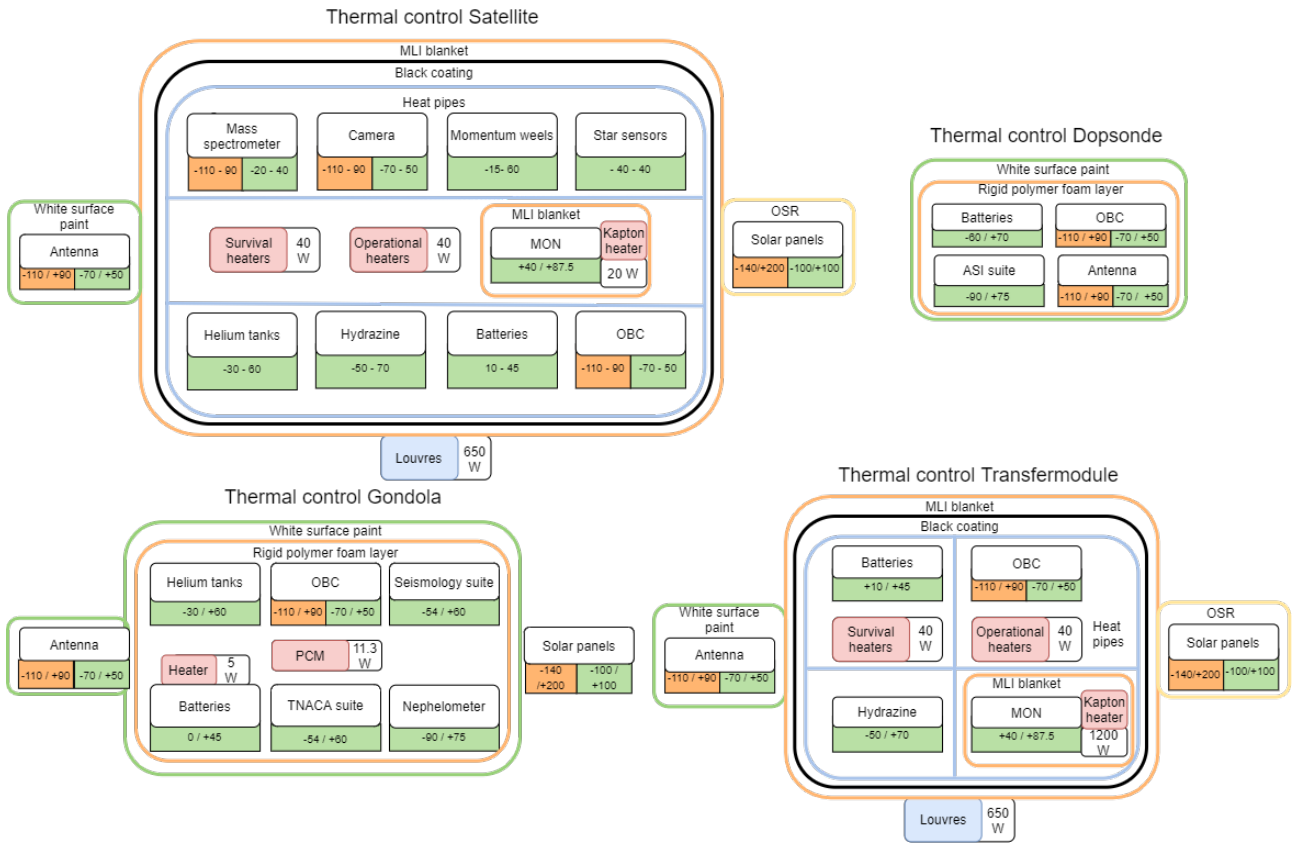


Figure 11.1: System architecture

### 11.2. Functional analysis

The main function of the thermal subsystem is to keep all the components of the mission in their operational temperature range, these temperature ranges can be seen in Table 11.2. Requirements that flow from these temperature ranges are shown in Table 11.3.

Table 11.2: Operational temperature ranges

Component	Temperature range (°C)	Component	Temperature range (°C)
OBC	-70 / + 50	Battery DRS	-60 / + 70
Antenna	-70 / + 50	Battery ARS	-40 / + 55
Momentum wheel	-15 / + 60	Solar panel	-140 / + 200
Star sensor	-40 / + 40	Camera	-70 / + 50
MON tank	+40 / + 88	Mass spectrometer	-20 / + 40
Hydrazine tank	-50 / + 70	Nephelometer	-90 / + 75
Helium tank	-30 / + 60	Seismology suite	-54 / + 60
attery ORB / TRM	+10 / + 45	TNACA suite	-23 / + 47
Battery ABT	0 / + 45	ASI suite	-90 / + 75

Table 11.3: Thermal subsystem requirement checklist

Identifier	Requirement	Compliance	Explanation in
TH-SP-01	The thermal control subsystem shall be able to maintain each subsystem in their required operational range.	✓	11.3.1
TH-SP-05	The spacecraft shall have an internal temperature between 293 K and 303 K.	✓	11.3.1
TH-SP-06	The temperature of the payload shall be maintained between 293 and 303 K.	✓	11.3.1
TH-AT-01	The thermal control subsystem shall be able to maintain each subsystem in their required operational range.	✓	11.3.2
TH-AT-03	The heat shield shall be able to withstand 773.4 W/cm <sup>2</sup> thermal loading.	✓	6.5.2
TH-AT-06	The temperature of the payload shall be maintained between 283 and 303 K	✓	11.3.2

### 11.3. Design approach

Due to the vastly different operational environments, different considerations are defining for each segment. Therefore, their design was approached differently, as will be discussed in the following subsections.

#### 11.3.1. Orbiter and transfer module

To determine the required capabilities for the thermal control system of the ORB and the TRM the most critical scenario's had to be analysed. These were found to be the following:

1. Transfer from Earth to Venus, deep space near Earth
2. Transfer from Earth to Venus, eclipse at Earth
3. Operational orbit at Venus, full sun at closest proximity to Venus
4. Operational orbit at Venus, eclipse at farthest distance from Venus
5. Operational orbit at Venus, full sun at closest proximity to Venus

In Figure 11.2 the most critical (passive) heat flows for the orbiter are given (for  $\alpha = 0.07$  and  $\epsilon=0.04$  insulation), here positive heat flows are into the spacecraft. The orientation of the vehicle also affects heat loss and absorption. In this analysis the worst possible case is taken, which for a peak heat scenario would be a maximum surface area facing the sun and planet, for the minimum case this would be the inverse. Both s/c are analysed in the same manner, with a few differences in s/c geometry, internal heat generation, internal configuration and orbit characteristics. Blanketing is the defining feature of any satellite's thermal system. The characteristics of the applied insulation are a driving factor in the heat balance between absorbed and radiated energy.

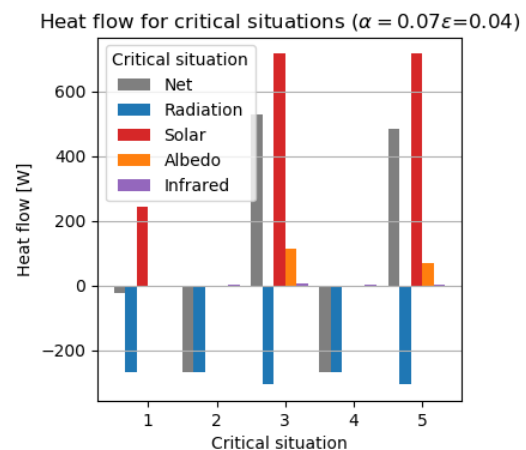


Figure 11.2: Heat flow orbiter during critical cases

In turn this will affect the required louvre area and heater power to dissipate or create extra heat. An iterative process was set up to find a suitable multi-layer insulation which would allow for a minimisation of these components. A combination of a Sheldahl Silver outer reflector layer [134], AAerotherm S10-150 as inner layer [135] and finally a kapton laminate [136] as inner cover. With an aerial density of 33, 160 and 74 g/m<sup>2</sup>, respectively. Such a lay-up yields an effective absorptivity of 0.07 and emissivity of 0.04. The net heat flow for this insulation can be seen in Figure 11.2. During a burn the engine will produce a high radiative flux towards the adjacent satellite wall. This has not been sized in depth however to account for this the inner layer of AAerotherm has been doubled in these walls. Finally a 20% margin was introduced for the MLI mass to account for clamps, sewing and tapes to attach the blanket to the primary structure. This MLI

blanket is also applied to the propellant tanks individually to avoid a sudden drop in internal temperature when propellant is released. During eclipse situations additional internal power must be generated to compensate for body emittance, seen in Figure 11.2 as radiation. This will be done by kapton heaters<sup>1</sup>, small films which can provide  $0.78 \text{ W/cm}^2$  at just  $0.4 \text{ g/cm}^2$ . These heaters are spread over all components in the spacecraft to provide heat if necessary. The deliverable total heater power is twice what is required during eclipse, which offers redundancy and the ability to selectively activate heaters to minimise an uneven heat distribution inside the s/c. In the case of a net positive heat flow (see scenario 3 and 5 in Figure 11.2) heat must be dissipated into space. Due to the low emittance design of the MLI the s/c will often have a net positive heat flow. To minimise power consumption the choice was made to implement louvres to increase body emittance in certain specific areas. With the louvres deployed, the emissivity in that area is increased from 0.04 to 0.88. The louvres should be deployed on the shadowed side of the s/c, as they also increase absorptivity.

To reduce the possibility of an uneven internal heat distribution while in a net heated scenario, the interior structure will be coated by a high emissivity black coating,  $\epsilon = 0.88$ . Additionally, heat pipes will be applied. These pipes can passively transport energy from high to low temperature areas where it can be dumped. This ability is specifically of importance for the efficient implementation of louvres into the spacecraft. 4 meters of a 1.27 diameter heat pipe with a 5080 W/cm performance will be applied for both s/c [137]. To ensure the antenna would not overheat while in full sunlight and albedo radiation, it was found a surface finishing with  $\frac{\alpha}{\epsilon} < 0.3$  was needed to keep the antenna's temperature below the specified  $+50^\circ\text{C}$ . Therefore silicone based white paint will be applied to the surface of the antenna.

When attached to the transfer module, the aeroshell has a significant inherent insulation and is assumed to be in continuous equilibrium, while in space. To still accommodate cooling or heating, the aeroshell is connected to the TRM via a 1 m passive heatpipe and will have heaters totalling a 40 W nominal power (80 W survival), which can be powered by the TRM or the internal battery. As already mentioned in Chapter 10, both a fraction of the front and the whole back of the solar panel will be covered by optical solar reflectors. The fraction was decided by looking at the average temperature of the solar panel at various stages of the mission, and finding the fraction that would lead to the most favourable temperatures, see Figure 11.3.

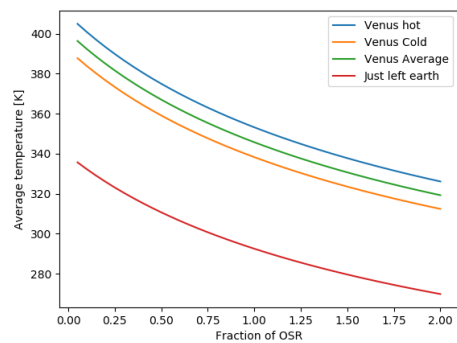


Figure 11.3: Solar panel temperature

### 11.3.2. Gondola

For the thermal design of the gondola there are two situations that need to be taken into account: day and night. There is no significant temperature or planetary radiation change during day and night. There is however a difference in heat fluxes due to solar and albedo radiation. This difference is modelled in the same way as is described in Chapter 7.

During the design process it became clear that passive thermal control methods would be preferable over active control, since there was a tight power budget. Three types of passive thermal control were identified to be suitable for the gondola: phase changing materials (PCM), surface finishing and insulation. Phase changing materials can absorb high amounts of energy during its phase change. What makes PCM's especially advantageous for the gondola, is the diurnal cycle. During the day there will be a heat flux into the gondola due to the solar and albedo radiation, while during the night the gondola will lose heat. The PCM can absorb part of the heat to keep the components from overheating during the day, and release this absorbed heat to help negate the heat loss during the night. Alkane 18 carbon atoms was found to be a suitable material, this is due its high latent and specific heat, 244000 and 2300 J/Kg respectively, and most importantly a melting temperature that lies between the maximum and minimum operating temperature at 301 K. The amount of energy that the PCM can absorb and release is governed by the following equation:

$$Q_{net} = M_{PCM} \cdot \frac{C_{ps} \cdot (T_m - T_i) + a_m \cdot \lambda_m + C_{pl} \cdot (T_f - T_m)}{1.1} \quad (11.1)$$

<sup>1</sup><http://electronicmaterials.dupont.com/kapton-rs-technical-library>, retrieved 14 June

Where  $C$  is the specific heat for either the liquid or solid phase of the PCM.  $a_m$  is an safety factor for the fused mass fraction set to 0.8, meaning only 80% of the mass fuses.  $\lambda_m$  is the latent heat of alkane 18 carbon. It is divided by 1.1 as an safety factor to stop the PCM from fully saturating. An extra 30% is added to the necessary PCM mass to account for conductive materials to evenly distribute the heat in the PCM. The choice of surface finishing was based on limiting the heat flux due to solar and albedo radiation during the day. White silicone based paint was chosen for both its low absorptivity (0.25) and low areal density (0.24 kg/m<sup>2</sup>) [40]. The insulation was chosen based on minimal mass and a low thermal conductivity to limit heat flow from the hot skin to the cooler inside, therefore rigid polymer foam was chosen for the insulation material ( $\rho = 45$  kg/m<sup>3</sup>,  $k = 0.025$  W/mK) [138]. Besides the passive thermal control, one active control method is added. Since batteries are very sensitive to temperature a patch heater of 5 W will be placed close by. This patch heater will be activated if the temperature of the battery gets colder than 10°C. The temperature of the subsystems will be monitored by thermostats placed all over the gondola and controlled by a thermal controller.

To determine the optimal combination of the insulation and PCM, a model was made. Seven heat fluxes are modelled: solar radiation, albedo radiation, planetary radiation, convection, conduction, radiation and internal heat, see Figure 11.4. The incoming solar radiation is determined using Equation 11.2. With  $J_{solar}$  being the solar radiation.  $A_{solar}$  is the area of the gondola which receives the solar radiation, which was assumed to be a quarter of the total area.

$$\dot{Q}_{solar} = J_{solar} \cdot A_{solar} \cdot \alpha \quad (11.2)$$

The albedo radiation is function of the solar radiation which is scaled with the view factor and albedo factor of Venus, which is 0.77,

$$\dot{Q}_{albedo} = \dot{Q}_{solar} \cdot F \cdot a \quad (11.3)$$

The planetary radiation, is the energy that Venus radiates back into space and atmosphere. This can be calculated with the black-body temperature of Venus, which was found to be 227 K [1],

$$\dot{Q}_{planetary} = \sigma \cdot F \cdot A_{planetary} \cdot T_{Venus}^4 \quad (11.4)$$

The view factor  $F$  used in the previous two equations can be calculated as follows,

$$F = \frac{r_{Venus}}{r_{Venus} + h} \quad (11.5)$$

The convection heat flux is calculated using Equation 11.6. The heat transfer coefficient  $h_c$  is evaluated at each moment, taking into account the film temperature, Prandtl, Reynolds and Nusselt numbers.

$$\dot{Q}_{convection} = h_c \cdot A \cdot (T_1 - T_2) \quad (11.6)$$

The conduction heat flux is determined with Equation 11.7. Here  $k$  is the thermal conductivity and  $t_{insulator}$  the thickness of the chosen insulator.

$$\dot{Q}_{cond} = \frac{k \cdot A(T_2 - T_3)}{t_{insulator}} \quad (11.7)$$

The internal and skin temperature ( $T_1$  and  $T_2$ ), change over time, which is calculated via:

$$\Delta T = \frac{\dot{Q}_{net} \cdot \Delta t}{m \cdot C} \quad (11.8)$$

$\dot{Q}_{net}$  is the net heat flux into the skin or internal part of the gondola.  $C$  is the heat capacity, for the skin the heat capacity of aluminium was used, while for the internal part of the gondola has an assumed heat capacity of 1000 J/Kg K [40]. The energy that the gondola radiates is modelled using Equation 11.9, where  $\epsilon$

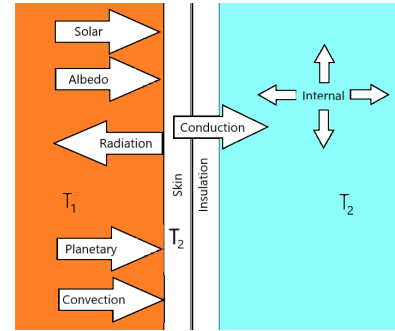


Figure 11.4: Gondola thermal model

is the emissivity of the chosen surface finish.

$$\dot{Q}_{rad} = \epsilon \cdot \sigma \cdot A \cdot (T_2^4 - T_1^4) \tag{11.9}$$

The internal heat was modelled by taking the average power during night and day and multiplying it by  $1-\eta$ , where  $\eta$  is the electrical efficiency assumed to be 0.3 [40]. As can be seen in Table 11.2, the minimum and maximum temperature range is determined by the battery, which has a temperature range of 0 - 45°C. The model then determines the lightest combination of PCM mass and insulator thickness that keeps the internal temperature within this range with a  $\pm 5^\circ\text{C}$  safety factor. The result from this model with the mass and thickness mentioned in Table 11.1 can be seen in Figure 11.5. This figure shows the internal temperature during one day and night cycle of 5.8 terrestrial days.

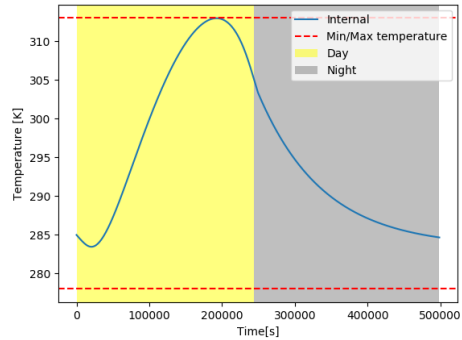


Figure 11.5: Internal temperature during one cycle

### 11.3.3. Dropsonde

During the dropsonde fall it will experience the highest temperatures of all the mission segments: 540 K at 25 kilometres. To keep the dropsonde from overheating it was again decided that only passive thermal control methods should be used due to power constraints. White paint and rigid polymer foam are also applied to the dropsonde. No PCM is used to keep the dropsonde as small and light as possible and the added benefit of releasing heat at colder temperatures is not needed. Temperature sensors or thermal controller are not installed, since there is no active thermal control in the dropsondes.

The thermal model described in the previous subsection is also used for the thermal design of the dropsonde with some adjustments. As can be seen in Figure 11.6, the radiation and solar heat fluxes are negligible compared to the convection heat flux, especially with a white paint surface finish. Therefore only convection, conduction, radiation and internal heat were used in the model. For the dropsonde, the most limiting maximum temperature is that of the on-board computer at  $+50^\circ\text{C}$ . The model finds the thinnest insulation possible, while keeping the internal temperature lower than this maximum temperature (with  $-5^\circ\text{C}$  for safety). Results are shown in Figure 11.7 and Figure 11.8. Since the  $5^\circ\text{C}$  is taken into account the probe will be able to shortly operate below 25 km. The internal temperature of the dropsonde starts at 300 K, instead of the maximum internal temperature of the gondola due to a couple of reasons. As shown in Chapter 14, the dropsondes are housed in the first level, separated from the internals of the gondola by thermal insulation. Due to the housing around the dropsondes no solar or albedo radiation can heat them up, only the planetary radiation and the atmosphere can reach them. This would lead to a temperature slightly higher than the atmospheric temperature. To take into account heating from the gondola and a safety factor, a starting temperature of 300 K was chosen.

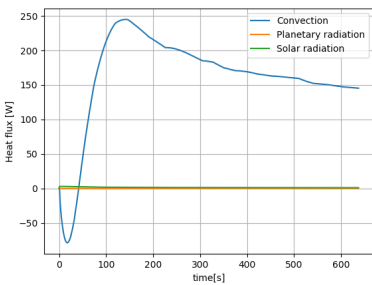


Figure 11.6: Heat fluxes during descent to 25 km with a white surface finish

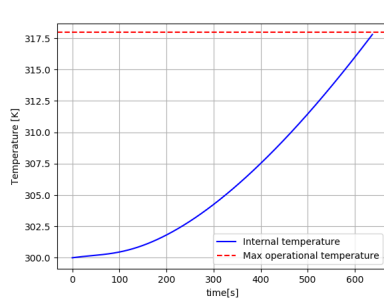


Figure 11.7: Internal temperature vs. time

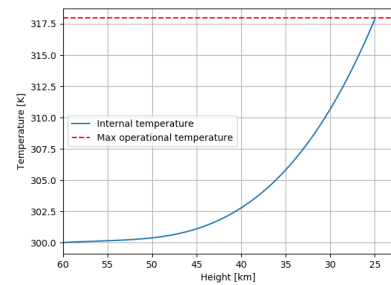


Figure 11.8: Internal temperature vs. height

### 11.4. Risk analysis

In this subsection, potential risks for the thermal control subsystem are identified and evaluated for their probability and impact on the mission. Measures to mitigate these risks are identified.

- TH1 **Flammability:** Polyurethane foam panels are highly flammable when exposed to fire or a spark. Probability: 2, Impact: 5; **Mitigation:** Insulation material will be treated by a fire retardant. New probability: 1, Impact: 4
- TH2 **Reaching maximum operating temperature:** During the mission lifetime some parts of the design can be heated till their maximum operating temperature, especially the skin. This could lead to major performance issues for these components, including structural failure. Probability: 2 Impact: 4; **Mitigation:** A safety factor of 20% has been taken in to account for both the insulation thickness and the PCM mass, this decreases the probability of subsystem overheating. New probability: 1, Impact: 4
- TH3 **Hot spots:** Uneven exposure to radiation, internal heat or due to conduction of structures. This could induce thermal stresses and degrade the performance in those spots. Probability: 4, Impact: 2; **Mitigation:** Extra analysis can be done to identify these possible hot spots. The conduction could be lowered at these spots or heat pipes could be implemented. New probability: 3, Impact: 1.
- TH4 **Environmental temperature fluctuations:** A different environmental temperature can prematurely saturate the PCM increasing the internal temperature beyond acceptable bounds. Probability: 4 Impact: 3; **Mitigation:** An sensitivity analysis is done into the impact of the atmospheric temperature, where the temperature is varied  $\pm 5^{\circ}\text{C}$  to see if the internal temperature stays in the operational limits. New probability: 3, Impact: 2.
- TH5 **Battery under-cooling** For the transfer module, orbiter and aerobot the battery dictated the coldest operational temperature. The battery under-cooling could permanently disable or degrade the performance of the battery. Probability: 3 Impact: 4. **Mitigation:** Heaters and temperature sensors are placed near the battery. New probability: 1, Impact: 4.

### 11.5. Sensitivity analysis

To check the sensitivity of the thermal model to changes in the environmental conditions or design changes, a sensitivity analysis was done. During the design phase the internal power consumption changed quite often, therefore an analysis was done into the effect of the internal heat on the subsystem mass. As can be seen in Figure 11.9, the required subsystem mass increases as the internal heat generation increases. It is therefore important to be regular check the internal heat of the design. Figure 11.10 shows the relationship between the atmospheric temperature, and maximum and minimum internal temperature. The effect of the atmospheric temperature was analysed, because the assumed value of 262.8 K is an average and during the mission it can change. It can be seen that even with a temperature increase of  $5^{\circ}\text{C}$ , the internal temperature does not exceed the operational limit of 323 K.

The thermal subsystem design for the space element is very sensitive to geometry alterations. Enlarging the overall surface would lead to a linear increase in required louvres surface and heater power. Care must be taken here to avoid a shape with large differences in projected solar. Such a squashed or elongated shape could drive the subsystem design to unreasonable power and louvres area requirements. The environmental effects on the design are well defined and do not pose a sensitivity issue. Only the orbit with respect to Venus could be altered such that the critical design scenarios change. However, in these cases the impact is expected to be minimal due to the low IR emissivity of the planet. Additionally, the preliminary design was performed for instantaneous critical scenarios whereas in practice the thermal capacity of the s/c increases the robustness of the thermal subsystem.

### 11.6. Verification and validation

The verification and validation of the used thermal control models described in the previous sections was done using several different methods.

**Unit tests** For the verification of the thermal model several unit test were performed. Constants such as the heat transfer coefficient, thermal conductivity and absorptivity were set to zero to see if the related heat fluxes would also become zero.

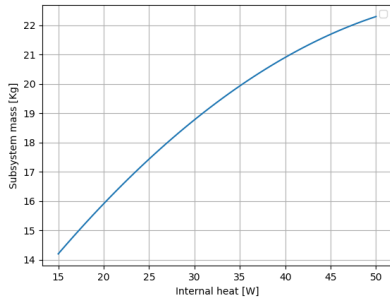


Figure 11.9: Internal heat vs. subsystem mass

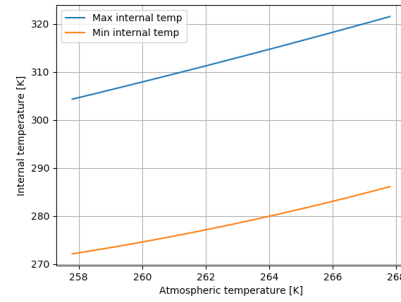


Figure 11.10: Atmospheric temperature vs. internal temperature

**Venus Flagship comparison** To validate the thermal model it will be compared to the thermal model used by NASA for its Flagship mission study [15]. There are two mayor differences between the models, the NASA model has an extra exterior insulation layer and the NASA model has cutouts for windows, which bypass the exterior insulation. To make comparison easier, an extra external insulation layer was added in the BLOON model and a bypass heat flux was added as function of the atmospheric temperature. By using design parameters from the Flagship mission, the models were compared. The two models generally match, see Figure 11.11. There is one noticeable difference, the internal temperature stays more or less constant at 35 °C in the NASA model while the BLOON thermal model the internal temperature steadily increases. This difference is easily explained, in the BLOON model the total energy that the PCM can absorb is evenly distributed during the cycle, while in real life and the NASA model a PCM absorbs most of the heat at its melting point, which is 35 °C for this model. This explains why the internal temperature plateaus around 30 °C in the NASA model and steadily keeps rising in the BLOON thermal model.

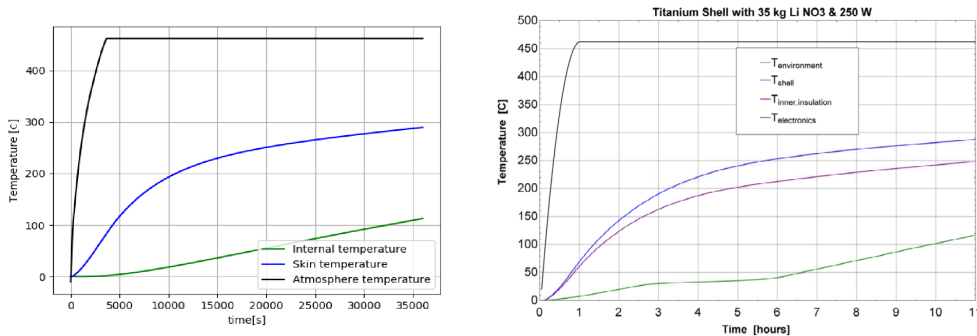


Figure 11.11: Left: BLOON thermal model. Right: NASA Flagship thermal model [15]

**Hand calculations** Furthermore, hand calculations were performed to check if the temperature increases were consistent with the net heat flux into that component. Furthermore, the insulator thickness, absorptivity, emissivity and PCM mass were varied from very small to very large values to check whether these thermal control methods were implemented correctly. Additionally, heat flow calculations were performed for arbitrary moments during the mission to verify the expected critical hot or cold scenarios.

**Comparison** Validation regarding the design of the space segment was done by comparing the sized thermal system to reference missions and mission proposals such as [15] and [32]. It was found that the power and louvres sizing done was realistic. A notable difference was the choice for a very low absorptivity reflector layer, allowing for a passive heat dissipation system.

# 12 Attitude Determination and Control System

The attitude determination and control system of the orbiter will consist of star sensors, momentum wheels and reaction control thrusters. The design of these orbiter components will be the primary discussion of this chapter. Furthermore, the transfer module ADCS will not be extensively designed, but will be briefly discussed. As explained in Chapter 7, the aerobot cannot control its flight path and does not require ADCS.

## 12.1. Design overview

The mass and power budget belonging to the ADCS of the orbiter is given in Table 12.1. Furthermore, it will prove useful to establish an internal satellite coordinate system. This is shown in Figure 12.1.

Table 12.1: Mass and power budget for the orbiter ADCS subsystem

Component	Amount (-)	Mass (kg)	Nominal power(W)	Peak power (W)
Star sensors	4	5.6	16	-
Momentum wheels	4	20	40	110
RCS thrusters (see Chapter 5)	6	4.3	-	-
RCS propellant	-	1.6	-	-

The rotational angle about the z-axis  $\alpha$  will be referred to as the yaw angle, the angle of rotation about the x-axis,  $\gamma$ , is called the roll angle. Furthermore, rotation about the y-axis, although not shown in Figure 12.1, is  $\beta$  and will be referred to as the pitch angle. Note that, a right-handed coordinate system is used in accordance with common practice, which means that the y-axis direction is 'into the page'.

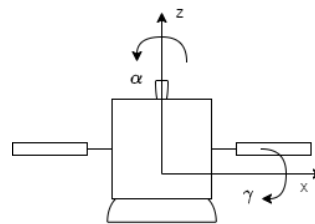


Figure 12.1: Internal coordinate system of the satellite

### 12.1.1. Approach to sustainability

The sustainability of the ADCS subsystem was considered using the three pillars of sustainability. This mainly meant that the material of components was taken into account for selection of ADCS actuators and stars sensors.

## 12.2. Functional analysis

The main functions of the ADCS subsystem are to determine and control the attitude of the space segments. The requirements which can be seen in Table 12.2, which were found using analyses of different types of manoeuvres.

Table 12.2: Requirements on attitude determination & control

Identifier	Requirement	Compliance	Explanation in
ORB-ADCS-02-A	The orbiter shall be able to determine its attitude with a minimum accuracy of 0.03 deg.	✓	Subsection 12.3.13
ORB-ADCS-02-B	The orbiter shall be to reach its target attitude with a minimum accuracy of 0.03 deg.	✓	Subsection 12.3.16
ORB-ADCS-03-A	The achievable slew rate of the orbiter shall be at a maximum 1.1 deg/s.	✓	Subsection 12.3.16
ORB-ADCS-03-B	The achievable slew rate of the orbiter shall be at a minimum 0.5 deg/s.	✓	Subsection 12.3.14
ORB-ADCS-04	The orbiter shall be able to remain operational after 1 attitude actuators fail.	✓	Subsection 12.3.14

### 12.3. Design approach

The design approach for the ADCS consists of determining slew rates and momentum storage of attitude manoeuvres and disturbances that are encountered in the mission. The transfer module is discussed briefly, while manoeuvres for communication and propulsive burns during orbit around Venus are discussed more in-depth. Subsequently, an analyses of the orbiter mass moment of inertia will be performed, before sizing and selecting the star sensors, momentum wheels and reaction control system thrusters.

#### 12.3.1. Transfer module attitude control considerations

The transfer module requires attitude determination and control during its orbit around Venus. It will wait for the orbiter to finish aerobraking, before it can insert the aeroshell into the Venusian atmosphere. During the orbit it will not have to perform scientific measurements and communication with Earth will be performed using a LGA for beacon mode type signals and commands. Due to the passive nature of the orbit the transfer module will be in, the slew manoeuvres the transfer module will have to perform are deemed to be unconstrained with respect to the time they have to be performed in. This greatly reduces the required slew rates the transfer module has to be able to achieve when compared to the orbiter. Opposed to this, the mass, and due to this the mass moment of inertia, will be higher than the mass of the orbiter. This is caused by the added mass of the aeroshell and aerobot. The ADCS components that will be added to transfer module will be star sensors and actuators similar to the orbiter. Performance in terms of slew rates and accelerations will be lower, but this will not be a problem due to the lack of time constraints on the manoeuvres it has to perform.

#### 12.3.2. Orbiter attitude control during orbit insertion and aerobraking

During orbit insertion high slew rates are required. The analysis of the exact manoeuvre is not part of the scope of this project. From literature, a value of 0.5 deg/s was found for comparable slew manoeuvres, [15, 47].

The initial aerobraking orbit of the orbiter is shown in Figure 12.2. During the aerobraking analysis in Chapter 5, it was assumed that the orbiter attitude was able to stay constant with respect to the orbital path. Due to the higher velocity of the orbiter at pericythe, that is where the most critical slew rate is required. In the initial aerobraking orbit this is around a timestamp of 46366 s from the start of the orbit. With the tangent lines plotted in the figure a slew angle of 62.9 deg over a period of 1500 s has to be achieved, this leads to an average slew rate of 0.042 deg/s. By evaluating two points that are closer together it was established that the slew rate converges to 0.049 deg/s, which is therefore the critical slew rate during the initial aerobraking orbit.

The final aerobraking orbit of the orbiter is shown in Figure 12.3. During the aerobraking analysis in Chapter 5, it was assumed that the orbiter attitude was able to stay constant with respect to the orbital path. Due to the higher velocity of the orbiter at pericythe, that is where the most critical slew rate is required. With the tangent lines plotted in the figure a slew angle of 75.3 deg over a period of 1500 s has to be achieved, this leads to an average slew rate of 0.05 deg/s. Moreover, when taking two points that are closer to each other, centred around the pericythe, it was found that the critical slew rate converges to 0.055 deg/s.

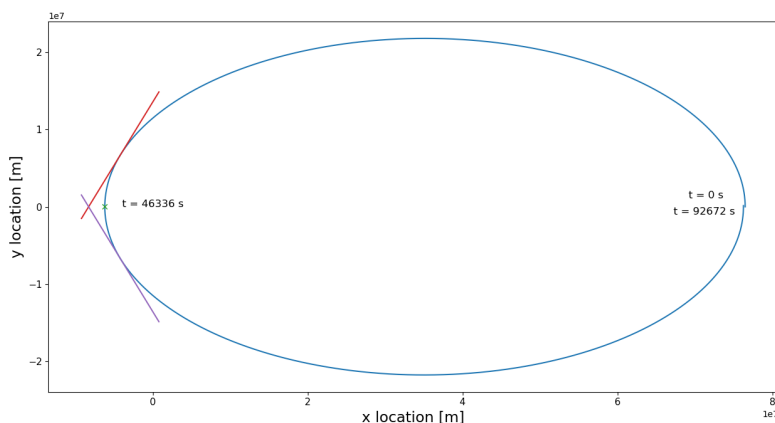


Figure 12.2: Attitude control for initial aerobraking orbit, showing required slew angle at pericythe with tangent lines

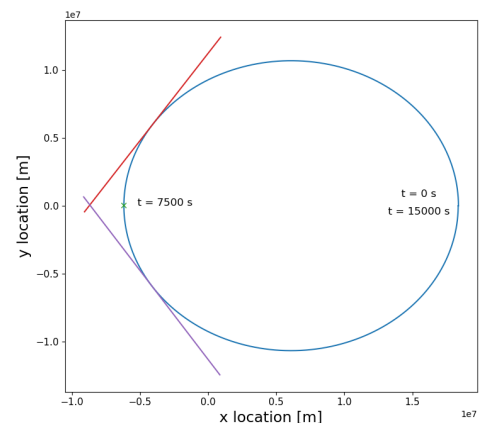


Figure 12.3: Attitude control for final orbit of aerobraking

### 12.3.3. Orbiter attitude control during communication with the balloon

To keep the antenna of the orbiter pointed at the balloon during the communication window, the orbiter is required to slew due to the fact that it orbits around Venus. The mean angular velocity of the orbiter with respect to a (stationary) balloon is 360 degrees divided by the period of the orbit 15485 seconds, which is approximately 0.023 deg/s. As the satellite will be communicating with the balloon when the satellite is around its apoclythe, where the linear velocity is at its lowest and the distance to Venus the largest, the angular velocity during this communication window will actually be lower than this value.

A lower limit value for the slew rate during communication with the balloon can be found using the geometry of the orbit and Venus, which is shown in Figure 12.4 for the critical scenario. It shows the communication signals between satellite and balloon, including a change of position of the balloon represented by the straight arrow. Furthermore, the change in angle of the satellite was found by determining the tangent lines from the start and end points of the communication window with the circle that represents Venus. The value that was found for the angle is 128 deg, which is indicated by  $\psi$ . As the communication window is 7455 seconds, this leads to an average slew rate of 0.017 deg/s. This is a lower limit, as the maximum slew rate during the communication will be higher.

Therefore, during the communication window the satellite will have to continuously slew at a rate between 0.017 to 0.023 deg/s. Note that this analysis takes into account both changes in longitude and latitude, as the worst case scenario was determined using geometry and not using physical phenomena. Besides this, the Venusian winds cause the balloon to undergo a north-drift that has a negligible magnitude for the time period of one communication window [139].

One characteristic was neglected up to this point, which is the fact that the balloon would also move out of the plane shown in Figure 12.4. The maximum angle would occur when the satellite has to slew between two points being on opposite sides of the equatorial plane. Note that this is a geometrical limit which will not occur in the mission as the aerobot will be above 20° latitude. The situation is shown in Figure 12.5. This would require the satellite to slew over an additional axis to keep pointing at the balloon. This angle can be approximated if we consider the orbiter at the apoclythe and using the radius of Venus  $\phi = 2 \cdot \arctan(6052/18384) = 36$  deg. Dividing this angle by the communication window time of 7455 s, finds an average slew rate of 0.005 deg/s.

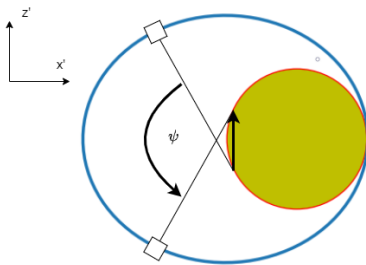


Figure 12.4: Slew angle due to balloon and satellite movement during communication window, North is negative  $x'$ -direction

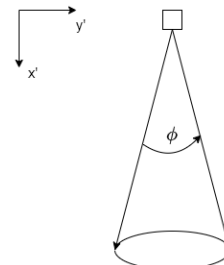


Figure 12.5: Slew angle due to out of  $x'z'$ -plane balloon movement

### 12.3.4. Orbiter attitude control during communication with Earth

When the satellite is communicating with Earth attitude control is required to stay pointed at Earth. A two hour communication window with Earth is required every six orbits, determined in Chapter 9.

In Figure 12.6 the angles  $\alpha$  and  $\beta$  shows the largest difference in angle that occurs during the orbit around Venus. Figure 12.6 show this line perpendicular the the major axis of the orbit, however this is most often not the case. The reason that the described situation is used in this analysis as this causes the largest angles  $\alpha$  and  $\beta$ , thus the most critical situation is analysed. Moreover, the critical distance between Venus and Earth is the minimum distance of 38 million km.

The angle  $\alpha$  can be calculated as the arctangent of the apoclythe (18,384 km from core) divided by the distance between Venus and Earth. Therefore  $\alpha = 0.0277$  deg. Then, the angle  $\beta$  can be calculated as the arctangent of the pericythe (6521.8 km from core) divided by the distance between Venus and Earth, thus  $\beta = 0.0098$  deg. The average slewrate during communication with Earth can then be calculated, by dividing the sum of  $\alpha$  and  $\beta$  by half the period of the orbit. Therefore, the average slewrate to keep the satellite pointed at Earth is approximately  $5 \cdot 10^{-6}$  deg/s.

The previous analysis disregarded the change in angle due to the relative distance changing between Venus and Earth. This angle can be calculated by taking into account the orbital velocities of the two planets around the sun. Venus and Earth rotate the sun in the same direction and in roughly the same orbital plane. This is shown in Figure 12.7.

The first situation is when Venus and Earth have velocities in opposite direction. Venus maximum orbital velocity is 35.3 km/s and Earth's maximum orbital velocity is 30.3 km/s, the maximum relative velocity can therefore be estimated to be 65.6 km/s, which occurs when the two planets are on opposite sides of the sun. Venus and Earth do not reach their maximum orbital velocities at the same time, therefore this will lead to an overestimation.<sup>1</sup> During the communication window with Earth of 2 hours the change in relative distance in the described situation is  $7200 \cdot 65.6 = 472320$  km. It occurs around a distance of 261 million km. The change in pointing angle in this situation is the arctangent of the change in relative distance divided by the distance, which is 0.1 deg. Therefore, the required slew rate is  $0.01/7200 = 1.4 \cdot 10^{-5}$  deg/s.

The second situation describes Venus and Earth have a velocity in the same direction, which occurs on one side of the sun at a distance of 38 million km. The critical relative velocity can now be found by taking the difference of minimum orbital velocities, 34.8 km/s and 29.3 km/s for Venus and Earth respectively. The difference between the two velocities is 5.5 km/s. Over a communication period of 2 hours this leads to a distance change of 39600 km and a change in angle of  $\arctan(39600/(38 \cdot 10^6)) = 0.06$  deg. A slew rate of  $0.8 \cdot 10^{-5}$  deg/s is required in the second situation.

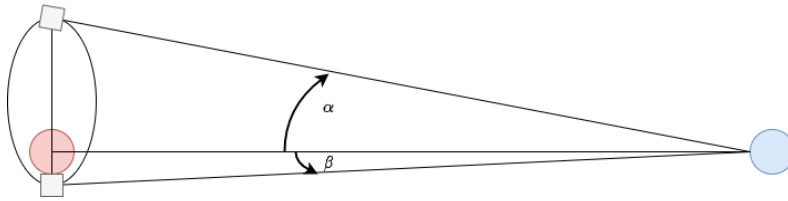


Figure 12.6: Slew angles during communication with Earth, not to scale

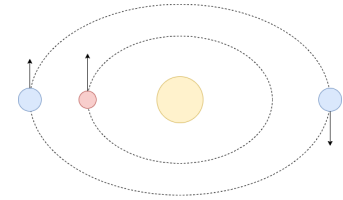


Figure 12.7: Relative velocities of Venus and Earth in two situations, not to scale

### 12.3.5. Orbiter attitude change between Venus pointing and Earth pointing

The first manoeuvre that will be discussed is the attitude change from Venus pointing to Earth pointing. The satellite will change from Venus pointing to Earth pointing once every six orbits (and back), as determined in the Chapter 9. To determine the minimal slew rate that is required to change the satellite attitude, two parameters of the manoeuvre have to be known: 1. The maximum slew angles in roll and pitch have to be known, as yaw does not change the pointing direction of the antenna. 2. The amount of time that is available for the manoeuvre.

Upper limits for the magnitude of the change in roll and pitch angle of the satellite can be set to 180 deg, this is due to the fact that it would be more efficient so slew in the opposite direction, if the required angle is higher. As only two hours of communication are required, there is still two hours available of the orbit. If a conservative buffer of 2000 s is taken for unaccounted attitude manoeuvres during a single orbit then the available time can be set to about 5200 s. Half of the 5200 s can be used to slew towards Earth and half of the time can be used to slew back to Venus. Furthermore, in a worst case scenario the momentum wheels can only be operated one at the time. Therefore, 180 deg of roll and 180 deg of pitch have to be performed sequentially. This leads to an average slew rate of  $360/2600 = 0.14$  deg/s for both roll and pitch.

### 12.3.6. Orbiter attitude control during propulsive burns

The orbiter path around the critical burn manoeuvre is shown in Figure 12.8. The main thruster of the orbiter needs to be aligned with the orbital path, so the burn will be applied in the correct direction. The tangent lines in this figure were used to calculate the required slew angle. For the tangent lines shown the calculated angle is 79.3 deg, which has to be achieved in a time of 2146 s. This leads to a slew rate of 0.037 deg/s. Moreover, when taking points closer together the slew rate converges to 0.049 deg/s. Therefore, the critical slew rate during this manoeuvre is 0.049 deg/s.

<sup>1</sup><https://nssdc.gsfc.nasa.gov/planetary/factsheet/venusfact.html> Retrieved in June 2020

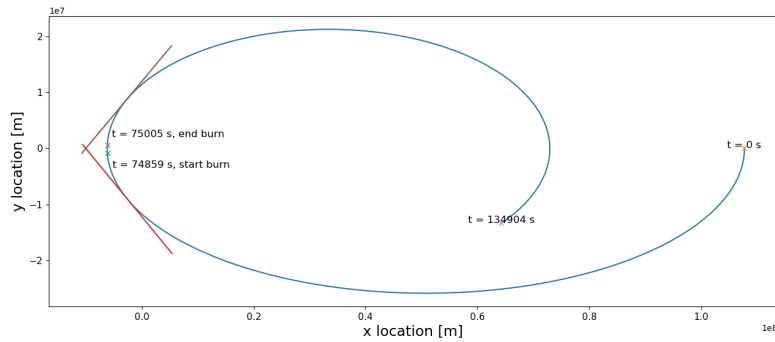


Figure 12.8: Slew angle during propulsive burn manoeuvre, plotted with tangent lines

### 12.3.7. Orbiter attitude control for scientific measurements

At this point, a neutral mass and ion mass spectrometer is carried by the orbiter. This instrument catches high velocity particles around the pericythe of the orbit. It does not require pointing. Furthermore, a camera is added to the orbiter. This camera will take images of the Venusian cloud layers and possibly be used for tracking of the aerobot, after algorithms have processed multiple images. Both these functions do not require significant pointing capabilities. Furthermore, it would be possible to add a pointing mechanism to the camera. Therefore, no orbiter attitude control analyses will be performed.

### 12.3.8. Orbiter attitude control for solar panels

The first point to discuss for attitude control of the satellite for the pointing of the solar panels is that the solar panels will be able to rotate about the solar panel arms. The solar panel arms are parallel to the  $x$ -axis defined in Figure 12.1. Therefore, no satellite roll control is required for pointing of the solar panels. The second similar point, is that the solar panels are hinged at the face of the satellite body. This will allow for a rotation about an axis parallel to the  $y$ -axis of the satellite as established in Figure 12.1, this will deem the satellite pitch control unnecessary for pointing of the solar panels.

### 12.3.9. Disturbance torque on orbiter due to solar pressure

Due to the symmetry of the spacecraft solar pressure torque is only created in a situation where the solar panels are under an angle from the hinge located at the satellite body. In this case, the horizontal component of the solar pressure creates a torque, because the solar panel arms are not located at the same height as the centre of gravity of the satellite.

The maximum force of the horizontal can be calculated using the solar irradiance of  $2600 \text{ W/m}^2$ , the speed of light  $c = 300 \cdot 10^8 \text{ m/s}$ , the solar panel area  $A = 1.6 \text{ m}^2$  and the maximum angle at which the solar panel can be pitched  $\theta = 60 \text{ deg}$ . The torque can then be found by multiplying it with the height difference of the centre of the solar panels to the centre of gravity of the satellite,  $dh_l$  and  $dh_r$ . It is conservatively estimated that the centre of gravity is  $0.25 \text{ m}$  below the hinge point of the arms. Furthermore, the solar panel arm is  $1.6 \text{ m}$  from satellite body to the centre of the panel. Therefore,  $dh_l = 1.6 \sin(60) - 0.25 = 1.1$  and  $dh_r = 1.6 \sin(60) + 0.25 = 1.6$ .

The relation between  $T = P/c \cdot A \cdot \sin(\theta) \cdot (dh_l - dh_r)$  can now be evaluated for a torque of  $T = -6.0 \cdot 10^{-6} \text{ Nm}$ . The negative sign just indicates a clockwise direction which is irrelevant for this analysis. Finally, it is assumed that accounting for the worst case scenario 5 % of the orbit time accounts for all the solar pressure torque. So over a period of 100 days, 2.5 Nms momentum storage is required.

### 12.3.10. Disturbance torque on orbiter due to gravity gradient

The effect of torque due to the difference in gravity at the top and bottom of the satellite by modelling the satellite as a slender rod with two point masses at the ends [137].

At pericythe,  $r = 6522 \text{ km}$  and the gravity gradient torque about the  $y$ -axis can now be found with the following relation  $T = 3\mu/r \cdot |I_{zz} - I_{yy}| \sin(\theta)$ . Similarly, the gravity gradient torque about the  $x$ -axis is  $T = 3\mu/r \cdot |I_{zz} - I_{xx}| \sin(\theta)$ .

Furthermore, the angle  $\theta$  is the difference between the actual satellite attitude and a nadir-pointing attitude. This angle can be constraint in multiple ways. First of all, there will not be gravity gradient torque for large angles, as the torque arises through a difference in height of the upper mass and lower mass. For higher angles of  $\theta$  the height difference is negligible. Furthermore, if  $\theta$  is zero there will actually be no moment arm, thus no torque is created either. The critical angle to be considered is about  $10 \text{ deg}$ .

Before the magnitude of the torque is calculated, it is important to discuss the time the satellite will take the critical attitude. For example, during the communication with the balloon the angle of the satellite can be considered to be very close to nadir pointing, as the balloon is in the Venusian atmosphere. When pointing the main antenna to Earth, the possibility that the satellite attitude takes on a small angle with respect to the nadir pointing line is negligible. Furthermore, propulsive burn manoeuvres are of short duration and the attitude will be about perpendicular to nadir-pointing. In all three situations, no gravity gradient torque has to be accounted for. So only during passive orbit operations gravity gradient torque can arise. However, this can be prevented by actively keeping the satellite pointed along the nadir line. For safety, an overall 5% of the orbit time around the pericythe, where keeping the satellite nadir pointed is most demanding, will have to be assessed.

The gravity gradient torque about the x-axis will have a magnitude of  $9.1 \cdot 10^{-5}$  Nm. For the mission duration of 100 days, this will lead to a momentum storage of 40 Nms. About the y-axis of the satellite the gravity gradient torque will be  $2.0 \cdot 10^{-5}$  Nm. Furthermore, this leads to a required momentum storage of 8.5 Nms over the mission period of 100 days.

### 12.3.11. Other disturbance torques: magnetic field, aerodynamic drag

Venus does not have an intrinsic magnetic field, furthermore the induced magnetic field due to the solar wind is about 15 nT [140]. Therefore, the disturbance torque due to a magnetic field can be ignored.

The density of the Venusian atmosphere at 200 km, which is the pericythe altitude, is already less than  $10^{-12}$  kg/m<sup>3</sup>. Furthermore, the satellite spends most of the orbital period significantly above 200 km. For these reasons disturbance torque due to aerodynamic drag can be neglected.

During aerobraking, the disturbance torque due to aerodynamic drag will be significant because the orbiter is around 150 km altitude in the Venusian atmosphere. However, as the distance between the center of pressure and center of gravity is unknown, the moment arm of the aerodynamic drag force is unknown as well. For now the analysis of aerodynamic disturbance torque of the orbiter falls out of the scope of the project. Furthermore, it is assumed that the margin of propellant taken in Chapter 8 will account for the extra need of momentum wheel desaturation.

### 12.3.12. Orbiter mass moment of inertia

A simplified model of the orbiter was shown in Figure 12.1. This model is used to determine the mass moment of inertia of the orbiter, so that this can be used to size the momentum wheels and reaction control thrusters at a later stage. Note that the y-dimension of the model is 'into the page', according to a right handed coordinate system.

An assumption made at this point is a uniform distributed mass inside the satellite body. This can be assumed, as the internal mass distribution lies closest to the center of gravity of the satellite, therefore this has the lowest impact on the overall mass moment of inertia. Besides this, for overall performance considerations the satellite it is attempted to have a balanced distribution, therefore the deviation from a uniform distribution is considered to be negligible. The main external components are the solar panels, the antenna dish and the main thruster. Solar panels are on the left and right of the body, the antenna is on the bottom and the thruster on the top of the model. For the mass moment of inertia calculations of the thruster and the antenna dish it was assumed that they can be modelled as a cone. These cones have the same height and radius at the tips as the original shapes of the antenna and thruster. Note that, especially for the antenna dish this is assumption causes an overestimation of the mass moment of inertia. This is due to the fact that for a cone more mass is further away from the centre of gravity than for a parabolic dish. Moreover, the y-axis and the z-axis are symmetry axes, therefore all the product moments of inertia  $I_{xy}$ ,  $I_{xz}$  and  $I_{yz}$  are zero.

Using the masses and dimension of the satellite body, solar panels, antenna and thruster as described in this subsection, the mass moments of inertia were found as follows. These values are for the satellite at beginning of life, so the satellite body mass includes full propellant tanks. Furthermore, the solar panels are not rotated along the arms or hinge. The values are:  $I_{xx} = 414$  kg m<sup>2</sup>,  $I_{yy} = 596$  kg m<sup>2</sup> and  $I_{zz} = 563$  kg m<sup>2</sup>.

### 12.3.13. Star sensor selection

Based on the slew rate analysis performed and including considerations for power, propulsion and TTC (like the link and power budgets) several optimal parameters for the star sensors were found. With these specifications in mind the Autonomous Star Sensor ASTRO 10 from Jena-Optronik was selected for this

mission. Important parameters are shown in Table 12.3. Two star sensors will be incorporated in the design, as this is the minimum required for obtaining the attitude in pitch, roll and yaw [47, 137]. The attitude determination accuracy equals  $1.5 \text{ arcsec} \approx 4 \cdot 10^{-4} \text{ deg}$  for roll and pitch and  $12 \text{ arcsec} \approx 0.003 \text{ deg}$  for yaw. Furthermore, two star sensors will be added as redundancy. These will be turned off until an error or failure of one of the main star sensors is detected.

Table 12.3: Important parameters of the star sensors

Parameter	Value	Unit	Parameter	Value	Unit
Mass	1360	g	Attitude re-acquisition	8	s
Operational temperature	-40 to 40	°C	Allowed slew rate	3	deg/s
Attitude accuracy (pitch/roll)	1.5	arcsec	Power consumption	8	W
Attitude accuracy (yaw)	12	arcsec	Lifetime	> 12	years

### 12.3.14. Momentum wheel selection

A first estimate of the moment wheel mass is done using known relations between the angular momentum of a satellite and reaction wheel mass [47]. The angular momentum can be determined by multiplying the moment of inertia in  $\text{kg/m}^2$  with the slew rate in  $\text{rad/s}$ . Using the mass moment of inertia values calculated in the previous subsection and a slew rate of  $0.5 \text{ deg/s}$  which equals  $0.0087 \text{ rad/s}$ , the estimates for the momentum wheel masses are 3.4, 4.1 and 4.0 kg for the x-, y- and z-oriented momentum wheels respectively. The wheel mass of 4.1 kg is taken as the critical value and an off-the-shelf product is sought that fits this mass estimate. Note that a fourth momentum wheel is added of the same size, as its main purpose is redundancy. The configuration of the four momentum wheels will be a pyramid shape, so the fourth momentum wheel covers all three dimensions. A brief overview of momentum wheels and their parameters are given in Table 12.4.

Table 12.4: Overview of reaction wheels

Reaction Wheel	Mass (kg)	Momentum storage (Nms)	Maximum torque (Nm)	Peak power (W)	Nominal power (W)
Bradford Engineering W18	5.2	18	0.265	168	29
Blue Canyon Technologies RW8	4.4	8	0.25	-	10
Honeywell HR061	5.0	12	0.055	80	15
Rockwell Collins RSI 12-75/60	4.9	12	0.075	90	20

First of all, the required momentum storage for the most demanding slew manoeuvre can be found by multiplying the mass moment of inertia in  $\text{kg/m}^2$  of the satellite by the slew rate in  $\text{rad/s}$ . The value found is  $596 \cdot (0.5/360 \cdot 2\pi) = 5.2 \text{ Nms}$ . Therefore, all the reaction wheels can perform this manoeuvre.

Taking into account the peak power limitations of the satellite the Honeywell HR061 are considered to be the most suitable momentum wheel. Furthermore, to decrease the amount of peak power it is decided to opt for sequential slewing for manoeuvres that require to change the attitude over multiple axes. Therefore the overall peak power of the momentum wheels lies at  $80 + 2 \cdot 15 = 110 \text{ W}$ . This is the situation where one momentum wheel is applying maximum torque, two momentum wheels are operating nominally and the fourth redundant momentum wheel is stand-by.

### 12.3.15. Reaction control system thrusters

The reaction control system will be primarily used for momentum wheel desaturation. First of all, the RCS thrusters use MON/MMH propellant with a vacuum specific impulse of 340 s, the same as the main thruster uses. This will be used later when determining the amount of propellant for the RCS thrusters.

Six reaction control system thruster blocks are required for momentum wheel desaturation, more specifically 3 pairs of symmetrically placed thruster blocks that cause roll, pitch and yaw rotations. A pair of thruster blocks for each dimension is required to keep the thruster induced motion purely rotational. Furthermore, the thruster block pair is required to only cause rotation about one axis. This will be done to prevent the simultaneous desaturation of one momentum wheel and the saturation of another. The reason

for the use of thruster blocks is the RCS is required to be able to cause rotation in both clock- and anticlockwise direction, a thruster block is actually two thrusters pointing in opposite directions.

The six thruster blocks are located outside of the satellite body. Optimal locations of the thrusters were identified and taking structural layout of the orbiter in mind the following orientation and location were selected for the roll thruster blocks and the yaw thruster blocks. **Two RCS roll thruster blocks:** aligned along the z-direction and located on the centroidal y-axis on opposite sides of the orbiter body. **Two RCS yaw thruster blocks:** aligned along the x-direction and located on the centroidal y-axis on opposite sides of the orbiter body. The identified optimal locations for the RCS pitch thruster blocks were interfering with either the antenna and main thruster or the solar panels. However, a small offset from the solar panels would be possible and only negligible interference with the solar panels is caused due to the orientation of the thruster blocks being perpendicular to the nominal solar panel orientation. **Two RCS pitch thruster blocks:** aligned along the z-direction, located with a small offset from the solar panel/centroidal x-axis on opposite sides of the orbiter body. It is recommended that the placement and design of the RCS thruster blocks is iterated with respect to the viable positions on the orbiter body at a later stage.

Assuming the centre of gravity of the satellite lies in the center of the satellite body, this means every thruster block has a moment arm of at least 0.85 m. This will be increased by putting the thruster blocks on arms to increase the distance between the thruster block and the satellite body to protect the orbiter from propellant exhaust. This arm is sized at 0.15 m. Therefore the total moment arm for each thruster is 1.0 m. Furthermore, these types of thrusters often provide low amounts of thrust, for example the Mars Reconnaissance Orbiter RCS thrusters provided  $0.9 \text{ N}^2$ . This iteration of the RCS will be sized using thrusters that provide 1 N of thrust. Therefore, a thruster block generates 1 Nm of torque.

The total momentum storage that needs to be dumped during mission can be attributed to the disturbance torque due to solar pressure and the disturbance torque due to the gravity gradient.  $T = 2.5 + 40 + 8.5 = 51 \text{ Nms}$ . 51 Ns of impulse is required. Therefore 1.6 kg of MON/MMH is required.

### 12.3.16. Orbiter attitude control performance analysis

First of all, the performance in terms of maximum achievable slew rates should be analysed. These rates can be determined by dividing the angular momentum storage of a momentum wheel by the mass moments of inertia. However, to account for saturation of the momentum wheels through disturbance torques only 8 of 12 Nms momentum storage is available. Therefore the maximum slew rates are a 1.1 deg/s roll rate, a 0.77 deg/s pitch rate and a 0.81 deg/s yaw rate.

Secondly, Figure 12.9 shows the quickest slew time for the critical 180 deg roll rotation and Figure 12.10 shows the quickest slew manoeuvre for the 180 deg pitch rotation. It can be seen that the combined time is approximately 700 s, which is significantly quicker than the 2600 s that is maximally allowed. Note that for both the roll and pitch manoeuvre the respective maximum slew rates are obtained.

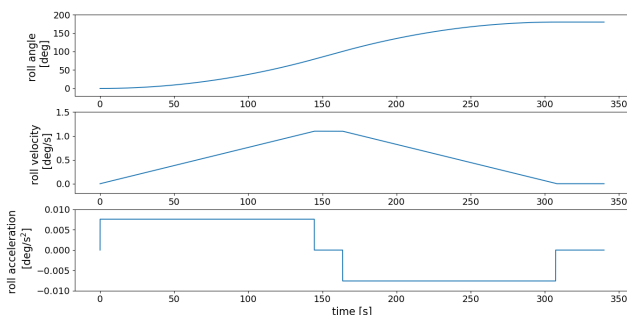


Figure 12.9: Quickest 180 deg slew about the x-axis

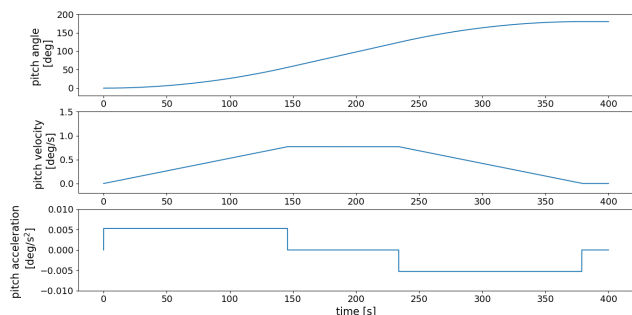


Figure 12.10: Quickest 180 deg slew about the y-axis

The second performance analysis consists of evaluating the momentum storage that is obtained when the orbiter has to achieve the required pointing accuracy of 0.03 deg during communication with the aerobot. As this is the most critical link budget, assessing the pointing accuracy in this phase will be most valuable. It is assumed that the star sensors have accurately acquired the attitude of the spacecraft and the momentum wheels have performed the slew manoeuvre to point either at Earth or the aerobot. Furthermore, during communication with the aerobot, at apocynthion, gravity gradient torque is assumed to be

<sup>2</sup><https://mars.nasa.gov/mro/mission/spacecraft/parts/propulsion/>, retrieved June 2020

negligible as it will be significantly lower than at pericythe due to the torque scaling inversely with the distance to Venus to the third power.

Therefore, the momentum storage for keeping the 0.03 deg stability will have to take into account the solar pressure torque only. The magnitude of the torque that has to be taken into account is  $6 \cdot 10^{-6}$  Nm created by solar pressure. Using the equation  $H = T/\theta \cdot P/4$ , where H is the required momentum storage in Nms,  $\theta$  is the pointing accuracy in rad, T the disturbance torque and P the satellite-aerobot communication window in s [141], the value for H, the required momentum storage during a communication window, is 21.3 Nm. The orbiter is able to store this over the four momentum wheels, note that the yaw angle of the orbiter can be freely controlled as this does not interfere with the pointing of the antenna, thus this could be used to make sure that this is stored in multiple momentum wheels.

## 12.4. Risk analysis

Several risks were identified and subsequently mitigated for the attitude determination & control system. The scales that were used to subjectively assess probability and severity of the risks are given in Section 15.1.

- A1 **Failure of a momentum wheel** leads to the inability of controlling the attitude of the spacecraft in one direction with the momentum wheels. Probability = 3, Severity = 4. **Mitigation:** A redundant momentum wheel is used in the orbiter, its orientation of can cover all the three slew angles, roll, pitch and yaw. New probability = 3, Severity = 2.
- A2 **Failure of multiple momentum wheels** leads to the inability of controlling the attitude of the spacecraft using only momentum wheels. Probability = 1, Severity = 5 **Mitigation:** The reaction control system thrusters can be used to control the orbiter attitude. The RCS thrusters are oriented such that they provide attitude control about all orbiter axes. However, due to the limited amount of propellant the impact of this risk is still deemed significant. Probability = 1, Severity = 4.
- A3 **Failure of star sensor** leads to degradation of the accurate positioning of the spacecraft. Probability = 1, Severity = 3. **mitigation:** For both the roll/pitch attitude determining star sensor and the yaw attitude determining star sensor a redundant star sensor is added. Probability = 1, Severity = 1.

## 12.5. Sensitivity analysis

A sensitivity analysis has been performed on the momentum storage required with a change in mass moment of inertia. This is shown in Figure 12.11. It is shown that with changes in moments of inertia of 20%, the angular momentum storage for a slew operation at 0.5 deg/s keeps being feasible using the selected momentum wheel.

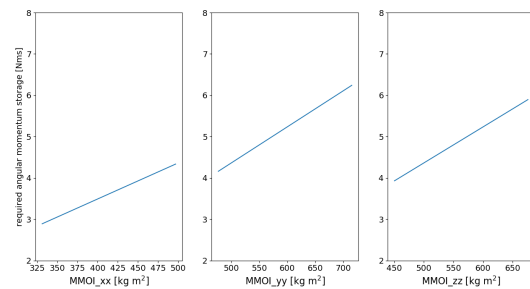


Figure 12.11: Sensitivity analysis on momentum storage due to change in mass moment of inertia

## 12.6. Verification and validation

Verification of the aerobraking and propulsive burn slew angle determination code and mass moment of inertia code was performed by means of unit test. Furthermore, a possibility of validating the mass moment of inertia code is discussed. First of all, **verification of the slew angle determination** consisted of unit testing the code with inputs of parallel and perpendicular lines. Furthermore, **the validation of slew angle determination** during a propulsive burn and aerobraking was done graphically with the manoeuvres plotted to scale. **Verification of the the mass moment of inertia code** was through unit testing known configurations. Examples are a 1 m<sup>3</sup> cube size satellite and an orbiter with point mass components for unit testing the Steiner terms. Finally, as means of **validation of the mass moment of inertia code**, the technical drawing program CATIA could be used. If a complete drawing of the orbiter is made with the correct dimensions it would provide a value for the mass moment of inertia about all axes.

# 13 Structures and Materials: Space Segment

In this chapter, the structural design of the two spacecraft will be discussed. In the first Section an overview of the orbiter and transfer module configurations is given. Afterwards the functional analysis and the approach to sustainability are presented in Section 13.2. Then in Section 13.3 the structural design is shown and in Section 13.4 and Section 13.5 the risks and sensitivity of the design are determined. Finally the verification and validation procedures are presented in Section 13.6.

## 13.1. Design overview

As shown in Chapter 3 the bus consists of a transfer module and an orbiter which are vertically stacked. The transfer module is positioned at the bottom as this is the heaviest to minimise bending moment induced by the launch loads. An overview is also presented in Chapter 3. The structure of the transfer module consists of a closed cylindrical shell to support the thermally insulated subsystems and an open truss structure for mounting the aeroshell, antenna and solar panels. The aeroshell is attached top down to allow for easier mounting and thus a reduction in structural mass. A shell was chosen as the primary structure as this allows for a closed section without adding an additional top panel, and because bending stresses will be very high due to the orbiter being stacked on top of it.

For the orbiter a nearly cubical box-shaped structure was chosen. Many modern spacecraft use this configuration as it is easy to manufacture and minimises the use of heavy corner joints [137]. For this particular mission it is even more advantageous as a box is beneficial for the thermal subsystem, which is a driving part of the design due to the relative proximity of the sun (see Chapter 11). Internally, the primary structure is in a H-shape. This design was chosen because it allows for better fitting of the subsystems and the two propellant tanks. This lay-out is mostly used for missions with a bi-propellant propulsion system and is also planned for the Envision mission [44, 93]. Lastly, the H-shape is also great for accessibility during the production phase.

An overview of the important dimensions of the primary structure of both spacecraft is given in Table 13.1. The cross-section of both are shown in Figure 13.1. For the second moment of area calculations done in subsequent sections, a thin wall assumption is made, which Table 13.1 validates. The distance  $a$  was picked in such a way that  $I_{xx} \approx I_{yy}$ .

Table 13.1: Structural data overview

Spacecraft	Dimensions	Face sheet thickness	Core Thickness	Total structural mass
Orbiter	1.7 x 1.7 x 1.2 m <sup>3</sup>	0.5 mm (2x)	8.6 mm	131.1 kg
TRM	R = 1.0 m   l = 1.3 m (shell)	0.5 mm (2x)	5.0 mm	183.3 kg

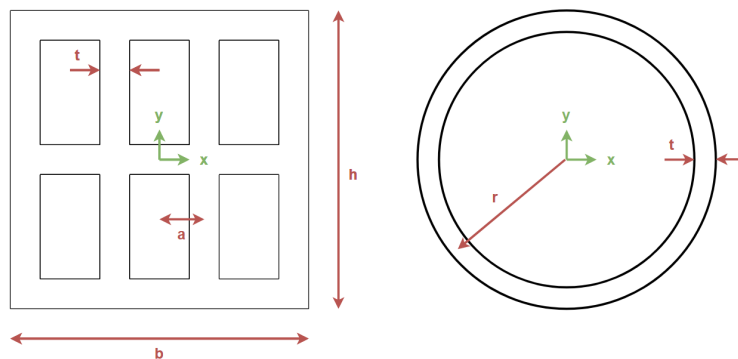


Figure 13.1: Cross section primary structure of the orbiter (left) and the transfer module (right)

### 13.1.1. Approach to sustainability

For the structural design sustainability was an important parameter. This mainly influenced the material choice. No rare materials were used for the design. Besides that, making sure that the structures are accessible for manufacturing greatly improves the safety of the people in the production line. Lastly, the aluminium alloys used for the structure are recyclable, which means that waste produced during manufacturing can be reused. In this way, all three pillars of sustainability are taken in to account.

## 13.2. Functional analysis

For the design of the structural elements presented in the previous section, it is important to check if they fulfil their function. The orbiter has five main functions. Firstly, the structure has to carry the loads during the orbiters life time. Secondly, the structure must be able to support all subsystems. Thirdly, the structure must have a deployment mechanism for the solar array and allow for pointing. Finally, the structure must protect the other subsystems from the space environment. The transfer module has all the orbiter's structural functions and also two more: it must be able to carry and deploy the aeroshell. The requirements that flow from these functions are shown in Table 13.2 and Table 13.3.

Table 13.2: Requirements on Structures and Materials of the Orbiter

Identifier	Requirement	Checkbox	Explanation in
ORB-SM-01	The design shall be able to support all subsystems	✓	13.1
ORB-SM-02	The design shall be able to accommodate the pointing requirements from all subsystems	✓	13.1
ORB-SM-03	The structure shall be able to withstand launch loads as defined in the Falcon 9 April 2020 user manual.[46]	✓	13.3.2
ORB-SM-04	The design shall prevent dynamic coupling between the orbiter and the Falcon 9. [46]	✓	13.3.2
ORB-SM-05	The materials shall be able to withstand the operational conditions.	✓	13.3.1
ORB-SM-06	The design shall allow manufacturing with current manufacturing methods.	✓	13.1

Table 13.3: Requirements on Structures and Materials of the Transfer Module

Identifier	Requirement	Compliance	Explanation in
TRM-SM-01	The design shall be able to support all subsystems	✓	13.1
TRM-SM-02	The design shall be able to accommodate the Aeroshell	✓	13.3.3
TRM-SM-03	The design shall allow for the separation of the Aeroshell	✓	13.3.3
TRM-SM-04	The structure shall be able to withstand launch loads as defined in the Falcon 9 April 2020 user manual.[46]	✓	13.3.2
TRM-SM-05	The design shall prevent dynamic coupling between the transfer module and the Falcon 9. [46]	✓	13.3.2
TRM-SM-06	The materials shall be able to withstand the operational conditions.	✓	13.3.1
TRM-SM-07	The design shall allow manufacturing with current manufacturing methods.	✓	13.1

## 13.3. Design approach

In this section the structural design of the orbiter and the transfer module are presented, which first discusses the material selection, then the failure modes and finally the determination of the structures and mechanisms.

### 13.3.1. Material selection

The selection strategy for picking the materials used for different structural elements in the space segments seeks the best match between the required properties and different material profiles. The first step in this

process is filtering out all material that cannot meet the constraints. Simply due to the environment that the spacecraft have to operate in and the shape that they have many materials can be discarded. Ordering materials can be done by the use of material indexes, which depend on shape. By looking at the methodology presented in [138], whereby the thickness is kept as a variable, it was found that for minimising the weight, materials should first be filtered based on specific stiffness ( $E/\rho$ ) [138]. This resulted in either aluminium alloys or carbon fibre reinforced polymers. Furthermore, when looking at the thermal properties of aluminium matrix composites it was found that they possess high-temperature capability, high thermal conductivity, low CTE, while still having high specific stiffness and strength [142]. This in combination with the current sandwich panel trend led to the decision to use aluminium sandwich panels [125]. For the core, aluminium honeycomb was picked after seeing it was used for Venus Express and also planned for EnVision [44, 93]. The main advantages of sandwich panels are their very light weight, very high flexural rigidity and excellent thermal insulation characteristics [143]. For these sandwich panels, it is valid to assume that the face sheets carry the normal stresses (uniform across the thickness), while the honeycomb core takes care of the shear stresses.

This decision still leaves thousands aluminium alloys open for both the face sheets and the core. For the face sheets, Aluminium alloys from the 2xxx, 5xxx and 7xxx series are taken into account as these are typically used for space missions. Within the scope of the project it is not possible to access every type of aluminium so the most common ones for each series have been used in the trade-off [144]. The properties of these aluminium alloys can be found in Table 13.4. For the aluminium honeycomb cells, even more options exist as the diameter of hexagonal cells greatly influences the properties as well as the material. Two options are listed in Table 13.5. Lastly, with this material choice the option exist to fill the honeycomb cells with foam. This would greatly improve sound absorption and shock absorption capabilities for a small increase in weight [145], but was deemed to be unnecessary.<sup>1,2</sup>

Table 13.4: Aluminium face sheet data sheet [146]

Material	E-modulus	Density	$\sigma_{yield}$	$\sigma_{ultimate}$	poisson ratio
Aluminium 2014-T6	73.1 GPa	2800 kg/m <sup>3</sup>	414 MPa	483 MPa	0.33 [-]
Aluminum 5083-H321 [125]	71.1 GPa	2660 kg/m <sup>3</sup>	268 MPa	367 MPa	0.33 [-]
Aluminium 7075-T6	71.7 GPa	2810 kg/m <sup>3</sup>	503 MPa	572 MPa	0.33 [-]

Table 13.5: Aluminium honeycomb core data sheet [125]

Material	Density	G-modulus, L	G-modulus, W
A3003-H19	54.4 kg/m <sup>3</sup>	260 MPa	130 MPa
A3003-H19	83.2 kg/m <sup>3</sup>	440 MPa	220 MPa

### 13.3.2. Primary structure design

Launch loads that are defined by the Falcon 9 launcher are applied to the configurations in the design overview to determine dimensions [46]. For this design phase it was assumed that the launch loads would be the constraining factor [47]. Sound pressures, sine vibrations, random vibrations, separation loads and transportation loads are assumed to be none constraining.

**Launch load** The highest loads that the spacecraft have to endure during their lifetime are the launch loads. The Falcon 9 user manual specifies the load factors during launch [46]. All extreme cases were taken into account in the calculations. The combined axial, lateral and bending loads on a thin walled cylinder can be calculated using Equation 13.1 [47]. For the positive load factors (which were found to be the most extreme) the transfer module has to also carry the loads of the orbiter as it is at the bottom. In this equation,

<sup>1</sup><http://www.matweb.com/search/DataSheet.aspx?MatGUID=e5de9f1161d34f71a34ae016723d097f&ckck=1>, retrieved on 16 May 2020

<sup>2</sup><http://www.matweb.com/search/DataSheet.aspx?MatGUID=4f19a42be94546b686bbf43f79c51b7d>, retrieved on 16 May 2020

$z$  is the maximum axial distance as can be found in Chapter 3. In Equation 13.2, a similar relation for the loads on the orbiter is presented [137]. For the orbiter the negative load factors lead to the highest applied load.

$$P_{eq,TRM} = P + \frac{2M}{R} = (m_{wet,TRM} + m_{wet,ORB})a_{axial} + \frac{2(m_{wet,TRM} + m_{wet,ORB})a_{lateral}z}{R_{shell}} \quad (13.1)$$

$$P_{eq,ORB} = P + \frac{Mc}{I} \cdot A = (m_{wet,TRM} + m_{wet,ORB})a_{axial} + \frac{(m_{wet,TRM} + m_{wet,ORB})a_{lateral}zh}{2I} \cdot A \quad (13.2)$$

**Failure** The first failure mode that is considered is yielding or breaking of the material. Equation 13.3 and Equation 13.4 relate the geometry and loads to the material properties. The core area is neglected, as the face sheets take all the normal stress. The load factors are determined based on international standards [147] ( $KQ = 1.25$ ;  $FOSY = 1.1$ ;  $FOSU = 1.25$ ).

$$\sigma_{yield} \geq \frac{KQ \cdot FOSY \cdot P_{eq}}{A} \quad (13.3) \quad \sigma_{ultimate} \geq \frac{KQ \cdot FOSU \cdot P_{eq}}{A} \quad (13.4)$$

**Buckling of sandwich sheets of the orbiter** The second failure mode is global buckling of the sandwich sheets. The critical buckling load is given by Equation 13.5 and depends on the supports and the loading direction [143]. In the launch configuration, the orbiter is assumed to be clamped at the bottom. Therefore a  $K$  value of 0.25 is assumed. The  $\langle EI \rangle$  neglects the core presence;  $L$  is the height of the box;  $k/\langle GS \rangle$  is given by Equation 13.6;  $G_c$  is the shear modulus of the core;  $t_f$  is the thickness of the face sheets; and  $t_c$  is the thickness of the core. The applied load multiplied by a safety factor ( $KQ \cdot FOSY$ ) must be lower than the critical buckling load.

$$F_{cr} = K \frac{\pi^2 \langle EI \rangle}{L^2 + \pi^2 \frac{\langle EI \rangle}{\langle GS \rangle} kK} \quad (13.5) \quad \frac{k}{\langle GS \rangle} = \frac{1}{G_c (t_c + 2t_f)} \quad (13.6)$$

**Buckling of cylindrical sandwich shell of the transfer module** For cylindrical shells the buckling occurs differently than for sheets. The critical load per unit of circumference of a long cylindrical sandwich shell is given by Equation 13.7 [148].  $\gamma$  is given by Equation 13.8 and represents the empirical knockdown factor, which is necessary to compensate for the discrepancy between linear buckling theory and experiments. Lastly  $\nu_f$  represents the Poisson-ratio of the face sheet. The applied load per unit circumference multiplied by a safety factor ( $KQ \cdot FOSY$ ) must be lower than  $N_{x,cr}$ .

$$N_{x,cr} = \gamma \frac{2E_f}{\sqrt{(1-\nu_f^2)}} \frac{t_c t_f}{R_{shell}} \left\{ 1 - \frac{E_f}{2\sqrt{(1-\nu_f^2)}} \frac{t_f}{R_{shell} G_c} \right\} \quad (13.7)$$

$$\gamma = 1 - 0.901 (1 - e^{-\phi}) \quad (13.8) \quad \phi = \frac{\sqrt{2}}{29.8} \sqrt{\frac{R_{shell}}{t_c}} \quad (13.9)$$

**Vibrational analysis** Lastly, dynamic coupling between the spacecraft and the launch vehicle should be prevented. The Falcon 9 manual states that the fundamental bending mode must be greater than 10 Hz and the fundamental axial mode greater than 25 Hz [46]. To check whether the design satisfies the requirements a preliminary vibrational analysis is performed as described in Inman et al. [149]. The system is modelled as a multiple degree of freedom undamped free vibration, as shown in Figure 13.2. The two spacecraft are modelled as a beam with a point mass at the top. The beams are in turn represented by an equivalent spring constant, which is defined by geometrical and material properties of the beam. Only the geometry of the primary structures, as presented in Section 13.3, is taken into account for the beams. The equivalent spring constant of the beam for accessing the the fundamental axial mode is given by Equation 13.10 and for the fundamental bending mode by Equation 13.11. In this equation  $I$  represents either  $I_{xx}$  or  $I_{yy}$  which were designed to be approximately equal as mentioned in Section 13.1. Since the stiffness of the core is

negligible it is ignored, but in reality this will have a small positive contribution. Further assumptions are that the system is linear time invariant and that the stiffness is proportional to the displacement.

$$k_{axial} = \frac{EA}{L} \quad (13.10)$$

$$k_{lat,x} = \frac{3EI}{L^3} \quad (13.11)$$

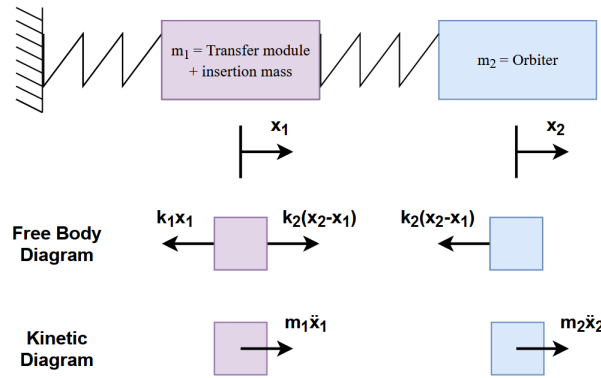


Figure 13.2: MDOF undamped mass spring system

In Figure 13.2, the free body and kinetic diagrams are drawn for axial motion, as is the standard [149], but for lateral motion all arrows can be rotated  $90^\circ$ . The spring constants already incorporate the loading case (axial or bending) and from this the equations of motion of the system were derived, which are presented in the  $M\ddot{\mathbf{x}} + K\mathbf{x} = 0$  form in Equation 13.12. Here  $M$  and  $K$  are dependent on the geometrical and material properties of the beams. Equation 13.13 can be solved for  $\omega$ . The natural frequency is given by Equation 13.14. For the axial natural frequencies  $k_1$  and  $k_2$  are found by Equation 13.10 for the cylindrical shell and the H-shaped box respectively. Similarly for the lateral natural frequencies,  $k_1$  and  $k_2$  are found by Equation 13.11. Finally,  $m_1$  and  $m_2$  are defined by the wet mass of the transfer module and the orbiter, respectively.

$$\begin{bmatrix} m_1 & 0 \\ 0 & m_2 \end{bmatrix} \begin{bmatrix} \ddot{x}_1 \\ \ddot{x}_2 \end{bmatrix} + \begin{bmatrix} k_1 + k_2 & -k_2 \\ -k_2 & k_2 \end{bmatrix} \begin{bmatrix} x_1 \\ x_2 \end{bmatrix} = \begin{bmatrix} 0 \\ 0 \end{bmatrix} \quad (13.12)$$

$$\det(K - \omega^2 M) = 0 \quad (13.13) \quad f_n = \frac{1}{2\pi} \omega \quad (13.14)$$

**Overview** For both the orbiter and the transfer module, global buckling was the driving failure mode. Aluminium 5083-H321 was picked for the face sheets as this results in the lightest structure for both spacecraft. A 0.5 mm thickness of the sheets was designed for, which is determined by the minimum sheet thickness before imperfections become driving for the design [150]. After iterating the design it was found that designing for this minimum face sheet thickness led to a lighter design for both spacecraft. This comes at the cost of thicker cores, but this is acceptable since the volume of the spacecraft was found not to be constraining (see Chapter 3). Due to this same reasoning, the lower density core was chosen, which resulted in a 5.0 mm core for the transfer module and a 8.625 mm core for the orbiter. Iterations of the core thickness were done in steps of 0.125 mm, as this was found to be the standard. This led to a primary structure weight of 23.9 kg for the transfer module and 62.8 kg for the orbiter.

Even if the natural frequencies were not constraining for the structural design, they are still important parameters. The axial natural frequencies are 54.0 Hz and 184.7 Hz and the lateral natural frequencies are 50.7 Hz and 157.1 Hz for the orbiter and the transfer module, respectively. For this  $E$  can be found in Table 13.4;  $A_{TRM}$  is  $0.0063 \text{ m}^2$ ;  $A_{ORB}$  is  $0.0119 \text{ m}^2$ ;  $I_{TRM}$  is  $0.0031 \text{ m}^4$ ;  $I_{ORB}$  is  $0.0041 \text{ m}^4$ ;  $L_{TRM}$  and  $L_{ORB}$  can be found in Table 13.1;  $m_{wet,TRM}$  and  $m_{wet,ORB}$  can be found in Table 16.2. The lateral natural frequencies seem quite high, but a sensitivity analysis shows that this is caused by the short height ( $Z$ ), relative to the width ( $X, Y$ ), which questions the validity of the assumption that only the primary structures are taken into account, since the height of the struts between the orbiter and the transfer module is considerable even if they are very stiff. Analysing this further would require vibrational analysis methods in a finite element

model. Dynamic finite modelling is however beyond the scope of this project and therefore left as a recommendation. Even if these lateral frequencies seem off they are far above the required 15 Hz so it is fair to assume that this will not disproportionately influence the design.

### 13.3.3. Mechanisms

Both the orbiter and the transfer module need a mechanism for deploying their solar panels and the transfer module needs an extra mechanism for separating from the aeroshell.

**Solar panel deployment** The design of the solar panel structure and deployment mechanisms for both the orbiter and transfer module were driven by the following trades:

- **Available external surface area of the spacecraft body and risk of shadowing.** The available external surface area of the spacecraft body could be utilised for body-mounted solar panels. However, body-mounted solar panels leave little space for mounting external apparatus, such as outward-facing scientific payload, radiators and antennae. The presence of these external items also lead to shadows cast on the panels, which lead to further losses in solar array effectiveness.
- **Pointing requirements of spacecraft and subsequent thermal considerations.** The placement of solar arrays are dependent on whether the spacecraft is required to point to a specific point consistently throughout its mission. The orbiter High Gain Antenna and side-mounted Low Gain Antenna, respectively, need to point towards Venus and Earth, (Chapter 9), within a polar orbit (Chapter 5). It was found that during the scientific mission there is a consistent plane that can always be normal to the sun vector, and as a result this heavily favours deployed solar array 'wings' with sun tracking. The pointing considerations also eliminates the option of body-mounted solar panels due to the consistent shadowing of certain faces while restricting roll-cooling of panels.
- **Area and dimensions of the spacecraft body.** Smaller spacecraft with less available area on the mounting side would require more intricate articulated systems and slender solar panel wings, which may introduce extra mass and complexity. Provisions for clamping devices are also required to fix folded solar panels to the body of the spacecraft.
- **Aerobraking manoeuvres.** The orbiter will undergo aerobraking manoeuvres to reduce its apocynthion height. As a result, the solar panel structure should be reinforced for the aerodynamic loads, requiring rigid substrate panel material.

To prevent shadowing of the solar array by the orbiter body and 3 m diameter High Gain Antenna, the array panels are spaced further outboard of the orbiter structure via two struts of 90 cm each, which in turn is connected to the solar array drive mechanism (SADM) on the solar array body. As the orbiter module experiences aerobraking forces, the struts and array panels will be reinforced by rigid aluminium honeycomb panels, which reduces the specific power of the solar array. For deployment, the orbiter solar array would include two hinges: one located at the joint between the strut and the array panel, and another with the strut and SADM. During launch, the array would be folded and clamped to the body of the orbiter, and would be unfolded, as depicted in Figure 13.3, at the start of the transfer trajectory to Venus. The mass of the solar panel itself is budgeted within the power subsystem mass budget, and the strut and SADM is budgeted in the structures section (Table 13.6) due to the extra mechanical provisions to ensure optimal solar coverage.

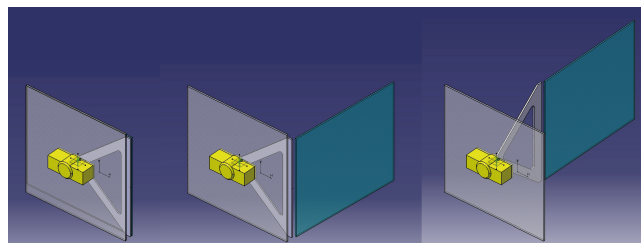


Figure 13.3: Cutout of the unfolding of the orbiter solar array (in turquoise), with the side panel of the body as reference.

As the transfer module does not experience aerobraking forces, the solar array substrate material can be made from lighter flexible substrate materials, which allows for alternate deployment mechanisms other than rigid hinges [147, 151]. The transfer module also has a less constraining pointing requirement, and it is assumed that the transfer module can slew itself to ensure optimal solar coverage. The inclusion of

outboard struts are not considered as a result. The masses for the SADM is included in Table 13.7.

**Aeroshell support structure and separation mechanism** The structure needed to mount the aeroshell on the transfer module is not something that could be done with preliminary calculations, as this is not treated in spacecraft structures books. Nevertheless, this is a substantial part of the mass of the structural subsystem and creating a load path is essential. Therefore, it was decided to make use of a similar strut structure as was proposed for the Venus flagship mission [15].

Adjustments were made to the truss structure, as BLOON contains a single 1098 kg aeroshell compared to two of 1963 kg for the Venus flagship mission. Furthermore, the truss structure is only used for mounting the aeroshell, solar panels and the antenna compared to all elements for Venus flagship mission. The design is presented in Figure 13.4. The truss structure weights 89.7 kg and 30% contingency factor is applied due to the uncertainty. Furthermore, this configuration requires an entry system latch and release systems for separation. The reliability of this mechanism is very important as it failure would mean mission failure. Therefore, the system will make use of three forward bipod fittings which have great heritage and will be tested intensively. The bipod fittings weigh 2 kg each [15].

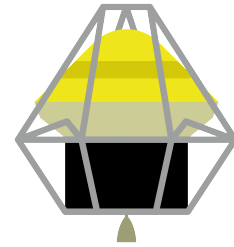


Figure 13.4: TRM truss structure

### 13.3.4. Mass budgets

Finally in Table 13.6 and 13.7, the mass budget of the structural subsystem of the orbiter and the transfer module are shown. All the current best estimates were treated in this chapter except for the equipment support structure. This was estimated to be 15% of the equipment mass of every subsystem [137]. This was applied to the subsystems after the use of safety factors. For this reason, no other safety factors were taken into account. For the strut structure of the transfer module a 30% contingency factor was applied due to the uncertainty. To the other elements a 25% contingency factor was applied following the current design phase [47].

Table 13.6: Mass budget structural design orbiter

Element	CBE Mass	Units	Contingency	Mass
Primary structure	62.8 kg	1	25%	78.5 kg
Equipment support structure	-	1	-	38.3 kg
Solar array drive mechanism[152]	1.7 kg	2	25%	4.3 kg
Solar panel struts	4.0 kg	2	25%	10.0 kg
total				131.1 kg

Table 13.7: Mass budget structural design transfer module

Element	CBE Mass	Units	Contingency	Mass
Primary structure	23.9 kg	1	25%	29.9 kg
Equipment support structure	-	1	-	25.0 kg
Solar array drive mechanism[152]	1.7 kg	2	25%	4.3 kg
Truss structure	89.7 kg	1	30%	116.6 kg
Birod separation mechanism	2.0 kg	3	25%	7.5 kg
total				183.3 kg

## 13.4. Risk analysis

Several risks were identified and subsequently mitigated for the structural design. The risks are subjectively judged on the probability of them occurring and the impact they could have on the mission. For scales, see Section 15.1.

- SM1 **Thin aluminium plates** Failure due to cracks and imperfections from manufacturing. Probability = 3, Severity = 5. **Mitigation:** Use of a minimum thickness. New Probability = 1, Severity = 5.
- SM2 **Separation failure** The aeroshell cannot separate. Probability = 2, Severity = 4. **Mitigation:** Use of bi-pod strut mechanism which has very high heritage. Probability = 1, Severity = 4.
- SM3 **Driving mechanism of solar panels fails** As the driving mechanism of the solar panel is a mechanical device exposed to the external environment, the lubricants of moving joints within the device will suffer from outgassing effects, leading to increased friction and mechanical wear on the device. The spacecraft will not be able to consistently face towards the sun vector, leading to significantly reduced mission capability. Probability = 2, Severity = 4. **Mitigation:** The outgassing and performance of lubricants was studied extensively in tribology studies by space agencies, and have published guidelines on mitigation strategies [153]. Commercial off-the-shelf drive mechanisms are qualified for a higher set number of actuations per mission than the mechanisms' operational lifetime and adequate performance even in reduced mechanism capability, therefore the usage of qualified drive mechanisms would reduce the probability and severity of failure. Probability = 1, Severity = 3.
- SM4 **Solar panel deployment failure** If the solar panels do not deploy, the satellite will receive inadequate power supply for nominal operation, leading to a total failure of the mission. Probability = 2, Severity = 5. **Mitigation:** Deployment mechanism will have redundancy in the hold-down and release mechanisms. Each hold-down clamp will have more than one cable-cutter that is capable of unclamping the folded solar array by itself, and procurement of hold-down and release mechanism elements will factor the qualified capability of the elements. New Probability = 1, Severity = 5.

### 13.5. Sensitivity analysis

Besides risk, the stability of the design when values change was analysed. As mentioned in the mass budget, sensitivity analysis was performed on the vibrational analysis. The sensitivity to the height of the structure, and the effect of changing the mass fraction between the orbiter ( $m_{wet,ORB}/m_{tot}$ ) and the transfer module ( $m_{wet,TRM}/m_{tot}$ ) was analysed as this changed constantly during the design. As can be seen in Figure 13.5, the effect of a changing mass fraction does not drive the design. Since the applied load does not depend on the design no sensitivity study was performed on that. Furthermore, calculations based on statistics were also not analysed. The last thing that has an influence is a change of geometrical properties. Except for the height of the structures, other geometrical properties do not seem to have a disproportionate influence on the design. This was checked by stress testing the code.

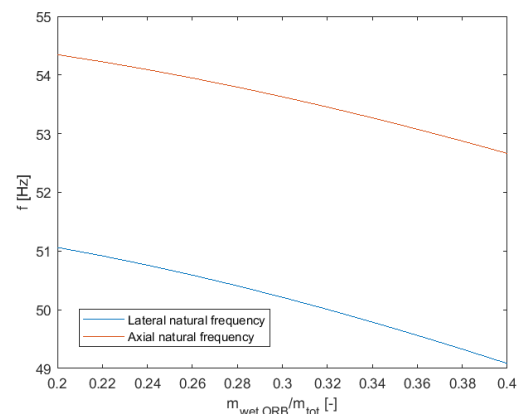


Figure 13.5: Natural frequencies for a varying mass fraction

### 13.6. Verification and validation

Unit testing was done for code verification. As mentioned in Section 13.3, optimally a dynamic finite element model analyses of the stresses and vibrations during launch would be performed. This is currently outside the scope of this design, but is strongly recommended for further research on the topic. FEM analysis is always the preferred validation method and would thus be essential [137, 147].

# 14 Structures and Materials: Atmospheric Segment

This chapter describes the structural, material and configuration design for the atmospheric mission items. The atmospheric segment covers the dropsonde, aerobot gondola, aerobot tether and aeroshell design, while the aerobot balloon design is covered separately in a standalone chapter in Chapter 7, and the space segment design covering the orbiter and transfer modules are covered in Chapter 13.

## 14.1. Design overview

The aerobot gondola is an octagonal structure made from aluminium honeycomb, encapsulating almost all interior elements from the Venusian environment. It houses the 25 dropsondes on one floor and the aerobot subsystems on a floor above it. The dropsonde is a teardrop-shaped single-use probe consisting of a spherical pressure vessel and an X-profile tail; most of the dropsonde subsystems are housed inside the spherical vessel, which is made from a thermoset glass fibre-reinforced composite. The aerobot tether is 50 m long and made of woven Kevlar coated with Teflon. The aeroshell is a 3 m diameter capsule consisting of a 45 ° rounded front shell, a back shell, balloon inflation system and structural harnessing for the aerobot.

Component	Amount (-)	Mass (kg)
Dropsonde (exterior and housing)	25	1
Gondola	1	15.7
Aerobot Tether	1	0.37
Aeroshell	1	260.2

Table 14.1: Overview of structural items' masses



Figure 14.1: Fully deployed aerobot gondola

### 14.1.1. Approach to sustainability: dropsonde shell material

The dropsonde exterior material needs to survive the extreme pressure, temperature and chemical environment of the lower atmosphere; normally this would require high-performance rare materials such as titanium and beryllium alloys, but the difficulty in machining for titanium and the toxicity of beryllium led to their rejection in the materials selection. Because more than 25 dropsondes will be produced for testing, qualification and the mission itself, the relative ease of fabrication for glass fibre-reinforced material is preferred.

## 14.2. Functional analysis

The goal of the structures and materials division for the atmospheric segments is to physically house and protect all aerobot subsystem items during the mission phases. Two configurations are considered: stowed and deployed. While stowed, the structural items should be stiff and strong enough to withstand G-loads from atmospheric entry. While deployed, the structural items should withstand expected operational loads and protect delicate aerobot systems from sulphuric acid attack. In between, requirements were defined to ensure the deployment mechanisms for movable items are reliable.

Table 14.2: Requirements on the structural systems on the atmospheric segment.

Identifier	Requirement	Compliance
AT-SM-G-01	The gondola shall protect the internal equipment from at most $0.1 \text{ gm}^{-3}$ of sulphuric acid exposure	✓
AT-SM-G-02	The gondola structure shall fully enclose and fix all internal equipment and deployables in at least 40 g load from atmospheric entry	✓
AT-SM-D-01	The dropsonde shall protect the internal equipment from at most $0.1 \text{ gm}^{-3}$ of sulphuric acid exposure at 540 K	✓
AT-SM-D-02	The dropsonde structure shall protect the internal equipment from 0.236 atm to 15.9 atm	<TBD>
AT-SM-D-03	The dropsonde deployment mechanism shall not have a single point of failure for each critical component	✓
AT-SM-D-04	The dropsonde exterior shall have a total drag coefficient of 0.15	<TBD>
AT-SM-T-04	The aerobot tether shall be able to nominally withstand gust loads of double the weight of the gondola	✓
AT-SM-A-01	The aeroshell structure shall fully enclose and fix the aerobot and required apparatus for deployment in 40 g load from atmospheric entry	✓
AT-SM-A-02	The aeroshell internal structure shall be capable of surviving at least 40 g from atmospheric entry	✓

### 14.3. Design approach

The design approach section discusses the design decisions made with respect to the individual atmospheric mission elements, with respect to the structural design, material choices and the configuration of integrated subsystems on the atmospheric mission elements.

#### 14.3.1. Dropsonde

As mentioned in the design overview, the dropsonde was designed for operation between 60-25 km altitude. The constraining conditions are the operational thermal, pressure and chemical environment ranges for the dropsonde external structure. While the pressure differential between 0.0236 MPa (0.236 bar) at 60 km altitude and 1.5 MPa (15 bar) at 25km altitude is within range of lightweight pressure vessel design, the maximum design temperature of 540 K (267 °C) requires the use of enclosed pressure vessels with thermal protection and feed-through interfaces with the environment. The combination of packing the dropsonde subsystems in a lightweight pressure vessel provides a unique design challenge. As the dropsonde is only active for around 27 minutes of operation, the design goal is to utilise reliable and lightweight materials.

The dropsonde comprises of a spherical pressure vessel with a X-tail shaped as a teardrop to fulfil the necessary required aerodynamic drag coefficient. Inside the pressure vessel are the DROPP scientific package, battery, thermal protection layer, data handling and processing stack, and the patch antenna. The placement of the temperature-sensitive patch antenna inside the pressure vessel requires the usage of radio-transparent shell material such as glass fibre-reinforced plastic (GRP) in a thermoset matrix. The X-tail includes a mount for firm clamping to the payload bay, the dropsonde is physically interfaced to the dropsonde payload bay either via tensioned cable, clamps or bolts, which will be severed by the payload bay separation system; an umbilical cable provides an electric and electronic interface to the dropsonde systems for activation and telemetry. Feed-through lines are channelled through the pressure vessel for electronic interfacing with the dropsonde, one at the mounting point of the MET patch and another on the trailing edge for the electronic umbilical with the aerobot gondola. For long-term protection from sulphuric acid attack on the dropsonde exterior, a coat of polytetrafluoroethylene (PTFE/Teflon) is used on the exterior on top of the white thermal coat.

A structural mass budget of 1 kg was assigned per dropsonde, including the exterior of the structure and the payload bay housing. It was suggested in the ESA 2004 Microprobe Study that a total mass of 100 g order of magnitude is feasible for dropsondes with a target altitude of about 30 km, but little other resources exist on the sizing of the dropsonde [32]. A more detailed mass estimate would be possible after determining the required thickness of material for the pressure vessel, as well as the mass of required mechanisms for the dropsonde payload bay.

### 14.3.2. Dropsonde payload bay

As for the dropsonde payload bay, the design direction was defined by reliability, deviation of centre-of-gravity from dropsonde releases, and separation mechanism complexity. Both the reliability and mechanism complexity design goals are positively related; a complex separation mechanism leads to reduced reliability and added mass. This leads to the selection of gravity-assisted release mechanisms for dropsonde separation.

The dropsonde payload bay contains 25 dropsonde slots arranged in a diamond arrangement, and are located on the bottom of the aerobot gondola to prevent collision with other aerobot subsystems (illustrated in Figure 14.3). For reliability of separation, during Venus operations the dropsonde slots are open to the Venusian environment with no mechanical doors providing a potential point of failure. The dropsondes are released sequentially from the outermost first, with the opposite dropsonde released subsequently to minimise gondola centre-of-gravity deviations. Each slot contains an individual release mechanism with a double redundancy of either bolt cutters or wire cutters actuated by pyrotechnics or thermal cutting; the release mechanisms would sever the physical and electrical interface between the gondola systems and the dropsonde. The slots would have a firm fit with the attached dropsonde to prevent excessive movement from forces during launch and atmospheric insertion, while not being too firm to impede dropsonde release; this is facilitated by a disposable lid structure which restricts the freedom of motion of the dropsondes while in the aeroshell, and is discarded along with the aeroshell after the atmospheric insertion phase.

### 14.3.3. Aerobot gondola

As the 60 km operating environment for the aerobot is at about 260 K (-13°C), 0.24 bar atmospheric pressure and exposed to at least 75% concentration of sulphuric acid, the aerobot gondola needs to entirely encapsulate and protect vulnerable hardware. In addition to that, the gondola also needs to withstand insertion G-loads and protect the gondola items from damage, while fitting into the aeroshell as well. The detailed structural design of the gondola is not treated, however several estimations were made regarding the mass budget of the structure, and recommendations for materials selection and internal configuration are given.

Bearing in mind the physical constraints placed by the aeroshell's conical internal space, the gondola's vertical profile should be as circular as possible. The optimal configuration would be a conical volume, but the round and tapered profile would lead to inefficient packing of the internal subsystems, especially for the mounting of solar panels and the internal payload items. The decision was made to have a rectangular side profile, and a trade-off was made to determine the vertical profile of the gondola, specifically between regular polygonal profiles such as a square or octagonal polygonal profile (Figure 14.2).

The trade-off criteria for the vertical profile are the range of coverage, aspect ratio and number of solar panels as well as the internal volume for a given bounded diameter. A polygon with a higher edge count would allow the gondola photo-voltaic power system to have an almost-hemispherical coverage of the solar environment, but leads to more slender solar panels which would shift the centre-of-gravity of the panel outboard, requiring heavier hinges and stiffening reinforcements to support operational loads. While it is also valid to use a square gondola in conjunction with more sophisticated solar array deployment systems, the square profile has significantly less cross-sectional area than an octagon or a hexagon for the same diagonal length, specifically 71% and 77% respectively. Due to these considerations, the octagonal profile was selected for the gondola's vertical profile.

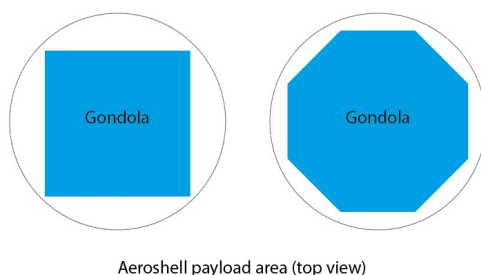


Figure 14.2: Trade-off between rectangular and polygonal top profile of the gondola.

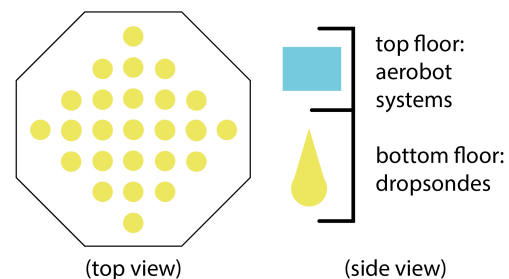


Figure 14.3: Gondola layout

After that, the gondola internal layout was determined. This layout can be seen in Figure 14.3. The

maximum radius for the gondola is 126.1 cm, and the structural weight of the gondola is determined to be 15.696 kg. This is gotten by determining the load at entry ( $369 \text{ m/s}^2$ ), together with safety factors (2 to get to ultimate load and 1.5 for design loads). With these loads, the stresses are then calculated. It was determined that the required thickness was lower than 0.5mm (the lowest thickness of aluminium available), which means that this is the thickness that will be used. The chosen material is AL7075, since this is the lightest material compared to yield stress. By taking a factor of 2.5 to include welds, bolts and minor variation in production quality, a weight of 15.696 kg was found.

For deployment, the top of the gondola will contain a tether winch device that will keep the gondola fixed under the aerobot balloon during the inflation process. As the inflation tanks and mechanisms are situated under the gondola, the inclusion of the winch device keeps inflation tubing short while mitigating large-amplitude oscillations before the aerobot slows down to subsonic speeds [15]. After the inflation phase, the inflation tanks are jettisoned and the winch will begin releasing the tether to reach the full 50 m of tether length. Further description of the operational relation between the winch and the tether is described in the subsequent section. Additionally, the 8 solar arrays and the 1 m boom required for the meteorology suite and seismology microbarometer is folded along the outer perimeter of the gondola, held down by a pyro/thermal cable cutter release mechanism. During deployment, the items will be unfolded by tension springs and latched into their operational configuration. The design of the hinge structure is not treated, and is a recommended point of future study.

#### 14.3.4. Aerobot tether

The tether that connects the gondola with the balloon was sized to have an empty internal core structure to leave room for power and data cables to the microbarometer. A 15mm diameter core was chosen for these cables. Subsequently, Kevlar was used to carry the loads of the gondola. For this, a nominal load of 300 kg was taken. To this load, a safety factor of 2 was determined to get ultimate loads and a factor of 1.5 to get design loads. For Venus, the gravity constant is  $8.87 \text{ m/s}^2$  was gotten, which means that the maximum design load of the tether is 7982 N. This indicates that the kevlar needs an area of  $2.218 \text{ mm}^2$ . Together with the XLPE resin that will be used due to its corrosion resistance, in a common ratio of 1:1, this will be  $4.435 \text{ mm}^2$ . For total corrosion resistance, an  $20 \mu\text{m}$  outer layer of teflon is needed. All added together, this means that the 50 m long tether has a radius of 7.62 mm and a weight of 0.368 kg. The tether is coiled around a circular guide of about 1 m diameter on the top side of the gondola; this is higher than the bend radius of the tether and the internal power and data cables, which are on the order of 10 cm of bending radius. The winch will carry the most of the gondola weight during the deployment phase until the tether is fully extended, where it will then function as a lateral support in nominal operations (Figure 14.4).

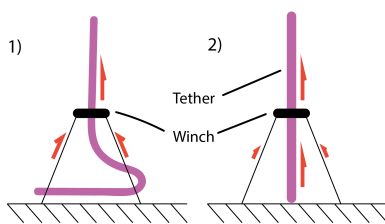


Figure 14.4: Depiction of the loads carried by the tether and winch, 1) during deployment and 2) after deployment.

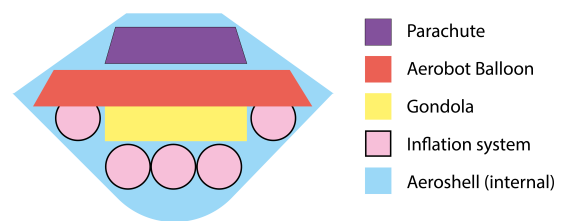


Figure 14.5: Diagram of internal layout of the aeroshell before atmospheric insertion.

#### 14.3.5. Aeroshell

The aeroshell outer structure was defined by the atmospheric entry division, and the size of the aeroshell was constrained by two main factors: the minimal volume from the required internal volume of the aeroshell and the maximal volume from the allowed physical dimensions set by the launcher payload fairing. The diameter of the gondola directly affects the diameter of the aeroshell and transfer module, which leads to a snowball effect increasing the gondola mass, aeroshell mass and transfer module mass.

The estimated mass of the aeroshell internal structure was done with reference to the Venus Flagship and Venus Climate Mission's (VCM) entry vehicle section [15, 16], and is summarised in Table 14.3. It was first assumed that the internal structure of the aeroshell vehicle would scale linearly with payload mass, and as the comparison shows, the structures to payload mass fraction has relatively good agreement with each

other at 37.1% to 42.4% percent mass fraction. As little other resources are available for further refinement of the mass estimate of the aeroshell structure, the heavier mass estimate of 130.45 kg from the VCM mission was used as a first-order estimate. The mass of the inflation system without helium was acquired from Section 7.6, totalling to 118.3 kg without plumbing. A comparison was made between VCM and BLOON due to the similar helium masses (21.8 kg vs 24.96 kg), and it was found that the VCM had a inflation system dry mass of 113.3 kg [16]. This led to an expected BLOON inflation system dry mass of 129.7 kg, inferring that 11.4 kg is used for plumbing and peripherals.

A general internal layout of the aeroshell with payload is included in Figure 14.5. It was decided to situate the helium tanks in the inflation system at the bottom of the gondola for post-insertion deployment considerations. The balloon would first inflate as mentioned in Chapter 7 with the gondola still directly under the balloon, and the inflation system would be jettisoned without concern of collision with the balloon subsystems after inflation. Using the current best estimated masses for the items and their position, the centre of gravity of the entire wet aeroshell totals to about 1058 mm from the leading edge, and is used for preliminary stability analysis of the aeroshell (Section 6.7).

Table 14.3: First order estimate (FOE) table detailing the structural mass of the aeroshell fittings (incl.drogue and main parachutes, internal frames, pyrotechnic devices and cabling) and inflation mechanisms. Note: the payload of the Flagship mission also incorporates a lander, the balloon payload is listed in parentheses [15, 16].

Mission	Payload [kg]	Structural [kg]	Inflation [kg]	Struct./payload	Infl./payload	BLOON structural [kg]	BLOON inflation [kg]
Flagship	845.7 (162.5)	314	127.1	0.371	0.782	113.6	-
VCM	260	110.8	135.1	0.426	0.519	<b>130.45</b>	<b>129.7</b>
BLOON	306 (FOE)			BLOON structural + inflation mass, FOE [kg]			260.2

## 14.4. Risk analysis

This section elaborates on notable risk factors that were expected and treated for the atmospheric segment. The following scales were used to subjectively assess probability and severity of the risks. Probability: 1 = Negligible, 2 = Low, 3 = Concerning, 4 = Likely, 5 = Certain. Severity: 1 = Negligible, 2 = Low effect on mission success, 3 = Partial mission success, 4 = Significant reduction in mission capability, 5 = Critical failure of mission.

- AS1 **Dropsonde release mechanism failure.** The dropsonde release mechanism fails to respond due to incorrect signal or mechanical failure of the mechanism, resulting in an unused dropsonde. Probability = 3, Severity = 3. **Mitigation:** Usage reliable mechanism elements like thermal knives and pyro knives with redundancy, when one element fails; Ample testing of release mechanism is warranted for identification of release system deficiencies; Implement health monitoring of the dropsonde release mechanism. Probability = 1, Severity = 3.
- AS2 **Dropsonde structural failure before target altitude.** As the dropsonde was designed for light mass, the dropsonde pressure vessel may fail and expose internal items to the Venusian atmosphere, leading to lost data. Alternatively, the dropsonde X-tail may fail from high temperatures or not provide ample stability, leading to the dropsonde tumbling and being unable to point the antenna upwards, causing lost data. Probability = 3, Severity = 5 (for dropsonde mission). **Mitigation:** The dropsonde structure would be subject to high-temperature and high-pressure testing, materials tolerance towards high-concentration and high-temperature chemical attack from a sulphuric acid environment. Aerodynamic testing of dropsonde structure for higher Reynolds number is needed. Probability = 1, Severity = 5
- AS3 **Strong oscillatory motions and whiplash-like shocks between balloon and gondola during deployment.** The deployment phase of the aeroshell introduces strong buffeting motions to the aerobot before it reaches low subsonic velocities. These strong buffeting motions may lead to failure of the joint between the balloon, the balloon-tether joint, the tether and the gondola-tether joint, risking mission failure. Probability = 4, Severity = 5. **Mitigation:** The aerobot tether is kept spooled prior to deployment, keeping the gondola fixed to the balloon during inflation, and the aeroshell descent system should continuously slow down the aerobot until the oscillatory motions are damped out. The tether is unspooled after inflation is complete and the oscillatory motions are sufficiently small. The inertial measurement unit in the aerobot gondola ASI instrument can be used to determine a

safe velocity and oscillation amplitude for unspooling. Testing for deployment shock loads and peak aerodynamic loads should be done. Probability = 4, Severity = 1.

AS4 **Aerobot tether tensile failure.** The aerobot tether carries a designed tension load of about 8 kN. The degradation of the tether from the chemical environment may lead to premature failure of the tether, leading to total mission failure. Probability = 3, Severity = 5; **Mitigation:** The tether material selection prioritises performance materials with sufficient resistance towards 85% concentration sulfuric acid. Testing of the tether material should be done in operational conditions, to determine a degradation factor, which can be incorporated in the tether design. Chemical-resistant coatings such as Teflon or Aclar allow for increased endurance. Probability = 2, Severity = 5.

### 14.5. Sensitivity analysis

As the structural design of the aerobot items are sensitive to the volume of the internal subsystems, several key design choices are highlighted in this section. The first item is the number of edges of the gondola's vertical profile. As the aeroshell is a conical volume, this leads to the inefficient packing of a cuboid gondola structure within. However, gondola shapes with non-square or numerous corners may lead to fabrication complexities and higher mass due to the number of corner joints. An octagonal vertical profile is used for more efficient usage of aeroshell internal volume, while a rectangular side profile was used to eliminate the added mass from non-square corner joints. Additionally, an increased aeroshell diameter subsequently increases the aeroshell internal volume, however this leads to further increases in mass of the aeroshell and the transfer module, in terms of propellant needed for transfer module manoeuvres and the structural mass needed to house the aeroshell. Due to that reason, a focus on effective usage of aeroshell volume while minimising the aeroshell diameter was made.

### 14.6. Verification and validation

During the integration of subsystems, the sizing of the individual subsystem items should fit within the gondola, which in turn should fit within the aeroshell. Due to the 3D nature of the fitting, a 3D parametric modelling software, DS CATIA was used for visually determining the placement positions of aeroshell items.

**Volume validation between gondola and aeroshell** During the detailed design phase, it was expected that several subsystem items' sizes would vary until the optimal size was decided upon. Several representative volumes were modelled in 2D and 3D using Adobe Illustrator and DS CATIA respectively for their parametric modelling capabilities, which allowed for changes in dimension and visual feedback regarding the placement of items. This was especially important for fitting the gondola and the inflation system items into the aeroshell's conical internal volume, allowing for accurate determination of the available clearances between items and a better confidence of whether the aeroshell diameter is sufficient enough for fitting all required items.

**Centre-of-gravity validation using parametric 3D modelling** Since the aeroshell structure was modelled in DS CATIA, the centre-of-gravity locations of the aeroshell front and back shells were more accurately known. This in turn improves the accuracy of the estimated aerodynamic stability of the aeroshell.

# 15 Risk, Reliability, Availability, Maintainability, and Safety

This chapter will shortly discuss the risk analysis performed throughout the design. Subsequently, an analysis of the reliability of the three main segments of the BLOON mission: the orbiter, the aerobot and the dro sondes is performed. Hereafter, analyses of the availability, maintainability and the safety of the mission are shown.

## 15.1. Risk analysis

During the risk analyses of the subsystems, risks with a high probability or with a high impact were mitigated accordingly. The mitigation of risks using redundancies, safety factors or other measures is used throughout the design to decrease to probability of risks occurring or to decrease the severity the risks will have. A risk map of all identified risks, before and after mitigation is shown in Figure 15.1 and Figure 15.2. On the left the risks before mitigation are given, while on the right risks after mitigation are given. Due to the general trend of risks moving towards the top and to the left, which means an overall decrease in probability and severity, it can clearly be seen that risks have been mitigated throughout the design phase.

Figure 15.1: Overview of all identified risks before mitigation

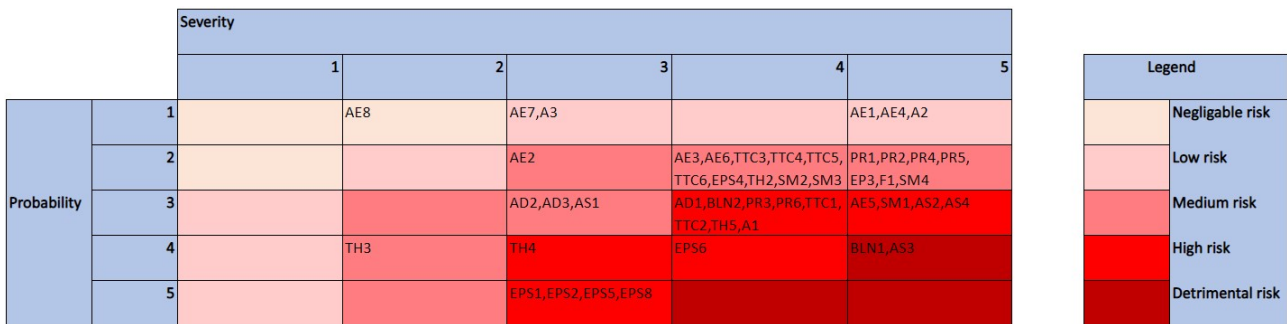
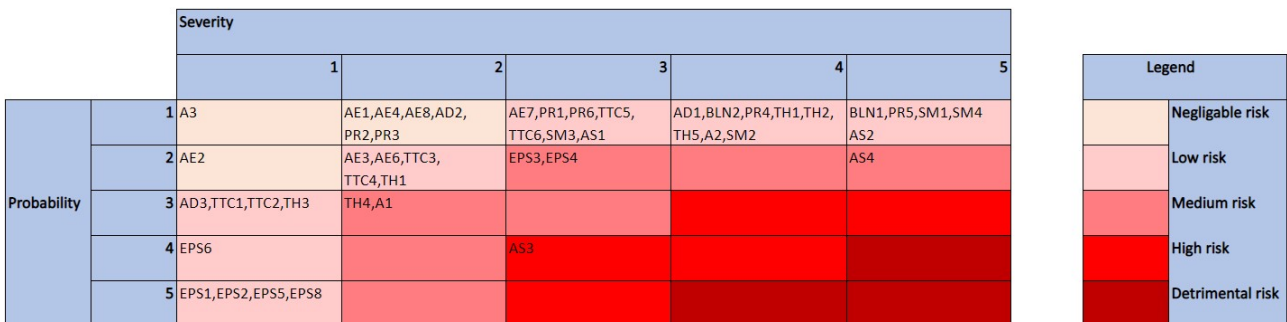


Figure 15.2: Overview of all identified risks after mitigation



It will be stated again that the following scales were used to subjectively assess probability and severity of the risks. Probability: 1 = Negligible, 2 = Low, 3 = Concerning, 4 = Likely, 5 = Certain. Severity: 1 = Negligible, 2 = Low effect on mission success, 3 = Partial mission success, 4 = Significant reduction in mission capability, 5 = Critical failure of mission. Furthermore, the risk identifiers are the ones used when describing the risks identified in Chapter 5 to Chapter 14.

### 15.2. Reliability analysis

The reliability of a system can be determined by using the fact that the total reliability equals the product of underlying component reliability. Note the difference between parts working in parallel and in series. Redundant or back up parts work in parallel with the main part, which increases the overall reliability of the system. Therefore, having redundant components is an important mitigation for parts that have a significant probability of failure. Overall, the use of redundant parts is common practice and applied often in this project, for example a redundant moment wheel in the ADCS subsystem or redundant transponders in the TTC subsystem.

For example, if the reliability of the main part and redundant part are both 90%, then the reliability of the parts working parallel is 99%. With the probability of both parts failing:  $P(\text{both parts fail}) = (1 - 0.9)^2 = 0.01$ . Therefore the reliability is 0.99 or 99%. The three segments that will be analysed for their reliability are the orbiter, the aerobot and the dropsondes. It is assumed that all the important failure risks are mitigated properly and that the design integrated these mitigations. However, the validation of the reliability will be performed using an iterative process where at a minimum one engineering model is used for initial testing, one model for qualification testing and one flight test model. If a model fails during a test, then a subsequent model will be tested. The requirements on the reliability of the segments are given in Table 15.1. Due to the lack of performed tests they can not be checked off at this stage and the checkboxes show 'to be determined'.

Table 15.1: User requirements on safety & reliability.

Identifier	Requirement	Compliance
US-SARE-01-A	The reliability of the orbiter shall be more than 90%.	<TBD>
US-SARE-01-B	The reliability of the high-altitude balloon shall be more than 90%.	<TBD>
US-SARE-02	At least 50% of the dropsondes shall operate successfully with a probability higher than 90%.	<TBD>

#### 15.2.1. Orbiter reliability

Figure 15.3 shows a preliminary reliability block diagram for the orbiter. The diagram does not include all the subsystem components, but it does indicate an overall subsystem reliability. The reliability values from this diagram were used as a reliability budget for the subsystem designs, which leads to a mission reliability of 0.93. It will be stated again that the reliability will have to be validated by post production testing.

Final notes on the diagram are that a successful orbit insertion can be assumed and there are no operations to be performed by the satellite after the 100 days mission ends, therefore the only phase to be assessed is the 100 day operational phase.

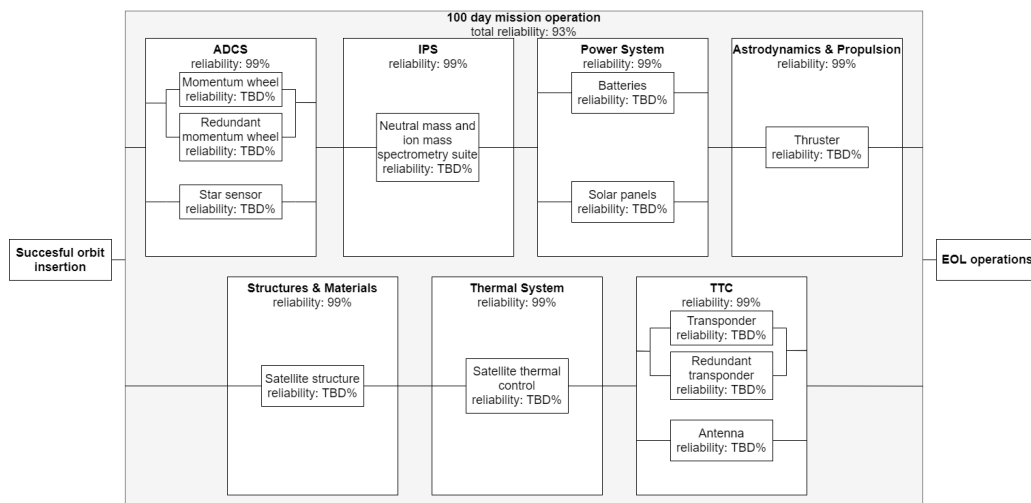


Figure 15.3: Reliability block diagram of the orbiter

**15.2.2. Aerobot reliability**

Figure 15.3 shows a reliability block diagram for aerobot. Again, a successful orbit insertion can be assumed, however atmosphere insertion and the 100 day operational phase should still be assessed. It is not required to perform operations after the 100 day mission is completed, therefore the phase after EOL will not be assessed. Note that not all components have been included in the diagram. However, the method of assessing the reliability is shown and that the subsystems were designed to adhere to this reliability values. This would then lead to an overall reliability of 0.92, including the atmospheric insertion phase. The validation of the reliability will be done by testing of the aerobot.

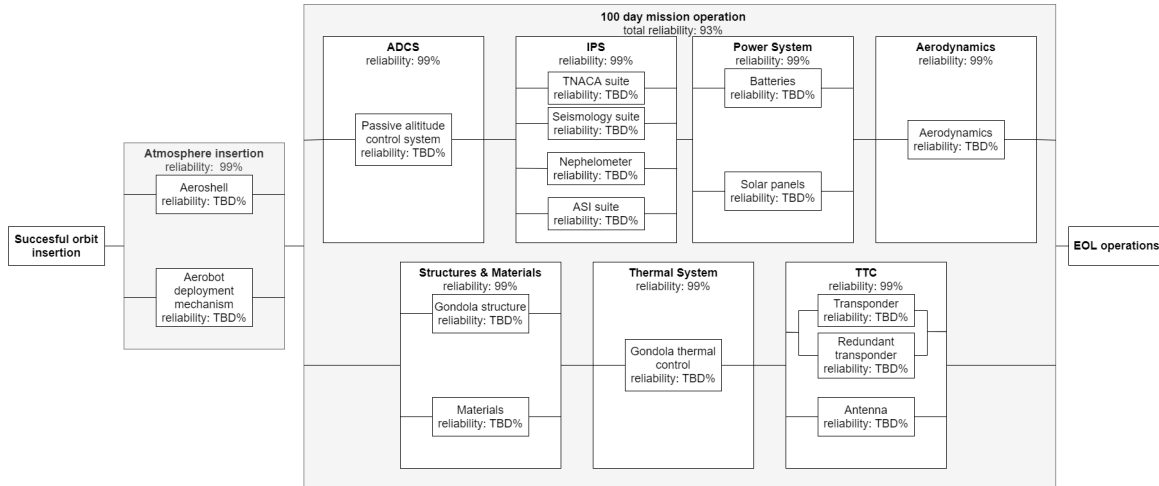


Figure 15.4: Reliability block diagram of one high altitude balloon

**15.2.3. Dropsonde reliability**

The mission is designed to bring 20 dropsondes, therefore a minimum of 10 are required to operate during the mission. Using this, the required reliability of the dropsondes,  $R_1$ , can be found by solving the inequality given in Equation 15.1. The left side of the inequality describes the cumulative probability of 10 or more dropsondes (out of 20) staying operational during the mission. Solving for  $R$  finds a minimum reliability of 0.62 or 62% for a single dropsonde.

However, if only 10 of the 20 dropsondes will work, then the dropsonde measurements do not fulfil the temporal resolution requirements. Therefore, more dropsondes have to be taken, preferably with a higher reliability so the mass budget will not be surpassed. To determine what the best amount of dropsondes is, the increase in mass and the required reliability of a single dropsonde should be assessed and subsequently be traded off. An overview of these parameters is given in Table 15.2.

Table 15.2: The effect of increasing amount of dropsondes on mass and reliability

Amount of dropsondes	$\Delta$ mass [%]	Required reliability [-]
22	10	0.95
23	15	0.92
24	20	0.90
25	25	0.87

It was decided to take 25 dropsondes out of which 20 or more are required to operate during the mission length with a probability of > 90%. This is described by the inequality in Equation 15.2, where  $R_2$  is this reliability. Solving the inequality finds a minimum reliability of 0.87 or 87% for a single dropsonde.

$$\sum_{n=10}^{20} R_1^n \cdot (1 - R_1)^{20-n} \cdot \frac{20!}{n! \cdot (20 - n)!} > 0.9 \quad (15.1)$$

$$\sum_{n=20}^{25} R_2^n \cdot (1 - R_2)^{25-n} \cdot \frac{25!}{n! \cdot (25 - n)!} > 0.9 \quad (15.2)$$

### 15.3. Availability

The availability of the mission can be established by looking at the timeline of the mission. First of all, the mission components must all be produced and tested before the launch date of 2031-05-30, so they are available for launch. The roughly 11 years that are still available are deemed enough for the completion of these phase. Secondly, during the operational phase of the mission the space segments must be available for communication with the ground. An analysis of the communication windows and the implementation of communication components was done in Chapter 9. With the design of the TTC subsystem in mind, the availability of the mission segments is therefore deemed satisfactory for command and data communication. Thirdly and finally, the availability of the mission is connected to the probability of the mission being operational after the 100-day operational phase. After the mission will complete the intended mission lifetime, it is still possible to communicate and perform scientific measurements until the segments fail. It is expected that the dropsondes will be the first segment to be unavailable. This is due to the dropsondes being limited to a quantity of 25 and having an expendable nature. Hereafter, the most likely segment to fail is the balloon as it is operational in the demanding Venusian atmosphere. The last expected mission segment to become unavailable is the orbiter, which can perform scientific measurements using a spectrometer and a camera until it fails, or more probable, until it is disposed into the Venusian atmosphere.

### 15.4. Maintainability

All the mission segments, most notably the orbiter, balloon and the dropsondes will be in orbit around Venus or are deployed in the Venusian atmosphere. Therefore, no physical human interaction is possible with the BLOON segments. However, several maintenance tasks can still be performed. First of all, by keeping an eye on the housekeeping data of the satellite and the balloon, any unexpected software errors can be fixed by sending software updates from the ground. For example, the software for the micro barometers on board of the balloon gondola could be updated to increase the performance of the seismologic measurements. As this is an untested instrument on interplanetary missions it could be a component that requires this type of maintenance. Secondly, the ground segment elements can be maintained during the mission. For example, the 70-m deep space network antennas are currently in the process of being decommissioned, while newer 34-m diameter antennas are set up to replace them. The maintenance of the deep space network ensures stable and high data rate communication.

### 15.5. Safety

Safety will be most important during the production and launch phases of the mission. First of all, the production of the segments requires the operation of heavy machinery and materials. Risk assessment and risk mitigation of the processes encountered in the production phase is considered to be out of the scope of the project. Secondly, during launch there are strict regulations for bystanders and ground operators. For example, the handling of hydrazine propellant will be performed by an operator in protective gear. These regulations will be executed by the launch site and will not be discussed at this stage.

# 16 Design Development

The design development chapter will consist of the design and development logic, the cost breakdown, sustainability and budget breakdown, thereby giving an insight into the organisation for if this mission is further developed. First the Design and development logic is given in Section 16.1, followed by the cost breakdown in Section 16.2 and sustainability in Section 16.3. Finally the budget breakdown is given in Section 16.4

## 16.1. Design and development logic

The mission described in this report can be further developed into an operational mission. The development logic in Figure 16.1 follows the main steps which must be taken before utilisation together with the required ESA qualification and reviews. In Appendix C the planning of this logic is presented in the form of a post-DSE Gantt chart.

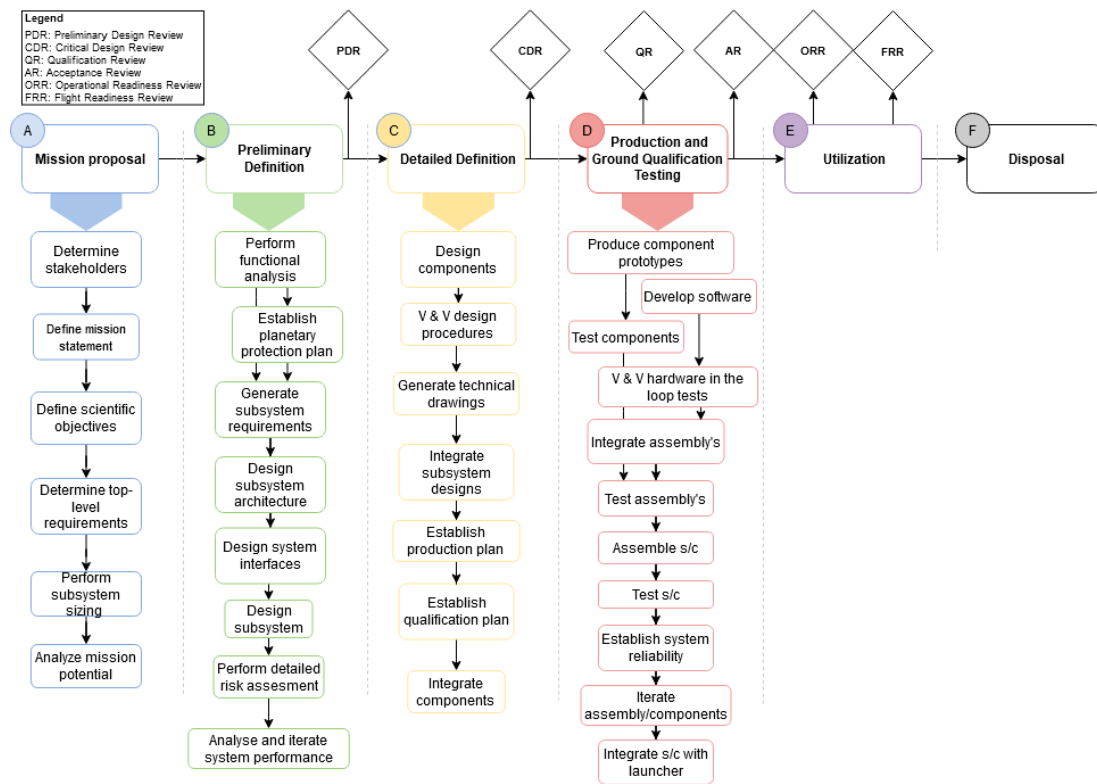


Figure 16.1: Design and development logic

## 16.2. Cost breakdown

To evaluate the cost requirements defined in Table 2.1 a cost breakdown structure is established in Chapter 2, shown in Figure 16.2. The production and development costs of each individual subsystems will not be evaluated due to the uncertainty in development time and production time. Instead, a selection of off-the-shelf components, high TRL and low TRL components will be highlighted to show for which components development time and resources are required. Next to this, production costs will be split into the different mission segments and estimated using comparable missions. It can be seen that the total costs range from €416.8 to 746.8 million.

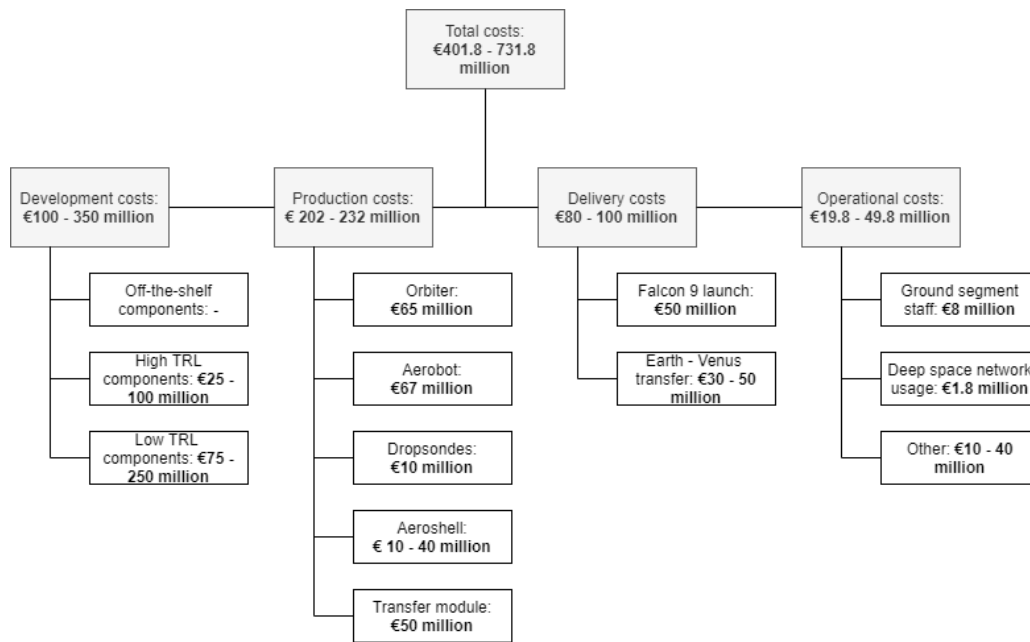


Figure 16.2: Cost breakdown structure of the BLOON mission

### 16.2.1. Development costs

**Off-the-shelf:** Off-the-shelf components require a negligible amount of development time and cost. These components are often tried-and-true due to their heritage on previous missions.

**High TRL:** Components with a high technical readiness level are components that are similar to off-the-shelf components or to heritage components of previous missions. However, the integration into the mission would require some development still. A ballpark estimate of the development cost for this type of components is €25 million to 100 million.

**Low TRL:** Components that have a low technical readiness level will require the most development cost. An example of a component that could have a low technical readiness level is the microbarometer used in the seismology suite. This instrument has only been tested on Earth, therefore there is much uncertainty in the operational feasibility of the instrument on Venus. A ballpark estimate of the development cost for this type of components is €75 million to 250 million.

### 16.2.2. Production costs

**Orbiter:** The costs of the orbiter can be estimated using the fact that it is an interplanetary spacecraft. Furthermore, the BLOON orbiter has a mass of around 460 kg. Therefore, using known production costs of comparable spacecraft, Venus Pioneer and the Mars Observer specifically [47], the costs can be estimated. Note that the currency is dollars from 2000. As the BLOON orbiter has a mass in between the two, the estimation leads to a value of \$49 million in 2000.

- Pioneer Venus s/c bus: \$38 million, 231 kg
- Mars Observer: \$77 million, 1018 kg

Therefore a rough estimate using this data would be €65 million in 2020 for the BLOON orbiter.

**Aerobot:** The Venus Flagship mission study reports the total cost associated with a High-Level Aerial segment similar to the BLOON aerobot to be approximately \$300 million [15]. From this value 25% can be seen as the production costs, which is \$75 million or €67 million. This value is used to estimate the costs of the aerobot, which includes both the superpressure balloon and the gondola carrying the scientific equipment.

**Dropsondes:** The dropsondes are less complex and significantly smaller in size than the orbiter and aerobot. Furthermore, it is known that the total costs of the probes in the Pioneer Venus mission was \$83 million.<sup>1</sup> However, these probes were deployed from the Pioneer Venus spacecraft, compared to the atmospheric deployment of the BLOON dropsondes. A final factor to be taken into account is the fact that the

<sup>1</sup><https://nssdc.gsfc.nasa.gov/nmc/spacecraft/display.action?id=1978-078D>, retrieved June 2020

dropsondes are identical copies of each other which would make the production process more efficient. All in all, a production cost of €10 million for 25 dropsondes is estimated.

**Transfer module:** The transfer module will carry the aerobot until the orbiter has finished aerobreaking, after which it will insert the aerobot into the Venusian atmosphere. It will not carry any scientific equipment, nor will it perform aerobreaking. For these reasons it will be less costly than the orbiter. An estimate of €50 million is made for the production of the transfer module.

**Aeroshell:** At this point, no sources were found that would provide an accurate estimate for the costs of the aeroshell. However, a ballpark estimate of €10 - 40 million can be made.

### 16.2.3. Delivery costs

**Falcon 9 Launch:** The launch of a Falcon 9 costs about €50 million.<sup>2</sup>

**Earth - Venus transfer:** Furthermore, the costs related for transfer will be primarily based on the cost of the propellant. The value for this is a ballpark estimate of €30 to 50 million.

### 16.2.4. Operational costs

**Deep Space Network usage:** The costs that are connected with the operation of the Deep Space Network used for communicating with the mission segments from Earth can be estimated for the 100 day mission duration. The costs with respect to the main downlink signal and the beacon mode signal can be calculated separately. The values for cost per hour are taken from the Deep Space Network manual [108], while the operational time is calculated in Chapter 9.

- Main downlink: 8.4 days · 5074 dollar/hr = \$ 1 million
- Beacon mode signal: 12.5 days · 3171 dollar/hr = \$ 0.95 million
- Total: \$ 2 million or €1.8 million

Furthermore, the cost for using the European VLBI Network for VLBI signals is not included due to a lack of clear costing schemes before officially entering a proposal, but due to the relative low usage of VLBI, it is assumed to be negligible compared to the DSN cost.

**Ground segment staff:** For the 100 day mission duration the costs associated with running a ground segment can be estimated. First of all, to make a size estimate of the ground segment of the BLOON mission, it is compared to the ESA European Space Operations Centre. This facility operates with a permanent staff of 250 people.<sup>3</sup> Multiple mission are operated from this centre, therefore a conservative estimate would be that a staff of 50 is required for operating the BLOON mission. The average hourly wage is set at €200. Therefore, the direct costs associated with the staff for a period of 100 days is  $50 \cdot 100 \cdot 8 \cdot 200 = €8$  million.

**Other:** There are other costs to be considered for the operational costs like maintenance or overhead costs of the facility used. However, no good estimation was able to be performed for these types of costs. A ballpark estimate for this value is €10 to 40 million.

## 16.3. Sustainability

A sustainability strategy is not only of importance during the design phase as was presented at the start of every chapter for the subsystems, but also greatly effects the development of the project. The design mostly has an effect on ensuring that the mission cannot compromise future investigation of Venus. However, sustainability is broader than the preservation of Venus. For the development phase the sustainability of Earth operations is important to guarantee that scientific missions can also be performed in the future. In Table 16.1 the requirements of Earth operations are specified.

<sup>2</sup><https://www.bloomberg.com/graphics/2018-rocket-cost/>, retrieved June 2020

<sup>3</sup>[https://www.esa.int/Enabling\\_Support/Operations/About\\_Operations](https://www.esa.int/Enabling_Support/Operations/About_Operations), retrieved in June 2020

Table 16.1: Compliance matrix sustainability of Earth operations.

Identifier	Requirement
US-SUST-08	Health of all affected shall be ensured conform ISO 45001 standards.
US-SUST-09	Safety of all affected shall be ensured conform ISO 45001 standards.
US-SUST-10	A life cycle assessment shall be performed as defined in ISO 14044.
US-SUST-11	Materials used shall be limited to those listed by ISO/TC20/SC14.
US-SUST-12	Joining chemicals shall be limited to those listed by ISO/TC20/SC14.
US-SUST-13	Chemicals used during production shall be limited to those listed by ISO/TC20/SC14.

Ensuring that all these requirements are met is in the hands of the contractor, but the design should allow for them to meet these requirements. The life cycle assessment (LCA), stated in US-SUST-06, shall be done following guidelines set out by ESA [10] which follows the mentioned ISO standard. The first step in the LCA is the life cycle inventory (LCI). Below the toxic material, chemicals and coatings that have been designed for are listed. This list is not exhaustive as different adhesives and production processes might extend this list. As described in the relevant subsystem chapter the use of these materials was minimised, but no feasible alternatives existed. Even though these materials are toxic they do comply with the standards in Table 16.1.

- **Propulsion** Mixed oxides of nitrogen (MON-1.3) is used as oxidiser and Monomethylhydrazine (MMH) as fuel. Helium is used as a pressurant. For exact quantities refer to Chapter 8.
- **Power** Lithium-ion batteries and AlInGaP/AlInGaAs/InGaAs/Ge solar panels. In-depth life cycle inventories of GaAs solar panels have been made by European Space Agency LCA Working Group [10] and the exact batteries can be found in Chapter 10.
- **Lifting gas** Helium is used as a lifting gas of which the exact quantities can be found in Chapter 7.
- **On-board computers** Trace amounts of the heavy metals like lead, chromium, cadmium and mercury.
- **Thermal insulation** Rigid polymer foam as specified in Chapter 11.
- **Structures** Teflon coating is used as chemical protection layer of the aerobot, dropsondes and tether. Fluoropolymer aclar 33C is coating is used for the balloon. Finally the aluminium panels us black paint as coating.
- **Launch** The Falcon 9 uses cryogenic liquid oxygen and rocket-grade kerosene (RP-1) as propellants. A total inventory of the materials and propellants is done by SpaceX and outside the control of the BLOON design. More information on that can be found in the Falcon 9 user manual [46]. The Falcon 9 boosters are reused which has to be taken in to account in the life cycle inventory.

Lastly the United Nations stresses the importance of communication within sustainability with Sustainable Development Goal number 17. For this reason it is important that the PR team of the missions uses the results of the mission to communicate the importance of the research towards the public. The research being done which is specified in Chapter 4 is highly relevant from environmental stand point. Therefor the commercially more interesting part of the instrumentation (read: imager) should be used to communicate the importance of sustainability.

## 16.4. Budget breakdown

In this section, the mass and power budget are shown and briefly discussed. The cost analysis can be found in Section 16.2, while subsystem specific budgets, for example the link budget and the delta V budget, can be found in their subsystem chapter.

### 16.4.1. Mass budget

The launcher has limited mass that it can bring to Venus. In Table 16.2, the mass budget of the mission can be found, in which the mass is broken down into their subsystem components, which are further broken down in their respective sections in this report. To all the masses, a value of 6.8% is used to account for cabling mass [116], except for the aeroshell, for which a value of 1 kg is chosen. This is discussed in Chapter 10. After that, a design margin of 10% is added for uncertainty in the following design phases and manufacturing (the design mass in Table 16.2). Since the orbiter has a payload mass capacity of 3960 kg, a budget was made to ensure that the mass would not exceed this maximum capacity. 330 kg was reserved for the fairings and the coupling of the payload with the launch vehicle. After that, iterations were done on dry mass values

to determine what the dry mass budgets for the orbiter and the transfer module would be. These are found to be 560 and 1770 kg respectively. These values are used to design towards and give an upper limit to the mass of that design. As can be seen in Table 16.2, both design masses are within the specified budget. The margin is sufficient enough that further investigation can be done to increase the scientific output of the mission by adding additional scientific instruments.

Table 16.2: Mass budget table of subsystems, all in kg. More details can be found in the respective subsystems

Subsystem	Dropsonde	Aerobot	Aeroshell	Transfer module	Orbiter
ADCS	-	-	-	25.6	25.6
Astrodynamics & Propulsion	-	-	-	79.8	41.6
Aerodynamics	-	78.7	15.4	-	-
Thermal	0.02	23.7	466.4	14.8	15.2
IPS	0.01	23.5	-	-	61.0
Power	0.05	34.6	7.3	26.6	41.0
Structures	1.00	16.1	260.2	183.3	131.1
TTC	0.35	14.4	-	22.2	74.2
Cabling (6.8%)	0.10	13.0	1.0	23.8	26.3
Subtotal	1.52	204.0	750.3	376.0	416.1
Margin (10%)	0.15	20.4	75.0	37.6	41.6
Other designs as payload	-	42.0	266.3	1091.6	-
Total dry mass	1.68	266.3	1091.6	1505.2	454.6
Total wet mass	1.68	266.3	1091.6	2167.0	718.0
Budget (dry)	-	-	-	1770.0	560.0

#### 16.4.2. Power budget

In Table 16.3, the power budget is shown, broken down into the power consumption related to each subsystem. Power losses due to cabling and voltage conversions are included as part of the power system's own power consumption. For the photovoltaic systems, power losses differ between eclipse and sunlight operations due to differences in electrical path losses; listed are eclipse losses, which are highest. Design totals include a 25% margin: of this 25%, 10% is intended to be available at launch for unforeseen operational conditions, and the remaining margin is used to account for the possibility of design changes.

The power budget is divided into different operational modes, to support more efficient operation when not all equipment is needed. Eight operational modes are distinguished, being:

1. **Cruise:** Transfer from Earth to Venus. All non-critical or scientific instrumentation hibernates during this phase.
2. **Operations:** Nominal operations, including observations with non-power-intensive scientific instrumentation.
3. **Communications:** Communications with the ground or space segment, depending on the system considered. This refers to main communications, some segments also allow for alternative (low-gain) communications.
4. **Slew:** Slew from one attitude to another, as required for pointing in preparation of communications or scientific observations.
5. **Burn:** Operation of equipment as required to execute trajectory corrections. All non-critical or scientific instrumentation is put into sleep mode during this phase.
6. **Very long baseline interferometry:** Calibration of aerobot tracking equipment is executed using direct Earth-aerobot communication.
7. **Dropsonde dropping:** Operations of the dropsonde when probing the lower atmosphere and supporting communication operations by the aerobot.
8. **Science:** Scientific observations by the aerobot using power-intensive equipment that cannot be operated at all times.

This is only a preliminary division: it is expected that a further subdivision will be made.

Table 16.3: Power consumption profile of the operational segments; totals include a 25% margin.

Consumption (W)	Cruise	Operations	Comms.	Slew	Burn	VLBI	Dropping	Science
<b>Orbiter</b>								
Propulsion	7.9	7.9	7.9	7.9	42.9			
ADCS	56.0	56.0	56.0	126.0	126.0			
IPS	16.0	35.3	35.3	35.3	16.0			
Power	94.1	100.9	122.1	113.8	116.7			
Thermal	197.0	197.0	197.0	197.0	197.0			
TT&C	72.6	72.6	150.6	72.6	72.6			
Contingency (25%)	110.9	117.4	142.2	138.2	142.8			
<b>Total</b>	<b>554.5</b>	<b>587.1</b>	<b>711.2</b>	<b>690.8</b>	<b>714.1</b>			
<b>Transfer module</b>								
Propulsion	7.9	7.9	7.9	7.9	42.9			
ADCS	56.0	56.0	56.0	126.0	126.0			
Power	89.3	89.3	93.3	102.2	112.2			
Thermal	161.0	161.0	161.0	161.0	161.0			
TT&C	14.9	14.9	36.9	14.9	14.9			
Other	102.0	102.0	102.0	102.0	102.0			
Contingency (25%)	107.8	107.8	114.3	128.5	139.7			
<b>Total</b>	<b>538.8</b>	<b>538.8</b>	<b>571.4</b>	<b>642.5</b>	<b>698.7</b>			
<b>Aerobot</b>								
IPS	0.0	1.0	1.0			1.0	1.0	70.4
Power	16.1	17.7	19.9			18.3	19.0	31.0
Thermal	0.0	5.0	5.0			5.0	5.0	5.0
TT&C	8.2	8.2	20.2			10.2	15.2	8.2
Contingency (25%)	6.1	8.0	11.5			8.6	10.1	28.7
<b>Total</b>	<b>30.4</b>	<b>39.9</b>	<b>57.7</b>			<b>43.1</b>	<b>50.3</b>	<b>143.3</b>
<b>Aeroshell</b>								
IPS	0.0							
Power	11.2							
Thermal	40.0							
Other	30.4							
Contingency (25%)	20.4							
<b>Total</b>	<b>102.0</b>							
<b>Dropsonde</b>								
IPS							0.1	
Power							0.3	
TT&C							3.1	
Contingency (25%)							0.9	
<b>Total</b>							<b>4.4</b>	

## 17 Conclusion and Recommendations

The mission need statement of this DSE project is: **Design a mission to measure Venus atmospheric conditions and tectonic activity.** The project objective statement was: **Design a system to perform in-situ measurements of the Venusian atmospheric conditions and tectonic activity of the crust for 100 terrestrial days, with 11 students over 10 weeks time.** Over the course of multiple report iterations, the project objective statement has been fulfilled and can help to answer the mission need statement.

The BLOON mission consists of two main operational elements: the aerobot, a high altitude balloon that loiters at 60 km in the Venusian atmosphere, and the orbiter, a satellite that orbits Venus in a highly elliptical polar orbit and relays scientific data back to Earth. An aeroshell is used to protect the aerobot during atmospheric entry and the aeroshell is surrounded by a transfer module that performs propulsive manoeuvres before arrival at Venus. The Venusian atmosphere down to 25 km is probed by 25 dropsondes. The mission will be able to launch in 2031 with 100 days of nominal scientific operations in 2033.

By measuring the concentration of particles, the composition of the atmosphere, wind patterns at different altitudes, and general atmospheric properties such as temperature and pressure, the aerobot and dropsondes will be able to fulfil the user requirements and can analyse the dynamics and makeup of the Venusian atmosphere. The aerobot will do this throughout its entire operational lifetime and one of the twenty-five dropsondes is released every five days. The dropsondes have a 1 km height resolution. This can help to answer the questions about the meteorological phenomena found on our sister planet. Infrasound measurements are also performed by the aerobot between 0.01 and 5 Hz and will be capable of measuring earthquakes and other acoustic background on Venus. Extended research is performed by the orbiter: measurements of the ionosphere at previously unexplored altitudes and images of Venus at the highest resolution to date make sure that the scientific value of the mission is as high as possible.

However, the fact that the project objective statement is fulfilled does not mean that the design process has to stop. There are recommendations for further research. Firstly, the user requirements regarding reliability could not be officially ticked off due to a lack of performed tests. It is recommended to perform live testing or extensive simulations in order to check that these can be met. In general, possibilities for extra science on the orbiter could be considered. Furthermore, the data rate of the dropsondes allows for more instrumentation. It is also possible to instead increase the sampling rate of the dropsondes to increase the measurement accuracy. In general, the shape of the dropsondes could be optimised and a more miniaturised payload might fit in the structure. The fact that the BLOON mission will take place in a similar time frame to the EnVision mission could allow for cooperation between the two missions.

Most of the other recommendations concern specific subsystems. For astrodynamics, it is recommended to research decay due to third body perturbation of the sun in more detail. A more detailed orbital analysis would also optimise the capture and insertion orbits. For propulsion, the pressure of the tanks can be analysed over time with a non-adiabatic solution. The tank design could also possibly be optimised by using metal-carbon fibres. For TTC it is recommended to perform more research in smaller considerations to availability, such as solar conjunction and rainfall. Research into the possibility of using the downlink signal to perform radio occultation could also be performed. Finally, the possibility to use the orbiter camera to track the aerobot visually could be viable. Regarding EPS, more research on the low depth-of-discharge use of high-energy, low-cycle batteries could be beneficial for system elements with a medium-high cycle life requirement, and the aerobot could benefit from a smaller PCDU. The thermal subsystem recommends to take a look at NASA's HEET heat shield, which should have reached a high enough TLR at the time of mission production. For ADCS, the use of an inertial measurement unit could be considered to improve the attitude determination. Finally, the structures subsystem proposes that finite element model (FEM) analysis during launch could optimise the mass of the payload structure. The structure of the aeroshell could also benefit by considering shapes with different half-angles.

All in all, the BLOON mission has successfully fulfilled its project objective statement, is capable of answering the mission need statement and also still allows room for further research possibilities.

# References

- [1] D. R. Williams. *Venus fact sheet*, Sep 2018.
- [2] K. De hulsters et al. *Remote sensing probe for the Venusian atmosphere and tectonics, Project Plan*. TU Delft, Apr 2020.
- [3] K. De hulsters et al. *Remote sensing probe for the Venusian atmosphere and tectonics, Baseline report*. TU Delft, May 2020.
- [4] K. De hulsters et al. *Remote sensing probe for the Venusian atmosphere and tectonics, midterm report*. TU Delft, May 2020.
- [5] Dr.ir. A.H. van Zuijlen Dr.ir. F.F.J. Schrijer. Project guide DSE, April 2020. TU Delft.
- [6] F. W. Taylor. *The Scientific Exploration of Venus*. Cambridge University Press, 2014.
- [7] *The Holy Bible: containing the Old and New Testaments*, 2010.
- [8] R. Herrick et al. *Goals, objectives, and investigations for Venus exploration: 2016*. VEXAG, NASA, 2016.
- [9] D.J. Stevenson et al. Probing the interior structure of Venus. Technical report, Keck Institute for Space Studies, 2015.
- [10] T. Maury et al. Application of environmental life cycle assessment (lca) within the space sector: a state of the art. *Acta Astronautica*, 2020.
- [11] Gro Harlem Brundtland, M Khalid, S Agnelli, S Al-Athel, and BJNY Chidzero. Our common future. *New York*, 8, 1987.
- [12] G. Kminek et al. The international planetary protection handbook. *Space Research Today*, 205:e1–e120, 2019.
- [13] A. Debus. *RNC-CNES-R14: Planetary protection requirements*. CNES, 2002.
- [14] J. L. Hall et al. Prototype design and testing of a venus long duration, high altitude balloon. *Advances in Space Research*, 42:1648–1655, 2007.
- [15] M. Bullock et al. *Venus Flagship Mission Study: Report of the Venus Science and Technology Definition Team*, 03 2009.
- [16] D. Grinspoon et al. *Venus climate mission*. NASA, 2009.
- [17] C. F. Wilson et al. The 2010 European Venus explorer (EVE) mission proposal. *Experimental astronomy*, 33(2-3):305–335, 2012.
- [18] L. S. Friedrich et al. A comparison of loon balloon observations and stratospheric reanalysis products. *Atmospheric Chemistry and Physics*, January 2017.
- [19] Y. Futaana et al. Solar wind interaction and impact on the Venus atmosphere. *Space Science Reviews*, 212(3-4):1453–1509, 2017.
- [20] S. Limaye et al. Venus atmosphere: Major questions and required observations. *Planetary Science Decadal Survey Inner Planets Panel*, 2009.
- [21] S. Krishnamoorthy et al. Detection of artificially generated seismic signals using balloon-borne infrasound sensors. *Geophysical Research Letters*, 45(8):3393–3403, 2018.
- [22] S. Krishnamoorthy et al. Aerial seismology using balloon-based barometers. *IEEE Transactions on Geoscience and Remote Sensing*, 57(12):10191–10201, 2019.
- [23] Venus Seismology Study Team. Probing the interior structure of venus. Technical report, Keck Institute for Space Studies (KISS), 2015.
- [24] R. Garcia et al. Detecting atmospheric perturbations produced by venus quakes. *Geophysical Research Letters*, 32(16), 2005.
- [25] A.J. Kliore et al. The venus international reference atmosphere. *Advances in Space Research*, 5(11), 1985.
- [26] Inc. Paroscientific. *Digiquartz Broadband Barometers*.
- [27] P. Lognonné et al. Seis: Insight’s seismic experiment for internal structure of mars. *Space Science Reviews*, 215(1):12, 2019.
- [28] B. Ragent et al. Pioneer Venus sounder and small probes nephelometer instrument. *IEEE Transactions on Geoscience and Remote Sensing*, GE-18(1):111–117, 1980.
- [29] H.B. Niemann et al. The gas chromatograph mass spectrometer for the Huygens probe. *Space Science Reviews*, 104(1/4):553–591, 2002.
- [30] P.R. Mahaffy et al. The sample analysis at Mars investigation and instrument suite. *Space Science Reviews*, 170(1–4):401–478, Apr 2012.
- [31] J. Balcerski et al. Leaves: Lofted environmental and atmospheric venus sensors, phase i final report. Technical report, Ohio Aerospace Institute & NASA Glenn Research Center, 2019.
- [32] N. Wells et al. Atmospheric microprobes for Venus: A preliminary probe design and localisation method. In *8th ESA Workshop on Advanced Space Technologies for Robotics and Automation*, ESTEC, Noordwijk, The Netherlands, 2004.
- [33] G. Hunter and D. Culley. *Extreme Environment Electronics in NASA’s Aeronautics Research*, pages 41–48. CRC Press, 2012.
- [34] K. Klaasen and R. Greeley. VEVA: Discovery mission to Venus: Exploration of volcanoes and atmosphere. In *International Conference on Low-Cost Planetary Missions*, 2000.
- [35] Y. Futaana et al. Solar wind interaction and impact on the Venus atmosphere. *Space Science Reviews*, 2017.
- [36] A. K. Singh and A. Bhargawa. Prediction of declining solar activity trends during solar cycles 25 and 26 and indication of other solar minimum. *Astrophysics and Space Science*, 364(12), 2018.
- [37] S. Barabash et al. The analyser of space plasmas and energetic atoms (aspera-4) for the venus express mission. *Planetary and Space Science*, 55(12):1772–1792, Oct 2007.
- [38] Benna M. et al. *MAVEN NGIMS PDS Software Interface Specification*. Mars Atmosphere and Volatile Evolution (MAVEN) Neutral Gas and Ion Mass Spectrometer (NGIMS) Team.
- [39] Jr. Waite, J. H. et al. The Cassini ion and neutral mass spectrometer (inms) investigation. *Space Science Reviews*, 114(1–4):113–231, Sep 2004.
- [40] B. Zandbergen. *Aerospace Design & Systems Engineering Elements I (spacecraft reader)*. TU Delft, 2020.

- [41] W.J. Markiewicz et al. Venus monitoring camera for Venus Express, planetary and space science. *Planetary and Space Science*, 55(12), 2007.
- [42] *KAI-101 Interline CCD Image Sensor*, May 2015.
- [43] G. Fjeldbo et al. The neutral atmosphere of Venus as studied with the Mariner V radio occultation experiments. *Astronomical Journal*, 76:123–139, 1971.
- [44] ESA study and CDF teams. *EnVision CDF study executive summary*, 2018.
- [45] United Launch Alliance and Lockheed Martin Commercial Launch Services. *Atlas V launch services users guide*, July 2010.
- [46] SpaceX. *Falcon user's guide*, January 2019.
- [47] W. J. Larson and J. R. Wertz. *Space mission analysis and design*. Microcosm, Inc., 1992.
- [48] K.F. Wakker. *Fundamentals of astrodynamics*. Faculty of Aerospace Engineering Delft University of Technology, 2015.
- [49] AZUR SPACE. *QJ Solar Cell 4G32C - Advanced*, 2019.
- [50] H. Toyota et al. Venus climate orbiter PLANET-C solar array development. In *8th European Space Power Conference*, volume 661, 2008.
- [51] Nørstrud H. Meese E.A. Simulation of convective heat flux and heat penetration for a spacecraft at re-entry. *Aerospace Science and technology*, pages 185–196, 2002.
- [52] K. Sutton and R.A. Graves. A general stagnation-point convective-heating equation for arbitrary gas mixtures. NASA technical report, Langley Research Center, 1971.
- [53] J. C. Ellison. Experimental stagnation-point velocity gradients and heat-transfer coefficients for a family of blunt bodies at Mach 8 and angles of attack. *Nasa technical note*, pages 1–26, 1969.
- [54] S. Lebonnois et al. Superrotation of Venus' atmosphere analyzed with a full general circulation model. *Journal of Geophysical Research: Planets*, 115, June 2009.
- [55] T. Kremic et al. Long-duration Venus lander for seismic and atmospheric science. *Planetary and Space Science*, 190, April 2010.
- [56] Dr. F. Oliviero and Phd. A. Cervone. *Aerospace Design & Syst. Eng. Elements II (AE-2111-II) slides*. TU Delft, 2018.
- [57] D. R. Williams. *Pioneer Venus Project Information*. NASA Goddard Space Flight Center, NASA, 2018.
- [58] E. Lakdawalla. Akatsuki's new orbit, first images, and science plans. *The planetary society*, 2015.
- [59] S. Kembale. *Interplanetary Mission Analysis and Design*. Springer, 2006.
- [60] *Lecture slides*. TU Delft, 2019.
- [61] P. Gallais. *Atmospheric re-entry vehicle mechanics*. Springer Science & Business Media, 2007.
- [62] J. Bertaux et al. A warm layer in Venus' cryosphere and high-altitude measurements of hf, hcl, h<sub>2</sub>o and hdo. *Nature*, 450(7170):646–649, 2007.
- [63] G Ben-Dor et al. A simple and accurate expression for the viscosity of nonpolar diatomic gases up to 10,000 k. *AIAA journal*, 23(4):636–638, 1985.
- [64] Crane. Flow of fluids through valves, fittings, and pipe. Technical report, Crane Company, 1988.
- [65] M.E. Tauber et al. Stagnation point radiative heating relations for Venus entry. Technical report, ERC Corp., Huntsville, Alabama, 2012.
- [66] R. Goulard. The coupling of radiation and convection in detached shock layers. *Journal of Quantitative Spectroscopy and Radiative Transfer*, 1(3-4):249–257, 1961.
- [67] M.E. Tauber and R.M. Wakefield. Heating environment and protection during Jupiter entry. *Journal of Spacecraft and Rockets*, 8(6):630–636, 1971.
- [68] R.W. Leonard et al. Design of a Mars entry "aeroshell". In *Buckling of structures*, pages 346–364. Springer, 1976.
- [69] G.A. Cohen. Structural optimization of sandwich and ring-stiffened 120 degree conical shells subjected to external pressure. NASA contractor report, Philco-Ford Corporation, Newport Beach, California, 1969.
- [70] J.M. Davies. *Lightweight sandwich construction*. John Wiley & Sons, 2008.
- [71] H.K. Tran et al. Phenolic impregnated carbon ablaters (PICA) as thermal protection systems for discovery missions. NASA technical memorandum 110440, Ames Research Center, 1997.
- [72] M.A. Covington. Performance of a light-weight ablative thermal protection material for the Stardust mission sample return capsule. NASA technical report, Eloret Corporation, 2005.
- [73] M. Mahzari et al. Sizing and margin methodology for dual-layer thermal protection systems. NASA technical report, Ames Research Center, 2018.
- [74] *Lecture #1: Stagnation Point Heating*. NASA, 2012.
- [75] D.K. Prabhu et al. Atmospheric entry studies for Venus missions: 45 sphere-cone rigid aeroshells and ballistic entries. NASA technical report, Ames Research Center, 2013.
- [76] A. Seiff and D. B. Kirk. Structure of the Venus mesosphere and lower thermosphere from measurements during entry of the Pioneer Venus probes. *Icarus*, 49(1):49–70, 1982.
- [77] Sighard F. Hoerner. Fluid dynamic drag, published by the author. *Midland Park, NJ*, pages 16–35, 1965.
- [78] C. Davies et al. Planetary mission entry vehicles quick reference guide. version 3.0. NASA technical report, Eloret Corporation, 2006.
- [79] S. Mohr and J. Ward. Helium production and possible projection. *Minerals 4*, 130–144, 2014.
- [80] L. A. Carson and W. J. Horn. *A Unified Thermal and Vertical Trajectory Model for the Prediction of High Altitude Balloon Performance*. Texas A&M University, NASA, 1981.
- [81] R. E. Farley. *BalloonAscent: 3-D Simulation Tool for the Ascent and Float of High-Altitude Balloons*. NASA, GSFC, Greenbelt, Maryland, 20771, 2005.
- [82] M. van den Berg and P. Falkner. *Study overview of the Venus entry probe*. ESTEC Noordwijk, 2007.
- [83] D. Singh. Venus nightside surface temperature. *Scientific reports*, 2019.
- [84] A. Migliorini et al. Investigation of air temperature on the nightside of Venus derived from VIRTIS-H on board Venus Express. *Icarus*, 217:640–647, 2012.

- [85] J. L. Hall et al. Second generation prototype design and testing for a high altitude venus balloon. *Advances in Space Research*, 44:93–105, 2008.
- [86] J. L. Hall et al. Technology development for a long duration, mid-cloud level Venus balloon. *Advances in Space Research*, 48:1238–1247, 2011.
- [87] M. S. Smith and E. L. Rainwater. Optimum designs for superpressure balloons. *Advances in Space Research*, 2004.
- [88] N. Yajima et al. *Scientific Ballooning*. Springer, Corona Publishing Co., Ltd, Tokyo, 2009.
- [89] MT Aerospace. *Spacecraft propellant tanks*, 2020.
- [90] D. Portugaels et al. Determination of aerodynamic force coefficients of octagonal lighting columns from wind tunnel experiments. *Proceedings of the 5th IASME / WSEAS International Conference on Fluid Mechanics and Aerodynamics*, 2007.
- [91] V. V. Kerzhanovich et al. Major progress in planetary aerobot technologies. In *2007 IEEE Aerospace Conference*, pages 1–11. IEEE, 2007.
- [92] J. A. Cutts et al. Technology perspectives in the future exploration of Venus. *Geophysical Monograph Series*, 2007.
- [93] P. Sivac and T. Schirmann. The Venus Express spacecraft system design. *Venus Express*, 2004.
- [94] Ariane group orbital propulsion. *10N, 200N, 400N chemical bi-propellant thruster family*.
- [95] F. V. Bel and M. Lang. The role of different parameters in the pressurant budget of Venus Express and its dynamic evolution during the mission. *ESASP*, 555:115–1, 2004.
- [96] R. Lescouzères et al. Propulsion system development and verification activities for the 2016 ExoMars trace gas orbiter. *Space Propulsion Conference 2014, SP2014 2968951*, 2014.
- [97] National Library of Medicine PubChem. *Compound Summary Dinitrogen tetroxide*.
- [98] National Library of Medicine PubChem. *Compound Summary Methylhydrazine*.
- [99] Titanium ti-6al-4v (grade 5), annealed. ASM Material Data Sheet.
- [100] J. Taylor. *The Deep Space Network: A Functional Description*. John Wiley & Sons, Inc., 2016.
- [101] M. Lindqvist. *European VLBI Network: Biennial Report 2017 - 2018*. European VLBI Network, Onsala Space Observatory, Nov 2018.
- [102] *Spectrum 101: An Introduction to National Aeronautics and Space Administration Spectrum Management*, Feb 2016.
- [103] S. Slobin et al. *DSN: 34-m BWG Stations Telecommunications Interfaces*. JPL, 2015.
- [104] J. Taylor et al. Cassini orbiter/Huygens probe telecommunications. *JPL*, page 3, 2002.
- [105] J. Oschlisniok et al. 3.6 cm signal attenuation in Venus’ lower and middle atmosphere observed by the radio science experiment VeRa onboard Venus Express. *Icarus*, pages 478–, 09 2012.
- [106] Consultative Committee for Space Data Systems. *Report Concerning Space Data System Standards: Bandwidth-Efficient Modulations*, Feb 2018.
- [107] T. Imamura et al. Radio occultation experiment of the Venus atmosphere and ionosphere with the Venus orbiter Akatsuki. *Earth Planet Sp*, 63:493–501, 2011.
- [108] S. Slobin et al. *NASA’s Mission Operations and Communications Services*. NASA, Oct 2014.
- [109] P.W. Kinnian and J.B. Berner. Two-way ranging during early mission phase. In *2003 IEEE Aerospace Conference Proceedings*, volume 3, pages 3–1441–3–1455. IEEE, 2003.
- [110] C.L. Thornton and J.S. Border. *Radiometric Tracking Techniques for Deep-Space Navigation*. John Wiley & Sons, 2005.
- [111] C. Thornton and J. Border. Range and doppler tracking observables. *JPL*, 2005.
- [112] L. Iess et al. Improved doppler tracking systems for deep space navigation. In *23rd International Symposium on Space Flight Dynamics*, 2012.
- [113] R.Z. Sagdeyev et al. Differential VLBI measurements of the Venus atmosphere dynamics by balloons: VEGA project. *Astronomy And Astrophysics*, 1992.
- [114] E. Choi. *Magellan Satellite Buses*, 2020.
- [115] Terma Space. *Modular medium power unit data sheet*, 2012.
- [116] C.D. Brown. *Elements of spacecraft design*. American Institute of Aeronautics and Astronautics, 2002.
- [117] J. R. Wertz et al. *Space mission engineering: the new SMAD*. Microcosm Press, 2011.
- [118] Wilfried Ley, Klaus Wittmann, and Willi Hallmann. *Handbook of space technology*, volume 22. John Wiley & Sons, 2009.
- [119] D. Heynderickx et al. ESA’s space environment information system (SPENVIS) - a WWW interface to models of the space environment and its effects. In *38th Aerospace Sciences Meeting and Exhibit*, page 371, 2000.
- [120] G. Landis et al. Atmospheric flight on Venus. In *40th AIAA Aerospace Sciences Meeting & Exhibit*, page 819, 2002.
- [121] AZUR SPACE. *Silicon bypass diode*, 2019.
- [122] Qioptiq. *Space-qualified Cover Glass*, 2020.
- [123] Qioptiq. *Space-qualified Optical Solar Reflectors*, 2020.
- [124] J. J. Wijker. *Spacecraft structures*. Springer Science & Business Media, 2008.
- [125] J.K. Paik et al. The strength characteristics of aluminum honeycomb sandwich panels. *Thin-walled structures*, 35(3):205–231, 1999.
- [126] F.C. Krause et al. Implementation of commercial Li-ion cells on the MarCO deep space CubeSats. *Journal of Power Sources*, 449:227544, 2020.
- [127] E. Darcy. *Passively Thermal Runaway Propagation Resistant Battery Module that Achieves > 190 Wh/kg*. NASA, 2016.
- [128] Terma Space. *Battery C/D regulation module data sheet*, 2012.
- [129] N. Anderson et al. 18650 cell bottom vent: Preliminary evaluation into its merits for preventing side wall rupture. NASA technical report, Johnson Space Center, 2016.
- [130] J. Giorgini et al. Magellan aerobrake navigation. *Journal of the British Interplanetary Society*, 48(3):111–122, 1995.

- [131] M. Keyser and E. Darcy. Driving factors for achieving safe, high performing li-ion battery designs. NASA technical report, National Renewable Energy Laboratory, 2016.
- [132] J. Haines. Power system design of the Venus Express spacecraft. In *3rd International Energy Conversion Engineering Conference*, page 5669, 2005.
- [133] H. Toyota et al. On-orbit operations of a power system for Japan's Venus explorer Akatsuki. In *E3S Web of Conferences*, volume 16, page 18004. EDP Sciences, 2017.
- [134] Sheldahl. *Redbook*, 2020.
- [135] RUAG Space. *Thermal insulation products*.
- [136] M. M. Finckenor and D. Dooling. Multilayer insulation material guidelines. NASA technical report, Marshall Space Flight Center, 1999.
- [137] C. D. Brown. *Elements of spacecraft design*. American Institute of Aeronautics and Astronautics, 2002.
- [138] M. Ashby et al. *Materials: engineering, science, processing and design - Third edition*. Butterworth-Heinemann, 2014.
- [139] A. Sanchez-Lavega and others. The atmospheric dynamics of Venus. *Space Science Reviews*, 2017.
- [140] Qing Chang et al. Magnetic field near Venus: Comparison between solar cycle 24 and previous cycles. *The Astrophysical Journal*, 2018.
- [141] S. Starin and J. Eterno. *Attitude Determination and Control Systems*. Microcosm Astronautics Books, 2011.
- [142] S.P. Rawal. Metal-matrix composites for space applications. *Jom*, 53(4):14–17, 2001.
- [143] D. Gay. *Composite materials: design and applications*. CRC press, 2014.
- [144] *ECSS-E-HB-32-20 Part 5A – Structural materials handbook – Part 5: New advanced materials, advanced metallic materials, general design aspects and load transfer and design of joints*. Noordwijk, The Netherlands, 2011.
- [145] T. Miyoshi et al. Alporas aluminum foam: production process, properties, and applications. *Advanced engineering materials*, 2(4):179–183, 2000.
- [146] R.C. Rice. *Metallic Materials Properties Development and Standardization (MMPDS): Chapters 1-4*, volume 1. National Technical Information Service, 2003.
- [147] M. Macdonald and V. Badescu. *The international handbook of space technology*. Springer, 2014.
- [148] J.P Peterson et al. Buckling of thin-walled circular cylinders. NASA technical report, Langley Research Center, 1968.
- [149] D.J. Inman et al. *Engineering vibration*. Prentice Hall, Englewood Cliffs, NJ, 1994.
- [150] J. Sinke. *Production of Aerospace Systems (AE3211-II) reader*. TU Delft, 2020.
- [151] H. S. Rauschenbach. *Solar Cell Array Design Handbook*. Van Nostrand Reinhold Company, 1980.
- [152] RUAG. *SEPTA 41 Solar array drive assembly*, 2012. Data sheet.
- [153] *ECSS-E-ST-33-01C: Space Engineering: Mechanisms*. Noordwijk, The Netherlands, 2009.

# A Hardware/Software Diagram

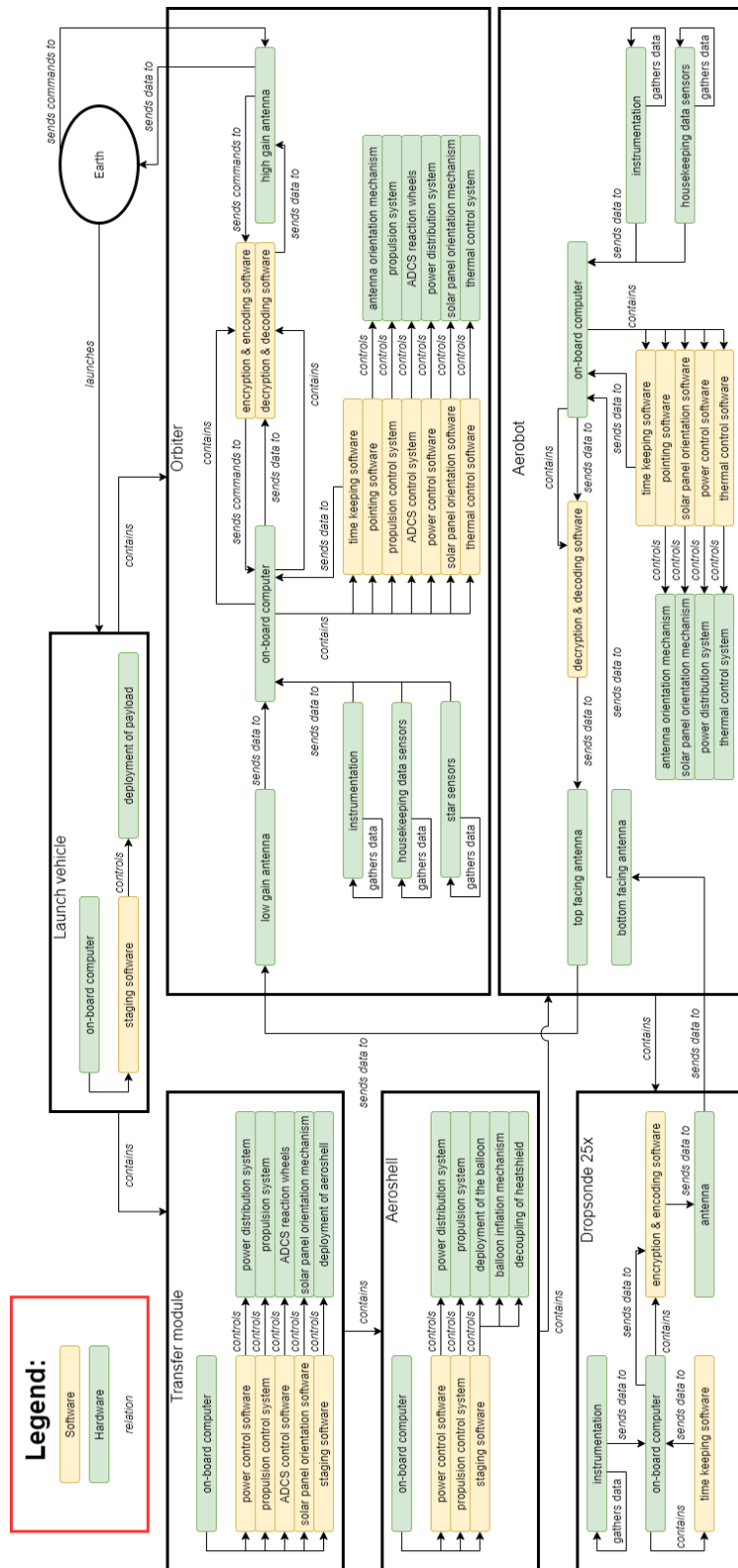


Figure A.1: Hardware/Software diagram

## B Logic Diagrams

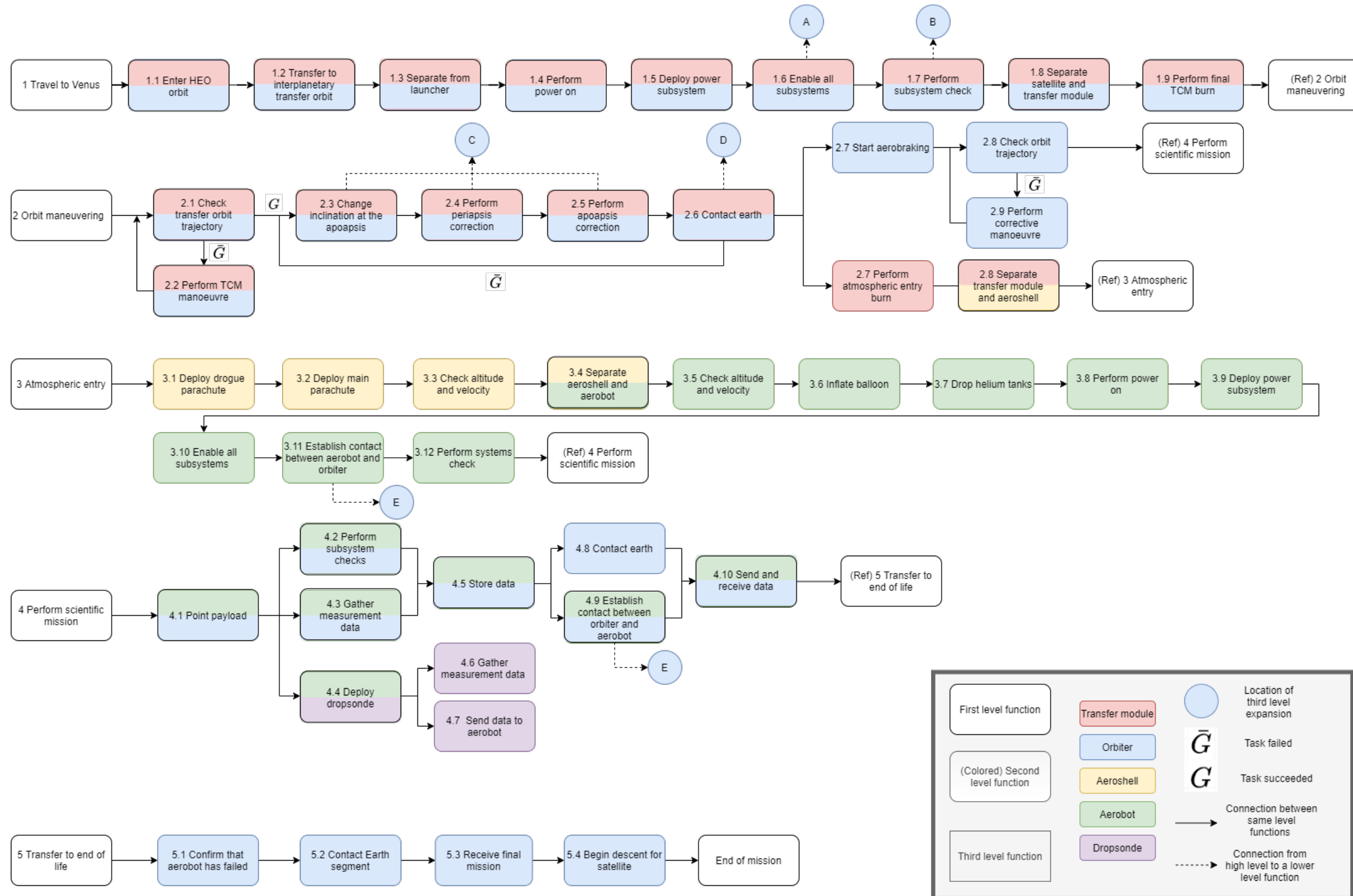


Figure B.1: Functional flow diagram

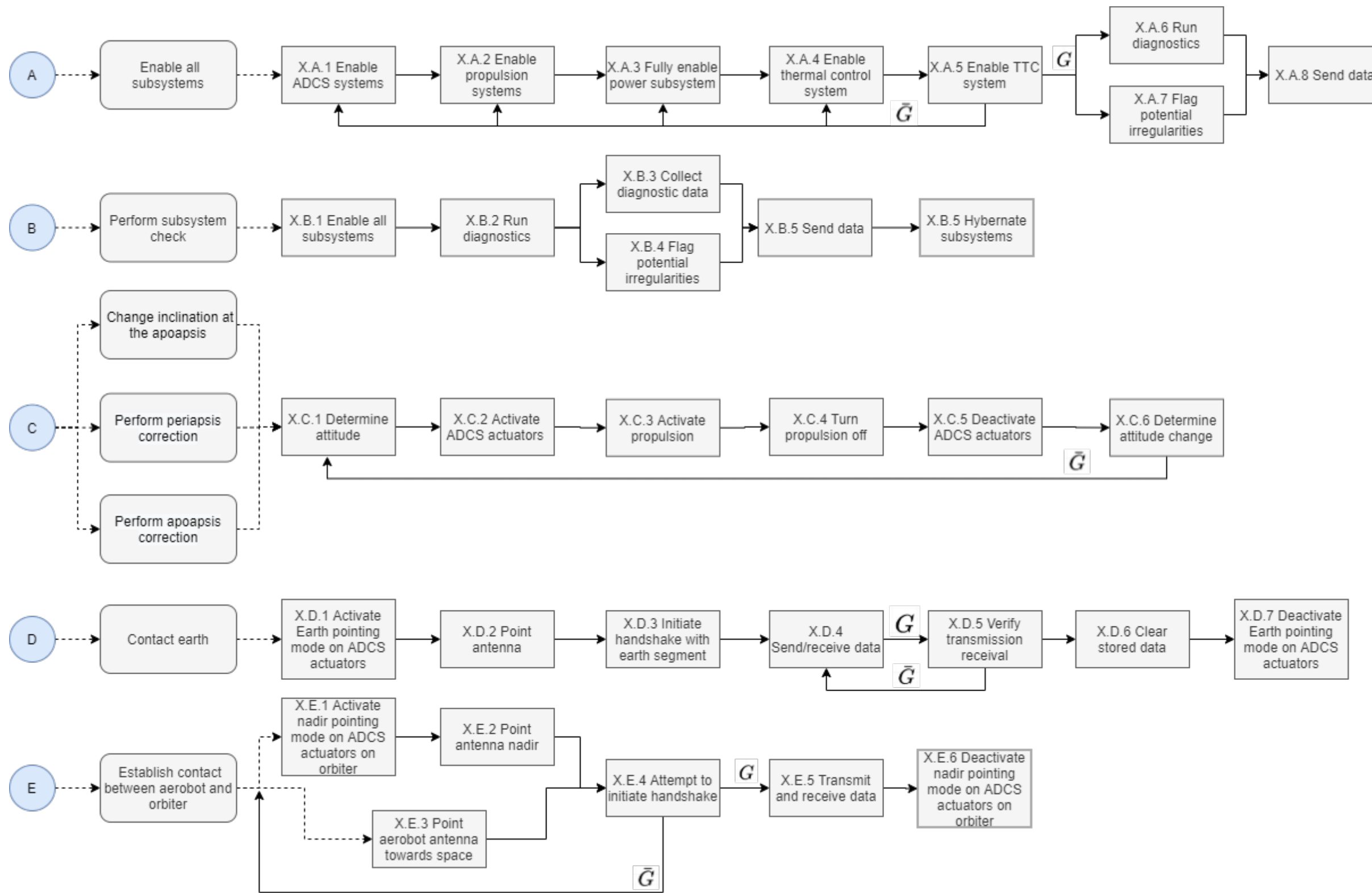


Figure B.2: Functional flow diagram

# C Project Gantt Chart



Figure C.1: Project Gantt chart